Theses and Dissertations

5-10-2014

Hydroflux Synthesis: A New and Effective Technique for Exploratory Crystal Growth

Michael William Chance
University of South Carolina

Follow this and additional works at: https://scholarcommons.sc.edu/etd

 Part of the Chemistry Commons

Hydroflux Synthesis:
A New and Effective Technique for Exploratory Crystal Growth

by

William Michael Chance

Bachelor of Science
Murray State University, 2007

Submitted in Partial Fulfillment of the Requirements

For the degree of Doctor of Philosophy in

Chemistry

College of Arts and Sciences

University of South Carolina

2014

Accepted by:

Hans-Conrad zur Loye, Major Professor

Daniel Reger, Committee Member

Harry Ploehn, Committee Member

Brian Benicewicz, Committee Member

Lacy Ford, Vice Provost and Dean of Graduate Studies

ii

Dedication

This work is dedicated to my family, my friends, and especially my wife.

Acknowledgements

Throughout my education, a number of individuals have contributed to my growth as an individual and as a scientist. I owe much to their efforts and would like to now try to express my gratitude in words.

First and foremost, I would like to thank my advisor, Dr. Hans-Conrad zur Loye. You have instilled a true passion for materials research in me. My interests are widely varied and I could have ended up in a number of fields, but I have found my true calling thanks to you. Having the freedom to do exploratory research has been challenging and rewarding. Thank you for your patience, your encouragement, and knowing when to motivate me.

Next, I would like to acknowledge the members of my Ph.D. committee. You have given your time and energy to help develop me as a scientist. Our discussions and your suggestions are greatly appreciated. Thank you, Dr. Dan Reger, Dr. Brian Benicewicz, and Dr. Harry Ploehn.

I am also grateful to Dr. Mark Smith for his efforts. He has solved a number of the crystal structures in this thesis. He has also been a gracious resource in the instances when he did not solve the structures. Thank you, Mark, for your willingness to assist a hobbyist crystallographer in learning.

Having shared many hours in the laboratory, I must thank a number of members of the zur Loye research group. Your discussions, ranging topics from research to the mundane, were often just what I needed to keep my focus on research or offer respite,

when necessary. I consider myself fortunate to have shared the lab with an excellent group that has included Dr. Peter Barber, Dr. Arief Wibowo, Allison Latshaw, Jackie Cantwell, Nathan Trenor, Karl zur Loye, Tim Ferreria, and Kendall Hughey. A number of other members have made significant contributions. Special thanks must go to Dr. Dan Bugaris and Dr. Jeongho Yeon; I am indebted to you both for your contributions to my research and growth as a scientist.

To the many dedicated teachers who challenged me at every level, thank you for giving your all. I have learned from watching my wife how demanding your job can be and how lucky I was to have you all as my teachers. I must especially thank Mrs. Lisa Devillez, whose passion for teaching chemistry is contagious. Dr. David Owen must be thanked for introducing me to inorganic chemistry. I will never forget the breakfast club and your dedication to teaching. Without it, I would not have delved into the "land of neglected dimensions."

Abstract

Exploratory crystal growth is the best way to discover new phases with potentially improved properties or new crystal structures that could lead to new properties. As time goes on and researchers explore the synthetic techniques in the literature, diminishing returns will be met. Innovation in the synthetic tools is necessary to keep the field of materials chemistry advancing at its rapid, current pace. By combining wet hydroxide flux synthesis and hydrothermal synthesis, a hybrid technique for crystal growth has been created.

Using hydroxide hydrofluxes, a number of new materials have been synthesized and their relevant physical properties have been characterized. New oxides, hydroxides and oxyhydroxides incorporating transition metals in reduced states, manganese in highly oxidized states, rare earth ions, and iron in a new and unusual framework have been grown by this method. These investigations demonstrate the capabilities of hydroflux synthesis as a new route for exploratory synthesis.

Table of Contents

List of Tables

List of Figures

xiv

xvi

Chapter 1: Introduction to the Exploratory Crystal Growth of Oxo-Compounds by the Hydroflux Method

Although the field of solid state chemistry or materials chemistry is ever-changing and constantly advancing, crystal growth and the search for new and improved materials are always at the forefront of the field. This can be seen by looking at proposal calls and what the funding agencies see as the most promising fields to fund. Many researchers have turned to nanomaterials in an effort to produce materials with superior properties, but crystal growth is still a major emphasis. Special emphasis is placed on innovation in design and synthesis of crystals or films, as well as studies involving structure-property relationships. The properties that are being stressed in these calls are mostly directly related to energy research, such as ionic and electronic conductivity in solids, dielectric materials for pulse power applications, hydrogen storage materials, photovoltaics, and battery materials. Other properties focused on are somewhat indirectly related to energy, such as solid state lighting materials, superconductors, thermoelectrics, extended solids for quantum computing, and catalysis.

Research in materials chemistry is well warranted due to its vast impact on industry and society. Numerous small companies are being created from or are directly benefiting from basic research performed in academia. With the political demands for "energy independence" and the push for "green" or "sustainable" energy and processes, solid-state chemists along with chemical engineers and solid-state physicists are vital to a number of established and emerging industries that are or will be having large effects on our society. These facts elude the average citizen and, though the fruits of materials research surround them, most are unaware of the prevalence of solid state materials in their daily lives.

The electronics industry is an example that easily illustrates the importance of materials discovery and innovation to the average person. The transition from vacuum tube technology to transistor technology led to the progressive miniaturization of electronic devices that continues to this day. Transistor technology grew out of work that was only possible through the growth of high purity semiconductor crystals (initially germanium, but silicon soon thereafter). Advances in semiconductor crystal growth have contributed to further decreasing component sizes that have given us access to mobile technology and communications on a level rivaling science fiction. Research in laser diode materials has led to rapidly increasing optical storage that allows consumers to enjoy high definition movies via Blu-ray discs. Advances in piezoelectric materials, lighting materials, microwave dielectrics, thin films, optical sensors, and semiconductors all combine to produce what some consider to be the pinnacle of modern consumer electronics, as well as the modern status symbol, the mobile phone.

It is obvious that in order to overcome a plateau in the innovation of materials performance, there must be innovation in the field of materials synthesis. This is a consequence of what Martin Jansen has described as an "Energy Landscape" in which all possible compounds for a given combination of elements correspond to local energy minima.[1-3] If we are to produce new materials with superior performance or previously unknown properties, we must be able to carry out syntheses under a number of vastly different conditions. These differences in conditions can give us products that are unique to that set of conditions, or at least cannot be achieved by more traditional methods. With this in mind, the merit of developing new synthesis techniques becomes apparent.

3

Oxides are a vast and exciting class of materials that find many applications. Due to the wide range of structure types and elemental compositions known, they are well researched and are utilized for a number of their exhibited properties. Despite having been the focus of investigations for nearly a century, there are still many new oxides to be synthesized and new ones are regularly reported. However, a large number of the compounds reported are substitutions performed on simple binary and ternary systems. There is a need to explore quaternary or more complex oxide systems because they are believed to be the best candidates for interesting physical properties and improved performance.[4,5] Other oxo-compounds, like oxohydroxides and oxide hydrates, are also of similar interest due to their analogous properties and their relationship to naturally occurring minerals.

While oxides can be produced in many forms (e.g. nanoscale materials, thin films, polycrystalline powders, or single crystals), single crystals are the preferred form for the initial characterization of new materials. The optoelectronic and magnetic properties are intricately intertwined with crystallographic structure. This necessitates the growth of single crystals of new materials, as single crystal structure solutions allow for conclusive studies of new structures that then allow for relationships to be formed with the observed physical properties. This is not as easily achieved with powder data, such as powder neutron data or synchrotron data for Rietveld refinements, because a good starting model for the structure is needed to refine the crystal structure. Single crystals also offer the possibility of measuring intrinsic physical properties. This is especially important when measuring electronic properties, which experience significant interference from grain boundaries. Anisotropic properties are often present in low-dimensional structures and

4

these interesting properties can only be accurately measured on oriented single crystals. With these overwhelming incentives, exploratory crystal growth has been the primary goal of a number of research efforts[6-7] and is the focus of this work.

A number of techniques already exist for oxide synthesis.[8] Each technique that has been developed has benefits and disadvantages in regard to the synthesis of certain materials. The ideal technique would offer the ability to synthesize complex metal oxides in any quantity desired with short reaction times, over a wide range of temperatures, and with no need for specialized equipment. It would also offer the ability to generate either oxidizing or reducing conditions, solubilize a wide range of precursors, and provide an easy way to isolate the crystals. Common techniques include vapor phase techniques such as molecular beam epitaxy and chemical vapor deposition, melt reactions such as self-melt or molten salt techniques, solid techniques such as traditional solid-state synthesis and high-pressure reactions, and soft chemical methods which include sol-gel, subcritical hydrothermal and solvothermal reactions, templated growths, and a number of other low temperature methods often classified as "*chemie douce*".

Vapor phase reactions present unique opportunities to study a number of surface and strain phenomena and are often utilized for the synthesis of known binary and ternary compositions. They also are not limited by reaction kinetics that can make synthesis through solid-solid interactions difficult. They, however, do not lend themselves to the synthesis and characterization of new materials because of the lattice-matching considerations that come into play in the growth of thin films.

Traditional solid state reactions are a robust and wonderful tool for the solid state chemist. Many compositions that can be formed by crystal growth can be made as a

5

polycrystalline powder given the right conditions. However, powders are not preferred for crystallographic studies and the solids state method is limited to thermodynamically favored compositions, which correspond to deeper minima on the energy landscape. The general rule for solid state reactions is to intimately mix the precursors and heat to two-thirds the melting point of the highest melting compound. Taking into consideration the fact that some oxides possess melting points upwards of 2000 ℃ and that the other oxides may thermally reduce when heated enough, it is apparent that the synthesis of some compounds by the traditional method presents a challenge.

High pressure reactions can lead to very interesting phases that often challenge what we conceptualize as the expected packing sequences or oxidation states.[9] These reactions, however, require specialized reactors and often require large amounts of laboratory space to house the necessary equipment to reach the stupendous pressures some of these reactions take place at. Due to their low throughput, they are not well suited to exploratory research, although they may be the only option when it comes to exploring what phases form at the center of planets and other astronomical objects.

Soft chemical methods are a rapidly growing area of materials chemistry with many varied techniques. Sol-gel methods offer a solution-based alternative to the traditional solid state method and are often employed as its substitute, especially when high surface area powders are desired.[10] Difficulties arise from the need to balance hydrolysis rates of precursors and, in some instances, the lack of suitable precursors for certain elements. After gel formation, there is most often the need for calcination to remove the solvent and any organic products. Depending on the composition, this may or may not induce a highly exothermic combustion reaction. If that is the case, the

6

possibility for producing metastable phases is mitigated. As with the traditional solid state method, there is little applicability for sol-gel methods in exploratory work given the need for *a priori* knowledge of the desired stoichiometry. Subcritical hydrothermal and solvothermal methods have been very successful at synthesizing a number of metastable phases and there are a number of researchers who have been quite successful using these methods for exploratory growth of a number of interesting oxo-compounds.[11-14] "*Chimie douce*" methods and templated reactions are very specific in that they require prior knowledge of the desired stoichiometry or require a host structure to perform intercalation, ion exchange, hydrolysis, or redox reactions on. Although this does lead to some interesting and unusual metastable phases,[15-19] some of which exhibit properties not found in the high-temperature analogues, it is not a suitable method for exploratory synthesis.

Melt techniques are often the method of choice for synthesizing single crystals. Self-melt techniques, such as the Czochralski or Bridgman-Stockbarger methods, are superior for the growth of large single crystals, but are limited in applicability in that most compounds do not melt congruently. Molten salt synthesis, also known as flux growth, is more broadly applicable and has become one of the most widely used techniques for exploratory crystal growth.[6,20] A number of salts melt at reasonably low temperatures and meet the requirements necessary to perform high temperature solution reactions; molten carbonates, halides, peroxides, superoxides, and hydroxides have been successfully used as fluxes for oxide crystal growth.[21-26]

The high temperature solution chemistry of hydroxide melts has been the focus of investigation for nearly fifty years. Researchers, the Stacy and zur Loye groups

7

predominately, began reporting experiments growing single crystals of multinary oxides from alkali- and alkaline earth hydroxides in the 90s.[27-30] They found that the relatively low melt temperatures (sometimes below 200 ºC), the ability to dissolve most elements, low toxicity, and the ability to control the oxygen chemical potential through atmosphere selection makes them nearly ideal fluxes for exploratory synthesis. Many new phases have been grown using hydroxide fluxes, some with new structure types and interesting properties. One of the limiting factors to this synthetic technique, although not necessarily a bad property to have, is the highly oxidizing nature of the hydroxide fluxes. This can lead to unusually high oxidation states for some elements, which opens up the possibility for the manifestation of different magnetic or electronic properties along with different structures that can be obtained by other growth methods.[31-33] A good example of this is the synthesis of the hypervalent copper oxides $LnCu_2O_4$ (Ln = La, Nd, Sm, Eu, Gd, Dy, Ho, Y, Er),[34] which were otherwise only reported by high pressure techniques.[35]

Wet hydroxide flux reactions are an extension of the hydroxide flux technique that takes advantage of the Lux-Flood oxoacidity of the hydroxide melts.[36,37] Similar to what is observed in water, the hydroxide ion itself autodissociates in melts to form H_2O and O^{2-}:

$$2OH^- \rightleftharpoons H_2O_{(sol)} + O^{2-}_{(sol)}$$
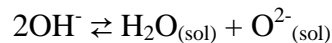
By adjusting the oxoacidity of the melt, one can affect the solubilities of metal oxides.[38-43] This is analogous to metal hydroxides in aqueous solutions, which dissolve readily under acidic conditions; some metal oxides show increased solubility in acidic hydroxide fluxes. This was observed to be of particular importance for the crystal growth of lanthanides.[44-47] Wet flux reactions are conducted within either sealed tubes or covered

8

crucibles to prevent dehydration of the melt and subsequent solidification. Sealed silver tubes allow for the working temperature range of the melt to be increased as well as the amount of water that can be added to the flux. The development of using sealed silver tubes in the zur Loye group has allowed for this technique to be explored extensively, yielding a number of novel phases.

Hydrothermal techniques differ significantly from flux growth techniques. Operating above the critical temperature of water generates significant pressure and the physical properties of water are significantly altered, which introduces new variables to the applied chemical forces on the reaction. Reactions above the critical point of water (374.2ºC) can take advantage of the unique physical properties of water as a supercritical fluid and use precursors that wouldn't normally be possible like some oxides, for example.[48] However, this also can be a detriment to the growth of crystal in some cases; many compounds prepared by true hydrothermal methods are powders. This is not necessarily the case, though, as many researchers do prepare high quality single crystals, often of considerable size, by hydrothermal techniques. This makes it an extremely attractive method for the synthesis of some optical materials. One of the least appealing things about this technique, however, is the specialized equipment required to safely contain the reactions. Due to this, the number of reactions that can be carried out at any given time is severely restricted, making it a less than ideal technique for exploratory research.

Sub-critical hydrothermal synthesis is a technique where the water is heated and pressurized autogeneously, but the reaction temperature remains below the critical temperature. The dielectric properties of water change with temperature and affect the

9

solubilities of precursors somewhat, but the pressure generated is an extra variable that can significantly impact crystal growth. Many subcritical hydrothermal reactions take advantage of mineralizers to solubilize species that normally would not participate in aqueous reactions, even at these elevated temperatures. Common mineralizers are boric acid, tungsten and molybdenum oxide, alkali carbonates, and alkali hydroxides. These change the way in which ions solvate in the solution and can facilitate crystal growth that would not be possible by this technique otherwise.

The question one can then ask is "when does a reaction cease to be a subcritical reaction and become a wet flux reaction?" A number of research articles from the former Soviet Union describe their experiments as having up to 50% by mass sodium hydroxide and 50% water in hydrothermal reactions carried out in gold ampules. Wet hydroxide flux reactions can use up to 15% water by mass in their synthesis. That leaves a large gap in between these two generalized compositions that seems to have been ignored by researchers. Researching this compositional regime in question led to the development of the hydroflux technique for crystal growth.

Hydroflux Synthesis

Hydroflux reactions can be broadly defined as solution reactions in which a melt is formed with water-soluble metal salt(s) and water that would not be an aqueous solution at room temperatures. For sodium and potassium hydroxide and their eutectic compositions, it was found that water-to-hydroxide molar ratios of between 1:1 and 4:1 create a flux with properties significantly different than a wet hydroxide flux or subcritical hydrothermal reaction. The reactions are carried out in relatively simple

10

vessels and take place at conveniently low temperatures (230 ℃ or less) in short time spans (on the order of 24 hours).

Pressure does not seem to be a significant factor in hydroflux reactions. Reactions are carried out in a polytetrafluoroethylene (PTFE)-lined stainless steel autoclave at temperatures typically between 180 and 230 ℃; the mechanical performance of PTFE above this point precludes the vessels from being used in reactions at any higher temperature. The need for having a sealed vessel is not to generate pressure to dissolve precursors or promote crystal growth, but to merely keep the hydroflux in its original state of hydration. As shown by the studies of copper oxidation states, the molality concentration of the hydroflux can profoundly affect the oxidation state of elements dissolved in a hydroflux. Preventing dehydration is necessary to deliberately control the reaction. In order to verify the negligible effect of pressure, reactions were opened during the heating cycle after sitting at their peak temperature for some period of time. No significant pressure is generated during these reactions, otherwise the hydroflux would boil or a significant water pressure would be observed.

Reaction temperature has been found to be less important than other factors. Most often, the crystal growth of compounds positively correlates with temperature. The crystal quality and size of most compounds synthesized by the hydroflux method has been found to be best at 230 ℃. In some instances, however, it has been found that a lower dwell temperature can positively impact crystal growth; such is the case for the nickel hexahydroxometallates detailed in chapter 2.

Reaction time is also an important factor in hydroflux reactions. This is plainly demonstrated in a number of the syntheses detailed herein. The hexahydroxometallates

11

detailed in chapter 2 were crystallized with as little as a 6-hour dwell time. The iron compounds discussed in chapter 2 were found to poorly crystallize if the dwell time of reactions was less than one day. For the rare earth silicates in chapter 4, it was found that the dissolution of the rare earth precursor determined the length necessary for the dwell time in order to crystallize the desired phases. Rare earth compounds synthesized from water-soluble precursors were synthesized in a shorter time, while those synthesized from oxide precursors necessitated the use of longer dwell times for digestion of the oxide. Essentially, hydrofluxes seem to be able to not only solubilize water-soluble precursors, but also most oxides as well as a number of metals (excluding the noble metals). When using oxides and metals as precursors, it seems that a longer dwell time is required for digestion (on the order of a few days) depending on the metal identity. This seems to mirror what is often observed in hydroxide flux reactions, where a longer digestion may be necessary with certain metals.[34]

The cooling and heating rates of a reaction can also have a strong effect on product formation. For a number of the experiments performed, a cooling rate of 0.3 ℃ or less per minute was found to promote single crystal growth. In some instances, faster cooling was not found to impact crystal growth, to a certain point. When carrying out exploratory synthesis in a hydroflux, it seems that a cooling rate of 0.3 ℃ or less per minute is sufficient for observing crystal growth in most cases. Heating rates were found to have little effect on most syntheses and for those in which it did, it cannot be determined whether or not the slower heating rate was important or the fact that the reaction was allowed to maintain an elevated temperature for a longer period of time. For most reactions, a heating rate of 5 ℃ per minute was found to be sufficient. This rate was

12

chosen because the programmable ovens used were easily able to ramp the internal temperature accordingly and meet the programmed set points in the time allotted.

Unlike wet hydroxide flux reactions, which can be performed in sealed tubes under selected atmospheres, hydroflux reactions cannot be carried out in an atmosphere other than air with the current equipment. PTFE is known to become gas permeable at elevated temperatures and is not suitable for reactions in which a controlled atmosphere is desired. Due to the highly corrosive nature of hydroxide hydrofluxes, there are few candidate materials for reaction vessels. PTFE appears to be the most practical material, despite its limitations. Because the atmosphere cannot be controlled, there is no way to control the oxygen chemical potential of the reaction. Reactions can be carried out in commercially available autoclaves with PTFE liners, allowing for a large number of simultaneous reactions with relatively low-cost equipment.

Despite the lack of atmosphere control in hydroflux reactions, there appear to be other ways to influence the oxidation state of metals in the solution. Experimentation with copper proved that the hydroflux composition has a profound impact upon oxidation states. Changing the alkali metal cation from sodium to a eutectic mixture of sodium and potassium (53% NaOH) and then to potassium drastically affects the product crystallized or precipitated. (Figure 1.1) Increasing the concentration of hydroxide tended to form more reduced products, which runs counter what is observed in the room temperature Pourbaix diagram for copper.

Later, it was found that precursor identity and reaction time also influence the oxidation state of metals. This is best demonstrated in the studies performed with manganese (Table 1.1). Starting with a low-valence precursor and a higher concentration

13

of water can maintain this oxidation state. In order to target trivalent manganese, it worked best to use manganese (III) precursors as opposed to a comproportionation reaction. Manganese (IV) is the most common oxidation state at standard conditions and can be obtained with a number of precursors and hydroflux conditions. Manganese (V) and (VI) can be targeted by using high hydroxide concentrations and using potassium permanganate as a precursor. This oxidation state control is much wider than what would be possible from a hydroxide flux because manganese (II) and (III) would not be expected products. This appears to be related to the aqueous solution chemistry of manganese. Manganese (II), (IV), and (VI) are all predicted to be stable in solution with (III) and (V) predicted to be unstable. This suggests that a hydroflux is indeed significantly different from both hydroxide fluxes and hydrothermal reactions.

Unlike hydroxide fluxes where alkali metal identity has a great effect on the melt autodissociation and, therefore, metal oxide solubilities, alkali metal identity does not seem to affect hydroflux reactions in the same fashion. Instead, hydroflux identity seems to influence the precipitated product's identity. Potassium hydrofluxes tend to promote the formation of hydroxide or oxohydroxide products while sodium hydrofluxes favor oxide formation. Lithium hydroxide is not a suitable hydroflux material, most likely because of its low solubility in water. This is similar to what is observed in hydroxide fluxes, where lithium hydroxide is a poor flux because of its very low autodissociation constant, creating a very basic, high melting flux quickly under ambient pressure.[42] Rubidium hydroxide and cesium hydroxide were not studied in depth due to the significantly higher cost per gram for the hydroxides. Alkali metal oxides can be used as a precursor to hydroxides by adding water. However, when alkali metal oxides were used

14

to synthesize a hydroflux the resultant products were different than what would be expected from the same reaction in the corresponding hydroflux made from hydroxides. This could be due to the presence of superoxide ions from the alkali metal oxide, which could create a very different hydroflux than one synthesized from hydroxides.

Investigations of crystallization using hydrofluxes have yielded a number of new compounds and demonstrate the broad applicability and effectiveness of hydrofluxes for exploratory crystal growth. A series of transition metal hydroxides were crystallized and are detailed in Chapter 2. Since the transition metals are in the reduced, +2 oxidation state, they were studied for their physical properties as well as their oxide decomposition products. A number of oxides incorporating group 6 metals were synthesized and are detailed in Chapter 3. Two series of rare earth silicates were crystallized from hydrofluxes and crystallographic and optical properties characterizations are reported in Chapter 4. A series of iron compounds that represent the first non-aluminosilicate zeolites were also synthesized from hydrofluxes and are detailed in Chapter 5, while Chapter 6 details new pentavalent manganese and arsenic compounds.

Conclusions

Several new compounds have been prepared and characterized through the development of the hydroflux method. Its utility as a tool for exploratory crystal growth is demonstrated by affecting the incorporation of a variety of elements into various structure types. As a new tool for materials research, hydroflux crystal growth offers a number of characteristics related to its parent techniques that make it attractive for exploratory crystal growth of new phases.
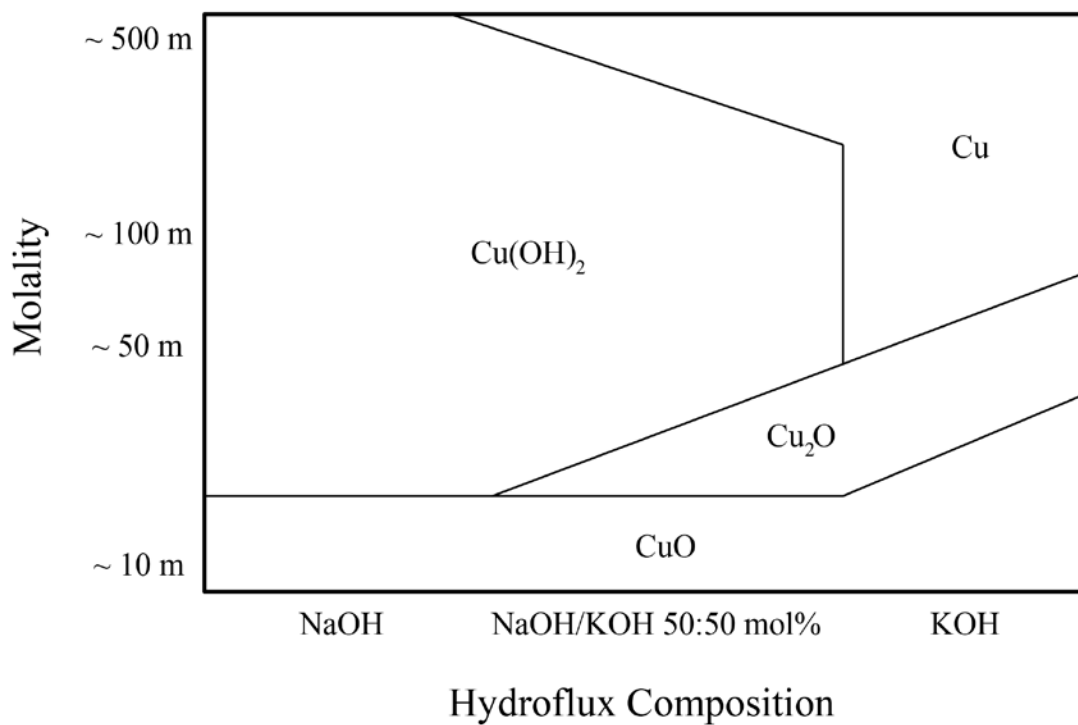
Figure 1.1. Precipitated copper product versus hydroflux composition.

Table 1.1. The effect of precursor on observed valence in manganese products.

Product Crystallized	Manganese valence	Manganese precursor
$Sr_2Mn(OH)_6$	II	$MnCl_2 \cdot 4H_2O$
Sr_2MnSbO_6	III	$Mn(C_5H_7O_2)_3$
$Na_2Mn_3O_7$	IV	MnO_2
$Sr_5(MnO_4)_3OH$	V	$KMnO_4$

References

1) Jansen, M. *Angew. Chem. Int. Ed.* **2002**, *41*, 3746.

2) Jansen, M.; Schön, J. C. *Angew. Chem., Int. Ed.* **2006**, *45*, 3406.

3) Liebold-Ribeiro, Y.; Fischer, D.; Jansen, M. *Angew. Chem.* **2008**, *120*, 4500.

4) DiSalvo, F. J. *Science*, **1990**, *247*, 649.

5) Poeppelmeier, K. R. *Chem. Mater.* **1998**, *10*, 2577.

6) Bugaris, D. E.; zur Loye, H.-C. *Angew. Chem., Int. Ed.* **2012**, *51*, 3780.

7) Mugavero III, S. J., Gemmill, W. R., Roof, I. P., zur Loye, H.-C., *J. Solid State Chem.* **2009**, *182*, 1950.

8) West, A. R. *Solid State Chemistry and its Applications*; John Wiley & Sons: New York, 1985.

9) Zhang, W.; Oganov, A. R.; Goncharov, A. F.; Zhu, Q.; Boulfelfel, S.E.; Lyakhov, A. O.; Stavrou, E.; Somayazulu, M.; Prakapenka, V. B.; Konôpková, Z. *Science,* **2013,** *342*, 1502.

10) Brinker, C. J.; Scherer, G. W. *Sol-Gel Science: The Physics and Chemistry of Sol-Gel Processing*; Academy Press: New York, USA: 1990.

11) Modeshia, D. R.; Walton, R. *Chem. Soc. Rev.* **2010**, *39*, 4303.

12) Sheets, W. C.; Mugnier, E.; Barnabe, A.; Marks, T. J.; Poeppelmeier, K. R. *Chem. Mater.* **2006**, 18, 7.

13) Yeon, J.; Sefat, A. S.; Tran, T. T.; Halasyamani, P. S.; zur Loye, H.-C. *Inorg. Chem.* **2013**, *52*, 6179.

17

14) Veltman, T. R.; Stover, A. K.; Sarjeant, A. N.; Ok, K. M.; Halasyamani, P. S.; Norquist, A. J. *Inorg. Chem.,* **2006**, *45*, 5529.

15) Chen, J.; Wang, S.; Whittingham, M. S. *J. Power Sources*, **2007**, *174*, 442.

16) Rebbah, H.; Desgardin, G.; Raveau B. *Mater. Res. Bull.* **1979**, *24*, 1125.

17) Gérand, B.; Seguin, L. *Solid State Ionics* **1996**, *84*, 199.

18) Delmas, C.; Borthomieu, Y. J. *Solid State Chem.* **1993**, *104*, 345.

19) Ollivier, P. J.; Mallouk, T. E. *Chem. Mater.* **1998**, *10*, 2585.

20) D. Elwell and H. J. Scheel, *Crystal Growth from High-Temperature Solutions*; Academic Press: New York, 1975.

21) Claridge, J. B.; Layland, R. C.; Henley, W. H.; zur Loye, H.-C. *Chem. Mater.* **1999**, *11*, 1376.

22) Frenzen, S.; Muller-Buschbaum, H. *Z. Naturforsch. B*, **1995**, *50b*, 581.

23) Reisner, B. A.; Stacy, A. M. *J. Am. Chem. Soc.* **1998**, *120*, 9682.

24) Smith, M. D.; Stalick, J. K.; zur Loye, H.-C. *Chem. Mater.* **1999**, *11*, 2984.

25) Stitzer, K. E.; Darriet, J.; zur Loye, H.-C. *Curr. Opin. Solid State Mater. Sci.* **2001**, *5*, 535.

26) Wehrum, G.; Hoppe, R. *Z. Anorg. Allg. Chem.* **1992**, *617*, 45.

27) Nguyen, T. N.; Giaquinta, D. M.; Davis, W. M.; zur Loye, H.-C. *Chem. Mater.* **1993**, *5* 1273.

28) Friedman, T. L.; Stacy, A. M. *J. Solid State Chem.* **1994***, 109*, 203.

29) Sandford, D.; Marquez, L. N.; Stacy, A. M. *Appl. Phys. Lett.* **1995**, *67*, 422.

30) Sunshine, S. A.; Seigrist, T. Schneemeyer, L. F. *J. Mater. Res.* **1997**, *12*, 1210.

31) Bharathy, M.; Khalsa, H. S.; Smith, M. D.; zur Loye, H.-C. *Solid State Sci.* **2009**, *11*, 294.

32) Stitzer, K. E.; Smith, M. D., Gemmill, W. R.; zur Loye, H.-C. *J. Am. Chem. Soc.* **2002**, *124*, 13877.

33) Mugavero, S. J.; Smith, M. D.; Yoon, W.-S.; zur Loye, H.-C. *Angew. Chem., Int. Ed.* **2009**, *28*, 215.

34) Luce, J. L.; Stacy, A. M. *Chem. Mater.* **1997**, *9*, 1508.

35) Chen, B.-H.; Walker, D.; Suard, E. Y.; Scott, B. A. *Chem Mater.* **1995**, *7*, 355.

36) Lux, H; Kuhn, R.; Neidermaier, T. Z. *Anorg. Allg. Chem.* **1959**, *298*, 285.

37) Flood, H.; Forland, T. *Acta Chem. Scand.* **1947**, *1*, 542.

38) Goret, J. *Bull Soc. Chim.* **1964**, *5*, 1074.

39) Goret, J.; Tremillon, B. *Bull. Soc. Chim.* **1966**, *9*, 2872.

40) Eluard, A.; Tremillon, B. *J. Electroanal. Chem.* **1968**, 18, 277.

41) Eluard, A.; Tremillion, B. *J. Electroanal. Chem.* **1970**, 26, 259.

42) Doisneau, R. G.; Tremillon, B. *J. Chim. Phys. PCB* **1974**, 71, 1445.

43) Combes, R. *The Solution Chemistry of Water in Melts.* In Ionic Liquids; Inman, D.; Lovering, D. G. Ed.; Springer US: New York, 1981; pp 305-337.

44) Keller, S. W.; Carlson, V. A.; Sanford, D.; Stenzer, F.; Stacy, A. M.; Kwei, G.H.; Alario-Franco, M. *J. Am. Chem. Soc.* **1994**, *116*, 8070.

45) Gemmill, W. R.; Smith, M.D.; Prozorov, R.; zur Loye, H.-C. *Inorg. Chem.* **2005**, *44*, 2639.

46) Gemmill, W. R.; Smith, M.D.; zur Loye, H.-C. *J. Solid State Chem.* **2004**, *177*, 3560.

19

47) Gemmill, W. R.; Smith, M.D.; zur Loye, H.-C. *J. Solid State Chem.* **2004**, *179*, 1750.

48) Byrappa, K.; Yoshimura, M. *Handbook of Hydrothermal Technology: A Technology for Crystal Growth and Materials Processing*; Noyes Publications: Norwich, NY, 2001.

Chapter 2: Crystal Growth of New Hexahydroxometallates Using a Hydroflux

INTRODUCTION

Exploratory crystal growth continues to be one of the most effective approaches for investigating phase space and for identifying new compositions with novel structures and properties. The two most commonly used techniques for crystallizing solid state inorganic materials rely on high temperature solutions (fluxes) or hydrothermal (supercritical water) methods.[1] Due to the success of lower temperature solvothermal and non-critical hydrothermal approaches for synthesizing organic-inorganic hybrids,[2-6] these methods have also been applied to the preparation of inorganic materials.[7-11] Among high temperature fluxes, molten hydroxides are one of the best solvents for oxides and have been shown to be very effective for the growth of high quality mixed-metal oxide single crystals.[12,13] In this chapter the synthesis of new hexahydroxometallates using a low temperature hydroflux, a hybrid approach between the aqueous hydrothermal and the molten hydroxide flux techniques, is described. We have recently introduced this technique for the growth of single crystals of platinum group metal containing hydroxides.[14]

Hydroxide fluxes are inorganic hydroxides, such as KOH or NaOH, which melt at conveniently low temperatures, 318 °C and 400 °C, respectively. Often eutectic mixtures of hydroxides, such as NaOH/KOH, are employed to reduce the melting point further. An alternative approach to lowering the melting point of hydroxides is to adjust the water content. Commercial hydroxides contain approximately 15 wt% water, which appreciably lowers the melting point versus the pure, anhydrous hydroxide. The intentional addition of extra water can further lower the melting point of hydroxide fluxes below 200 °C by forming a very low temperature melt and ultimately an aqueous solution. The term

hydroflux has been suggested for the compositional regime where the melt has a very high water content, yet is not an aqueous solution.[1] A hydroflux is thus best thought of as a combination of subcritical hydrothermal and flux techniques (Figure 2.1). In this compositional regime, a melt (hydroflux) forms at very low temperatures, making it possible to use simple polytetrafluoroethylene (PTFE) lined pressure vessels for containing the reaction. Little pressure is generated during the crystal growth process, as the water is solvated in the flux. The closed pressure vessels are needed only to seal the reaction to prevent dehydration, which would result in the re-solidification of the hydroxide and changes in the chemical properties of the flux during the course of the reaction.

Complex metal hydroxides, or hydroxometallates, are a relatively small class of inorganic compounds that were initially reported in the early 20th century[15-17] and usually consist of a combination of an electropositive alkali or alkaline earth metal and a first row transition metal or a main group metal. Examples of these materials include the silicon-free hydrogarnets[18,19] and the hexahydroxometallates[20-25] which include the well explored hydroxystannates.[26-35] Although the hydroxometallates have been known for a relatively long time, the lack of high quality crystals has precluded extensive structural characterization in many instances. Their thermal behavior, investigated in some cases by thermogravimetric analysis, has been reported to often follow a general reaction scheme (Scheme 1), which consists of dehydration and the formation of an oxide product.

$$A_xB_y(OH)_z \rightarrow A_xB_yO_{z/2} + z/2\ H_2O \qquad \text{(Scheme 1)}$$
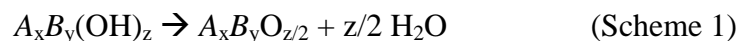
Based on this reaction scheme, hydroxometallates can be used as precursors to explore the low temperature formation of oxides and the potential discovery of new low

temperature ternary – or if starting with more complex hydroxometallates – quaternary or even higher mixed metal oxides.

In this chapter, the synthesis, structure, and magnetic characterization of a series of novel mixed metal hexahydroxometallates $A_2B(OH)_6$ (A = Sr, Ba; B = Mn, Ni, Co, Cu) is reported. In addition, the suitability of these hexahydroxometallates to function as precursors for the synthesis of oxides was investigated and is detailed within.

EXPERIMENTAL METHODS

Reagents. The following reagents were used as obtained: KOH (Fisher Scientific, ACS grade pellets), NaOH (Fisher Scientific, ACS grade pellets), Sr(OH)$_2$•8H$_2$O (Alfa Aesar, 99%), Sr(NO$_3$)$_2$ (Fisher Scientific, ACS Grade), Ba(OH)$_2$•8H$_2$O (Alfa Aesar, 99%), Ba(NO$_3$)$_2$ (Alfa Aesar, 99.95%), MnCl$_2$•4H$_2$O (Alfa Aesar, 97%), CoCl$_2$•6H$_2$O (B&A Chemicals, ACS grade), Ni(NO$_3$)$_2$•6H$_2$O (Alfa Aesar, Technical Grade), and CuO (Alfa Aesar, 99.5%).

Crystal Growth. All products were synthesized in 23 mL PTFE-lined stainless steel autoclaves. A typical synthesis involved reacting approximately 8-12 g of alkali metal hydroxide(s), stoichiometric quantities of alkaline earth and transition metal precursors, and 6-8 g of water at 180-230 ºC for 12-24 hours. Alkaline earth precursors investigated include chlorides, hydroxides, and nitrates. The transition metal precursor selection profoundly impacted phase purity and crystal quality. Transition metal precursors investigated included acetates, chlorides, nitrates, and oxides. For each individual composition, the optimal precursors varied.

Sr$_2$Mn(OH)$_6$: 2 mmol of Sr(OH)$_2$•H$_2$O and 1 mmol of MnCl$_2$•4H$_2$O were added to a hydroflux consisting of 0.11 mol of KOH and 0.1 mol of NaOH and 0.33 mol of

distilled water. This mixture was heated to 230 ℃ at a rate of 5 ℃/min and held for 24 hours before being cooled at a rate of 0.2 ℃/min to 80℃.

Ba$_2$Mn(OH)$_6$: 2 mmol of Ba(OH)$_2$•H$_2$O and 1 mmol of MnCl$_2$•4H$_2$O were added to a hydroflux consisting of 0.11 mol of KOH and 0.1 mol of NaOH and 0.33 mol of distilled water. This mixture was heated to 230 ℃ at a rate of 5 ℃/min and held for 24 hours before being cooled at a rate of 0.2 ℃/min to 80℃.

Sr$_2$Co(OH)$_6$: 1.5 mmol of Sr(OH)$_2$•H$_2$O and 1 mmol of CoCl$_2$•6H$_2$O were added to a hydroflux consisting of 0.11 mol of KOH and 0.1 mol of NaOH and 0.33 mol of distilled water. This mixture was heated to 230 ℃ at a rate of 5 ℃/min and held for 24 hours before being cooled at a rate of 0.2 ℃/min to 80℃.

Ba$_2$Co(OH)$_6$: 1.5 mmol of Sr(OH)$_2$•H$_2$O and 1 mmol of CoCl$_2$•6H$_2$O were added to a hydroflux consisting of 0.11 mol of KOH and 0.1 mol of NaOH and 0.33 mol of distilled water. This mixture was heated to 230 ℃ at a rate of 5 ℃/min and held for 24 hours before being cooled at a rate of 0.2 ℃/min to 80℃.

Sr$_2$Ni(OH)$_6$: 2 mmol of Sr(NO$_3$)$_2$ and 1 mmol of Ni(NO$_3$)$_2$•6H$_2$O were added to a hydroflux consisting of 0.23 mol of KOH and 0.33 mol of distilled water. This mixture was heated to 180 ℃ at a rate of 5 ℃/min and held for 24 hours before being cooled at a rate of 0.3 ℃/min to 80℃.

Ba$_2$Ni(OH)$_6$: 2 mmol of Ba(NO$_3$)$_2$ and 1 mmol of Ni(NO$_3$)$_2$•6H$_2$O were added to a hydroflux consisting of 0.23 mol of KOH and 0.33 mol of distilled water. This mixture was heated to 200 ℃ at a rate of 5 ℃/min and held for 24 hours before being cooled at a rate of 0.3 ℃/min to 80℃.

Ba₂Cu(OH)₆: 2 mmol of Ba(OH)$_2$•H$_2$O and 1 mmol of CuO were added to a hydroflux consisting of 0.11 mol of KOH and 0.1 mol of NaOH and 0.33 mol of distilled water. This mixture was heated to 230 ℃ at a rate of 5 ℃/min and held for 24 hours before being cooled at a rate of 0.2 ℃/min to 80℃.

The ranges of reaction conditions that yielded the desired hydroxides are detailed in Table 2.1. The resulting hydroxides were sonicated in methanol and collected by vacuum filtration. Due to the presence of carbonate impurities in the alkali metal hydroxides and the propensity of alkaline media to sequester carbon dioxide, crystals of alkaline earth carbonates readily form during the course of these reactions. These crystals of barium and strontium carbonate are often large (approximately 0.5 to 1 cm) and can be removed by mechanical separation.

To inhibit the formation of carbonates, a number of experimental strategies were investigated. Sealing the reactions in an inert atmosphere (N$_2$) did not prevent the formation of carbonate byproducts. This may be due to either the natural propensity for NaOH and KOH to sequester CO$_2$ from the atmosphere or the tendency for fluoropolymers to become permeable to gas exchange at elevated temperatures.[36,37] To eliminate the alkali hydroxides as a possible carbonate source, experiments with K$_2$O and Na$_2$O/Na$_2$O$_2$ as precursors were carried out, but the products of these reactions vastly differed from those involving hydroxide precursors. Pre-treating the hydroflux with barium or strontium salts followed by filtration of the formed carbonates yielded inconsistent results. Investigations into the possibility of an alkaline earth hydroflux yielded only modest amounts of the hexahydroxometallates with significant transition metal hydroxide and amorphous byproducts. The most promising method of eliminating

26

carbonate formation was the introduction of a mineralizer. In the preparation of strontium hexahydroxometallates, WO_3 inhibits the formation of carbonates completely and also promotes crystal growth along specific directions for each system, resulting in significantly elongated crystals. (Figure 2.2)

Scanning Electron Microscopy. Single crystals were analyzed via scanning electron microscopy with an FEI Quanta scanning electron microscope operating in low-vacuum mode. Energy-dispersive spectroscopy (EDS) verified the presence and approximate ratios of the metals in each compound.

Infrared Spectroscopy. IR spectra were recorded with a Perkin Elmer Spectrum 100 FT-IR spectrometer. All samples were ground to a powder using an agate mortar and pestle and four scans ranging from 4500 cm^{-1} to 600 cm^{-1} were averaged.

Thermogravimetric Analysis. All compounds were heated under flowing air or nitrogen at a rate of 100 mL/min in a TA Instruments SDT Q600 with alumina pans as the sample container. Samples were heated at a rate of 10 ºC/min to 1000-1200 ºC.

Powder X-Ray Diffraction. Phase identification/purity was determined by powder X-ray diffraction using either a Rigaku DMAX-2100 or a Rigaku Ultima IV powder X-ray diffractometer with Cu Kα radiation ($\lambda = 1.5418$ Å). Samples were ground to a fine powder and data were collected from 10 to 80º 2θ with a step size of 0.04º.

Magnetic Measurements. The DC magnetic susceptibilities of $Sr_2Mn(OH)_6$, $Ba_2Mn(OH)_6$, $Sr_2Co(OH)_6$, $Ba_2Co(OH)_6$, $Sr_2Ni(OH)_6$, and $Ba_2Ni(OH)_6$ were measured as a function of temperature using a Quantum Design MPMS SQUID magnetometer. The polycrystalline samples were placed in a gelatin capsule. For a typical temperature sweep experiment, the sample was first cooled to 5 K under zero-field cooled (zfc) conditions

27

and data were collected upon warming to 300 K in an applied field of 1000 Oe. Then the sample was field cooled (fc) to 5 K from room temperature in 1000 Oe while data were collected.

Structure Determination. Single crystal X-ray diffraction data were collected at 298 K on a Bruker SMART APEX CCD diffractometer (Mo Kα radiation, $\lambda = 0.71073$ Å). The crystal-to-detector distance was 5.048 cm. Crystal decay was monitored by re-collecting the initial 50 frames at the end of the data collection process. Data were collected by a scan of 0.3° in ω in groups of 606 frames at φ settings of 0°, 90°, 180°, and 270°. The exposure time was 20 s frame^{-1}. The collection of intensity data was carried out with the program SMART.[38,39] Cell refinement and data reduction were carried out with the use of the program SAINT+.[38,39] A numerical absorption correction was performed with the use of the program SADABS.[38,39] The program SADABS was also employed to make incident beam and decay corrections. The structure was solved with the direct methods program SHELXS and refined with the full-matrix least-squares program SHELXTL.[40] After H atoms were located by difference Fourier syntheses, O-H bond lengths were restrained to d = 0.85(2) Å using the DFIX command. Final refinements included anisotropic displacement parameters for the metal and O atoms, and isotropic displacement parameters for the H atoms. In all structures, restrained refinement of H-atom parameters resulted in physically reasonable displacement parameters (similar in magnitude to the parent O atoms) and no unacceptably short interatomic contact distances, providing strong support for the reported positions. A secondary extinction correction was also applied. Additional experimental details are given in Table 2.2 and the Supporting Information. Selected metrical details are presented in Table 2.3.

RESULTS AND DISCUSSION

Synthesis. Single crystals of the hexahydroxometallates, $Sr_2Mn(OH)_6$, $Ba_2Mn(OH)_6$, $Sr_2Co(OH)_6$, $Ba_2Co(OH)_6$, $Sr_2Ni(OH)_6$, $Ba_2Ni(OH)_6$, and $Ba_2Cu(OH)_6$, were grown from a hydroflux, Figure 2.3, using the conditions listed in Table 2.1. Crystals of $BaCO_3$ or $SrCO_3$ tended to form as a second phase due to the presence of sodium and potassium carbonate in the hydroxide reagent along with carbon dioxide sequestered from the surrounding atmosphere. Close to single-phase samples could be obtained by separating the carbonate crystals from the hexahydroxometallate crystals with a sieve. Strontium carbonate could be eliminated from the strontium hexahydroxometallates with the addition of WO_3 as a mineralizer, but when used with the barium analogues, ternary and quaternary oxide byproducts were formed.

The nature of the reagents and the quantities of the different hydroxides used had a significant influence on the degree of crystallinity and the identity of the products that were isolated from the reaction mixture. For example, the synthesis of both $Sr_2Mn(OH)_6$ and $Ba_2Mn(OH)_6$ worked best if $MnCl_2 \cdot 4H_2O$ was used as the manganese source instead of $Mn(CH_3COO)_2$ for crystal growth, as the use of $Mn(CH_3COO)_2$ resulted in the formation of microcrystalline powders of $SrMnO_3$ as a secondary phase. Also, using larger ratios of NaOH/KOH to the alkaline earth metals and transition metals led to the formation of $NaMnO_2$ and $BaMnO_3$, rather than single crystals of $Sr_2Mn(OH)_6$ and $Ba_2Mn(OH)_6$. For the cobalt containing phases, $CoCl_2 \cdot 6H_2O$ was found to be the superior starting material over the oxides Co_3O_4 and Co_2O_3 and $Co(NO_3)_2 \cdot 6H_2O$, although all yielded the hydroxometallates, albeit in lesser yield. Single-phase hydroxocobaltates were only obtained when using $CoCl_2 \cdot 6H_2O$ as the cobalt source. Interestingly, while the

above syntheses of the manganese and cobalt containing hexahydroxometallates worked when using either NaOH, KOH, or a eutectic mixture of the two as the hydroflux, the synthesis of $Sr_2Ni(OH)_6$ and $Ba_2Ni(OH)_6$ succeeded only in a KOH based hydroflux, with crystallization optimized at a lower operating temperature of 180 ºC.

It is apparent that while the different precursors used influenced the reaction outcome, it is difficult to explain fully why specific conditions and reagents led to specific outcomes. Nonetheless, observations during experimentation do show some definite trends. The use of metal chloride or metal nitrate salts, in general, resulted in improved crystallization of the hydroxometallates compared to the use of metal oxides or metal organic salts (acetate, acetylacetonate, oxalate, etc.). In addition, the metal oxidation state in the starting reagent, more than anything, affected the specific product(s) obtained as well as the relative ratio of the products when more than once phase crystallized. These results are consistent with what has been observed for the crystallization of platinum metal hydroxometallates,[14] where reagents such as $H_2[PtCl_6]$, $Pd(NH_3)_2Cl_2$, and K_2PdCl_6, resulted in the formation of numerous compositions.

The hydroflux itself, a combination of water with NaOH, KOH, or a mixture of NaOH/KOH, acting as the solvent for crystal growth, appeared to have only a small influence on the reaction outcome. However, the addition of barium and strontium hydroxides to the hydroflux created a more reactive reaction environment, no doubt aided by the presence of the large divalent cations that are readily incorporated into the product structures. One might anticipate that expanding this line of research to include other large di- or trivalent cations will likely be successful.

Structures. All members of this series were solved in the $P2_1/n$ space group of the monoclinic crystal system. The structures of the Zn and Cu members have been described in the literature as analogues of the Li_2O structure.[25] $Ba_2Cu(OH)_6$ was reported previously in the alternate setting $P2_1/c$, but has been included in this investigation in order to normalize the series.[20] In each instance, the alkaline earth element coordinates to eight oxygen atoms in what can be described as either a highly distorted square antiprism or a distorted bicapped trigonal prism. These polyhedra are corner and edge shared to form a three-dimensional framework. All transition metals are octahedrally coordinated by oxygen, where the octahedra are isolated from each other. These octahedra are framed by eight alkaline earth polyhedra (Figures 2.4 & 2.5). Two formula units are contained in each unit cell (Figure 2.6).

As is expected, the average transition metal-to-oxygen bond length decreases across the period from manganese to nickel for both the strontium and barium analogues (Table 2.3). The barium hexahydroxocuprate is an exception in that the copper is in a distorted octahedral coordination environment due to the Jahn-Teller distortion. The average alkaline earth metal-to-oxygen bond lengths differ between the strontium and barium analogues with the barium compounds having slightly longer bonds by 0.153-0.193 Å, as expected given the large size of barium. The smallest difference in bond lengths was observed for the nickel analogues and the greatest difference was observed for the manganese analogues. Within the strontium series, the strontium bond distance with oxygen is essentially constant (2.642(1)-2.640(1) Å). However, the barium analogues appear to exhibit a slight contraction in the barium to oxygen bond distances

across the period (2.824(1)-2.794(1) Å), with the copper analogue, again, being an exception.

Infrared Spectroscopy. As shown in Figure 2.7 and Figures 2.8-2.13, the spectra of all the hexahydroxometallates have two broad absorption bands in the 3400-3600 cm^{-1} range, consistent with the presence of hydroxyl groups in the structure. Each hexahydroxometallate structure has three unique hydroxide groups that are hydrogen bonded, broadening the bands.

Bond Valence Analysis. The bond valence analysis results listed in Table 4 were obtained using parameters by Brown.[41] The bond valence sums are all close to what is expected, $A = +2$, $B = +2$, and OH = -1, confirming the divalent oxidation states of the metals. Sutovic reported similar BVS results in the reinvestigation of $Sr_2Cu(OH)_6$.[42]

Thermogravimetric Analysis. It is well known that mixed metal hydroxides, oxalates, nitrates and acetates can be used as precursors in the preparation of interesting oxides.[43] Often, solid solutions or mixtures of two separate hydroxides have been prepared and then converted into the corresponding oxide. There are a number of instances where this technique of precipitating a mixed hydroxide product has been used to form perovskites. For example, Vidysagar *et al.* synthesized solid solutions of composition $Ln_{1-x}M_x(OH)_3$ (*Ln* = La, Nd; *M* = Cr, Fe) with metal nitrate solutions and NaOH and generated the corresponding perovskite products at low temperature.[44] A number of iridium and osmium perovskites were synthesized in a similar manner by Sarkozy.[45,46] Less often have *crystallized* hydroxides been studied for their oxide thermal conversion products. Morán–Miguélez and colleagues studied the crystallization of the

so-called silicon-free hydrogarnets with composition $A_3B_2(OH)_{12}$.[19] They reported that the thermal conversion mechanism proceeds by the general reaction given in Scheme 2:

$$A_3B_2(OH)_{12} \rightarrow A_3B_2O_6 + 6H_2O \ (T = 1000 \ ^\circ C) \quad \text{(Scheme 2)}$$
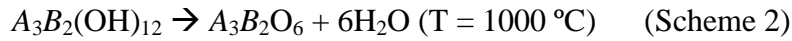
Similarly, Li and coworkers reported details about the thermal behavior of the chromium, iron, and aluminum hydrogarnets of strontium.[47] Their analysis concluded that for these hydroxides a loss of four waters occurred between 260 and 330 ℃. One interesting finding was that $Sr_3Al_2O_6$ was readily produced at temperatures of only 600 ℃, compared with 1600 ℃ reported for a traditional solid-state reaction.[48] It is, of course, also possible for some reactions to phase separate and generate mixed phase products, as was observed for the thermal decomposition of $Sr_3Cr_2(OH)_{12}$ into SrO and $SrCrO_4$.

$Sr_2Cu(OH)_6$, a previously reported structural analogue of the title series, was utilized by Shimakawa and colleagues as a single-source precursor for the preparation of Sr_2CuO_{3+x}, a phase which can be superconducting under certain processing conditions.[49] Nagai and co-workers used calcium-substituted $Sr_2Cu(OH)_4 \cdot H_2O$ and barium-substituted $Sr_2Cu(OH)_6 \cdot H_2O$ prepared as powders by the method introduced by Scholder as precursors for oxides in the (Ba, Sr, Ca)-Cu-O system.[50,51] Such reactions demonstrate the utility of using hydroxometallates as precursors to overcome diffusion barriers, allowing reactions to be carried out at lower temperatures. The low reaction temperatures can possibly lead to the isolation of new, metastable materials. To learn more about mixed metal hydroxides as potential oxide precursors, where the precise atomic ratio coupled with atomic level mixing to minimize cation diffusion should prove beneficial, we decided to study the thermal decomposition behavior of this series of isostructural hexahydroxometallates.

33

Thermogravimetric analyses of the new hexahydroxometallates were performed in air and the decomposition products are given in Table 2.5. A careful analysis of the powder X-ray diffraction patterns collected on samples isolated at each temperature where a plateau was evident in the data indicates that the hexahydroxometallates dissociate into alkaline earth hydroxides and other, transition metal-containing products. All of the hexahydroxometallates studied show a first weight loss between 210-350 ºC in air, which corresponds to the breakdown of the hydroxide lattice, yielding corresponding oxides at higher temperature (Figures 2.14-2.26). The stoichiometry of the final products is dependent upon the metal identities and does not follow a general reaction scheme.

Thermal decomposition of $Sr_2Mn(OH)_6$ under an inert atmosphere occurs in four steps (Figure 2.15). The first weight loss is observed by 260 ºC with a product of $Sr_2MnO_4(OH)$.[52] A very small weight loss is seen around 400 ºC followed by another small weight loss around 640 ºC. Varying amounts of both $Sr_2MnO_4(OH)$ and Sr_2MnO_4[53] are present during these changes. The final weight loss is observed between 850 and 900 ºC, followed by as gradual loss all the way to 1100 ºC. The decomposition product above 900 ºC is pure Sr_2MnO_4 and by 1100 ºC matches $Sr_2MnO_{3.615}$ reported by Gillie and coworkers.[54] TGA data corroborates this with an experimentally observed loss of mass between 150 ºC and 1100 ºC (ignoring loss of residual crystal water) of 85% versus a theoretical loss of 86.2% assuming complete conversion of the initial hydroxide to the corresponding stoichiometric oxide. Experiments performed in both air and N_2 flow yield the same product, although experiments performed in air showed the eventual thermal breakdown of $Sr_2MnO_{4-\delta}$ into $SrCO_3$ and $Sr_7Mn_4O_{15}$[55] while this phenomenon was not observed under N_2 flow in the temperature range studied. The previously described solid

34

state syntheses of Sr_2MnO_4 and $Sr_2MnO_{3.615}$ were reported to take place at 1650 °C and 1350 °C, respectively, and the use of a single-source precursor significantly lowers the preparation temperature.

Analogous to the thermal decomposition of $Sr_2Mn(OH)_6$ to Sr_2MnO_4, $Ba_2Co(OH)_6$ is thermally converted to Ba_2CoO_4 under N_2 flow. This low dimensional oxide has previously been synthesized by Boulahya and colleagues, who characterized its electronic and magnetic properties.[56] The synthesis temperature using $Ba_2Co(OH)_6$ is similar to that utilized in the solid state synthesis previously described (900 °C) and it does not appear that a single-source precursor offers an advantage in this case. Powder X-ray diffraction analysis of the decomposition products at varying temperatures indicates that $Ba_2Co(OH)_6$ decomposes into $BaCoO_{3-\delta}$[57] and $BaCO_3$ at 375 °C instead of converting into stoichiometric products in a step-wise fashion as is the case with $Sr_2Mn(OH)_6$.

Although no other compositions studied yielded a stoichiometric oxide product, the synthesis temperatures for some of these products are noteworthy. Some compounds are prepared at or above previously reported temperatures, such as $Ba_3Mn_2O_8$ (900 °C),[58] $BaMnO_3$ (500 °C),[59] $BaNi_{0.85}O_{2.5}$ (1100 °C).[60] Other decomposition products are produced at temperatures lower than any previous literature report, such as $Sr_2Ni_2O_5$ (375 °C vs. 1000 °C),[61] $Sr_6Co_5O_{15}$ (420 °C vs. 1000 °C),[62] $BaNiO_3$ (325 °C vs. 450 °C[63] or 600 °C[64]), $Ba_3Co_2O_6(CO_3)_{0.6}$ (525 °C vs. 750 °C),[65] and $Sr_9Ni_{6.64}O_{21}$ (810 °C vs. 880 °C).[66] In these cases, starting with a single-source precursor reduces diffusion distances and results in a lower preparation temperature when compared to standard solid-state synthesis. However, as the precursor is non-stoichiometric with respect to the resultant oxide, alkaline earth hydroxide or carbonate byproducts are produced. These byproducts can be

washed away in most cases with dilute acid without decomposing the oxide product. The thermal decomposition of $Sr_2Co(OH)_6$ in a N_2 atmosphere yielded unknown products which do not match any known pattern for an oxide containing strontium and/or cobalt. Attempts to isolate this poorly crystalline product were unsuccessful as strontium hydroxide was a major byproduct and treatment with dilute acid decomposed the oxide rapidly.

Magnetism. The temperature dependence of the magnetic susceptibility (χ) for the nickel, cobalt, and manganese analogues, measured under zfc and fc conditions, were investigated. Temperature dependence of the inverse susceptibility data were fit to the Curie-Weiss law where $\chi = C/(T-\theta)$; C is the Curie constant, θ is the paramagnetic Weiss temperature. All samples show purely paramagnetic behavior down to 5 K.

Due to the presence of small amounts of residual carbonate impurities, as well as potential amorphous phases such as $Ni(OH)_2$, the magnetic moments are approximate due to the uncertainty in sample mass. $Sr_2Mn(OH)_6$ and $Ba_2Mn(OH)_6$ exhibit effective moments of 5.41 μ_B and 5.74 μ_B, respectively, which are close to that expected for Mn^{2+} (μ_{eff} = 5.92 μ_B, S = 5/2). (Figures 2.27 & 2.28) Some $Sr_2Co(OH)_6$ and $Ba_2Co(OH)_6$ crystals contained small black inclusions, most likely a cobalt oxide, that affects the measured moment. It was not possible to completely remove this byproduct from the synthesized crystals and it was present in quantities too small for identification. Nonetheless, the magnetic data support strictly paramagnetic behavior for $Sr_2Co(OH)_6$ and $Ba_2Co(OH)_6$ as shown in Figure 2.29 and 2.30, respectively. $Sr_2Ni(OH)_6$ and $Ba_2Ni(OH)_6$ also display paramagnetic behavior and their data are shown in Figures 2.31 and 2.32, respectively.

CONCLUSION

A series of new transition metal hexahydroxometallates was synthesized using a hydroflux technique. $Sr_2Mn(OH)_6$, $Ba_2Mn(OH)_6$, $Sr_2Co(OH)_6$, $Ba_2Co(OH)_6$, $Sr_2Ni(OH)_6$, $Ba_2Ni(OH)_6$ and $Ba_2Cu(OH)_6$ have been prepared and structurally characterized by single crystal X-ray diffraction. Infrared spectroscopy confirms the presence of and differences in bond lengths of the three crystallographically distinct hydroxide groups. Thermal decomposition in air and nitrogen has been investigated and the subsequent products are reported for the six new compounds. The magnetic properties of the compounds were measured, with simple paramagnetic behavior exhibited for all six hexahydroxometallates.
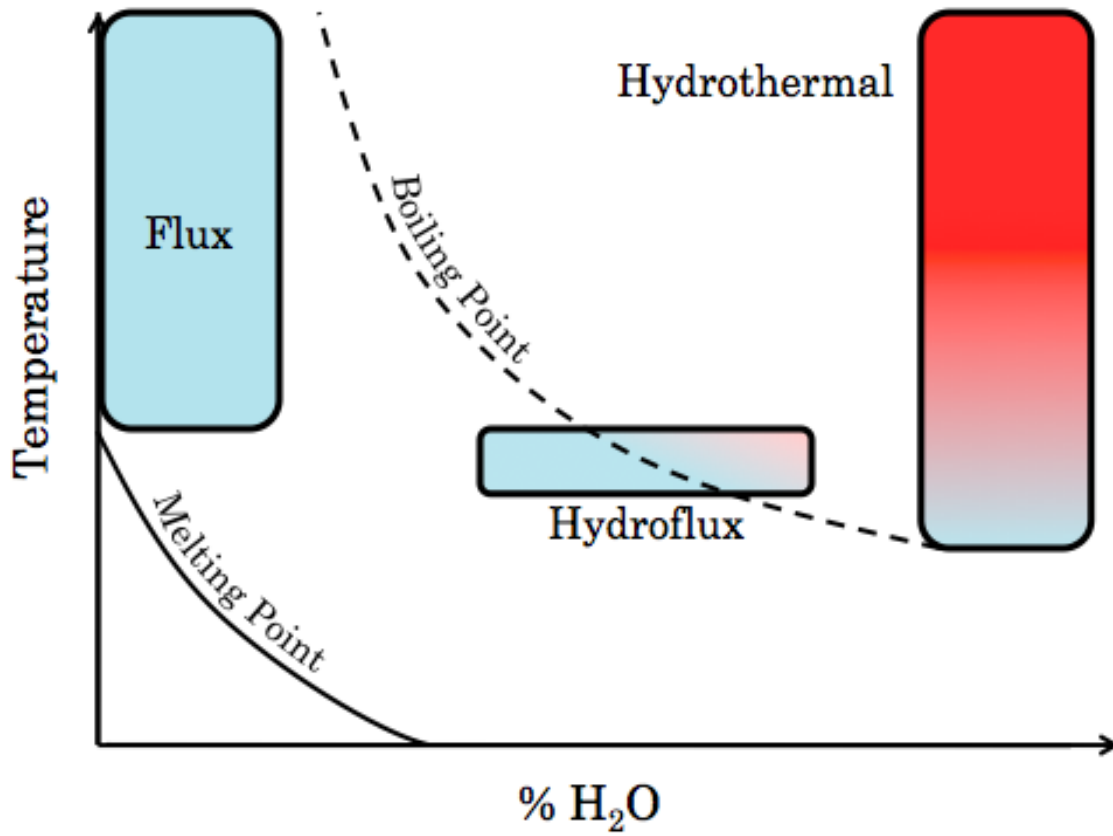
Figure 2.1. Comparison of hydrothermal, flux, and hydroflux techniques with respect to temperature and water content. Red denotes a high vapor pressure, while blue denotes little to no vapor pressure.
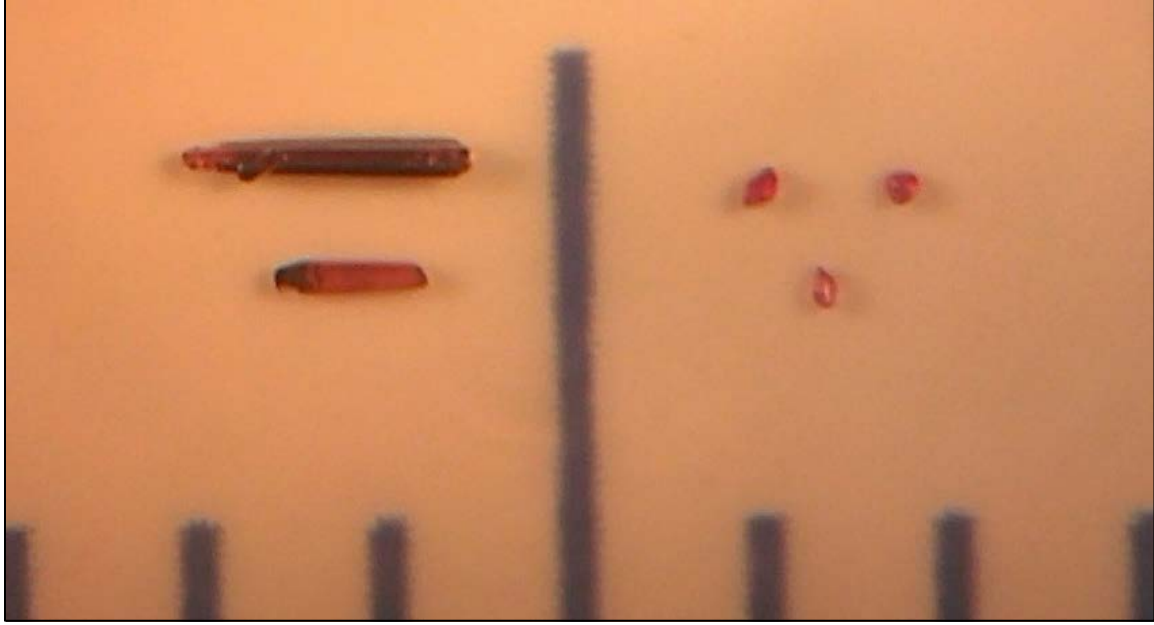
Figure 2.2. $Sr_2Co(OH)_6$ crystals grown in the presence of WO_3 mineralizer (left) exhibit a different crystal morphology and increased size compared with crystals grown without WO_3 (right). Graduations are in millimeters.
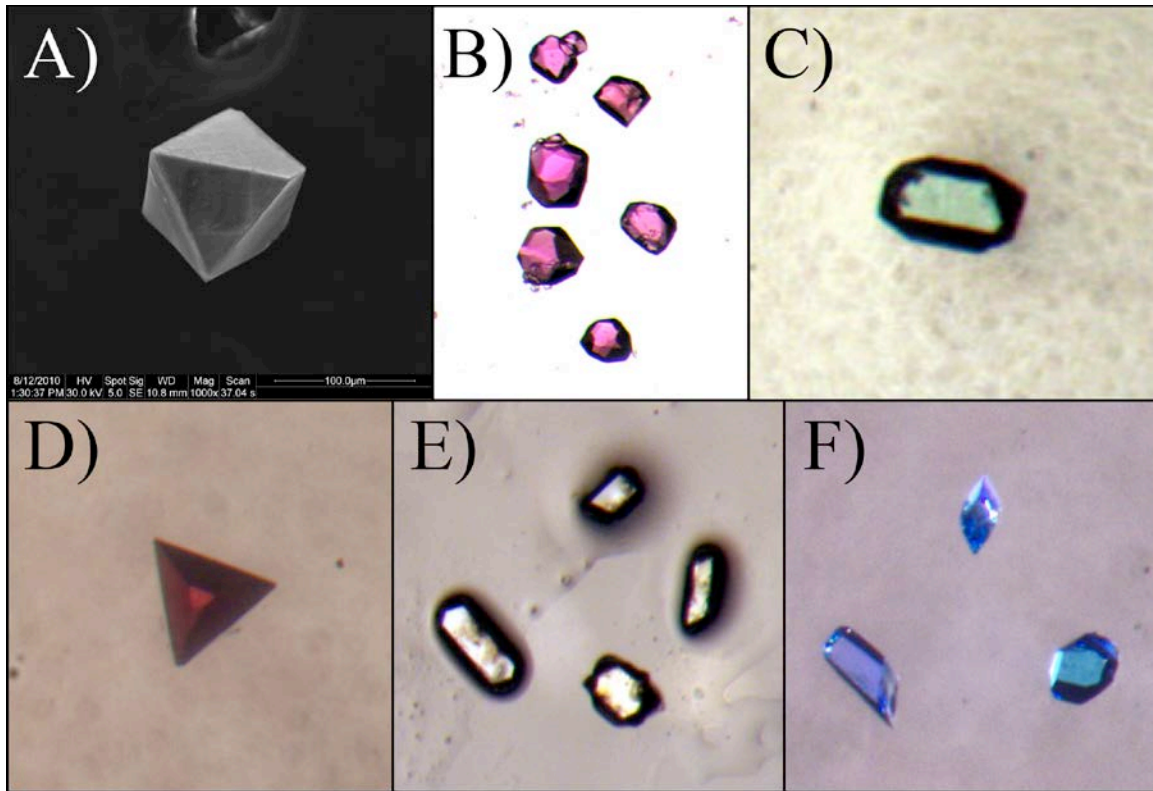
Figure 2.3. SEM image of a) $Sr_2Mn(OH)_6$ and optical images of b) $Sr_2Co(OH)_6$, c) $Sr_2Ni(OH)_6$, d) $Ba_2Mn(OH)_6$, e) $Ba_2Co(OH)_6$, and f) $Ba_2Cu(OH)_6$.
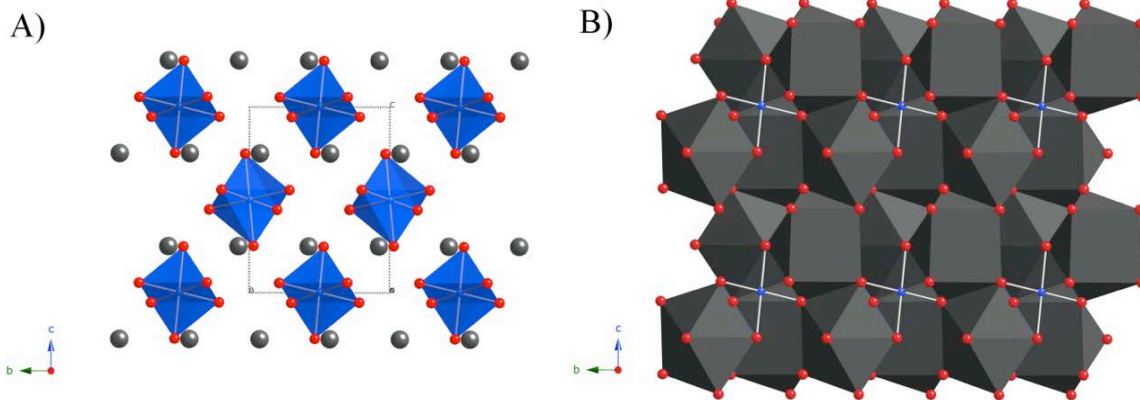
Figure 2.4. Extended structure of $Sr_2Co(OH)_6$ with the cobalt octahedra featured in blue and strontium atoms shown in gray (a), and with the strontium polyhedra shown in gray with the cobalt coordination in blue (b). Oxygen atoms are shown in red and hydrogen atoms are omitted for clarity.
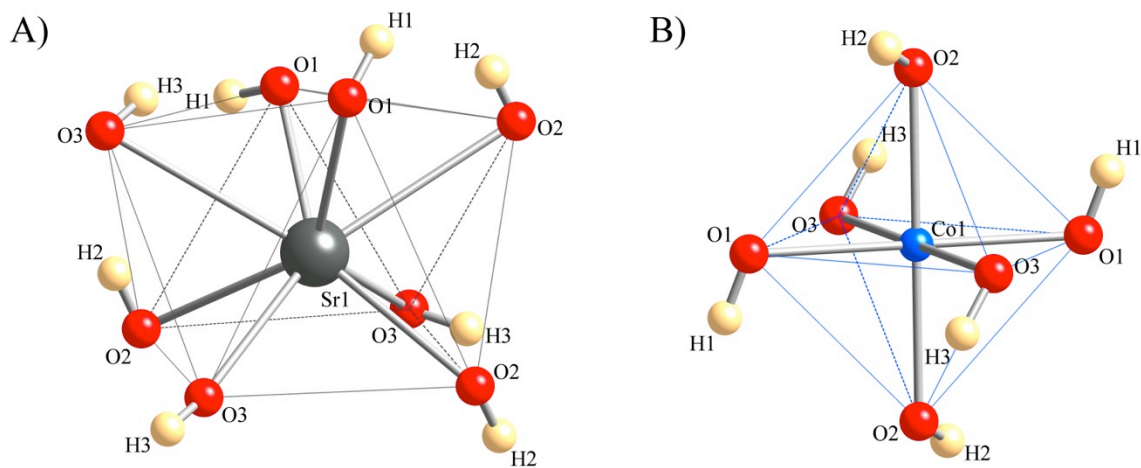
Figure 2.5. Local coordination environments of the strontium (a) and cobalt (b) atoms in $Sr_2Co(OH)_6$.
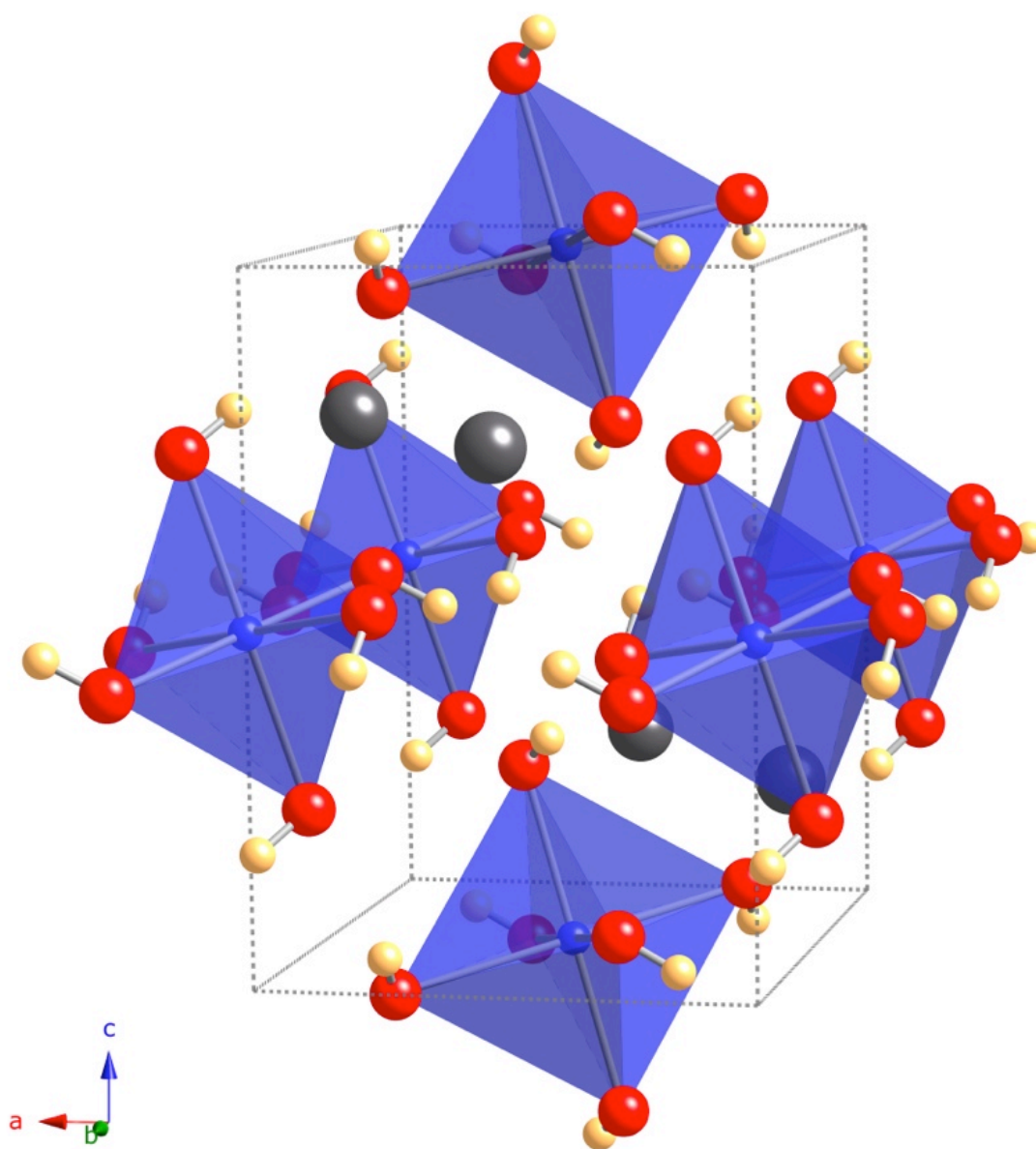
Figure 2.6. Unit cell of $Sr_2Co(OH)_6$ with strontium in gray, cobalt in blue with its coordination polyhedra in blue, oxygen in red, and hydrogen atoms in light orange.
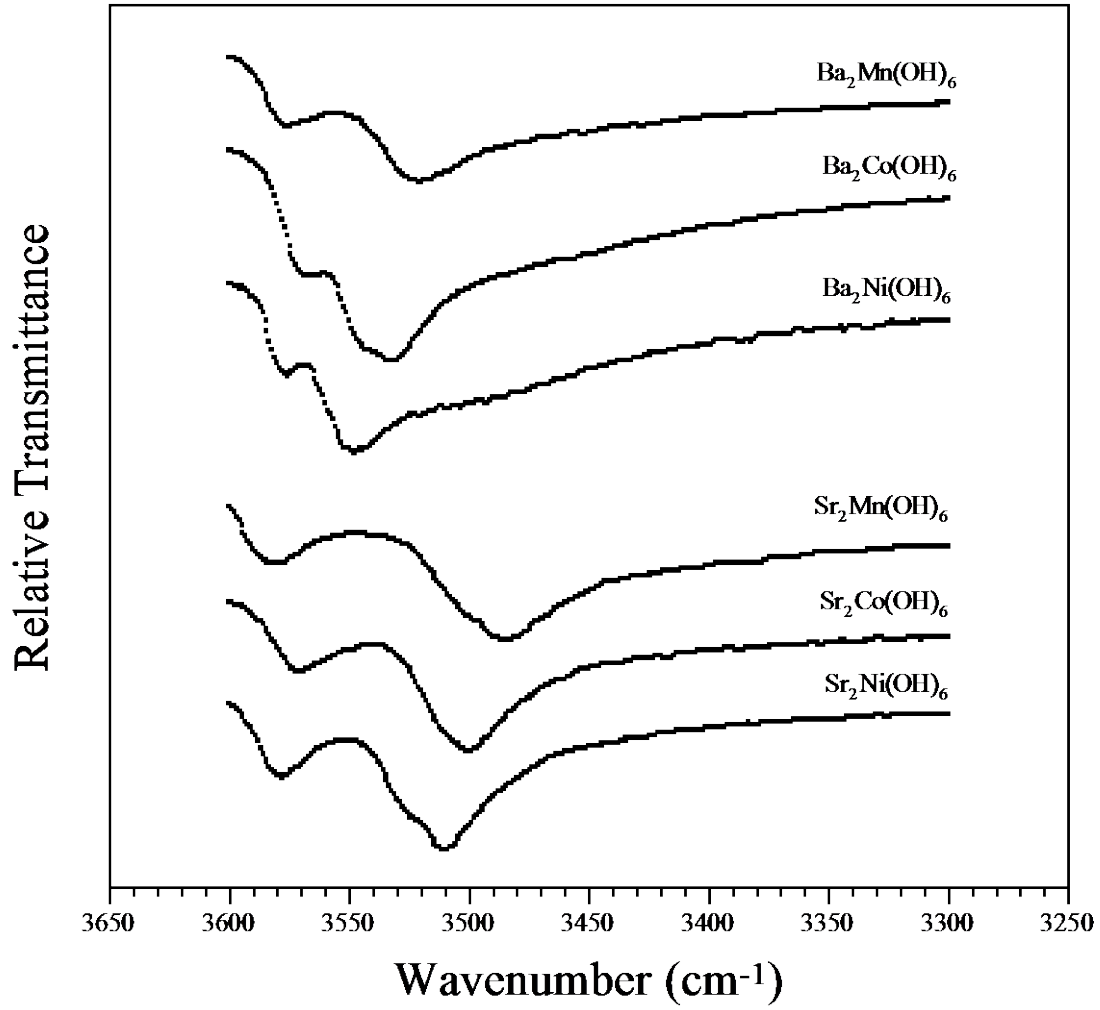
Figure 2.7. IR absorption spectra for selected hydroxides from 3650-3250 cm^{-1}.
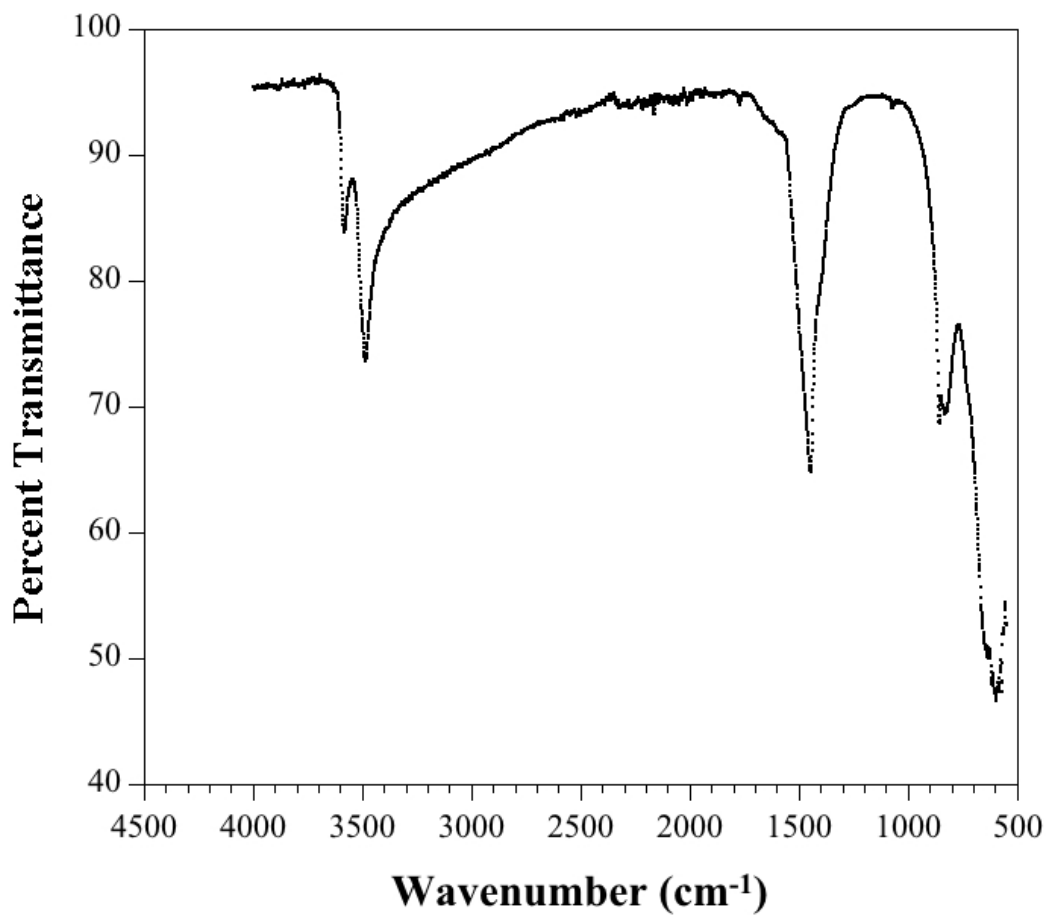
Figure 2.8. IR spectrum at room temperature for $Sr_2Mn(OH)_6$.
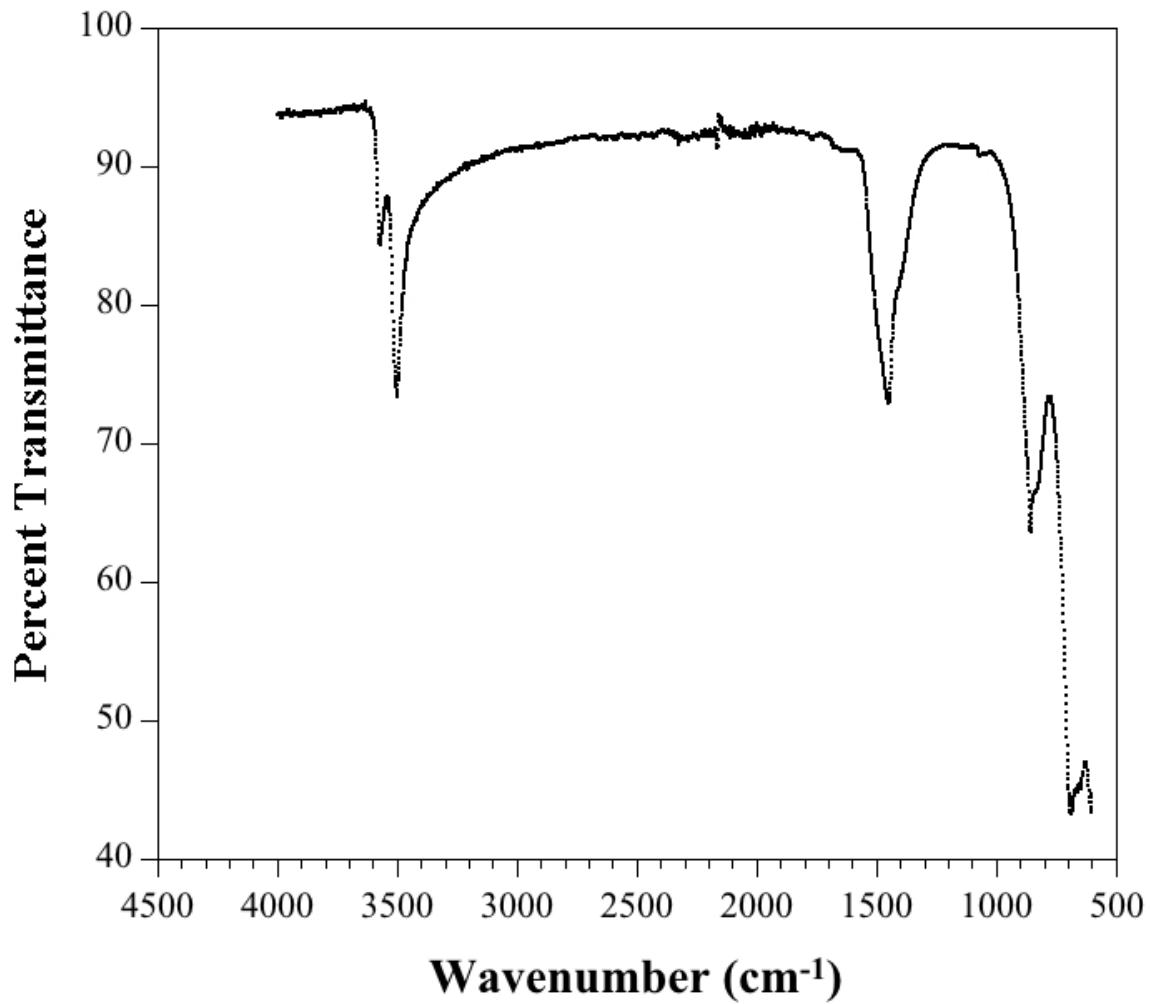
Figure 2.9. IR spectrum at room temperature for $Ba_2Mn(OH)_6$.
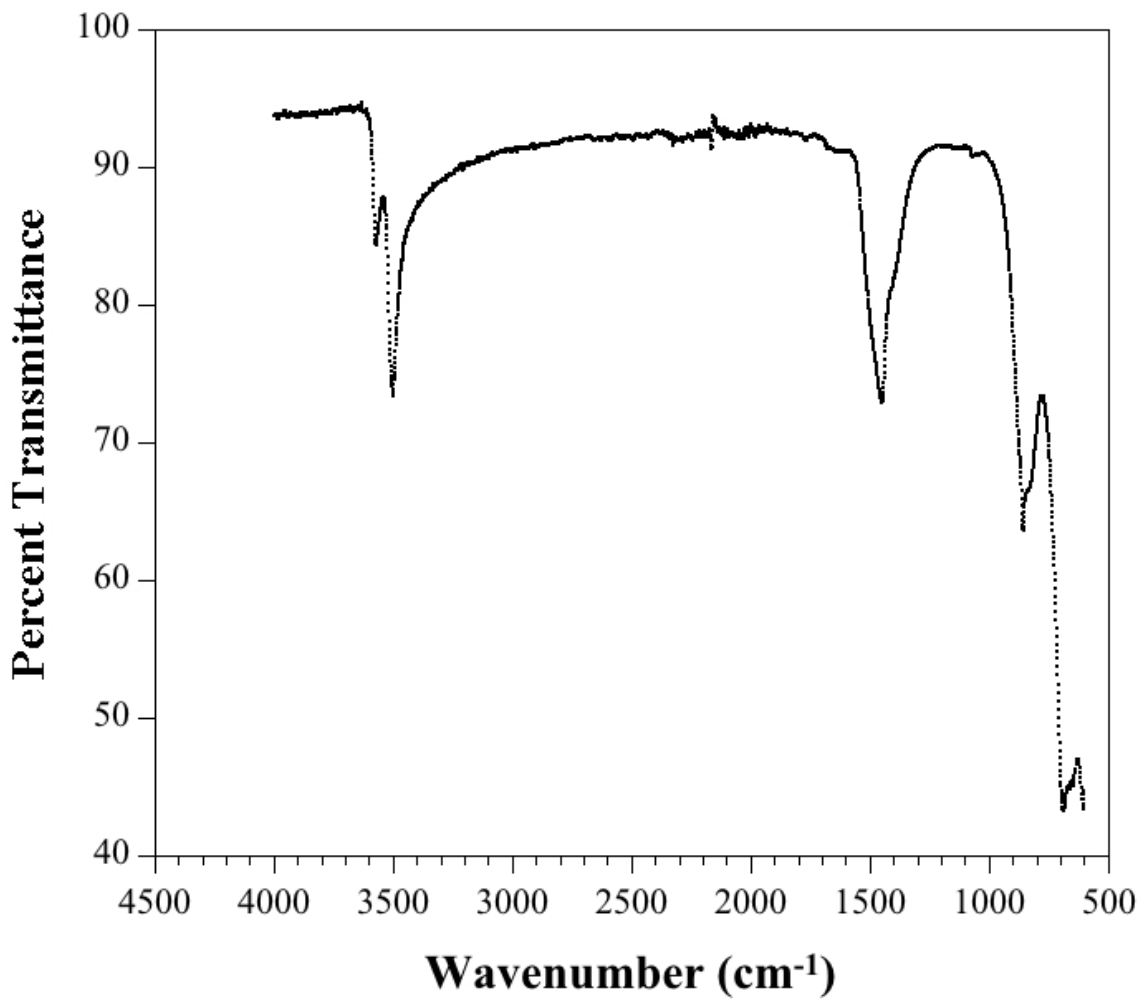
Figure 2.10. IR spectrum at room temperature for $Sr_2Co(OH)_6$.
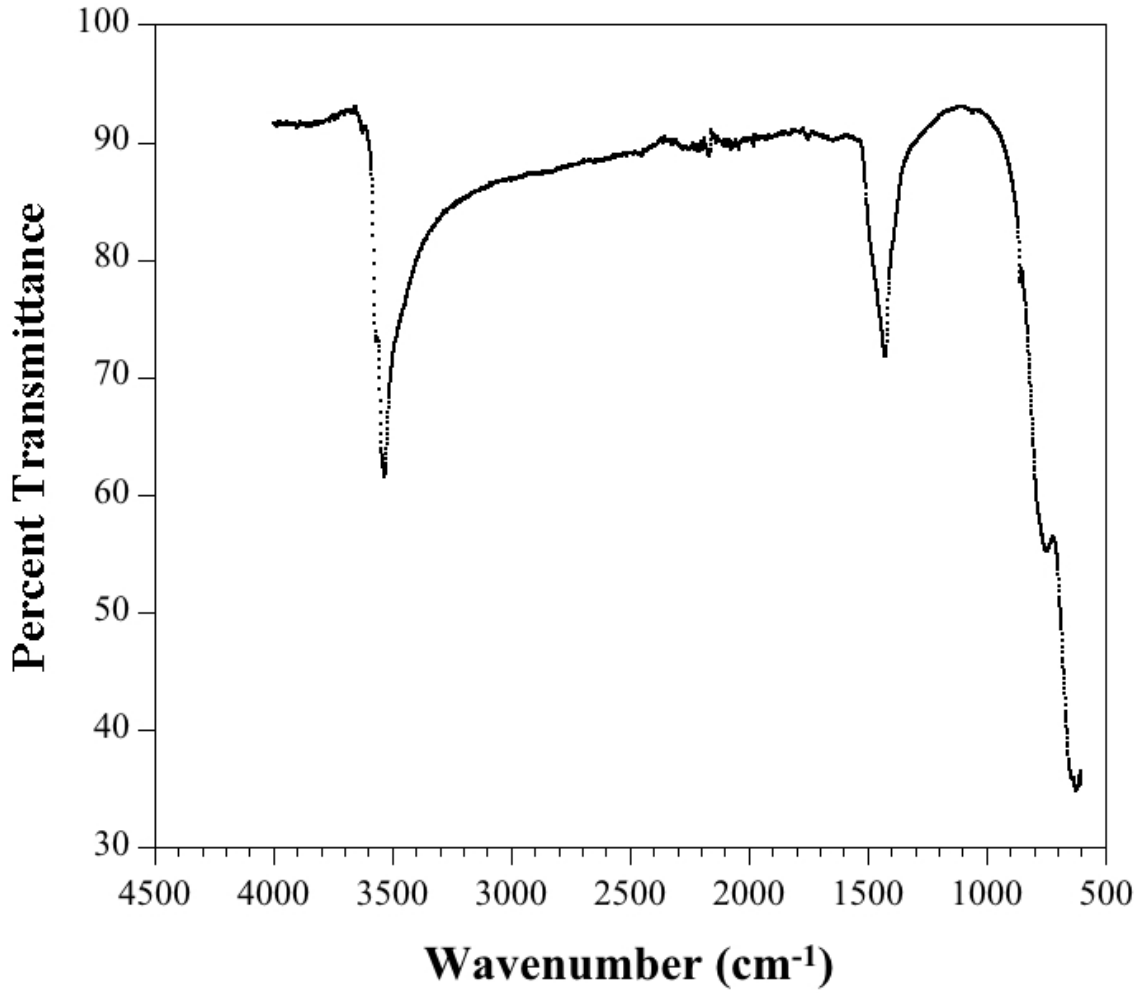
Figure 2.11. IR spectrum at room temperature for $Ba_2Co(OH)_6$.
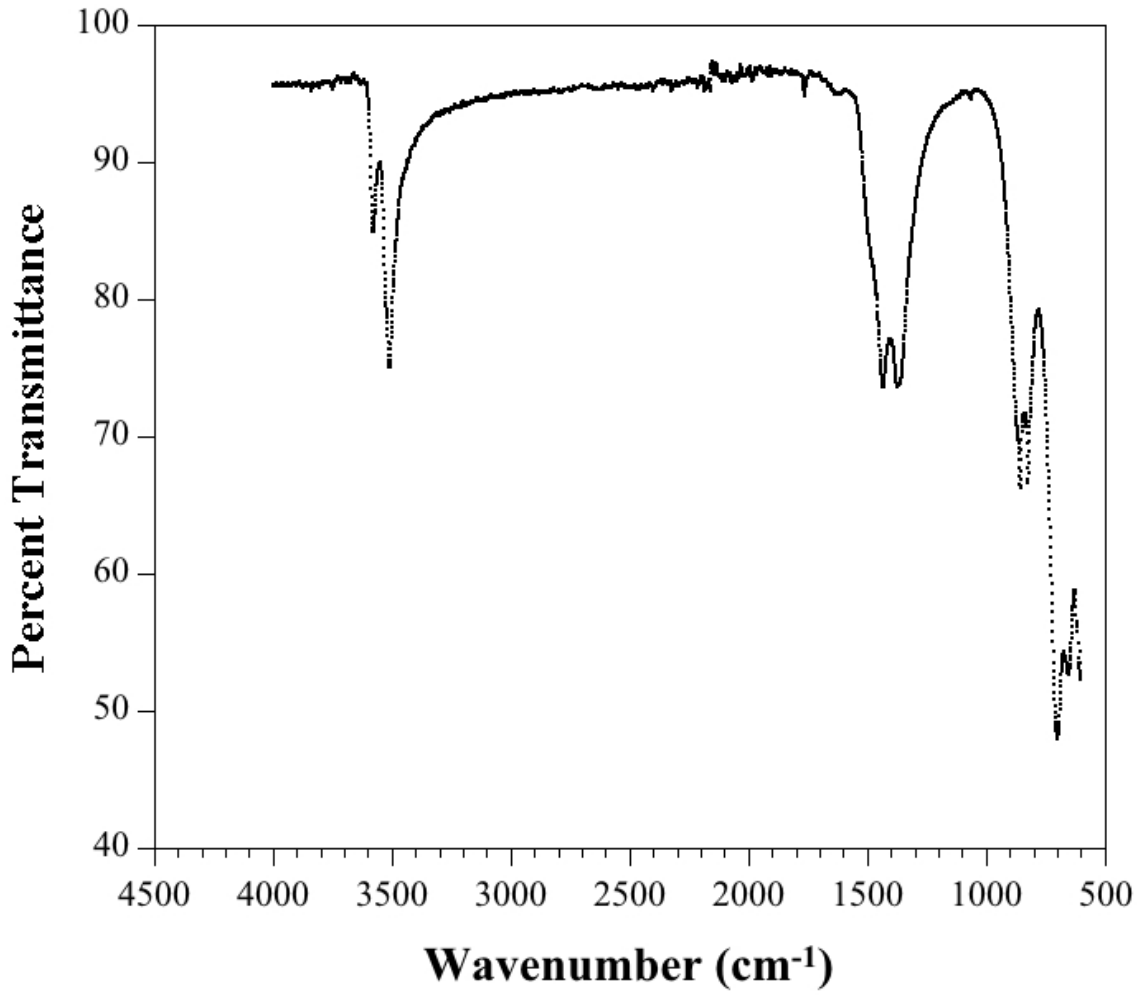
Figure 2.12. IR spectrum at room temperature for $Sr_2Ni(OH)_6$.
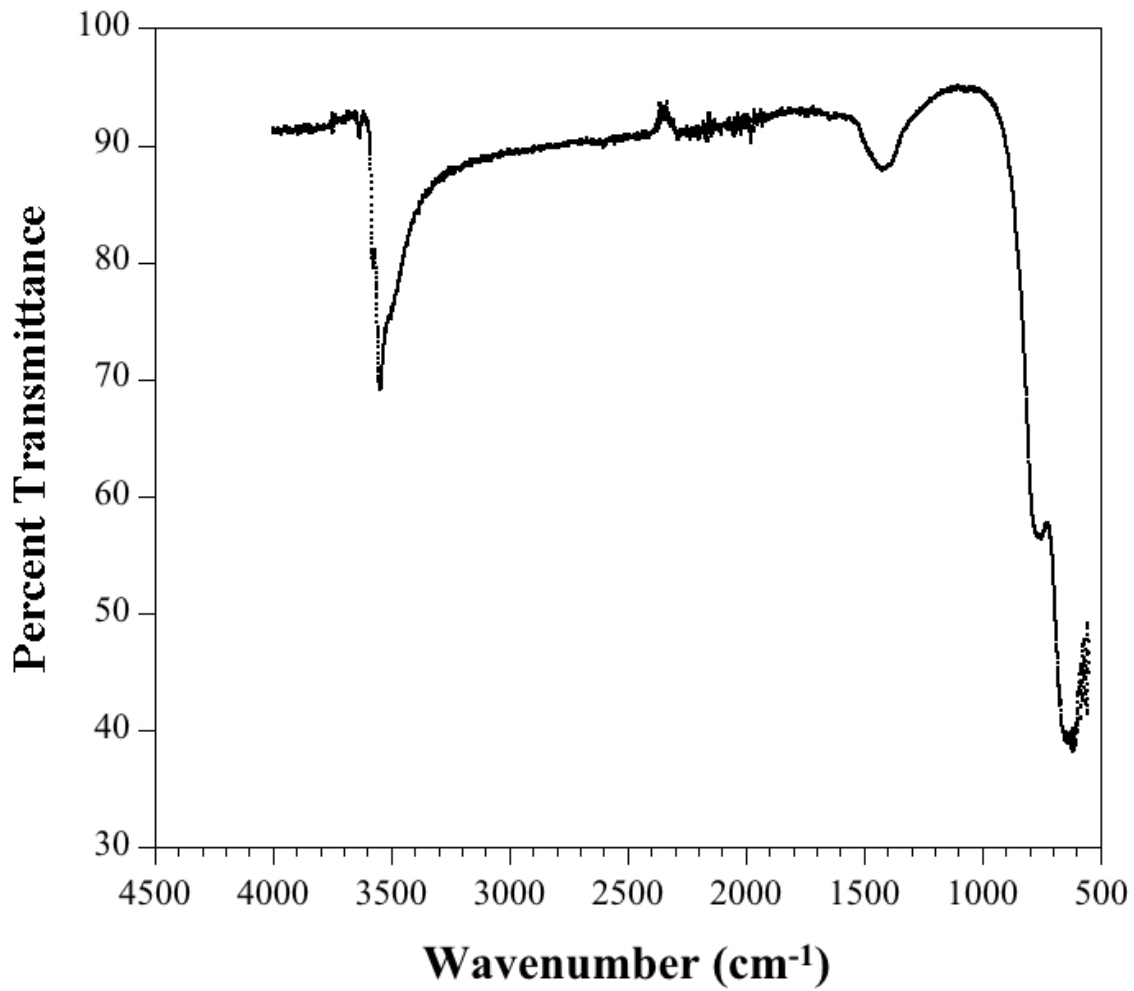
Figure 2.13. IR spectrum at room temperature for $Ba_2Ni(OH)_6$.
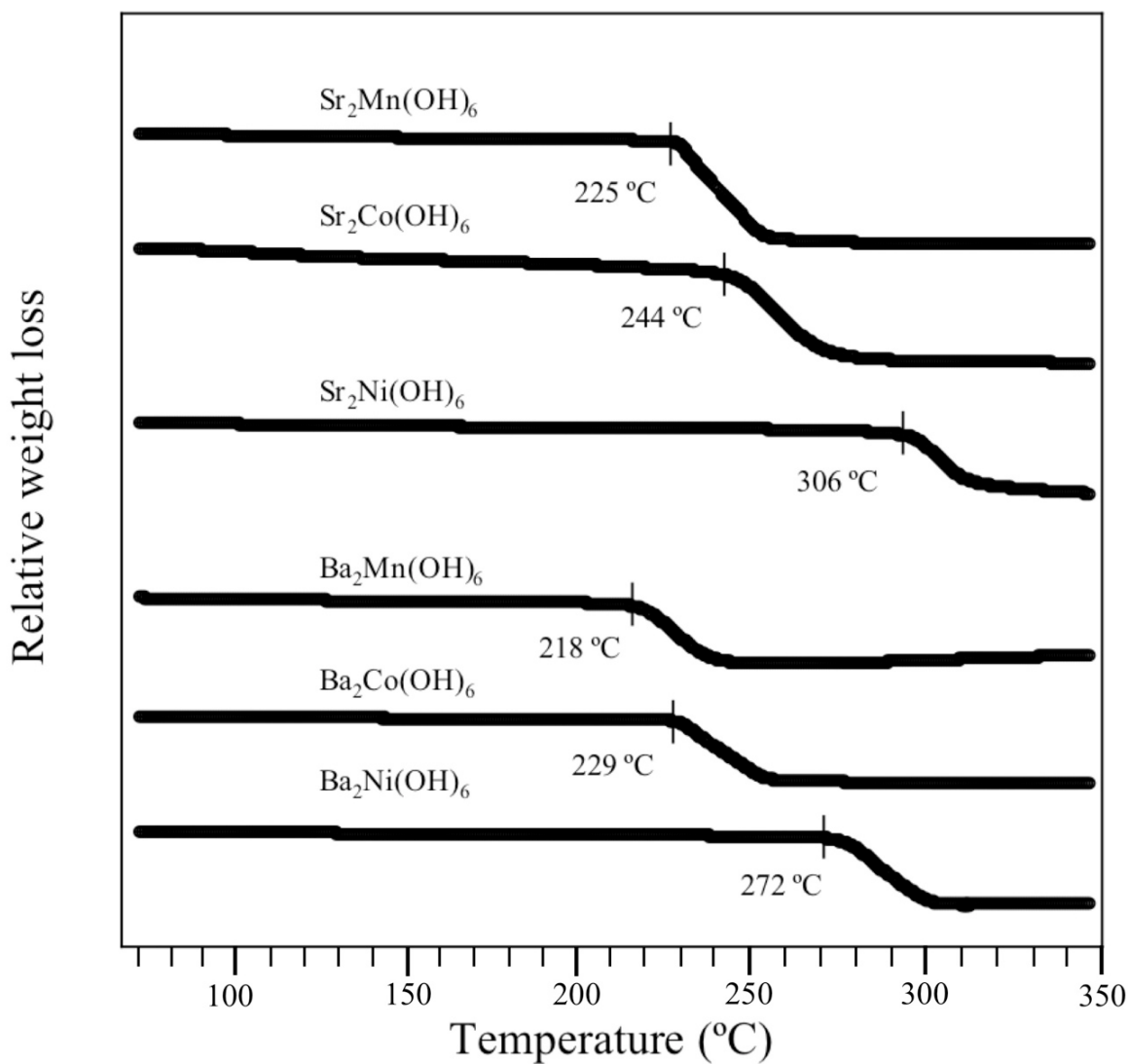
Figure 2.14. Thermogravimetric analysis (TGA) data for selected hydroxides in air. Temperatures for the breakdown of the hydroxide lattice are indicated.

50
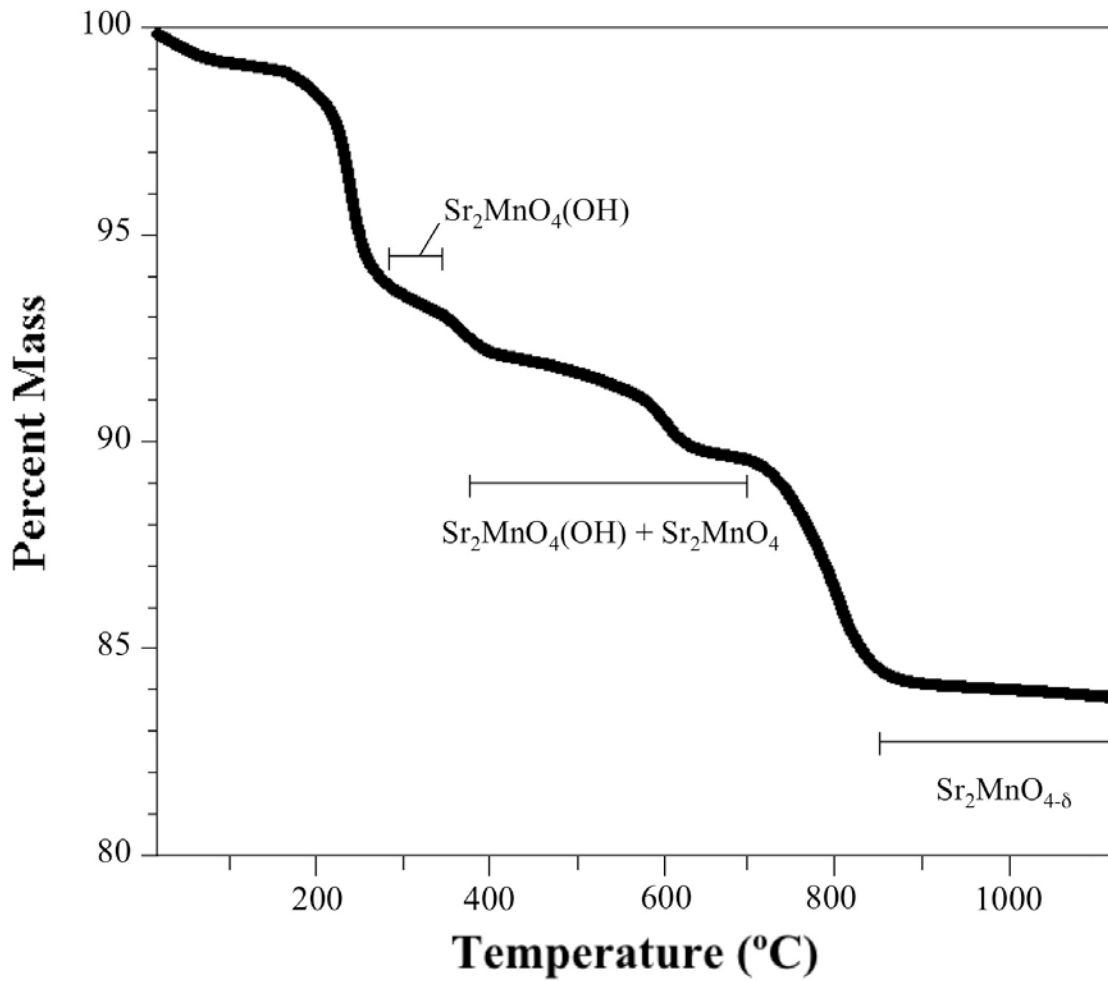
Figure 2.15. TGA data plot for $Sr_2Mn(OH)_6$ in air with sample composition indicated at various temperature ranges.
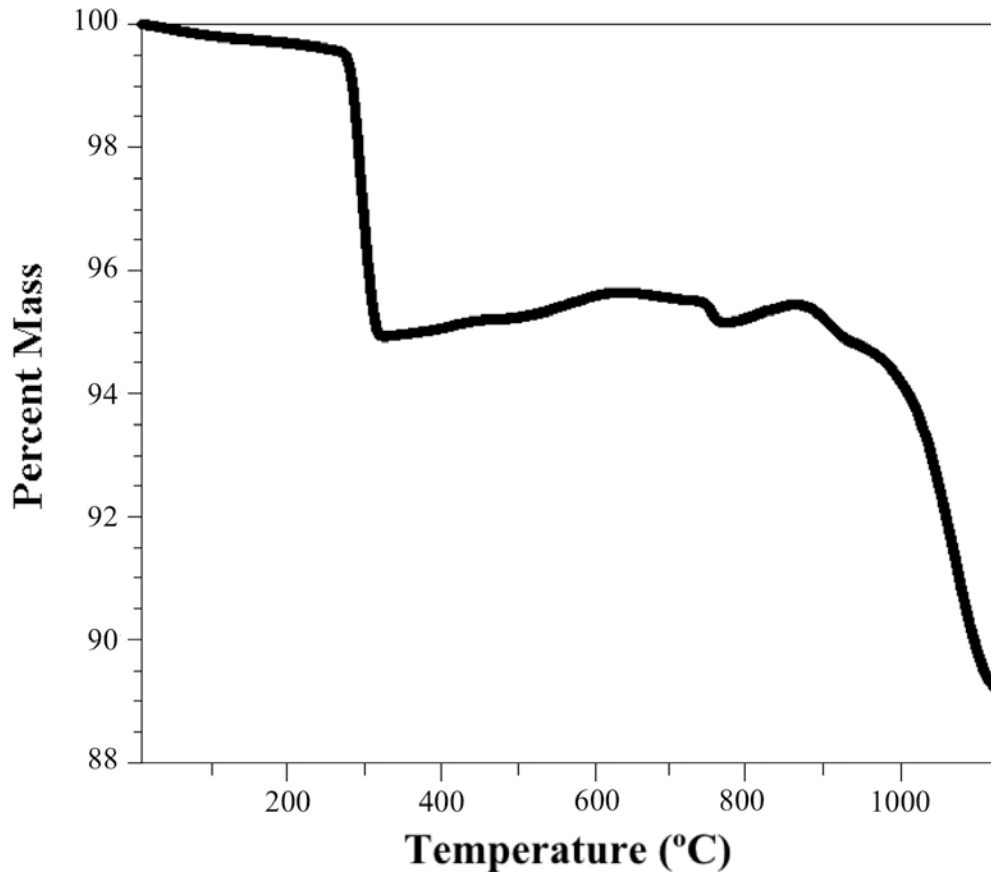
Figure 2.16. TGA data plot for $Ba_2Mn(OH)_6$ in air.
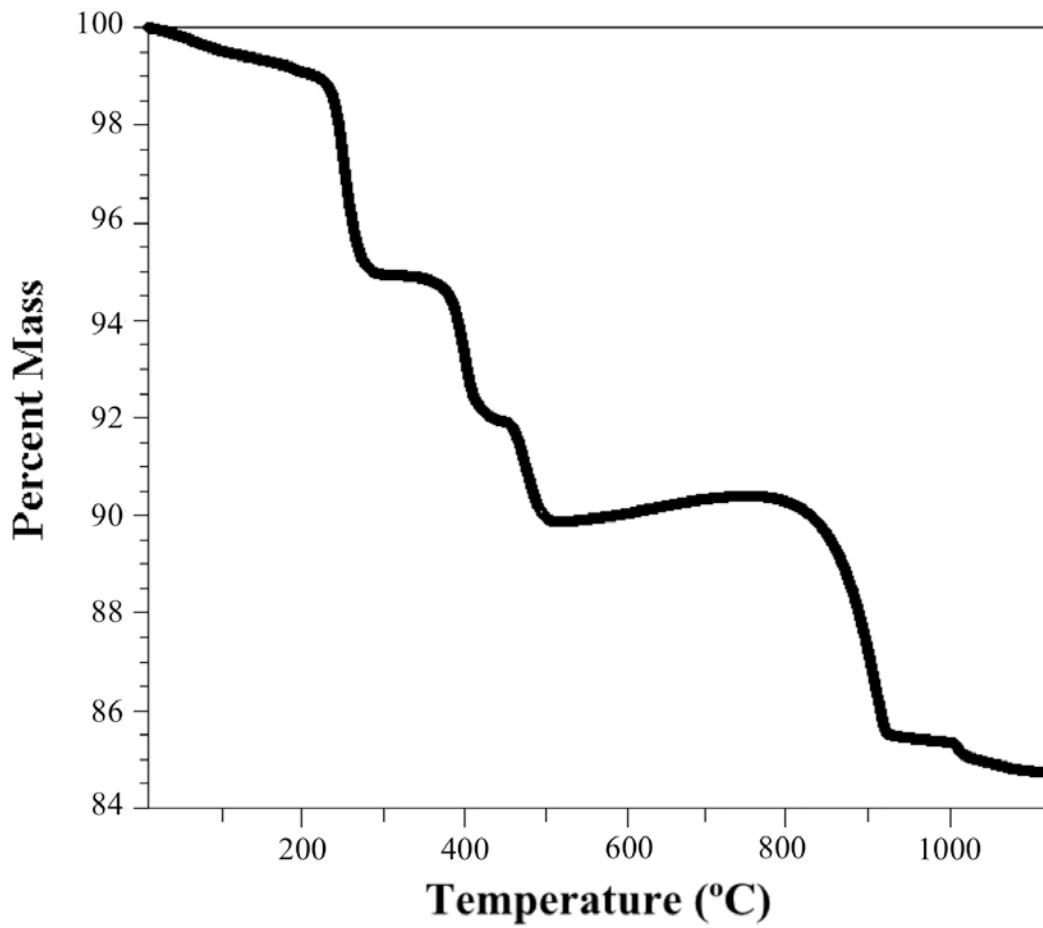
Figure 2.17. TGA data plot for $Sr_2Co(OH)_6$ in air.
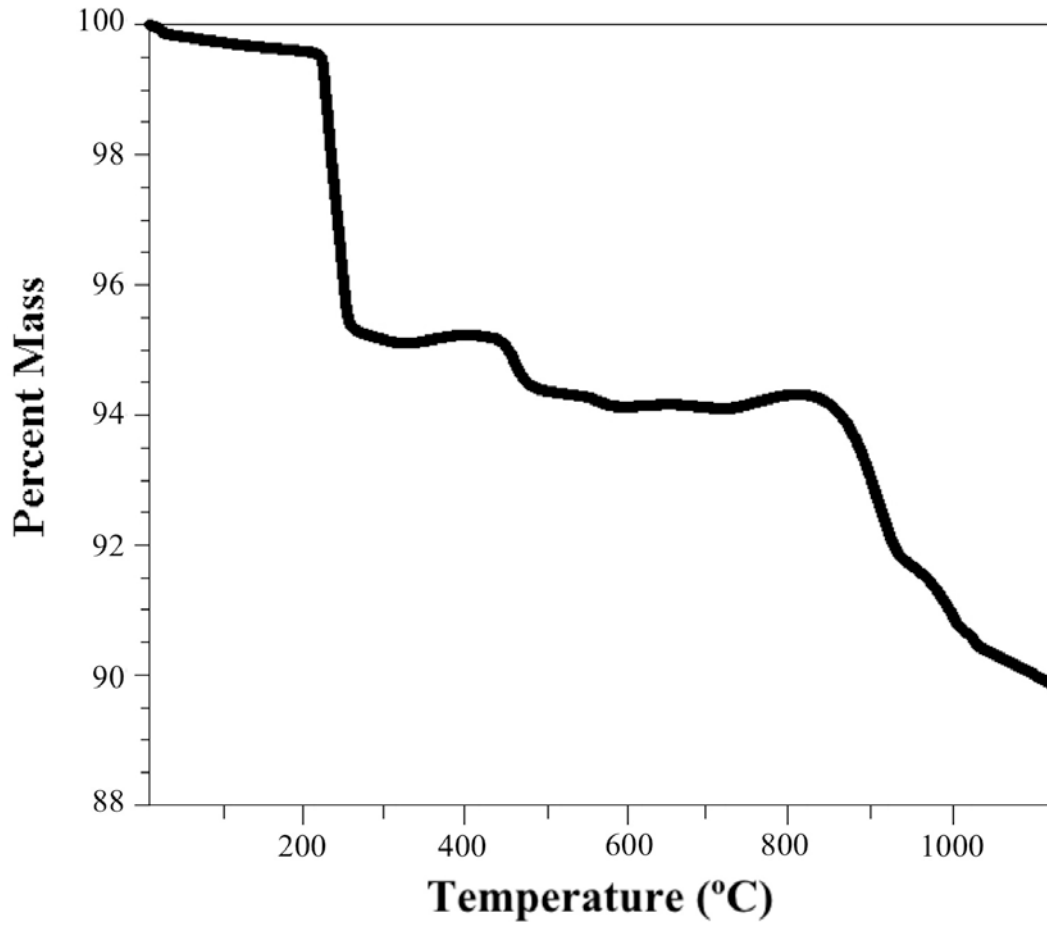
Figure 2.18. TGA data plot for $Ba_2Co(OH)_6$ in air.
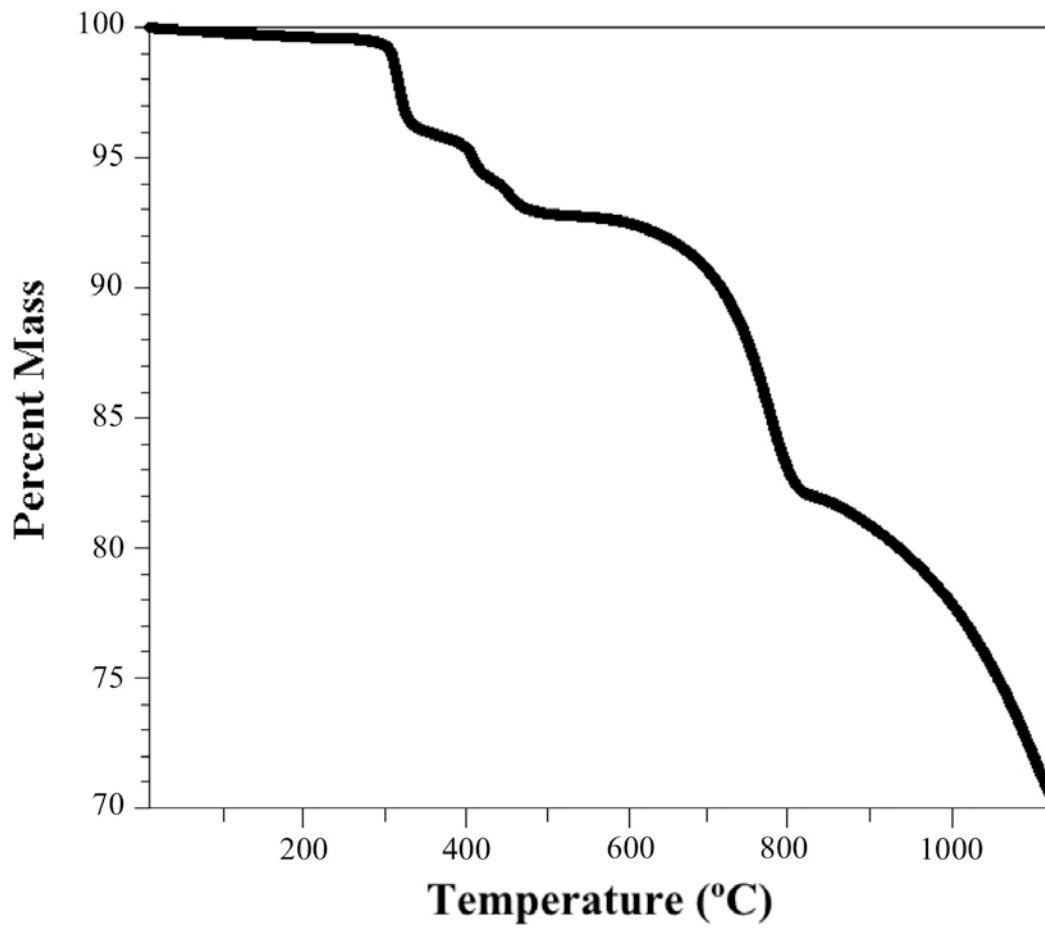
Figure 2.19. TGA data plot for $Sr_2Ni(OH)_6$ in air.
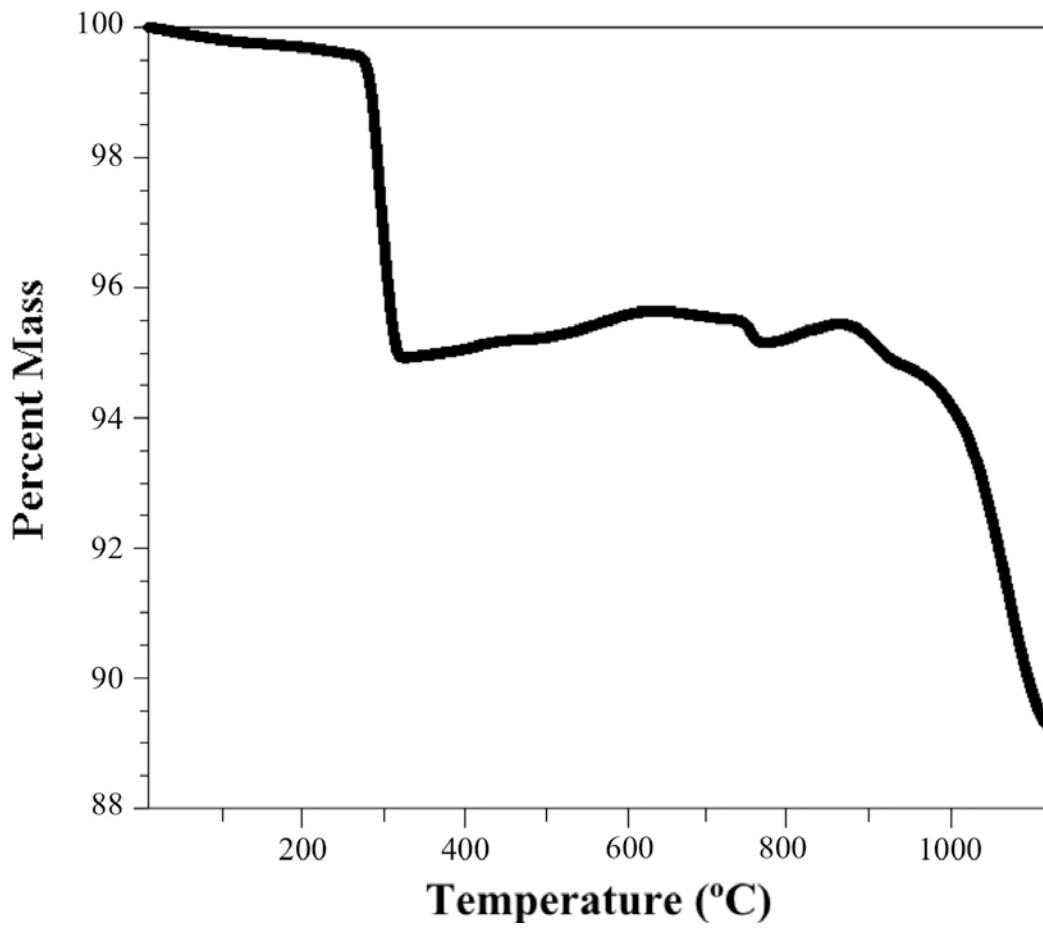
Figure 2.20. TGA data plot for $Ba_2Ni(OH)_6$ in air.
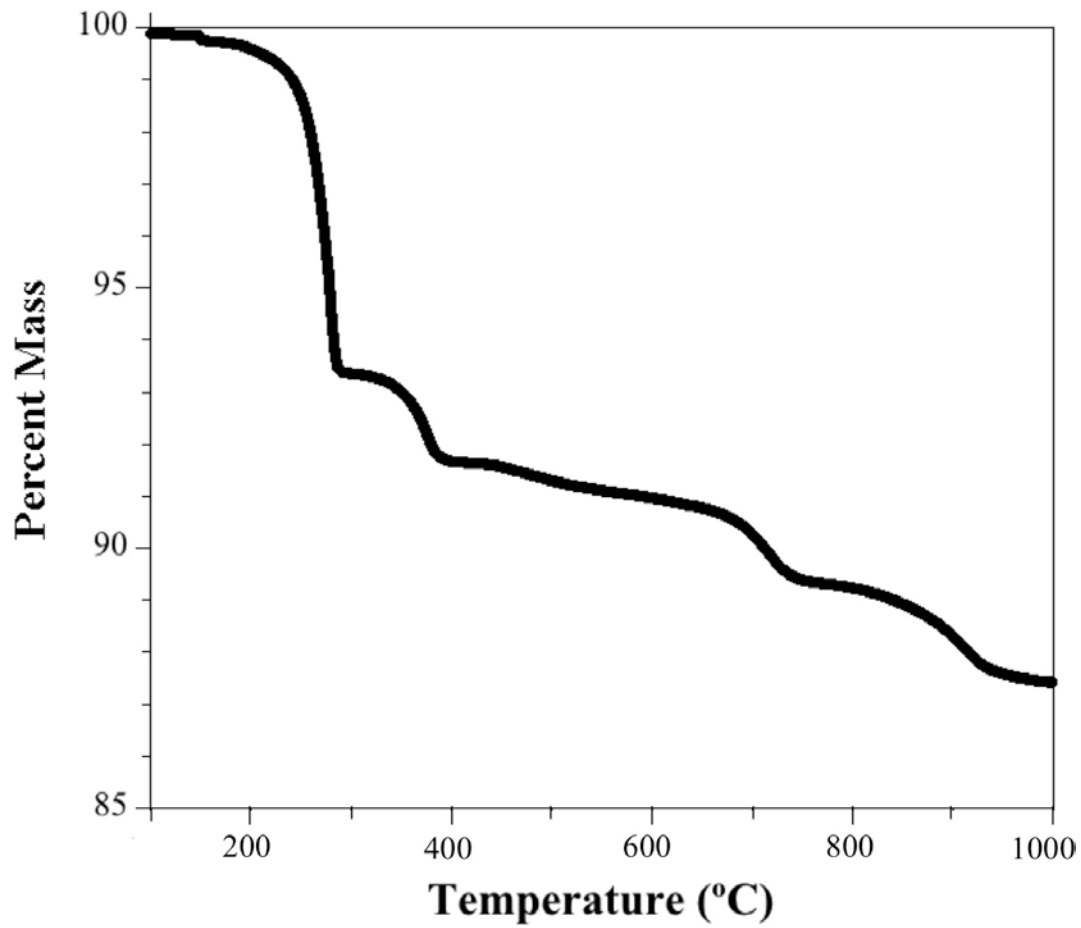
Figure 2.21. TGA data plot for $Sr_2Mn(OH)_6$ in nitrogen.
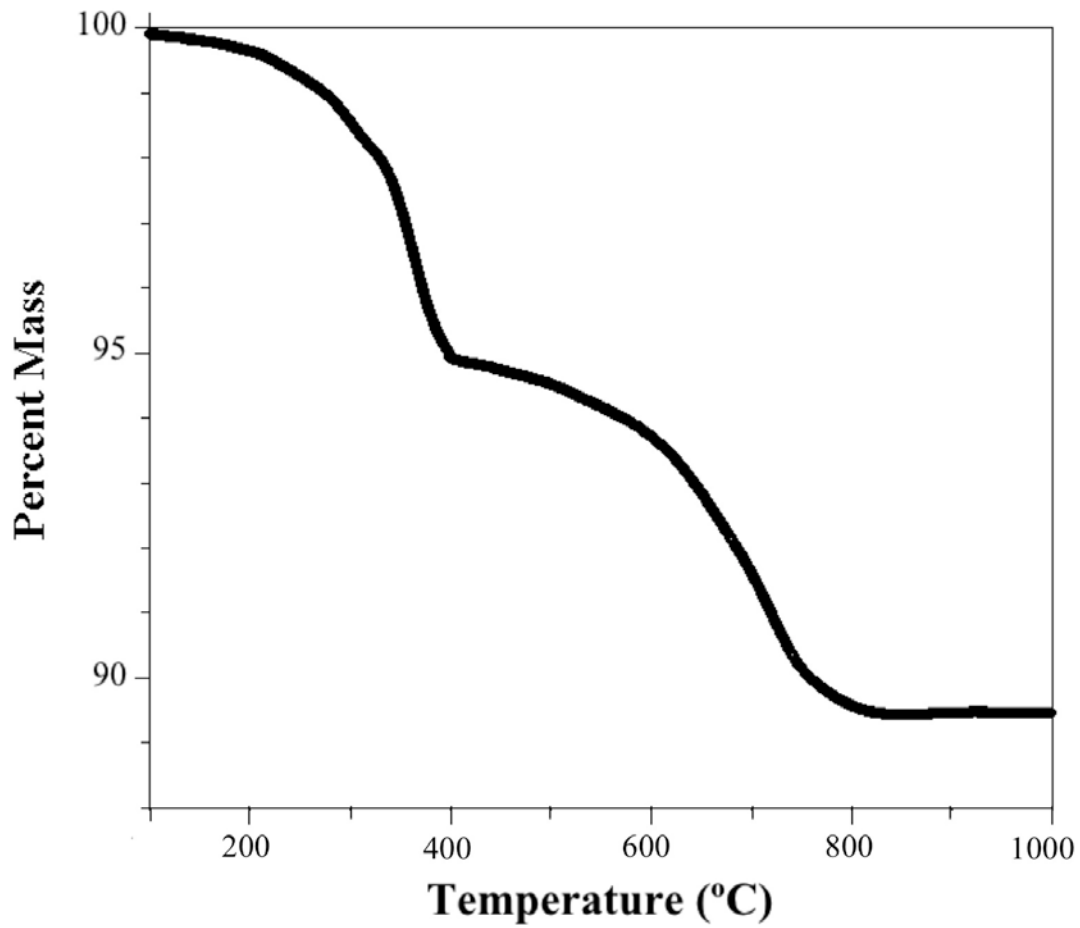
Figure 2.22. TGA data plot for $Ba_2Mn(OH)_6$ in nitrogen.
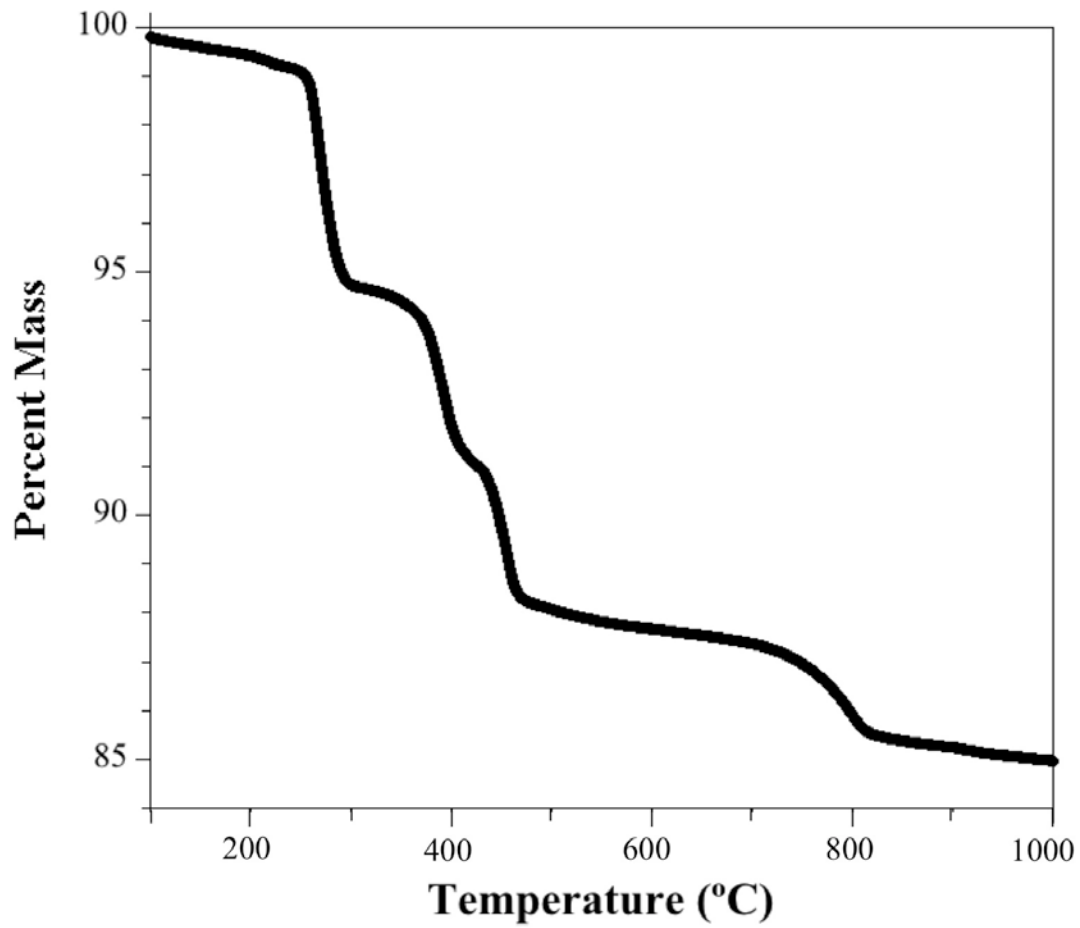
Figure 2.23. TGA data plot for $Sr_2Co(OH)_6$ in nitrogen.
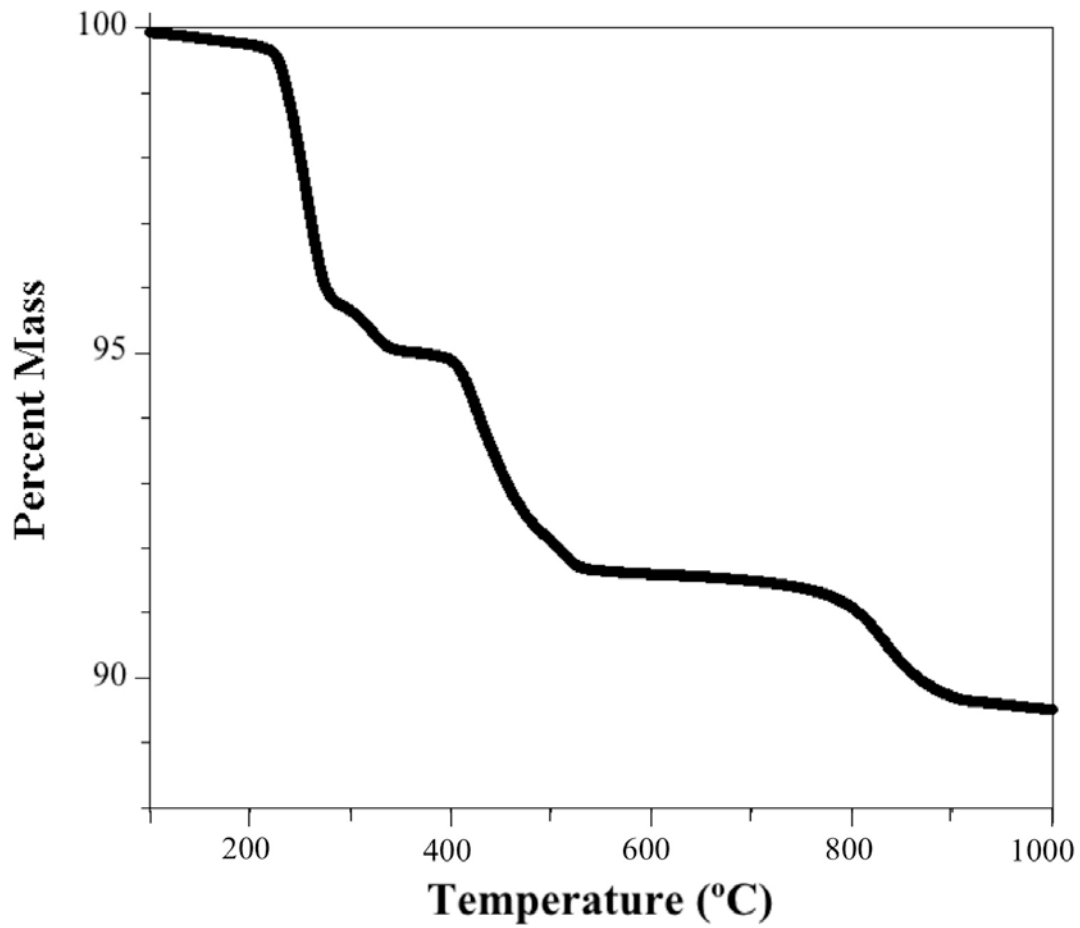
Figure 2.24. TGA data plot for $Ba_2Co(OH)_6$ in nitrogen.
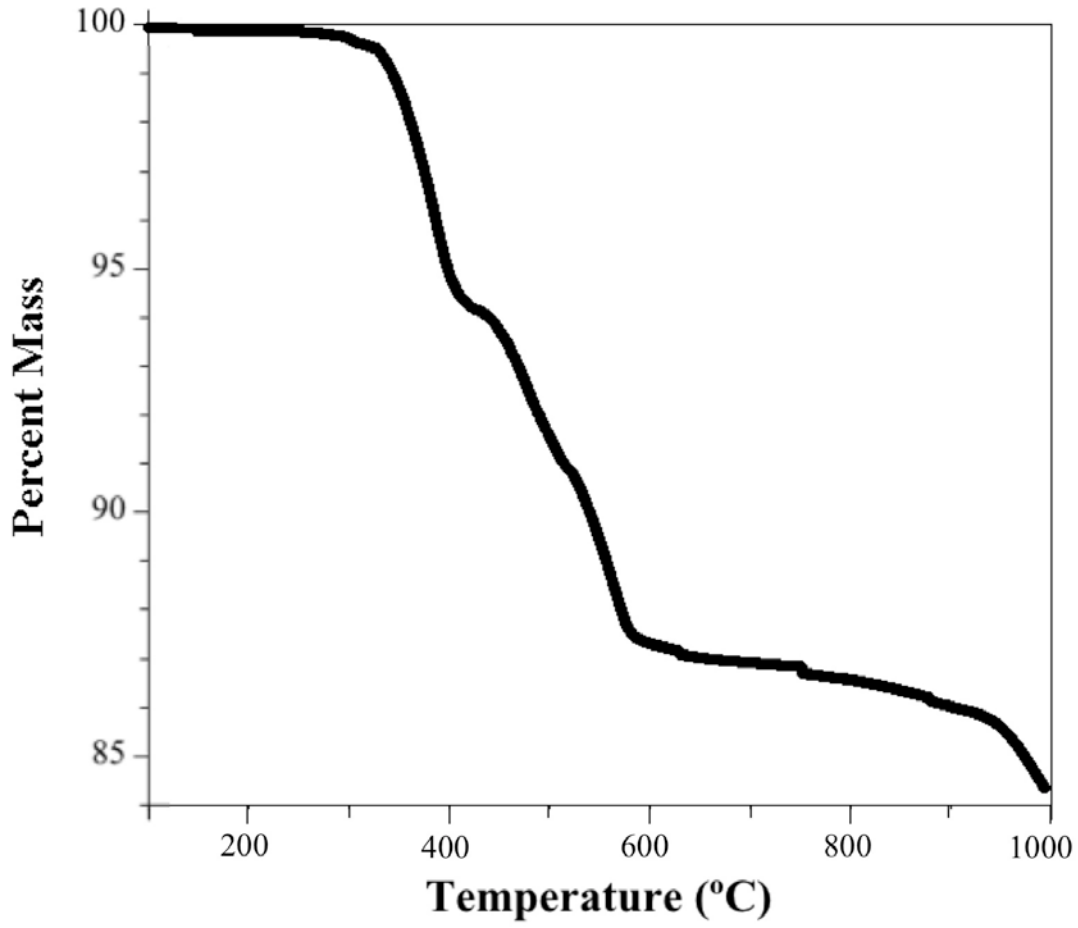
Figure 2.25. TGA data plot for $Sr_2Ni(OH)_6$ in nitrogen.
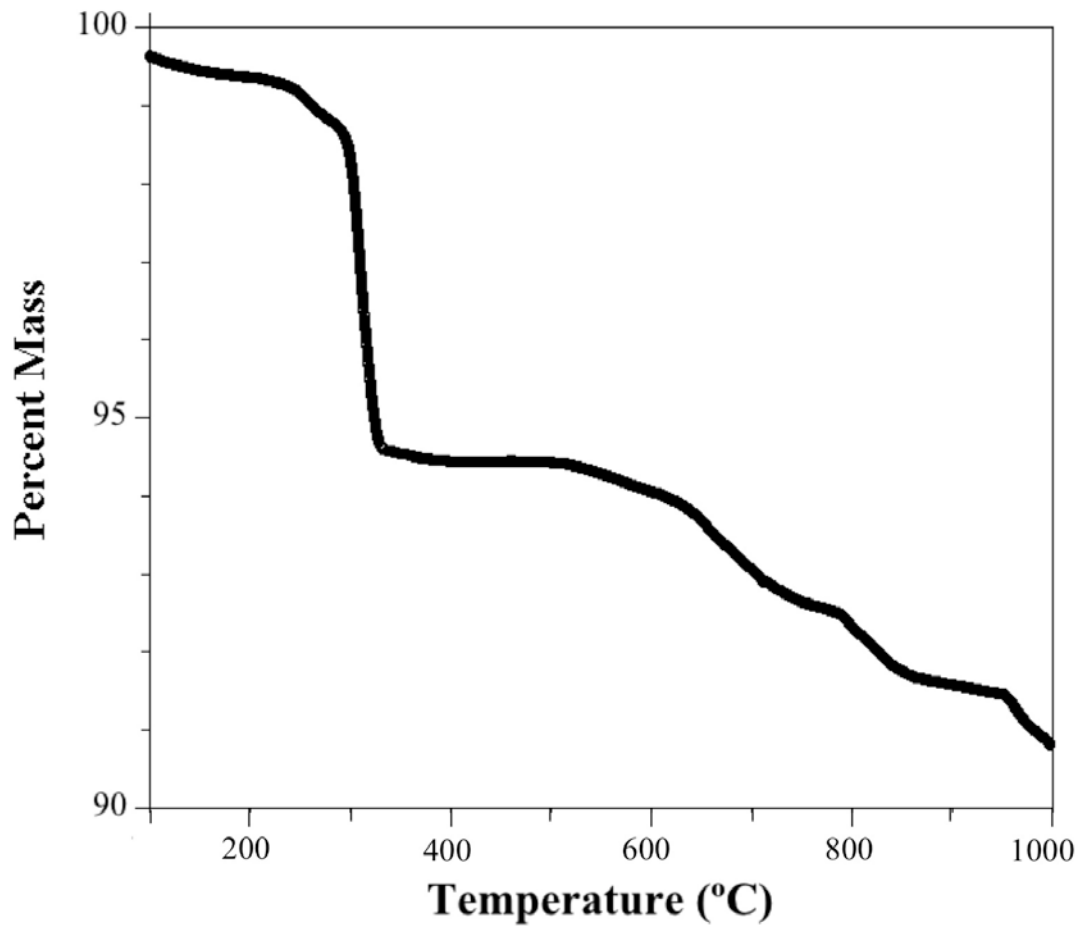
Figure 2.26. TGA data plot for $Ba_2Ni(OH)_6$ in nitrogen.
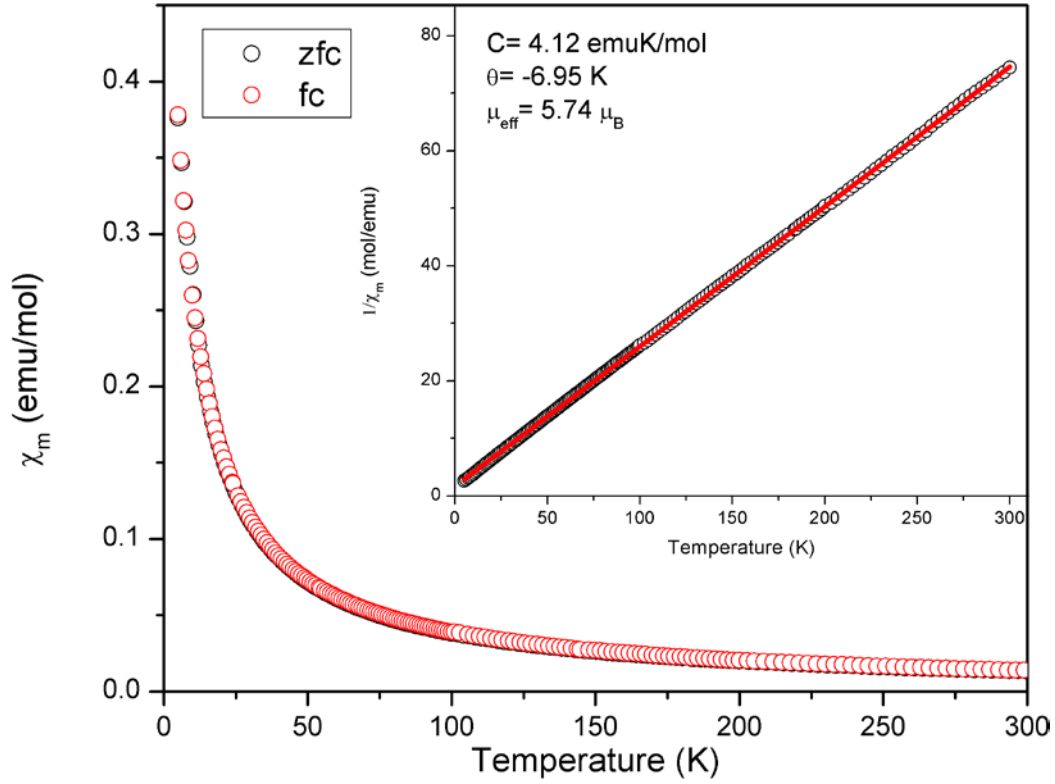
Figure 2.27. Temperature dependence of the molar magnetic susceptibility, χ_m, of $Sr_2Mn(OH)_6$. All measurements were carried out in an applied field of 1000 Oe. The inverse susceptibility vs. temperature plot is shown inset with the Curie-Weiss law fit of the region of best linearity.

63
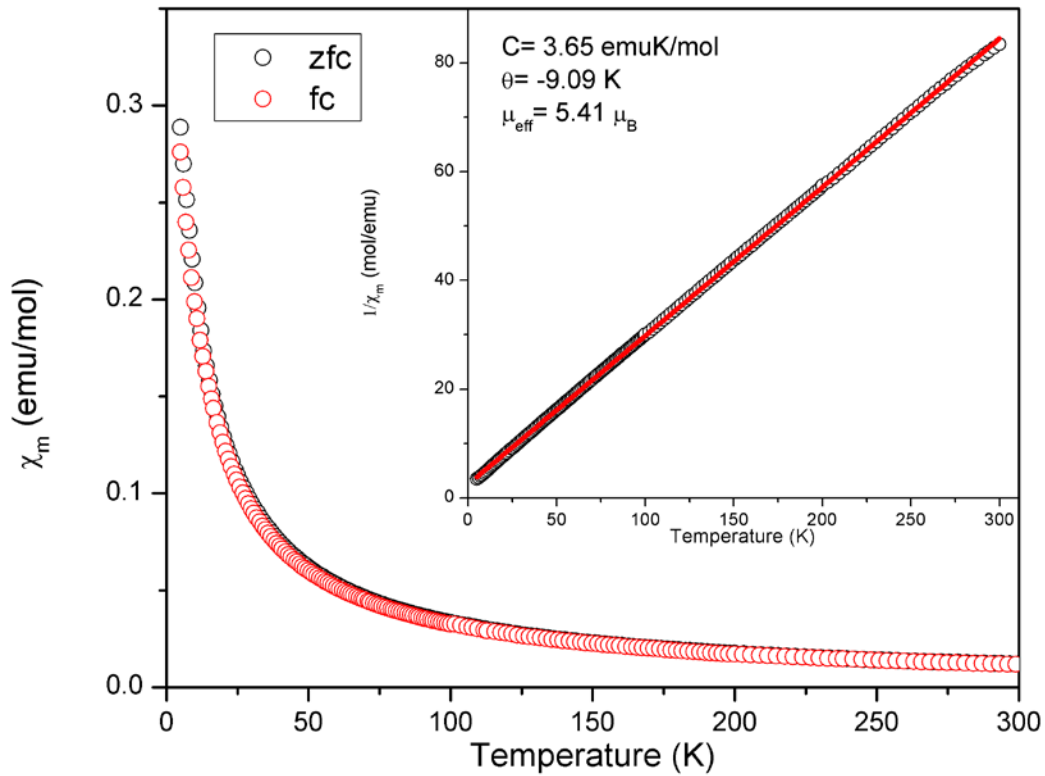
Figure 2.28. Temperature dependence of the molar magnetic susceptibility, χ_m, of $Ba_2Mn(OH)_6$. All measurements were carried out in an applied field of 1000 Oe. The inverse susceptibility vs. temperature plot is shown inset with the Curie-Weiss law fit of the region of best linearity.

64
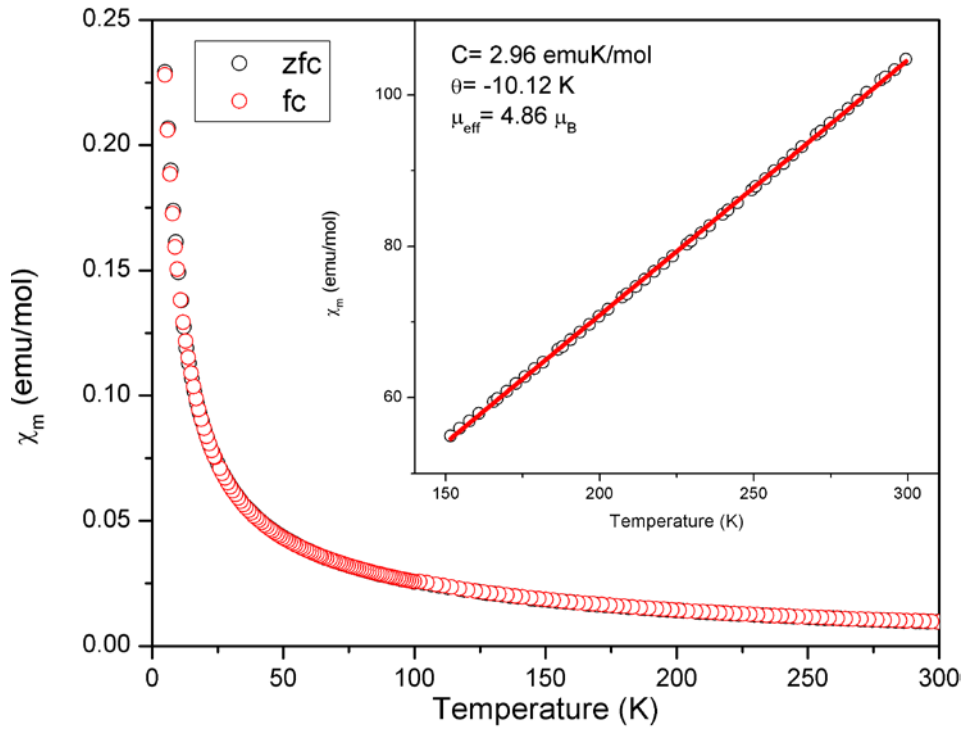
Figure 2.29. Temperature dependence of the molar magnetic susceptibility, χ_m, of $Sr_2Co(OH)_6$. All measurements were carried out in an applied field of 1000 Oe. The inverse susceptibility vs. temperature plot is shown inset with the Curie-Weiss law fit of the region of best linearity.

65
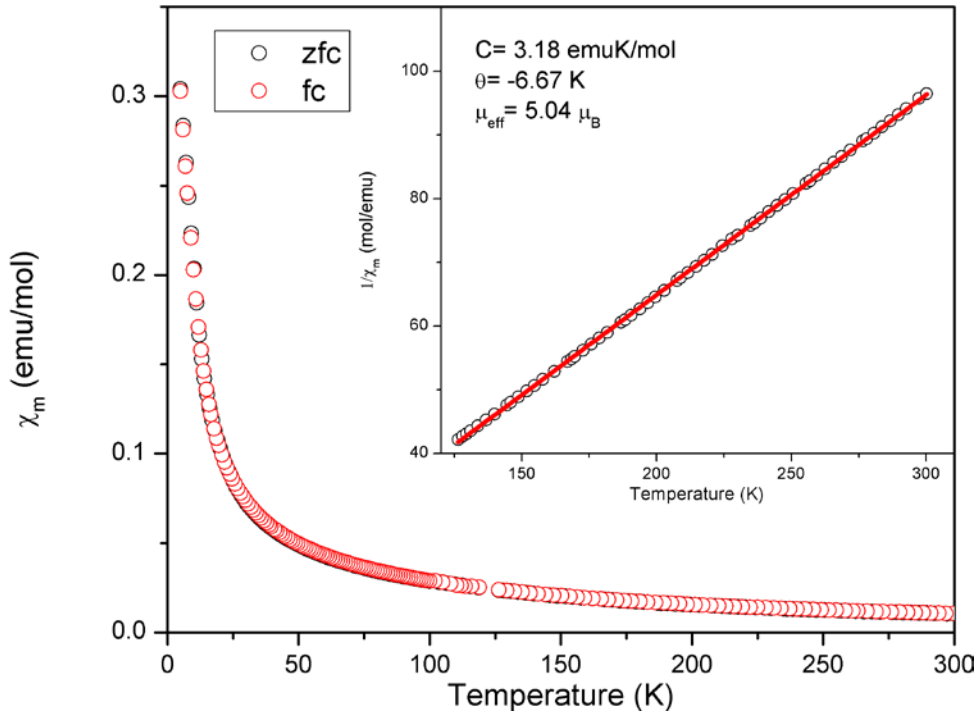
Figure 2.30. Temperature dependence of the molar magnetic susceptibility, χ_m, of $Ba_2Co(OH)_6$. All measurements were carried out in an applied field of 1000 Oe. The inverse susceptibility vs. temperature plot is shown inset with the Curie-Weiss law fit of the region of best linearity.

66
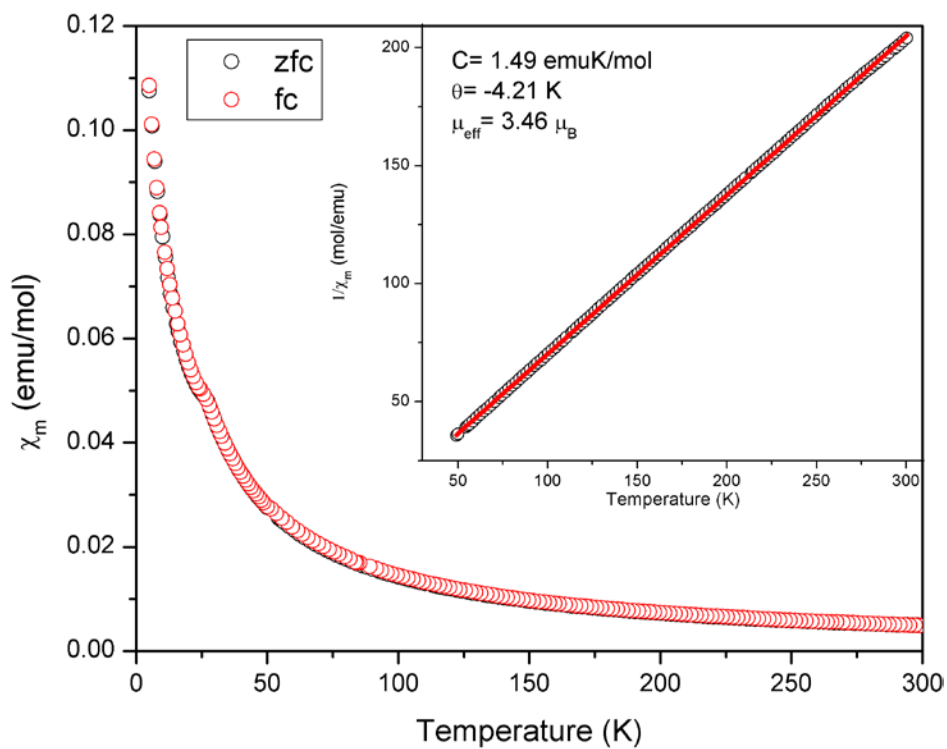
Figure 2.31. Temperature dependence of the molar magnetic susceptibility, χ_m, of $Sr_2Ni(OH)_6$. All measurements were carried out in an applied field of 1000 Oe. The inverse susceptibility vs. temperature plot is shown inset with the Curie-Weiss law fit of the region of best linearity.
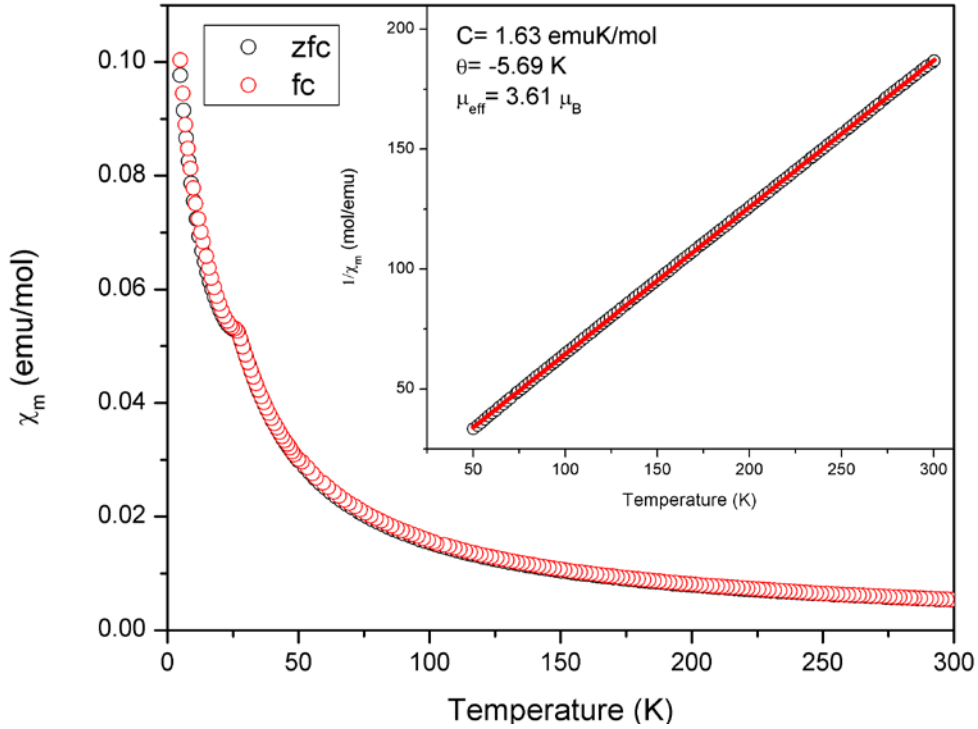
Figure 2.32. Temperature dependence of the molar magnetic susceptibility, χ_m, of $Ba_2Ni(OH)_6$. All measurements were carried out in an applied field of 1000 Oe. The inverse susceptibility vs. temperature plot is shown inset with the Curie-Weiss law fit of the region of best linearity.

Table 2.1. Range of working reaction conditions for the synthesis of hexahydroxometallates via the hydroflux method.

Product	Temperature Profile	Hydroflux Composition	Alkaline Earth Precursor	Transition Metal Precursor	Yield
$Sr_2Mn(OH)_6$	ramp 5 ℃/min to 200-230 ℃, hold 12-24 h, cool to 80 ℃ at 1-0.1 ℃/min	0.2-0.25 mol KOH/NaOH (53:47) or KOH and 0.3-0.4 mol H_2O	2 mol $Sr(OH)_2 \cdot 8H_2O$ or $Sr(NO_3)_2$	1 mmol $MnCl_2 \cdot 4H_2O$	87%
$Sr_2Co(OH)_6$	ramp 5 ℃/min to 200-230 ℃, hold 12-24 h, cool to 80 ℃ at 1-0.1 ℃/min	0.2-0.25 mol KOH/NaOH (53:47) or KOH and 0.3-0.4 mol H_2O	1.5 mmol $Sr(OH)_2 \cdot 8H_2O$ or $Sr(NO_3)_2$	1 mmol $CoCl_2 \cdot 6H_2O$	75%
$Sr_2Ni(OH)_6$	ramp 5 ℃/min to 180-230 ℃, hold 12-36 h, cool to 80 ℃ at 1-0.1 ℃/min	0.2-0.25 mol KOH and 0.3-0.4 mol H_2O	2 mmol $Sr(NO_3)_2$	1 mmol $Ni(NO_3)_2 \cdot 6H_2O$	93%

$Ba_2Mn(OH)_6$	ramp 5 ℃/min to 200-230 ℃, hold 12-24 h, cool to 80 ℃ at 1-0.1 ℃/min	0.2-0.25 mol KOH/NaOH (53:47) or KOH and 0.3-0.4 mol H_2O	2 mmol $Ba(OH)_2 \cdot 8H_2O$ or $Ba(NO_3)_2$	1 mmol $MnCl_2 \cdot 4H_2O$	85%
$Ba_2Co(OH)_6$	ramp 5 ℃/min to 200-230 ℃, hold 12-24 h, cool to 80 ℃ at 1-0.1 ℃/min	0.2-0.25 mol KOH/NaOH (53:47) or KOH and 0.3-0.4 mol H_2O	1.5 mmol $Ba(OH)_2 \cdot 8H_2O$ or $Ba(NO_3)_2$	1 mmol $CoCl_2 \cdot 6H_2O$	75%
$Ba_2Ni(OH)_6$	ramp 5 ℃/min to 180-230 ℃, hold 12-36 h, cool to 80 ℃ at 1-0.1 ℃/min	0.2-0.25 mol KOH and 0.3-0.4 mol H_2O	2 mmol $Ba(NO_3)_2$	1 mmol $Ni(NO_3)_2 \cdot 6H_2O$	93%
$Ba_2Cu(OH)_6$	ramp 5 ℃/min to 200-230 ℃, hold 12-24 h, cool to 80 ℃ at 1-0.1 ℃/min	0.2-0.25 mol KOH/NaOH (53:47) or KOH and 0.3-0.4 mol H_2O	2 mmol $Ba(OH)_2 \cdot 8H_2O$ or $Ba(NO_3)_2$	1 mmol CuO	90%

Table 2.2. Crystallographic Data for $A_2B(OH)_6$ (A = Sr, Ba; B = Mn, Co, Ni, Cu)[a]

compound	$Sr_2Mn(OH)_6$	$Sr_2Co(OH)_6$	$Sr_2Ni(OH)_6$	$Ba_2Mn(OH)_6$	$Ba_2Co(OH)_6$	$Ba_2Ni(OH)_6$	$Ba_2Cu(OH)_6$
formula weight (g/mol)	332.23	336.22	336.00	431.67	435.66	435.44	440.27
color and habit	brown, prism	pink, prism	green, prism	brown, prism	pink, prism	green, prism	blue, prism
a (Å)	5.801(1)	5.764(1)	5.762(1)	6.154(1)	6.085(1)	6.0840(12)	6.034(1)
b (Å)	6.132(1)	6.135(1)	6.129(1)	6.333(1)	6.227(1)	6.1806(12)	6.438(1)
c (Å)	8.139(2)	8.097(2)	8.080(2)	8.548(2)	8.495(2)	8.4429(17)	8.384(2)
β (°)	91.14(3)	90.80(3)	90.73(3)	90.86(3)	90.69(3)	90.68(3)	92.51(3)
V (Å^3)	289.5(1)	286.3(1)	285.3(1)	333.1(1)	321.8(1)	317.45(1)	325.4(1)
ρ_c (g cm^{-3})	3.812	3.900	3.911	4.304	4.496	4.555	4.493
μ (mm^{-1})	20.465	21.383	21.849	13.521	14.609	15.164	15.167
$F(000)$	310	314	316	382	386	388	390
crystal size (μm^3)	200 x 88 x 70	64 x 62 x 58	100 x 58 x 54	114 x 96 x 76	82 x 62 x 40	53 x 50 x 42	90 x 82 x 56
θ_{max} (°)	32.17	32.12	31.91	32.05	31.78	28.28	31.96
index ranges	-8 ≤ h ≤ 8;	-8 ≤ h ≤ 8;	-8 ≤ h ≤ 8;	-9 ≤ h ≤ 9;	-8 ≤ h ≤ 8;	-8 ≤ h ≤ 8;	-8 ≤ h ≤ 8;

71

	$-9 \leq k \leq 9$; $-12 \leq l \leq 12$	$-8 \leq k \leq 8$; $-11 \leq l \leq 12$	$-9 \leq k \leq 9$; $-11 \leq l \leq 11$	$-9 \leq k \leq 9$; $-12 \leq l \leq 12$	$-9 \leq k \leq 9$; $-12 \leq l \leq 12$	$-9 \leq k \leq 8$; $-11 \leq l \leq 11$	$-9 \leq k \leq 9$; $-12 \leq l \leq 12$
reflections collected	4753	4539	4595	5042	5155	4136	5246
independent reflections	1000	943	956	1102	1079	786	1097
goodness-of-fit on F^2	1.149	1.182	1.143	1.180	1.115	1.037	1.105
R indices (all data)	$R1 = 0.0183$ $wR2 = 0.0485$	$R1 = 0.0160$ $wR2 = 0.0328$	$R1 = 0.0151$ $wR2 = 0.0317$	$R1 = 0.0143$ $wR2 = 0.0335$	$R1 = 0.0126$ $wR2 = 0.0304$	$R1 = 0.0157$ $wR2 = 0.0338$	$R1 = 0.0141$ $wR2 = 0.0333$
largest peak and diffraction hole (e$^-$ Å^{-3})	0.876/-0.725	0.517/-0.523	0.376/-0.538	0.617/-0.908	1.105/-0.692	1.193/-1.254	0.537/-1.184

[a] For all structures, $T = 298(2)$ K, $\lambda = 0.71073$ Å, the space group is $P2_1/n$, and $Z = 2$.

Table 2.3. Selected Bond Distances (Å) and Angles (°) for $A_2B(OH)_6$ (A = Sr, Ba; B = Mn, Co, Ni, Cu)

	$Sr_2Mn(OH)_6$	$Sr_2Co(OH)_6$	$Sr_2Ni(OH)_6$	$Ba_2Mn(OH)_6$	$Ba_2Co(OH)_6$	$Ba_2Ni(OH)_6$	$Ba_2Cu(OH)_6$
A-O(3)	2.478(2)	2.490(2)	2.500(1)	2.671(2)	2.661(2)	2.657(2)	2.641(2)
A-O(2)	2.494(2)	2.519(2)	2.531(1)	2.705(2)	2.710(2)	2.704(2)	2.715(2)
A-O(1)	2.506(2)	2.526(2)	2.534(2)	2.701(2)	2.687(1)	2.679(2)	2.732(2)
A-O(1)	2.539(2)	2.547(2)	2.550(2)	2.760(2)	2.751(1)	2.738(2)	2.748(2)
A-O(3)	2.642(2)	2.643(2)	2.639(2)	2.848(2)	2.832(2)	2.809(2)	2.831(2)
A-O(2)	2.681(2)	2.689(2)	2.687(2)	2.920(2)	2.905(2)	2.883(2)	2.923(2)
A-O(3)	2.873(2)	2.851(2)	2.840(2)	2.998(2)	2.965(2)	2.951(2)	2.946(2)
A-O(2)	2.923(2)	2.858(2)	2.841(2)	2.985(2)	2.938(2)	2.928(2)	2.930(2)
B-O(2) x 2	2.097(2)	2.055(2)	2.039(1)	2.150(2)	2.085(1)	2.065(2)	1.969(2)
B-O(1) x 2	2.166(2)	2.104(2)	2.084(1)	2.193(2)	2.114(2)	2.098(2)	1.955(2)
B-O(3) x 2	2.256(2)	2.224(2)	2.191(1)	2.315(2)	2.252(2)	2.197(2)	2.804(2)

73

O(1)-*B*-O(1)	180.0	180.0	180.00(8)	180.0	180.0	180.00(13)	180.0
O(1)-*B*-O(2)	89.09(6)	89.14(6)	89.34(6)	89.79(7)	89.76(6)	89.37(9)	88.75(7)
O(1)-*B*-O(3)	89.05(6)	89.64(6)	89.97(6)	89.38(6)	89.95(6)	89.71(9)	88.49(6)
O(2)-*B*-O(2)	180.0	180.0	180.0	180.0	180.0	179.999(1)	180.0
O(2)-*B*-O(3)	88.70(6)	87.92(6)	87.87(6)	89.15(6)	89.28(6)	89.60(9)	86.88(6)
O(3)-*B*-O(3)	180.0	180.0	180.0	180.00(8)	180.0	180.00(7)	180.0

Table 2.4. Calculated bond valence sums for the synthesized compounds

$A_2B(OH)_6$	$Sr_2Mn(OH)_6$	$Sr_2Co(OH)_6$	$Sr_2Ni(OH)_6$	$Ba_2Mn(OH)_6$	$Ba_2Co(OH)_6$	$Ba_2Ni(OH)_6$	$Ba_2Cu(OH)_6$
A	2.12	2.08	2.06	1.97	2.05	2.11	2.03
B	2.16	1.85	1.91	1.91	1.74	1.82	1.96
O1	1.03	0.97	0.97	0.94	0.93	0.94	1.06
O2	1.13	1.06	1.06	1.03	1.01	1.06	1.12
O3	1.03	0.98	0.99	0.96	0.97	1.03	0.83

Table 2.5. Decomposition products of the hexahydroxometallates in air and nitrogen as determined by powder X-ray diffraction

Hydroxometallate	Decomposition Product(s)	Temperature (ºC)
$Sr_2Mn(OH)_6$	Air – $Sr_2MnO_{4-\delta}$	900
	N_2 – $Sr_2MnO_{4-\delta}$	900
$Sr_2Co(OH)_6$	Air – $Sr_6Co_5O_{15}$ + $SrCO_3$	420
	N_2 – $Sr(OH)_2$ + Unidentified products	800
$Sr_2Ni(OH)_6$	Air – $Sr_9Ni_{6.61}O_{21}$ + $SrCO_3$	815
	N_2 – $Sr_2Ni_2O_{5\pm\delta}$ + $Sr(OH)_2$	375
$Ba_2Mn(OH)_6$	Air – $Ba_3Mn_2O_8$ + $BaMnO_3$	710
	N_2 – $BaMnO_{3-x}$ + $BaCO_3$	800
$Ba_2Co(OH)_6$	Air – $Ba_3Co_2O_6(CO_3)_{0.6}$ + $BaCO_3$	525
	N_2 – Ba_2CoO_4	900
$Ba_2Ni(OH)_6$	Air – $BaNi_{0.83}O_{2.5\pm\delta}$ + $BaCO_3$	1100
	N_2 – $BaNiO_3$ + $BaCO_3$	325

References

1) Elwell, D.; Scheel, H. J. *Crystal Growth from High Temperature Solutions*; Academic Press: New York, 1975;

2) Dong, Y.-B.; Smith, M. D.; zur Loye, H.-C. *Angew. Chem. Int. Ed.* **2000**, *39*, 4271.

3) Ellsworth, J. M.; zur, L., H.-C. *Dalton Trans.* **2008**, 5823.

4) Férey, G.; Mellot-Draznieks, C.; Serre, C.; Millange, F.; Dutour, J.; Surblé, S.; Margiolaki, I. *Science* **2005**, *309*, 2040.

5) Su, C.-Y.; Goforth, A. M.; Smith, M. D.; Pellechia, P. J.; zur Loye, H.-C. *J. Am. Chem. Soc.* **2004**, *126*, 3576.

6) Zhang, W.; Ye, H.-Y.; Xiong, R.-G. *Coordin. Chem. Rev.* **2009**, *253*, 2980.

7) Aidoudi, F. H.; Byrne, P. J.; Allan, P. K.; Teat, S. J.; Lightfoot, P.; Morris, R. E. *Dalton Trans.* **2011**, *40*, 4324.

8) Aldous, D. W.; Lightfoot, P. *J. Fluorine Chem.* **2012**, *144*, 108.

9) Gautier, R.; Donakowski, M. D.; Poeppelmeier, K. R. *J. Solid State Chem.* **2012**, *195*, 132.

10_ Raw, A. D.; Ibers, J. A.; Poeppelmeier, K. R. *J. Solid State Chem.* **2013**, *200*, 165.

11_ Li, M.-R.; Walker, D.; Retuerto, M.; Sarkar, T.; Hadermann, J.; Stephens, P. W.; Croft, M.; Ignatov, A.; Grams, C. P.; Hemberger, J.; Nowik, I.; Halasyamani, P. S.; Tran, T. T.; Mukherjee, S.; Dasgupta, T. S.; Greenblatt, M. *Ange. Chem., Int. Ed.* **2013**, *52*, 8406.

12) Mugavero, S. J.; Gemmill, W. R.; Roof, I. P.; zur Loye, H.-C. *J. Solid State Chem.* **2009**, *182*, 1950.

13) Bugaris, D. E.; zur Loye, H.-C. *Angew. Chem., Int. Ed.* **2012**, *51*, 3780.

14) Bugaris, D. E.; Smith, M. D.; zur Loye, H.-C. *Inorg. Chem.* **2013**, *52*, 3836.

15) Scholder, R.; Felsenstein, R.; Apel, A. *Z. Anorg. Allg. Chem.* **1933**, *216*, 138.

16) Scholder, R.; Pätsch, R. *Z. Anorg. Allg. Chem.* **1934**, *220*, 411.

17) Scholder, R.; Hendrich, G. *Z. Anorg. Allg. Chem.* **1939**, *241*, 76.

18) Kwestroo, W.; van Gerven, H. C. A.; van Hal, H. A. M. *Mater. Res. Bull.* **1977**, *12*, 161.

19) Morán-Miguélez, E.; Alario-Franco, M. A.; Joubert, J. C. *Mater. Res. Bull.* **1986**, *21*, 107.

20) Dubler, E.; Korber, P.; Oswald, H. R. *Acta Crystallogr B* **1973**, *29*, 1929.

21) Henning, T.; Jacobs, H. *Z. Anorg. Allg. Chem.* **1992**, *616*, 71.

22) Hinz, D. *Z. Anorg. Allg. Chem.* **2000**, *626*, 1004.

23) Ivanov-Emin, B. N.; Il'inets, A. M.; Zaitsev, B. E.; Kostrikin, A. V.; Spiridonov, F. M.; Dolganev, V. P. *Zh. Neorg. Khim.* **1990**, *35*, 2285.

24) Jacobs, H.; Bock, J. *Z. Anorg. Allg. Chem.* **1987**, *546*, 33.

25) Stahl, R.; Jacobs, H. *Z. Anorg. Allg. Chem.* **1998**, *624*, 17.

26) Buscaglia, M. T.; Leoni, M.; Viviani, M.; Buscaglia, V.; Martinelli, A.; Testino, A.; Nanni, P. *J. Mater. Res.* **2003**, *18*, 560.

27) Faust, G. T.; Schaller, W. T. *Z. Kristallogr.* **1971**, *124*, 116.

28) Jacobs, H.; Stahl, R. *Z. Anorg. Allg. Chem.* **2000**, *626*, 1863.

29) Kamaha, S.; Reuter, H. *Z. Anorg. Allg. Chem.* **2009**, *635*, 2058.

30) Noerlund, C. A.; Hazell, R. G. *Acta Chem. Scand.* **1969**, *23*, 1219.

31) Reuter, H.; Bargon, G. *Z. Anorg. Allg. Chem.* **1997**, *623*, 1978.

32) Strunz, H.; Contag, B. *Acta Crystallogr.* **1960**, *13*, 601.

33) Troyanov, S. I.; Kostrikin, A. V.; Spiridonov, F. M.; Lin'ko, I. V.; Ezhov, A. I.; Martynova, S. V.; Zaitsev, B. E. *Zh. Neorg. Khim.* **2001**, *46*, 572.

34) Wrobel, G.; Piech, M.; Dardona, S.; Ding, Y.; Gao, P.-X. *Cryst. Growth Des.* **2009**, *9*, 4456.

35) Yang, S.; Zavalij, P. Y.; Whittingham, M. S. *Acta Crystallogr., Sect. C: Cryst. Struct. Commun.* **2001**, *C57*, 228.

36) Dobson, J. V.; Taylor, M. J. *Electrochim. Acta* **1986**, *31*, 235.

37) Dobson, J. V.; Taylor, M. J. *Electrochim. Acta* **1986**, *31*, 231.

38) SHELXTL Version 6.14, Bruker Analytical X-ray Systems, Inc. Madison, Wisconsin, USA 2000.

39) SMART Version 5.625, SAINT + Version 6.45, and SADABS Version 2.05, Bruker Analytical X-ray Systems Inc., Madison, Wisconsin, USA 2001.

40) Sheldrick, G. M. *Acta Crystallogr.* **2008**, *A 64*, 112.

41) Brown, I. D. *The Chemical Bond in Inorganic Chemistry: The Bond Valence Model*; Oxforrd University Press: 2006;

42_ Sutovic, S.; Karanovic, L.; Poleti, D. *Acta Crystallogr. C* **2009**, *65*, i48.

43) Wold, A.; Dwight, K. *Solid State Chemistry: Synthesis, Structure, and Properties of Selected Oxides and Sulfides*; Chapman & Hall: New York, 1993; pp 70-76.

44) Vidyasagar, K.; Gopalakrishnan, J.; Rao, C. N. R. *J. Solid State Chem.* **1985**, *58*, 29.

45) Sarkozy, R. F.; Chamberland, B. L. *Mater. Res. Bull.* **1973**, *8*, 1351.

46) Sarkozy, R. F.; Moeller., C. W. C., B. L. *J. Solid State Chem.* **1974**, *9*, 242.

47)   Li, G.; Feng, S.; Li, L.; Li, X.; Jin, W. *Chem. Mater.* **1997**, *9*, 2894.

48)   McLune, W. F., Ed. Swarthmore, PA, 1989; pp Card No. 24-1187.

49)   Shimakawa, Y.; Jorgensen, J. D.; Mitchell, J. F.; Hunter, B. A.; Shaked, H.; Hinks, D. G.; Hitterman, R. L.; Hiroi, Z.; Takano, M. *Physica C* **1994**, *228*, 73.

50)   Nagai, I.; Kato, M.; Koike, Y. *Physica C* **2000**, *338*, 84.

51)   Scholder, R.; Schwochow, E. F. *Angew. Chem., Int. Ed.* **1966**, *5*, 1047.

52)   Baran, E. J.; Aymonino, P. J. *Monatsh. Chem.* **1969**, *100*, 1674.

53)   Bouloux, J.-C.; Soubeyroux, J.-L.; Flem, G. L.; Hagenguller, P. *J. Solid State Chem.* **1981**, *38*, 34.

54)   Gillie, L. J.; Wright, A. J.; Hadermann, J.; Van Tendeloo, G.; Greaves, C. *J. Solid State Chem.* **2002**, *167*, 145.

55)   Kriegel, R.; Feltz, A.; Walz, L.; Simon, A.; Mattausch, H., J. *Z. Anorg. Allg. Chem.* **1992**, *617*, 99.

56)   Boulahya, K.; Parras, M.; González-Calbet, J. M.; Amador, U.; Martinez, J. L.; Fernández-Díaz, M. T. *Chem. Mater.* **2006**, *18*, 3898.

57)   Zanne, M.; Courtois, A.; Gleitzer, C. *Bull. Soc. Chim. Fr.* **1972**, *12*, 4470.

58)   Weller, M. T.; Skinner, S. J. *Acta Crystallogr. C* **1999**, *55*, 154.

59)   Christensen, A. N.; Ollivier, G. *J. Solid State Chem.* **1972**, *4*, 131.

60)   Campá, J. A.; Gutiérrez-Puebla, E.; Monge, M. A.; Rasines, I.; Ruìz-Valero, C. *J. Solid State Chem.* **1994**, *108*, 230.

61)   Takeda, Y.; Hashino, T.; Miyamoto, H.; Kanamaru, F.; Kume, S.; Koizumi, M. *J. Inorg. Nucl. Chem.* **1972**, *34*, 1599.

62) Harrison, W. T. A.; Hegwood, S. L.; Jacobson, A. J. *J. Chem. Soc., Chem. Commun.* **1995**, 1953.

63) Lander, J. J. *Acta Crystallogr.* **1951**, *4*, 148.

64) Krischner, H.; Torkar, K.; Kolbesen, B. O. *J. Solid State Chem.* **1971**, *3*, 349.

65) Boulahya, K.; Amador, U.; Parras, M.; González-Calbet, J. M. *Chem. Mater.* **2000**, *12*, 966.

66) Campá, J.; Gutiérrez-Puebla, E. M., A.; Rasines, I.; C., Ruiz-Valero. *J. Solid State Chemistry* **1996**, *126*, 27.

Chapter 3: Hydroflux Synthesis of Group 6 Metal Oxides

Chapter 3.1: Synthesis, Structure, and Optical Properties of a Series of Quaternary Oxides, $K_2Ba(MO_4)_2$ (M = Cr, Mo, W)

Introduction

Crystal growth of quaternary and higher order oxides is by no means trivial. In order to improve the odds of finding novel compositions with potentially new or improved properties, it is necessary to continuously improve the tools with which the solid state chemist works. For example, molten salts and hydrothermal reactions are staples in the modern toolbox and, historically, alkali metal hydroxides have been a common mineralizer for hydrothermal reactions.[1-6] In the past few decades, many new compositions have been synthesized using molten hydroxide fluxes, particularly, wet hydroxide fluxes or reactions in which water has been purposefully added, to control the acid-base chemistry of the molten flux as described by the Lux-Flood concept of oxo-acidity.[7, 8]

As more water is added to a hydroxide melt, this wet hydroxide flux will transform into a hydrothermal reaction and vice versa. However, there is a region between the two compositional regimes in which the properties of the reaction media are very much like that of a wet hydroxide flux, but where some of the characteristics of the hydrothermal media are still present. The term hydroflux has been suggested for such a reaction media in which the water content is very high, yet the melting point is above the boiling point of water.[9,10]

Palmierite-related oxides have been of interest for a number of properties, including luminescent behavior, ionic conductivity, and ferroelasticity.[11-15] With the focus of many syntheses involving these oxides being the creation of solid solutions to manipulate the electronic and optical properties, it is paramount to have a firm

84

understanding of the crystal structure of the frameworks with which the solid state chemist can tinker.

The series of quaternary oxides, $K_2Ba(MO_4)_2$ (M = Cr, Mo, W), is known, but have only been prepared and characterized as powders previously.[16-18] At one point, $K_2Ba(CrO_4)_2$ was used as a corrosion-resistant pigment and metal alloy primer,[19-21] while $K_2Ba(MoO_4)_2$ has been studied as a host for luminescent rare earth ions for lighting applications.[11,22-24] Rare earth doped $K_2Ba(WO_4)_2$ was also recently investigated for its luminescent properties. The fact that all appear to have only been prepared as polycrystalline powders to date, but were readily obtained as single crystals from a hydroflux, highlights the effectiveness of the low temperature hydroflux approach for opening up reaction pathways to complex oxides.

In this chapter, a new pathway for the synthesis and the first structural characterization by single-crystal X-ray diffraction of this series of quaternary oxides is presented. Optical properties of the materials are determined and compared to relevant oxides.

Experimental Details

Crystal Growth

Crystals of the title series were grown using hydroxide-based hydrofluxes. Reactions were carried out in PTFE-lined, 23 mL Parr autoclaves. The hydroflux consisted of 11 grams of KOH (Fisher, certified ACS pellets) and approximately 6 grams of distilled water for $K_2Ba(CrO_4)_2$ and $K_2Ba(MoO_4)_2$. For $K_2Ba(WO_4)_2$, a hydroflux composed of 5.5 grams of KOH and 3.9 grams of NaOH (Fisher, certified ACS pellets) and 6 grams of water were employed. Stoichiometric quantities of metal precursors were

85

added to the hydrofluxes. The binary oxides, MoO_3 (Alfa Aesar 99.95%) and WO_3 (Alfa Aesar 99.9%), and the complex oxide K_2CrO_4 (Alfa Aesar, 99% min) were used as the molybdenum, tungsten, and chromium precursors, respectively. During the reaction, the autoclave was sealed to prevent water loss that would otherwise raise the melting point and increase the difficulty of flux removal. The reactions were heated to 230 ºC at a rate of 5 ºC/min, held for 12 h, and then cooled at a rate of 0.3ºC/min to 60 ºC. Single crystals were isolated by decanting the still-molten hydroflux and rinsing the remaining portion with methanol, followed by sonication of the product.

Single Crystal X-Ray Diffraction

Single crystal X-ray diffraction data were collected with the use of graphite monochromatized Mo Kα radiation (λ = 0.71073 Å) at 298 K on a Bruker SMART APEX CCD diffractometer. The crystal-to-detector distance was 5.048 cm. Crystal decay was monitored by recollecting the 50 initial frames at the end of the data collection. Data were collected by a scan of 0.3° in ω in groups of 600 frames at φ settings of 0°, 90°, 180°, and 270°. The exposure time was 20 s/frame for each collection. The collection of intensity data was carried out with the program SMART.[25] Cell refinement and data reduction were carried out with the use of the program SAINT+.[25] A numerical absorption correction was performed with the use of the program SADABS. The program SADABS was also employed to make incident beam and decay corrections.[25] The structure was solved using the direct methods program SHELXS and refined with the full-matrix least-squares program SHELXTL.[26] Potassium and barium occupancies were restrained in order to keep the necessary charge for *M*. The final refinement included anisotropic displacement parameters. The atomic coordinates for synthetic Palmierite,

86

$K_2Pb(SO_4)_2$, were used as a starting model for the refinement. Satisfactory R values were achieved for all compounds. The largest difference map extrema are +0.559 and -0.728, +0.846 and -1.226, and +1.104 and -1.163 e$^-$/Å^3 for the Cr, Mo, and W analogues, respectively.

Relevant crystallographic information from the single-crystal structure refinements is compiled in Table 3.1 and atomic positions for the title compounds are given in Table 3.2. Selected interatomic distances are tabulated in Table 3.3.

Energy-Dispersive Spectroscopy (EDS)

Elemental analysis was performed on the crystals using an FEI Quanta 200 scanning electron microscope (SEM) with EDS capabilities. The crystals were mounted on carbon tape and analyzed using a 30 kV accelerating voltage and an accumulation time of 15 s. As a qualitative measure, the EDS confirmed the presence of each element and corroborated the approximate elemental ratios.

UV-Visible Spectroscopy

A Perkin-Elmer Lambda 35 UV-visible spectrophotometer was used to collect diffuse-reflectance data in the range of 200-800 nm at room temperature. PTFE was used as a white standard.

Luminescence

A Perkin Elmer LS 55 Fluorescence Spectrometer was used to measure emission and excitation spectra of the title compounds. The excitation wavelengths were 242, 295 nm, and 340 nm for $K_2Ba(CrO_4)_2$, 239 and 298 nm for $K_2Ba(MoO_4)_2$, and 244 and 282 nm for $K_2Ba(WO_4)_2$. The emission wavelengths were 484 nm for $K_2Ba(CrO_4)_2$, 416 nm

for $K_2Ba(MoO_4)_2$, and 428 nm $K_2Ba(WO_4)_2$. All measurements were conducted at room temperature.

Results and Discussion

Single crystal structure solutions show that the title compounds crystallize in the space group R-$3m$ and take on the Palmierite structure. The structure can be described as consisting of layers of isolated MO$_4$ (M = Cr, Mo, W) tetrahedra that are interspersed by cations in an unusual 6-coordinate, distorted octahedral environment having six equal bonds. These slabs, in turn, are separated from each other by bi-layers of cations in 10-coordinate environments that share edges with the distorted octahedra. (Figure 3.1). It is well known that potassium and barium can substitute for each other because of their very similar radii. Anti-site mixing is present in this structure and as expected from the ionic radii, potassium predominately occupies the larger 10-coordinate site (referred to hereafter as the K-site) and barium favors the smaller 6-coordinate site (referred to hereafter as the Ba-site). The presence of anti-site mixing leads to structural formulas of $(K_{0.913(3)}Ba_{0.087(3)})_2(Ba_{0.825(3)}K_{0.175(3)})(CrO_4)_2$, $(K_{0.888(2)}Ba_{0.112(2)})(Ba_{0.775(3)}K_{0.225(3)})(MoO_4)_2$, and $(K_{0.772(3)}Ba_{0.228(3)})_2(Ba_{0.545(6)}K_{0.455(6)})(WO_4)_2$.

This ratio of mixing between the two sites for the potassium and barium atoms appears to be related to the M cation identity. This can be traced to the interconnection between the structural units. The edges of the MO$_4$ tetrahedra are the edges of the K-site and frame the six "equatorial" oxygens. Also, one axial oxygen, O(2), is corner-shared with the MO$_4$ tetrahedra. As the ionic radius of M increases (down the group from chromium to tungsten) the tetrahedra expand. This expansion, in turn, leads to a shortening of the axial oxygen bond. As the axial bond shortens, the equatorial bonds

88

lengthen. The three other bonds to this site are three pseudo-axial oxygens that are shared with the distorted octahedral site. As the tetrahedra expand and the equatorial bonds lengthen, the bond between O(1) and Ba(1)/K(1) remains essentially constant. Though the bond length remains constant, the dihedral angle between Ba(1)/K(1) and any two pseudo-axial oxygens of the K-site increases with the expansion of the tetrahedral site. (Table 3.3) All of these incremental adjustments in the structure sum to produce compression of the K-site axially and expansion equatorially with increasing group 6 metal radius. This leads to a negative relationship between the *c* and *a* parameter for this series (Figures 3.2 and 3.3). It is worth noting that this trend is also observed in the lattice parameters of the structurally analogous series $Ba_3V_2O_8$,[27] $Ba_3Cr_2O_8$,[28] and $Ba_3Mn_2O_8$[29] with a nearly identical slope and good linearity. The percent mixing of the two sites, taken as the fraction of the barium substituted on the K-site, increases nonlinearly with the increase in size of the group 6 metal cation. The chromium and molybdenum analogue show mixing of approximately 9% and 11%, while the tungsten analogue has a markedly higher amount of mixing (~23%).

One potential explanation for this mixing comes from the observed bond distances for the K- and Ba-sites. The equatorial bonds are longest and axial bonds shortest for the tungsten analogue. A survey of bond distances in oxides results in a reported range of 2.62-3.11Å for K-O bonds in a 10-coordinate environment. The K(1)-O(2) bond in the tungsten analogue is within experimental error one of the shortest K-O bonds reported for potassium in 10 coordinate environments. The K(1)-O(2) bond is within the expected range for the chromium and molybdenum analogues with the molybdenum analogue being very close to the low end of the range. The Ba-site distances

89

are well within the ranges reported for both potassium and barium in 6-coordinate environments in oxides, however. The greater axial compression of the K-site with increasing M radius appears to lend itself to a greater degree of site mixing because of the slightly smaller radius of barium.

The diffuse reflectance spectra of the compounds were measured. Crystals of the chromium analogue are yellow in color and the molybdenum and tungsten appear colorless (Figure 3.4). When ground to a powder, however, the molybdenum analogue appears to have a faint yellow tint, as corroborated by the diffuse reflectance data (Figure 3.5). Of the three, the chromium analogue shows the highest absorbance. All three spectra show relative maxima around 263 and 374 nm.

The fluorescence spectra of the compounds were measured and are shown in Figures 3.6-3.8. The tungsten and molybdenum analogues, as expected from the weak absorbance, show very weak luminescence. This is not unexpected given the previous report of strongly quenched luminescence in $Rb_2Pb(MoO_4)_2$ at room temperature.[30] The chromium analogue, however, shows stronger photoluminescence than the tungsten and molybdenum analogues. The emission wavelength observed for the chromate ($\lambda_{max} = 484$ nm) is similar to that observed for another Palmierite analogue, $Ba_3V_2O_8$ ($\lambda_{max} = 490$ nm).[31] Though luminescence in the chromate ion is usually reported at low temperatures, it is known that the structure type and surrounding cations greatly affect the luminescence.[32,33] Spek and collaborators suggested that the luminescence of $Ca_4K_2(CrO_4)_5 \cdot 2H_2O$ and other chromates may hinge on the substitution of alkali metals into the lattice, which induces luminescent traps.[34]

90

Conclusions

Single crystals of a family of quaternary oxides $K_2Ba(MO_4)_2$ (M = Cr, Mo, W) have been grown for the first time using a hydroxide hydroflux. The compounds crystallize in space group R-$3m$ and, according to single-crystal X-ray diffraction structure determination, are isostructural with the mineral Palmierite. All compounds show anti-site mixing of the potassium and barium. The degree of mixing appears to be determined indirectly by the M-O bond distance. Diffuse reflectance spectra and room-temperature luminescence were measured for each compound.
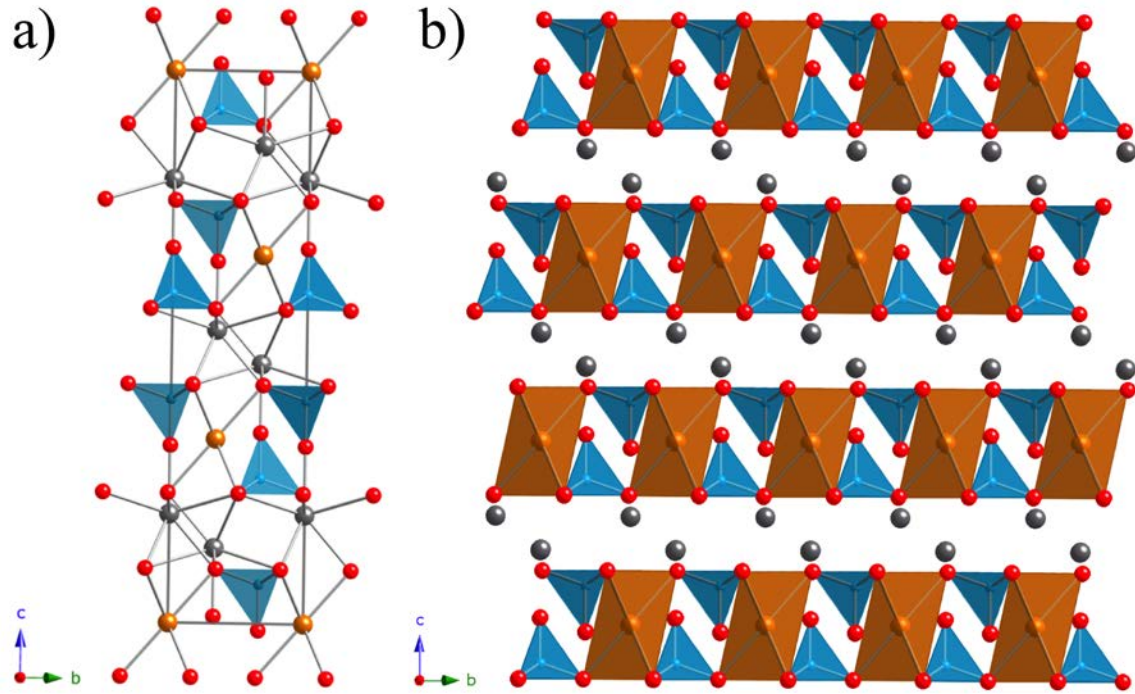
Figure 3.1. a) Unit cell of the $K_2Ba(MO_4)_2$ structure. Ba atomic sites are shown in orange, K sites in gray, oxygen atoms in red, and MO_4 tetrahedra are represented in blue. b) extended structure view of the $K_2Ba(MO_4)_2$ structure with Ba sites shown in orange polyhedra and MO_4 tetrahedra in blue to emphasize the layering.
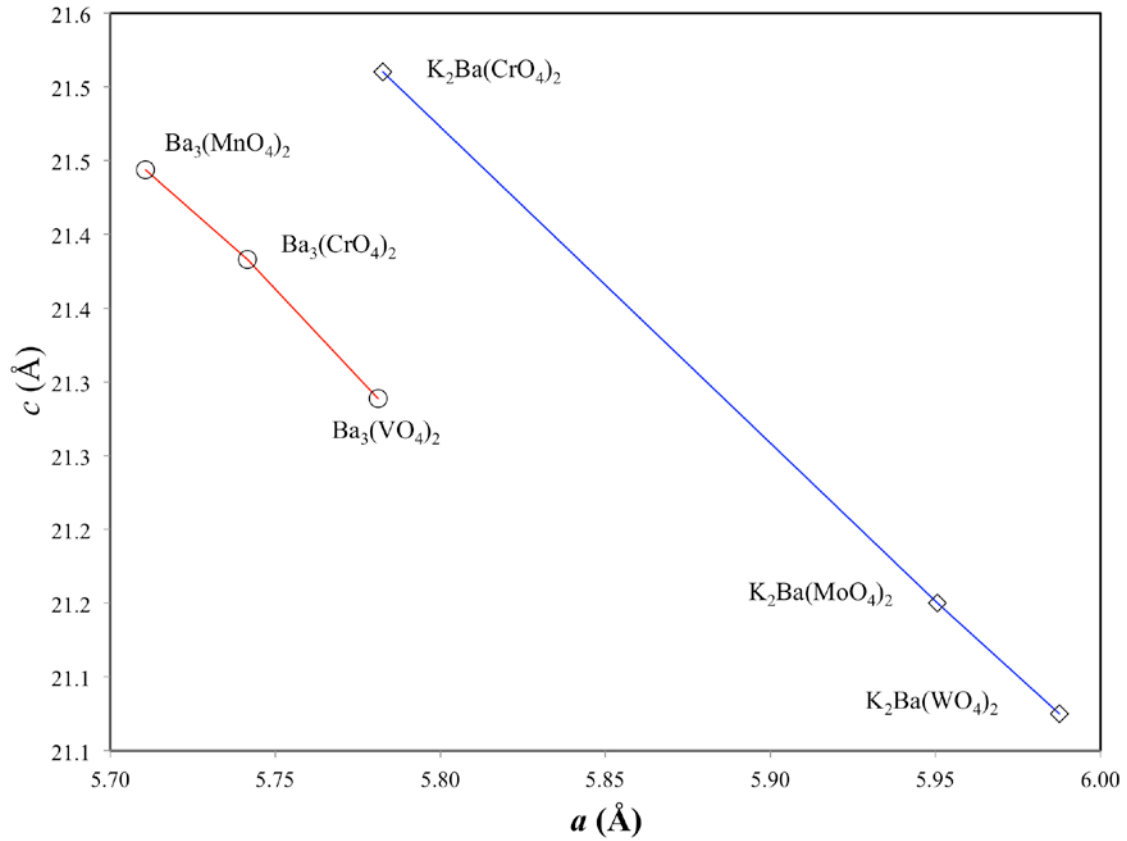
Figure 3.2. Relation between *c* and *a* lattice parameters in the K$_2$Ba(MO$_4$)$_2$; M = Cr, Mo, W series and Ba$_3$(MO$_4$)$_2$; M = Mn, Cr, V
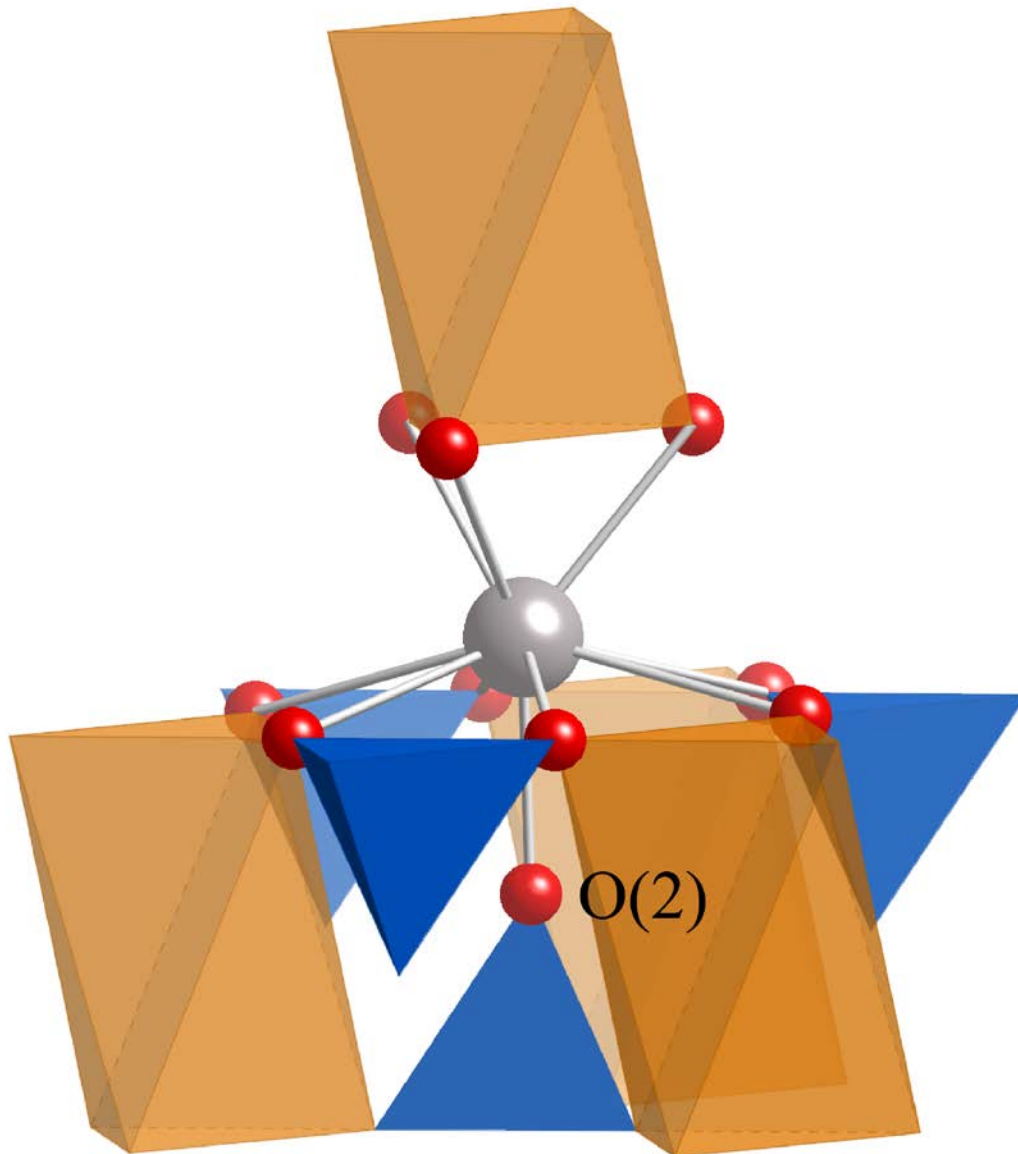
Figure 3.3. Environment of the K-site in the Palmierite structure with the K(1)/Ba(1) shown in gray, MO$_4$ tetrahedra shown in blue, and the Ba(2)/K(2) site in orange. The nine oxygen bonds with K(1)/Ba(1) are shown with O(1) unlabeled and O(2) explicitly labeled.
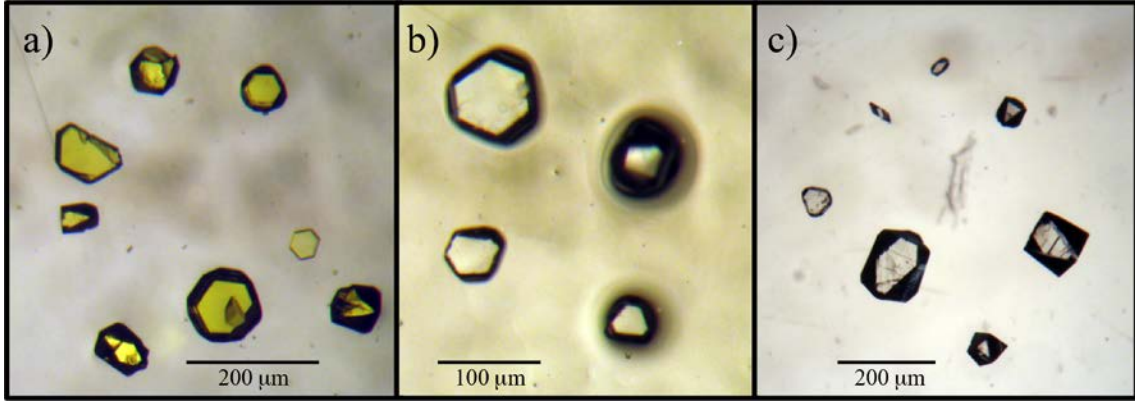
Figure 3.4. Optical images of crystals of a) $K_2Ba(CrO_4)_2$, b) $K_2Ba(MoO_4)_2$, c) $K_2Ba(WO_4)_2$
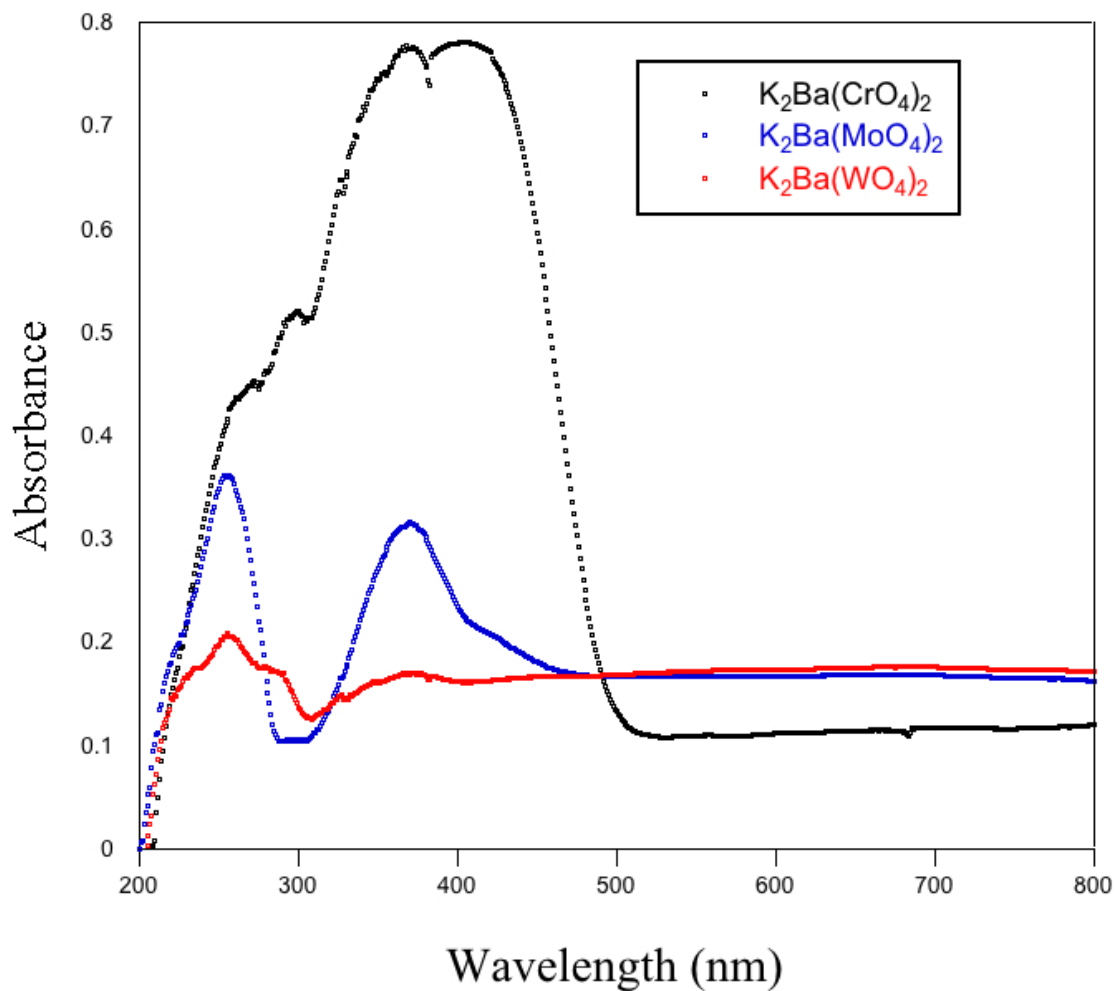
Figure 3.5. Diffuse reflectance spectra of $K_2Ba(CrO_4)_2$ (black), $K_2Ba(MoO_4)_2$ (blue), and $K_2Ba(WO_4)_2$ (red)
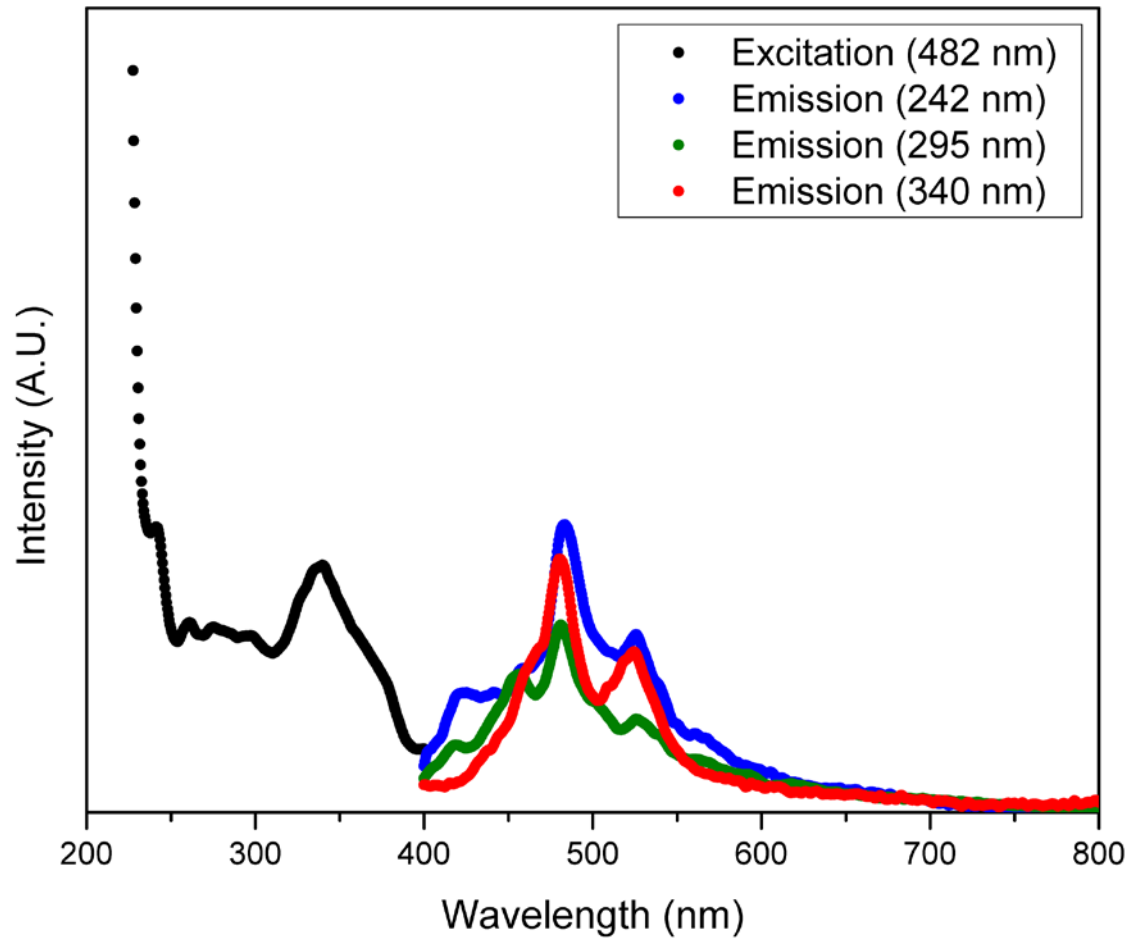
Figure 3.6. Fluorescence spectra of $K_2Ba(CrO_4)_2$
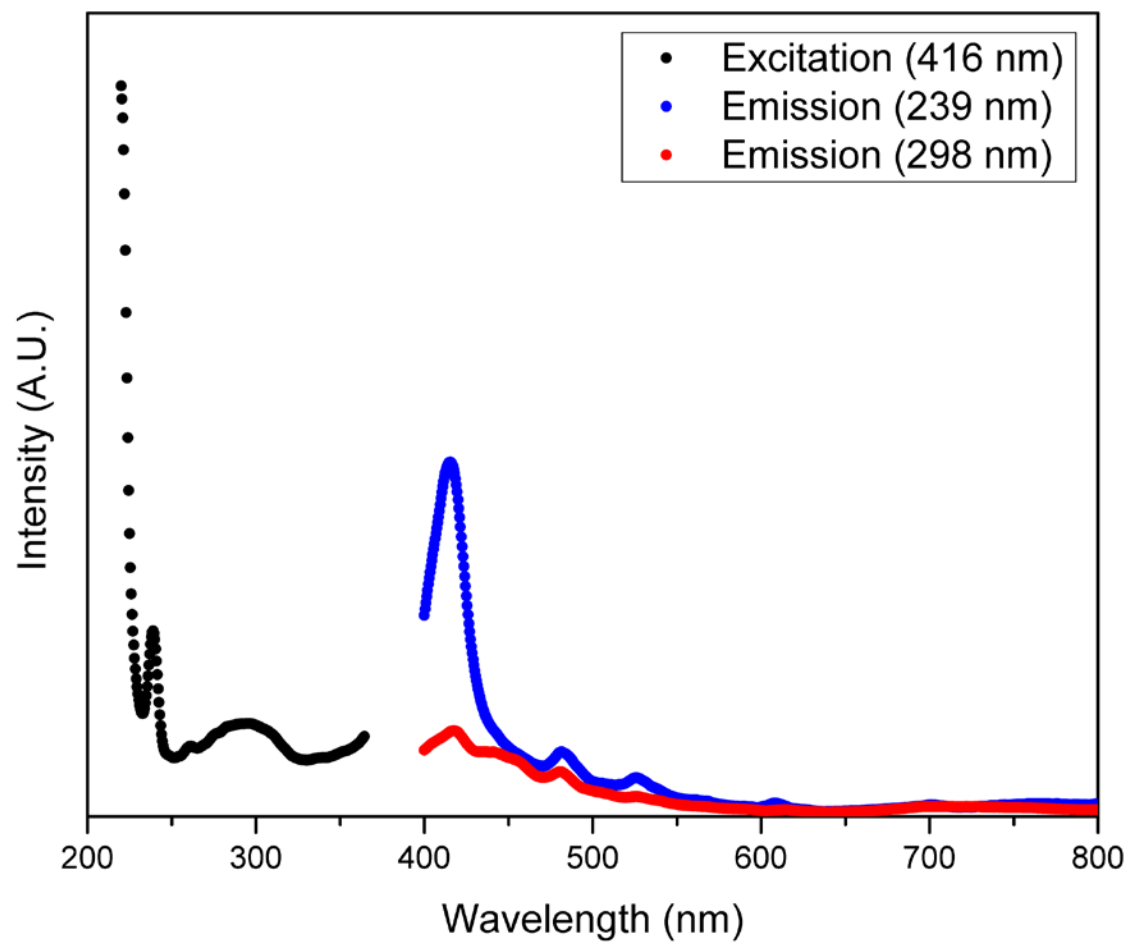
Figure 3.7. Fluorescence spectra of $K_2Ba(MoO_4)_2$
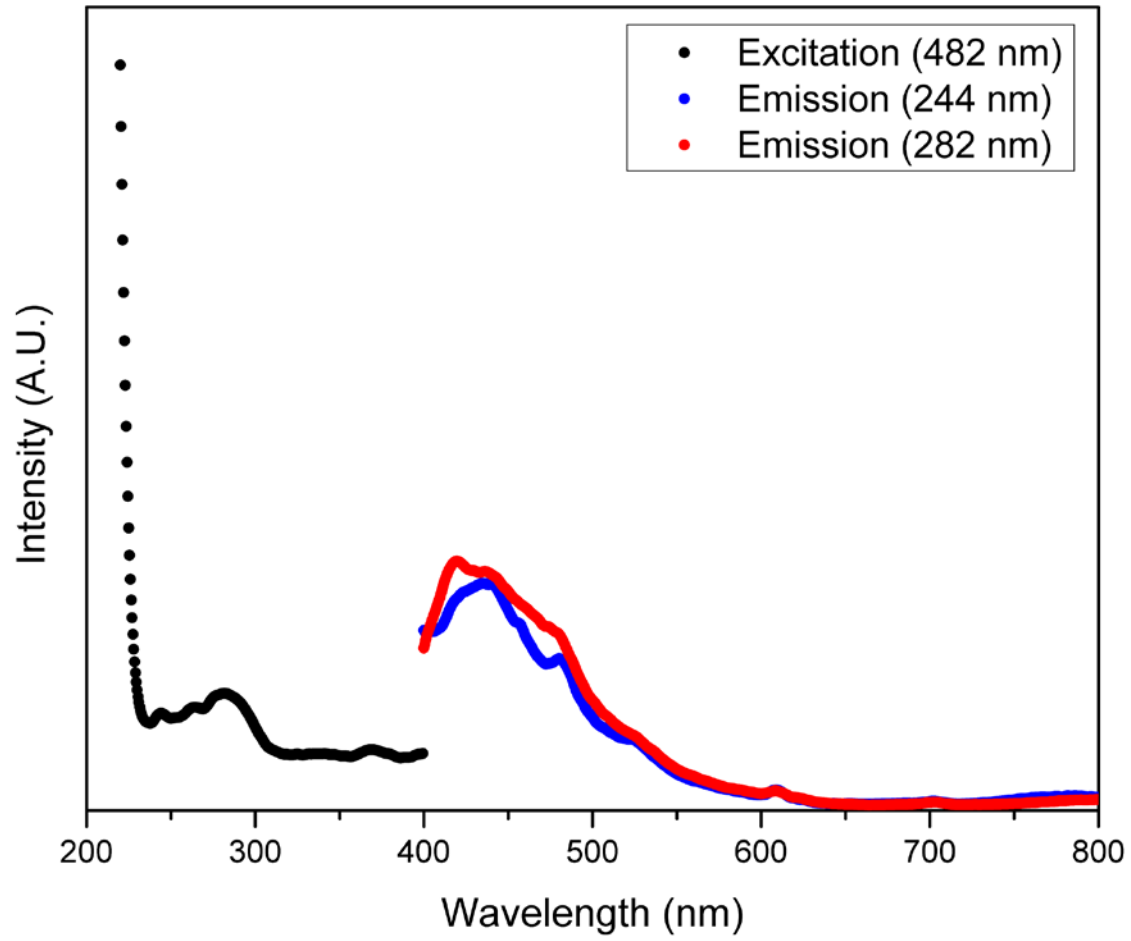
Figure 3.8. Fluorescence spectra of $K_2Ba(WO_4)_2$

Table 3.1. Crystal structure and refinement data for $K_2Ba(MO_4)_2$ (M = Cr, Mo, W).

compound	$K_2Ba(CrO_4)_2$	$K_2Ba(MoO_4)_2$	$K_2Ba(WO_4)_2$
formula weight	447.54	535.42	711.24
color and habit	yellow prism	colorless prism	colorless prism
space group	R-3m	R-3m	R-3m
Z	3	3	3
a (Å)	5.7826(16)	5.9505(4)	5.9876(3)
c (Å)	21.510(12)	21.150(3)	21.075(3)
V (Å^3)	611.3(4)	648.57(12)	654.34(9)
ρ_c (g cm^{-3})	3.647	4.113	5.415
μ (mm^{-1})	8.426	8.331	31.731
F(000)	618	726	918
crystal size (mm)	0.05 x 0.05 x 0.01	0.53 x 0.20 x 0.20	0.10 x 0.08 x 0.08
θ_{max} (°)	28.44	31.66	31.48
index ranges	$-7 \leq h \leq 7$;	$-8 \leq h \leq 8$;	$-8 \leq h \leq 8$;
	$-7 \leq k \leq 7$;	$-8 \leq k \leq 8$;	$-8 \leq k \leq 8$;
	$-28 \leq l \leq 28$	$-31 \leq l \leq 31$	$-30 \leq l \leq 30$
reflections collected	1876	2520	3616
independent reflections	217	307	309
goodness-of-fit on F^2	1.354	1.252	1.246
R indices (all data)	$R1$ = 0.0290, wR2 = 0.0633	$R1$ = 0.0369, wR2 = 0.0659	$R1$ = 0.0200, wR2 = 0.0449

100

| largest difference peak/hole (e Å^{-3}) | 0.559/-0.728 | 0.846/-1.226 | 1.104/-1.163 |

For all structures, T = 298(2) K and λ = 0.71073 Å.

Table 3.2. Atomic coordinates and equivalent isotropic displacement parameters for $K_2Ba(MO_4)_2$ (M = Cr, Mo, W). U_{eq} is defined as one-third of the trace of the orthogonalized U_{ij} tensor.

	x	y	z	U_{eq}	occupancy
$K_2Ba(CrO_4)_2$					
Ba(1)	0	0	0	0.0221(4)	0.825(7)
K(1)	0	0	0	0.0221(4)	0.175(7)
Ba(2)	0.6667	0.3333	0.13119(7)	0.0216(7)	0.087(3)
K(2)	0.6667	0.3333	0.13119(7)	0.0216(7)	0.913(3)
Cr	0.3333	0.6667	0.07275(6)	0.0154(5)	1
O(1)	0.1762(4)	0.3523(8)	0.09786(16)	0.0233(10)	1
O(2)	0.3333	0.6667	-0.0037(3)	0.041(2)	1
$K_2Ba(MoO_4)_2$					
Ba(1)	0	0	0	0.0290(4)	0.775(3)
K(1)	0	0	0	0.0290(4)	0.225(3)
Ba(2)	0.6667	0.3333	0.13573(6)	0.0228(4)	0.1122(17)
K(2)	0.6667	0.3333	0.13573(6)	0.0228(4)	0.8878(17)
Mo	0.3333	0.6667	0.07056(3)	0.0172(3)	1
O(1)	0.1731(4)	0.3463(9)	0.09801(19)	0.0320(10)	1
O(2)	0.3333	0.6667	-0.0111(3)	0.054(3)	1
$K_2Ba(WO_4)_2$					
Ba(1)	0	0	0	0.0236(4)	0.545(6)

102

K(1)	0	0	0	0.0236(4)	0.455(6)
Ba(2)	0.6667	0.3333	0.13611(7)	0.0183(4)	0.228(3)
K(2)	0.6667	0.3333	0.13611(7)	0.0183(4)	0.772(3)
W	0.3333	0.6667	0.070671(19)	0.01259(17)	1
O(1)	0.1735(4)	0.3471(10)	0.0983(2)	0.0257(11)	1
O(2)	0.3333	0.6667	-0.0122(3)	0.048(3)	1

103

Table 3.3. Selected interatomic distances (Å) and angles (°) for $K_2Ba(MO_4)_2$ (M = Cr, Mo, W).

	$K_2Ba(CrO_4)_2$	$K_2Ba(MoO_4)_2$	$K_2Ba(WO_4)_2$
Ba(1)/K(1)-O(1)	2.738(4) x6	2.735(4) x6	2.744(5) x6
O(1)-Ba(1)/K(1)-O(1)	67.13(13)	68.81(14)	69.21(16)
Ba(2)/K(2)-O(2)	2.741(7)	2.637(7)	2.612(10)
Ba(2)/K(2)-O(1)	2.842(4) x3	2.761(4) x3	2.754(5) x3
Ba(2)/K(2)-O(1)	2.9635(12) x6	3.0811(11) x6	3.0988(13) x6
M-O(2)	1.645(7)	1.726(7)	1.746(10)
M-O(1)	1.651(4) x3	1.750(4) x3	1.757(5) x3

Referencess

1) Bugaris, D. E.; zur Loye, H.-C. *Angew. Chem., Int. Ed.* **2012**, *51*, 3780.

2) Bugaris, D. E.; Hodges, J. P.; Huq, A.; zur Loye, H. C. *J. Solid State Chem.* **2011**, *184*, 2293.

3) Gu, H.; Hu, Y.; Wang, H.; Yang, X.; Hu, Z.; Yuan, Y.; You, J. *J. Sol-Gel Sci. Techn.* **2007**, *42*, 293.

4) Pires, F. I.; Joanni, E.; Savu, R.; Zaghete, M. A.; E., L.; Varela, J. A. *Materi. Lett.* **2008**, *62*, 239.

5) Byrappa, K.; Jain, A. *J. Mater. Res.* **1996**, *11*, 2869.

6) Tsai, C.-J.; Yang, C.-Y.; Liao, Y.-C.; Chueh, Y.-L. *J. Mater. Chem.* **2012**, *22*, 17432.

7) Flood, H.; Forland, T. *Acta Chem Scand* **1947**, *1*, 592.

8) Lux, H. Z. *Z. Elektrochem.* **1939**, *45*, 303.

9) Bugaris, D.E.; Smith, M.D.; zur Loye, H.-C. *Inorg. Chem.* **2013**, *52* (7), 3836-3844.

10) Chance, W.M.; Bugaris, D.E.; Sefat, A.S.; zur Loye, H.-C. *Inorg. Chem.* **2013**, *52* (20), 11723-11733.

11) Li, Q.; Huang, J.; Chen, D. *J. Alloys Compd.* **2010**, *509*, 1007.

12) Leonidova, O. N.; Leonidova, E. I. *Solid State Ionics* **2008**, *179*, 188.

13) Grzechnik, A. *Chem. Mater.* **1998**, *10*, 1034.

14) Sahoo, P. P.; Gaudin, E.; Darriet, J.; Row, T. N. *Inorg Chem* **2010**, *49*, 5603.

15) Saha, D.; Sahoo, P. P.; Madras, G.; Row, T. N. G. *RSC Adv.* **2012**, *2*, 10505.

16) Schwarz, H. *Naturwissenschaften* **1965**, *52*, 206.

17) Bandrowska, C.; Bunter, E.; Fiolna, J.; Haczek, L.; Dabrowski, B.; Grzywaczewski, T.; Zmuda, D. *Pol.* **1968**, *(PL55337)*, 2 pp. Addn. to Pol. 53847.

18) Trunin, A. S.; Shter, G. E.; Serezhkin, V. N. *Zh. Neorg. Khim.* **1975**, *20*, 2209.

19) Kastens, M. L.; Prigotsky, M. J. *J. Ind. Eng. Chem.* **1949**, *41*, 2376.

20) Efremov, V. A.; Trunov, V. K. *Kristallografiya* **1974**, *19*, 989.

21) Rao, B. R.; Mehdi, S.; Hussain, M. R. *Z. Anorg. Allg. Chem.* **1965**, *335*, 206.

22) Klevtsov, P. V.; Kozeeva, L. P.; Protasova, V. I.; Kharchenko, L. Y.; Glinskaya, L.,A.; Klevtsova, R. F.; Bakakin, V. V. *Kristallografiya* **1975**, *20*, 57.

23) Li, Q.; Huang, J.; Chen, D. *Appl. Phys. B: Lasers Opt.* **2011**, *103*, 521.

24) Efremov, V. A.; Gizhinskii, A. R.; Trunov, V. K. *Kristallografiya* **1975**, *20*, 138.

25) *SMART Version 5.625, SAINT+ Version 6.45 and SADABS Version 2.05, Bruker Analytical X-ray Systems, Inc., Madison, Wisconsin, USA, 2001*

26) *SHELXTL Version 6.14, Bruker analytical X-ray Systems, Inc., Madison, WI, 2000*

27) Weller, M.T.; Skinner, S.J. *Acta Crystallogr. Sect. C* **1999**, *55*, 154.

28) Aczel, A.A.; Dabkowska, H.A.; Provencher, P.R.; Luke, G.M. *J. Cryst. Growth* **2008**, *310*, 870.

29) Azdouz, M.; Manoun, B.; Essehli, R.;Azrour, M.; Bih, L.; Benmokhtar, S. *J. Alloys Compd.* **2010**, *498*, 42.

30) Slepukhin, V. K.; Palvanov, V. P.; Efremov, V. A. *Khim. Tverd. Tela* **1977**, *1*, 74.

31) Park, K.-C.; Mho, S.-i. *J. Lumin.* **2007**, *122-123*, 95.

32) Miller, R. M.; Tinti, D. S. *J. Lumin.* **1986**, *36*, 143.

33) Dalhoeven, G. A. M.; Blasse, G. *Chem. Phys. Lett.* **1980**, *76*, 27.

106

34) Spek, A. L.; Duisenberg, A. J. M.; Coremans, C. J. M.; Van der Waals, J. H. *J. Lumin.* **1996**, *69*, 319.

107

Chapter 3.2: Synthesis, Crystal Structure, and Optical Properties of

Dibarium Tungstate Hydrate, $Ba_2WO_5 \cdot H_2O$

Introduction

Ternary and quaternary tungstates are of particular interest for optical and dielectric properties. Hydrothermal treatment of WO_3 or other tungsten precursors is often used to grow crystals of complex tungstates,[1-6] and the use of molten fluxes for the synthesis of tungstates is equally common.[7-11] The use of low temperature fluxes, such as hydroxides, in exploratory crystal growth reactions can lead to the discovery of new phases.[12] A new ternary oxide hydrate, $Ba_2WO_5 \cdot H_2O$, was grown using a hydroflux created by adding alkali metal hydroxides and water together in quantities that result in a solid at room temperature that, however, melts at a lower temperature than the neat hydroxide.[13,14] To our knowledge, $Ba_2WO_5 \cdot H_2O$ is the first barium tungstate hydrate obtained in the absence of surrounding Keggin ions, and the only barium tungstate hydrate rich in electropositive cations. Unlike the other cation-rich hydrates, such as $Na_2WO_4 \cdot 2H_2O$,[15] $Li_2WO_4 \cdot 2H_2O$,[16] and $KLiWO_4 \cdot H_2O$[17] in which the tungsten is found in a tetrahedral environment, the tungsten in the title compound is coordinated to six oxygen atoms in edge-shared, distorted octahedra dimers. The $[W_2O_{10}]^{8-}$ structural unit is a well-known structural motif for tungstates.[18-21] The corresponding oxide, Ba_2WO_5,[22] is known and while the tungsten is coordinated to six oxygen atoms in this structure the polyhedra are corner-shared and form 1-D zigzag chains. The synthesis and crystal structure of $Ba_2WO_5 \cdot H_2O$ is discussed herein.

Experimental

Materials and method

A single crystal of $Ba_2WO_5 \cdot H_2O$ was grown from a hydroxide hydroflux. The reaction vessel was a PTFE-lined, 23 mL Parr autoclave. The hydroflux consisted of 11

grams of KOH (Fisher, certified ACS pellets) and 6 grams of distilled water. To this hydroflux, 2 mmols of $Ba(NO_3)_2$ (0.5226 g), 1 mmol of WO_3 (Alfa Aesar, 99.99%), and an excess (~0.4 g) of Zn metal (Johnson Matthey, 99.999%) were added. $Ba_2WO_5 \cdot H_2O$ was only attainable employing zinc metal as a mineralizer, with $Zn(NO_3)_2$, $ZnCl_2$, ZnO, and $Zn(OH)_2$ all failing to produce the title compound. During the reaction, the autoclave was sealed to prevent water loss that would raise the melting point and heated to 230 ºC at a rate of 5 ºC/min, held for 24 h, and then cooled at a rate of 0.3 ºC/min to 60 ºC. Crystals were isolated by decanting the molten hydroflux followed by sonication in methanol.

Crystallographic study

X-ray intensity data from a colorless, prismatic crystal (approximate dimensions 0.063 x 0.024 x 0.023 mm^3) were measured at 153(2) K on a Bruker SMART APEX CCD diffractometer (Mo Kα radiation, λ = 0.71073 Å).[23] The raw area detector data frames were reduced with SAINT+.[23] Data were corrected for absorption effects using the multi-scan technique implemented in SADABS.[23] The reported unit cell parameters were determined by least-squares refinement of large sets of strong reflections taken from each data set. Full-matrix least-squares refinement against F^2 of the structural models and difference Fourier calculations were performed with SHELXTL.[24] The two hydrogen atoms could not be located in the structure with certainty.

The most important crystallographic data from the single crystal structure refinements for $Ba_2WO_5 \cdot H_2O$ are found in Table 3.4. Atomic positions and selected interatomic distances are listed in Tables 3.5 and 3.6, respectively.

Infrared Spectroscopy

IR spectra were recorded with a Perkin Elmer Spectrum 100 FT-IR spectrometer. The sample was ground to a powder using an agate mortar and pestle and four scans ranging from 4500 cm^{-1} to 600 cm^{-1} were averaged.

UV-Visible Spectroscopy

A Perkin-Elmer Lambda 35 UV-visible spectrophotometer was used to collect diffuse-reflectance data in the range of 200-800 nm at room temperature. PTFE was used as a white standard. Raw data were converted from reflection to absorbance by the Kubelka-Munk function.

Luminescence

A Perkin Elmer LS 55 Fluorescence Spectrometer was used to measure emission and excitation spectra of the title compounds. The excitation wavelengths studied were 277 and 340 nm. The maximum emission wavelengths observed were 423 nm when excited at 277 nm and 462 nm when excited at 340 nm. All measurements were conducted at room temperature.

Results and Discussion

$Ba_2WO_5 \cdot H_2O$ crystallizes in the space group $P2_1/n$. Detailed crystallographic information is presented in Table 3.4, atomic coordinates are listed in Table 3.5, and selected interatomic distances are highlighted in Table 3.6. To the best of our knowledge, this compound crystallizes in a unique structure type. The structure can be thought of as a layered structure characterized by alternating barium double layers and layers containing $[W_2O_{10}]^{8-}$ dimers as shown in Figure 3.9. The $[W_2O_{10}]^{8-}$ dimeric unit is shown in Figure 3.10 with bond angles listed in Table 3.7. Tungsten is displaced toward O5 and away from the center of the unit toward O3 and O2. The tungsten octahedra are edge-shared

111

through the longest equatorial oxygen bonds (W-O1). These dimers are separated by barium and are canted with respect to the c-axis and each layer alternates tilt with respect to this axis as per the screw axis. Barium is present in both irregular 9-coordinate polyhedra (Ba1) and in 8-coordinate distorted antiprisms (Ba2). The local barium environments are shown in Figure 3.11. Barium polyhedra are face-, edge-, and corner-shared to form a framework around the tungsten dimers. The 9-coordinate polyhedra are face-shared to each other through O6 and O5 and corner-shared to each other through O2. Each square antiprism is face–shared to two 9-coordinate polyhedra through O1, O5 and O6 to one and through O2, O3, and O4 to another. Each square antiprism is also edge-shared to one 9-coordinate polyhedra through O2 and O3 and corner-shared to two face-sharing 9-coordinate polyhedra through O6. The square antiprisms are edge-shared to each other through O3 and O6 and form zig-zag chains along [101] lattice vector. Overall, the structure can be thought of as chains of 8-coordinate barium linked together by corrugated sheets of 9-coordinate barium that, together, form a 3-D framework around the isolated $[W_2O_{10}]^{8-}$ units (Figure 3.12).

The hydrogen atoms were not located in this structure. O6 has the longest interoxygen distance (3.006 Å) and is the only oxygen not bound to tungsten. During the structure solution process, one hydrogen atom was located in the difference map at a distance of 0.847 Å from O6 and approximately 2.410 Å from O4. The second hydrogen could not be located and freely refined. Attempts to place the second hydrogen in a physically reasonable position (attached to O6 and closest to O1 and O5) resulted in drift toward the nearest heavy atom. Bond valence sums[25] for all six oxygen atoms are listed in Table 3.8. The low bond valence sums for O6 and O4 corroborate the placement of the

first hydrogen, but the fact that the second hydrogen was unable to be located between O6 and O1, O2, or O5 coupled with the slightly lower sum for O5 compared with the other nearby oxygen atoms suggests that the hydrogen may be disordered about this cavity (Figure 3.13). There is no known tungsten hydroxide, and of the tungstates known to contain hydrogen, only two oxohydroxides exist, $NdWO_4(OH)$[26] and $AlWO_3(OH)_3$[27], and all others are hydrates or hydroxide hydrates, thus supporting the assumption that the compound is a hydrate.

Infrared spectroscopy is often useful for confirming geometries of specific coordination polyhedra and also for confirming specific functional groups. The data, shown in Figure 3.14 provide insight into both in this case. The absorption bands observed at 3531 and 3488 cm^{-1} are indicative of the asymmetric (ν_3) and symmetric (ν_1) stretching frequency of O-H bonds in water, respectively. The broader absorption band observed at 1462 cm^{-1} is due to the bending mode (ν_2) of the crystal water. Absorption bands due to the metal oxygen bonding take place at much lower wavenumber. Five bands are observed down to the lowest value observable due to instrument limitations (650 cm^{-1}). All are sharp with the bands observed at 753 and 704 cm^{-1} being the strongest. No other previous reports of the $[W_2O_{10}]^{8-}$ group report the infrared spectra of this unit, although Blasse assumed their data from β-Li_4WO_5 to be evidence of either pairs of edge-shared tungsten octahedral or chains. A comparison of the five absorption bands observed versus the first five reported bands for β-Li_4WO_5 are given in Table 3.9.

$Ba_2WO_5 \cdot H_2O$ is optically clear and shows pale blue/green luminescence under UV excitation (Figure 3.15). Extrapolating the onset of the absorbance observed in the UV-visible spectrum gives a value of 3.14 eV for the band gap. Weak luminescence is

113

observed at room temperature with maximum emission occurring at 425 nm when the excitation wavelength is 277 nm and at 462 nm when the excitation wavelength is 340 nm. There also appears to be a shoulder, also at 462 nm, when the excitation wavelength is 277 nm (Figure 3.16). It is unclear how these results compare to other, previously reported structures with an analogous tungsten environment, due to absence of data from the literature. Jiang and colleagues recently performed spectroscopic studies on $Nd_2W_2Te_2O_{13}$, but only reported the near-IR luminescence.[28] Blasse's report on β-Li_4WO_5 supposed the structure to feature the $[W_2O_{10}]^{8-}$ dimer. He reported the low temperature luminescence to have considerable intensity from 465-470 nm, depending on the temperature.[17] The emission was reported to have a quenching temperature of 300 K, according to Kroger's definition.[29] The emission observed at 462 nm under both excitation wavelengths with $Ba_2WO_5 \cdot H_2O$ is likely of similar origin.

Conclusions

$Ba_2WO_5 \cdot H_2O$ was synthesized from a low temperature hydroflux method. This structure features the rare $[W_2O_{10}]^{8-}$ dimeric subunit. For the first time, room temperature infrared spectroscopy, UV-visible spectra, and luminescence data are presented for a structure featuring this subunit. The compound is weakly luminescent at room temperature and, given the reports of vastly enhanced luminescence in β-Li_4WO_5 at low temperatures, it would be interesting to study this compound at liquid nitrogen or even liquid helium temperatures.

Acknowledegements
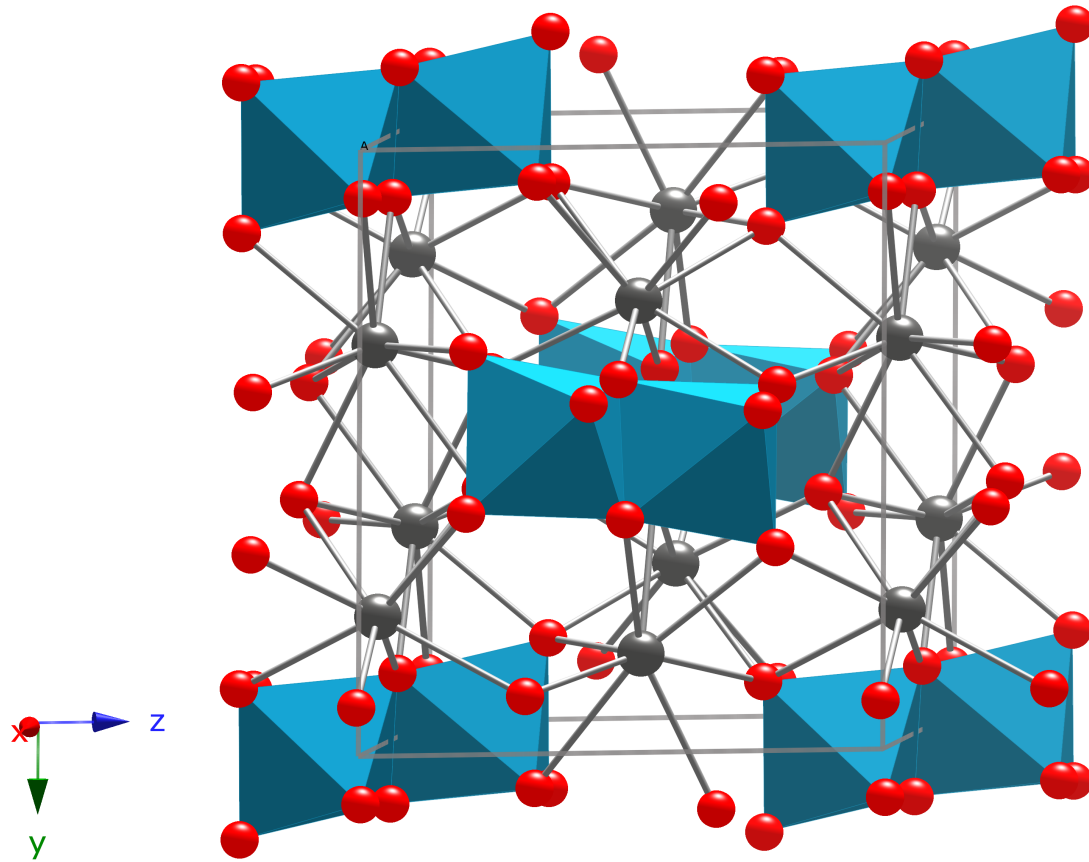
Figure 3.9. Ball-and-stick representation of $Ba_2WO_5 \cdot H_2O$. Barium atoms are shown in grey, oxygen on red, and $[W_2O_{10}]^{8-}$ units are shown in light blue.
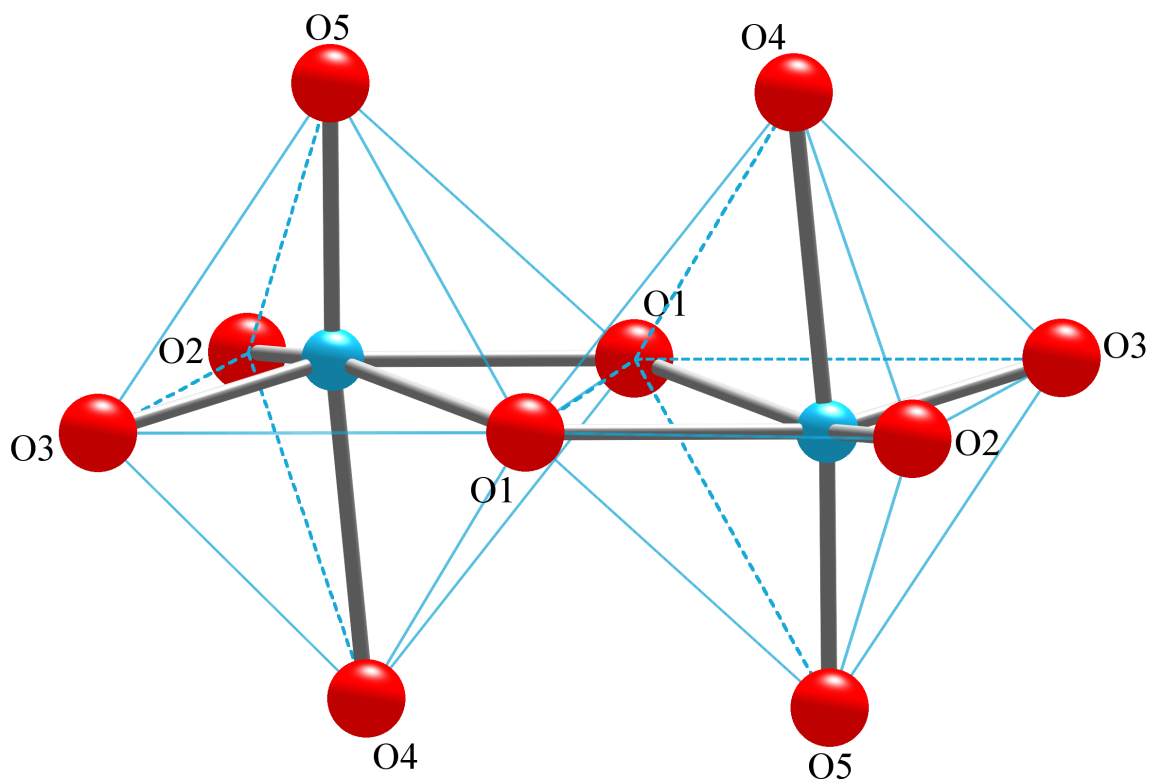
Figure 3.10. Ball-and-stick representation of the $[W_2O_{10}]^{8-}$ dimeric unit with tungsten shown in light blue and oxygens labeled according to their crystallographic site.
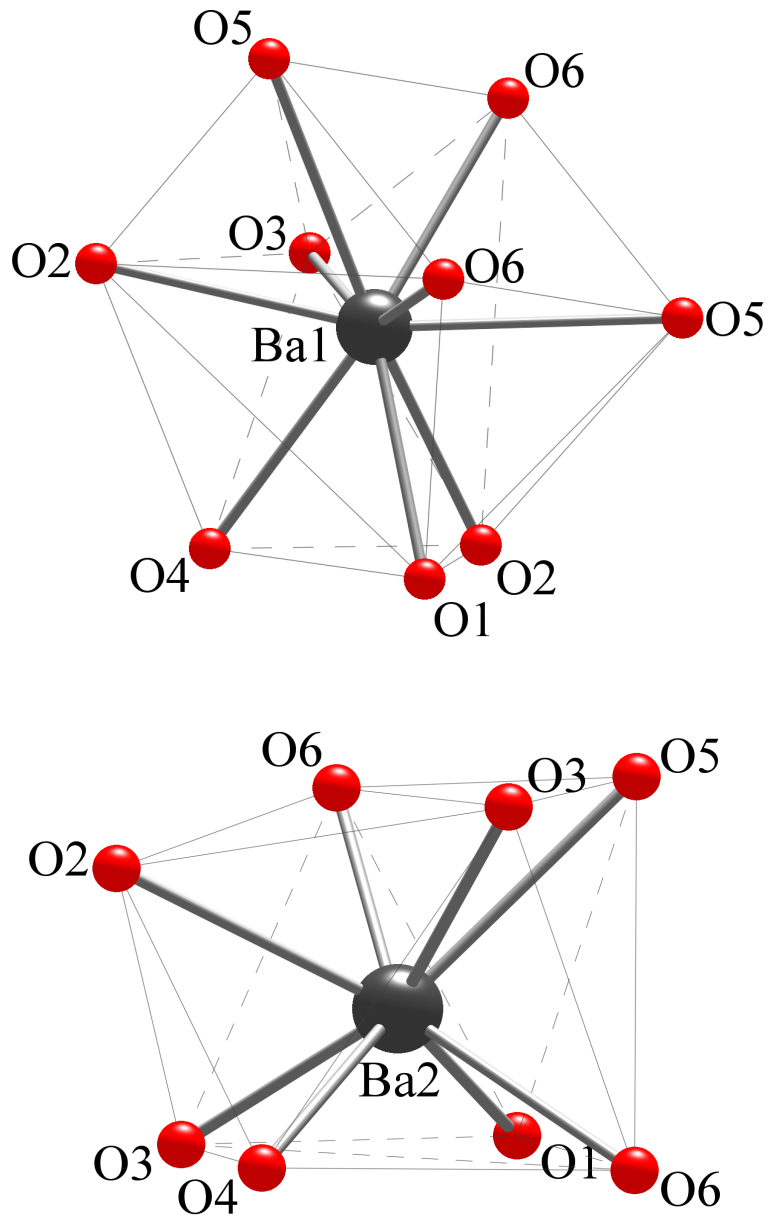
Figure 3.11. Local coordination environments of Ba1 and Ba2.
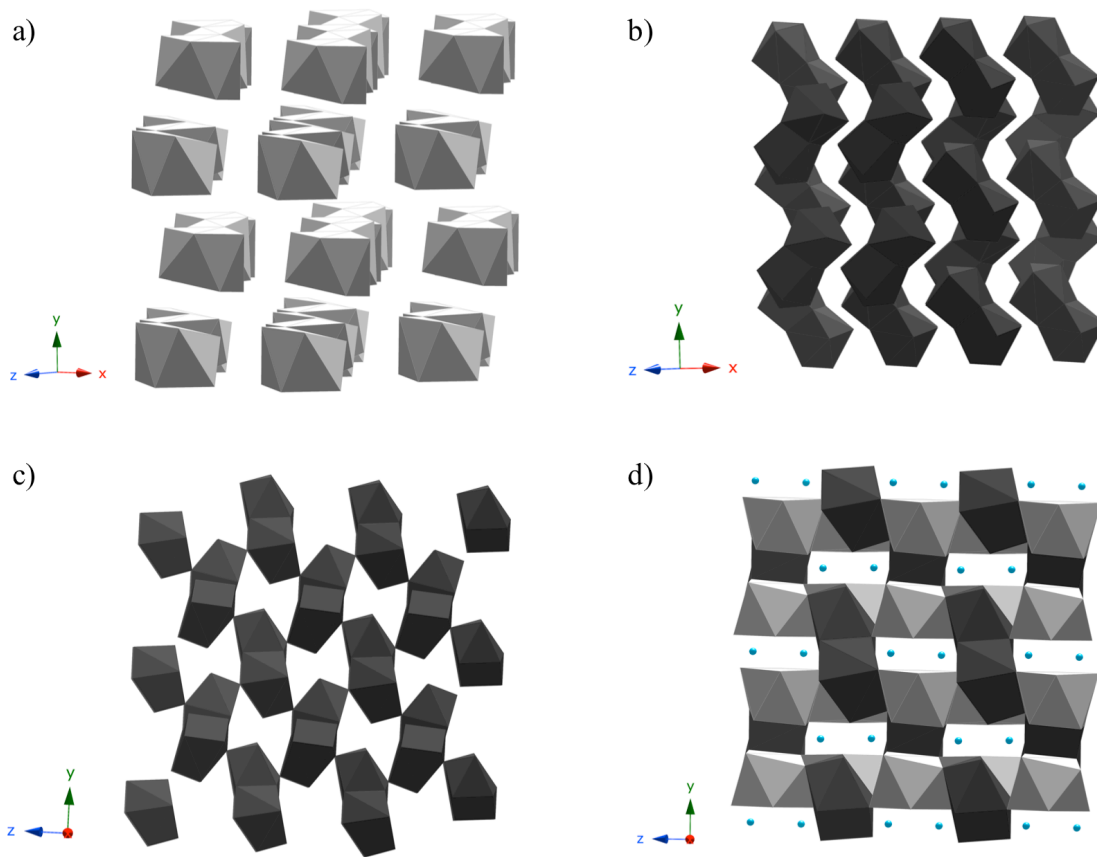
Figure 3.12. a) 1-D chains formed by edge-shared 8-coordinate barium polyhedra, shown in light grey b) Corrugated sheets of 9-coordinate barium polyhedra, shown in dark grey c) Edge- and corner-shared 9-coordinate barium polyhedra form the corrugated layers d) Polyhedral view displaying the framing of the tungstate dimers by the two different barium environments.
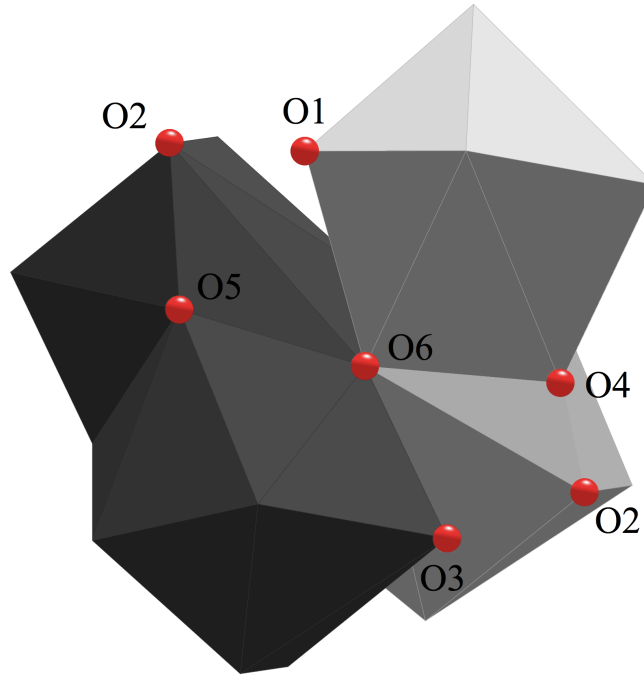
Figure 3.13. Coordination environment around O6, the suggested water of crystallization. 8-coordinate barium and 9-coordinate barium polyhedra are shown in light grey and dark grey, respectively.
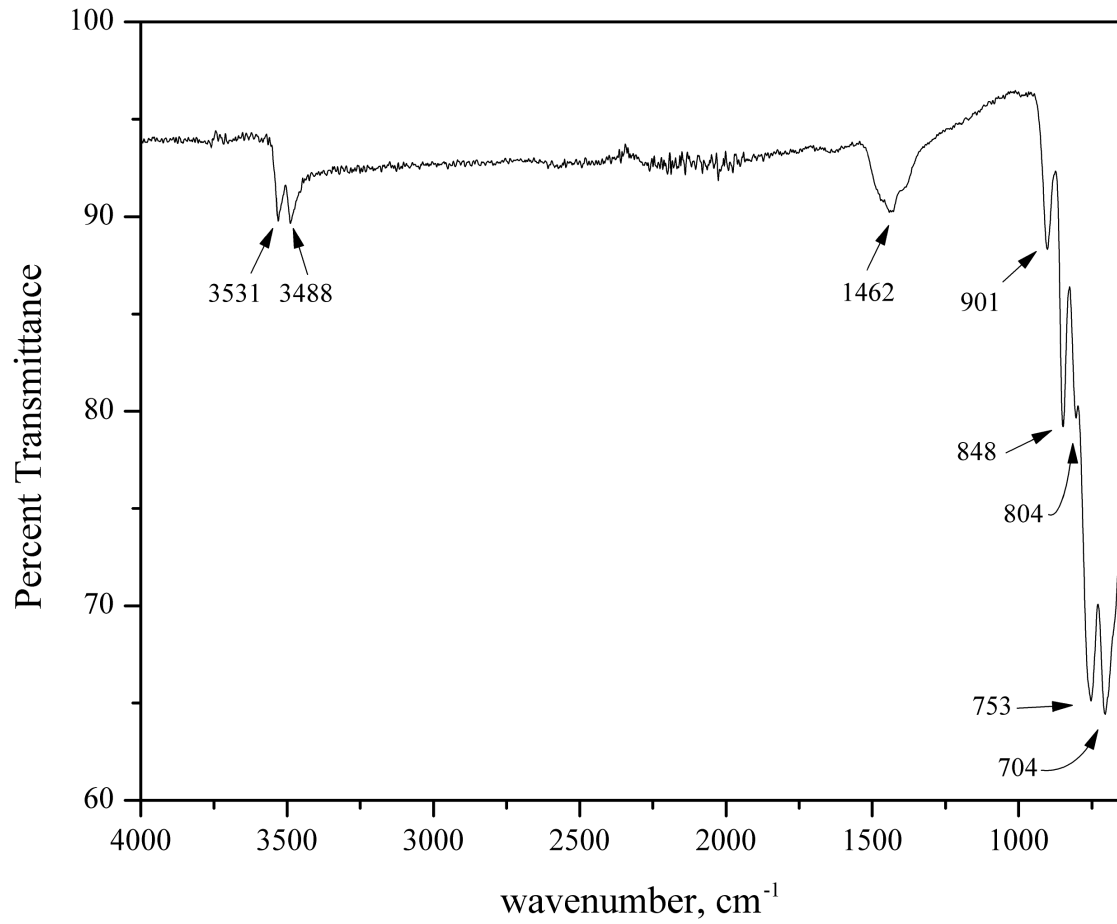
Figure 3.14. Infrared spectroscopy data for $Ba_2WO_5 \cdot H_2O$ with absorption bands labeled.
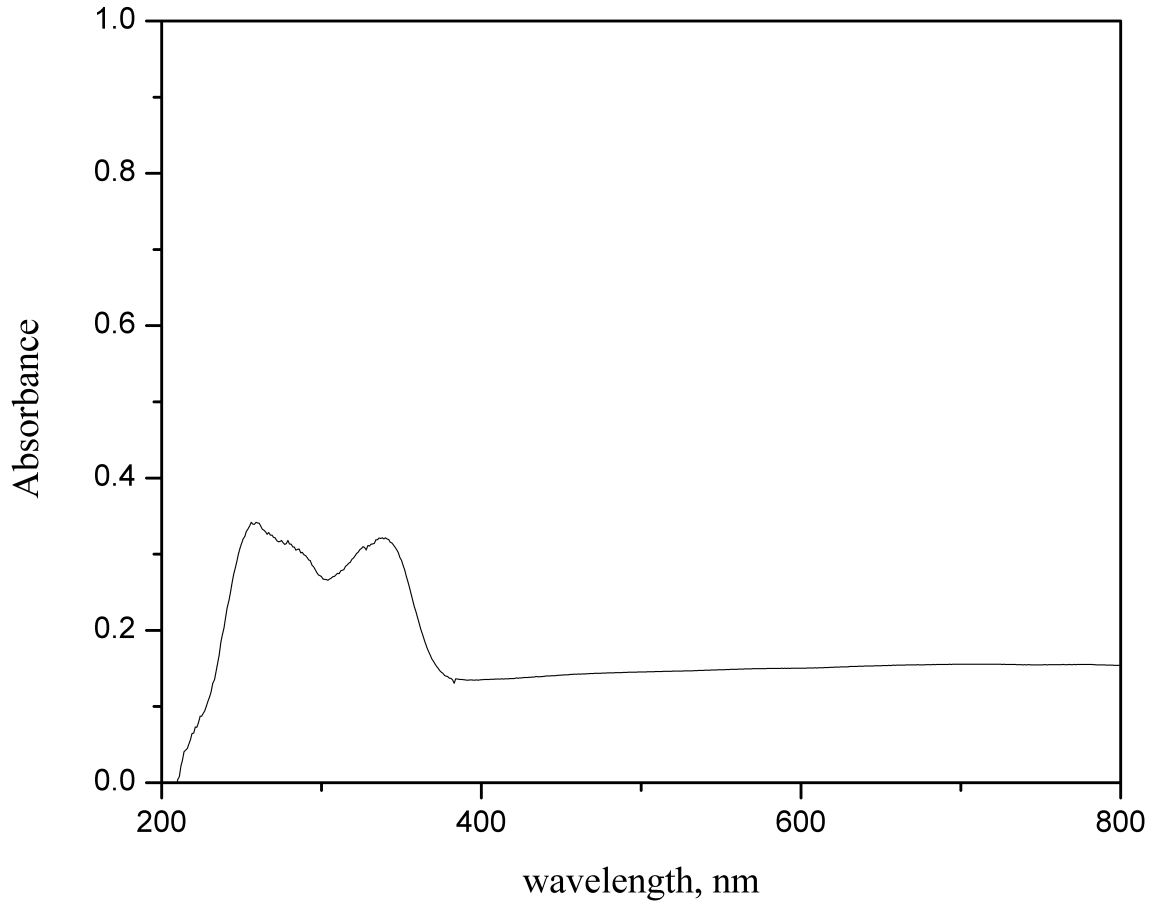
Figure 3.15. Room temperature, UV-visible absorption spectra for $Ba_2WO_5 \cdot H_2O$.
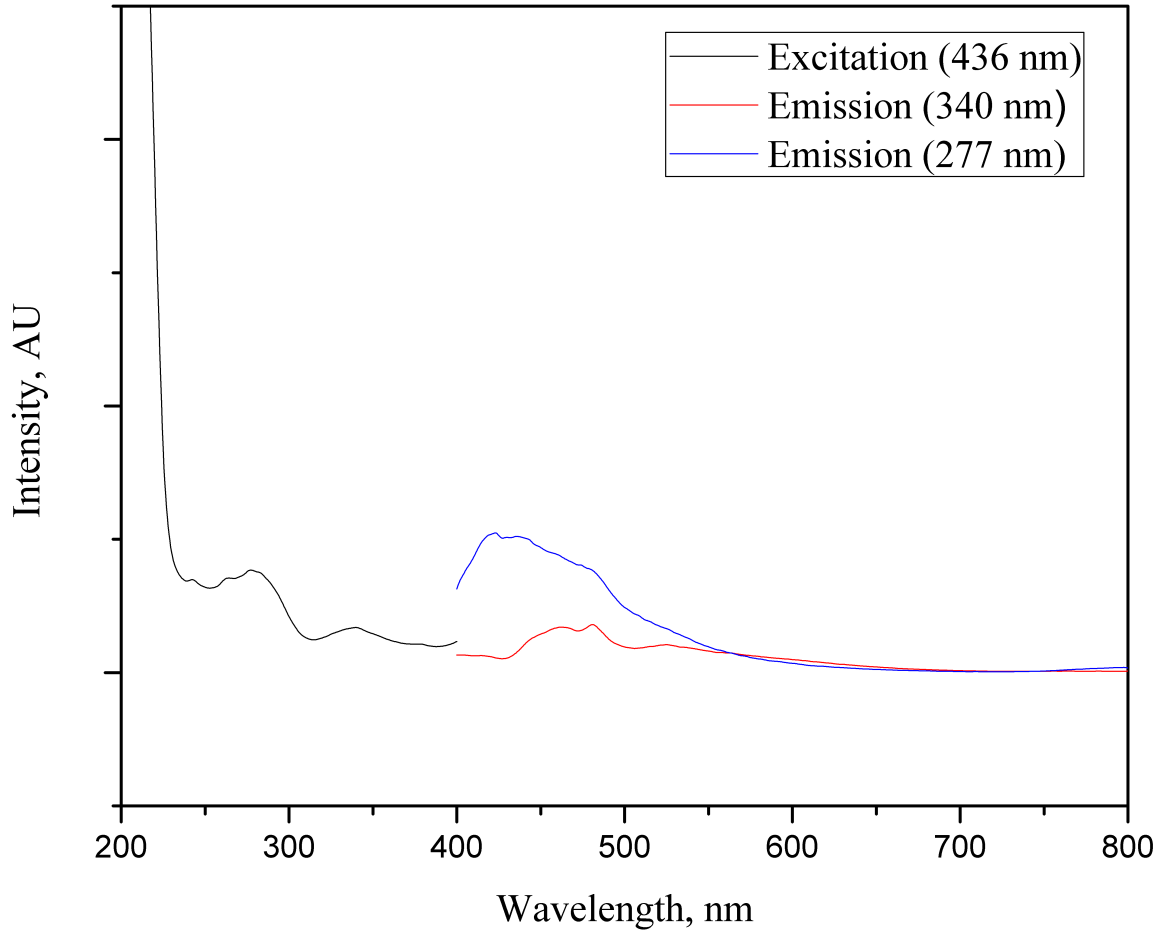
Figure **3.16.** Room temperature luminescence data for $Ba_2WO_5 \cdot H_2O$.

Table 3.4. Crystal structure and refinement data for $Ba_2WO_5 \cdot H_2O$.

Empirical formula	$Ba_2WO_5 \cdot H_2O$
Color & Shape	Colorless prism
Crystal size	$0.063 \times 0.024 \times 0.023$ mm^3
Formula weight	556.416 g/mol
Temperature	153(2) K
Wavelength	0.71073 Å
Crystal system	Monoclinic
Space group	$P2_1/n$
Unit cell dimensions	$a = 7.6710(15)$ Å
	$b = 9.853(2)$ Å
	$c = 8.5520(17)$ Å
	$\beta = 111.84(3)°$
Volume	600.0(2) Å3
Z	4
Density (calculated)	6.161 Mg/m3
Absorption coefficient	32.064 mm-1
Reflections collected	10167
Independent reflections	1492 [R(int) = 0.0347]
Absorption correction	Semi-empirical from equivalents
Data / restraints / parameters	1492 / 0 / 83
Goodness-of-fit on F^2	1.161
Final R indices [I>2sigma(I)]	$R_1 = 0.0215$, $wR_2 = 0.0452$

123

R indices (all data) $R_1 = 0.0229$, $wR_2 = 0.0457$

Largest diff. peak and hole   1.316 and -1.096 e$^-$Å^{-3}

Table 3.5. Atomic coordinates and equivalent isotropic displacement parameters for $Ba_2WO_5 \cdot H_2O$.

$Ba_2WO_5 \cdot H_2O$	x	y	z	$U_{(eq)}$ (Å^2)[a]
W	0.01562(3)	0.49677(2)	0.31550(3)	0.00462(8)
Ba1	0.61524(5)	0.34357(4)	0.97724(5)	0.00637(10)
Ba2	0.60953(5)	0.27654(4)	0.47852(5)	0.00590(10)
O1	0.0745(6)	0.6166(4)	0.5167(5)	0.0055(8)
O2	-0.0184(6)	0.3360(5)	0.2041(5)	0.0077(9)
O3	0.1541(6)	0.5943(4)	0.2248(5)	0.0069(8)
O4	0.2868(6)	0.4080(5)	0.4756(6)	0.0092(9)
O5	-0.2092(6)	0.5731(5)	0.2030(5)	0.0084(9)
O6	0.4311(6)	0.4008(5)	0.1734(6)	0.0092(9)

[a] $U_{(eq)}$ is defined as one-third of the trace of the orthogonalized Uij tensor.

Table 3.6. Selected interatomic distances for $Ba_2WO_5 \cdot H_2O$.

Bond	Value (Å)
W-O1	1.967(4)
W-O1[iii]	2.101(4)
W-O2	1.817(5)
W-O3	1.807(4)
W-O4	2.202(5)
W-O5	1.797(4)
Ba1-O1[ii]	2.720(4)
Ba1-O2[i]	2.759(5)
Ba1-O2[iv]	2.803(4)
Ba1-O3[iii]	2.961(4)
Ba1-O4[iv]	2.809(5)
Ba1-O5[i]	2.953(5)
Ba1-O5[iii]	3.030(5)
Ba1-O6[i]	2.625(4)
Ba1-O6[iii]	2.791(5)
Ba2-O1[iii]	2.649(4)
Ba2-O2[iv]	2.706(4)
Ba2-O3[ii]	2.778(4)
Ba2-O3[iii]	2.815(4)
Ba2-O4	2.786(4)
Ba2-O5[ii]	2.810(4)

Ba2-O6	2.743(5)
Ba2-O6[iv]	2.976(5)
Ba2-O4[iii]	3.196(5)

Symmetry codes: (i) x, y, z, (ii) -x+1/2, y+1/2, -z+1/2 (iii) -x, -y, -z (iv) x-1/2, -y-1/2, z-1/2

Table 3.7. Bond angles from the $[W_2O_{10}]^{8-}$ unit.

O5-W-O4	174.55(18)°
O1-W-O1$^{\text{iii}}$	73.85(19)°
O1$^{\text{iii}}$-W-O2	83.99(18)°, 154.43(19)°
O2-W-O3	103.39(19)°
O3-W-O1	95.11(18)°
O5-W-O3	98.5(2)°
O5-W-O1$^{\text{iii}}$	94.84(18)°
O5-W-O2	99.3(2)°

Table 3.8. Bond valence sums (B.V.S.) for all oxygen atoms.

Atom	Bonds	Distances (Å)	Bond Valence	B.V.S.
O1	W-O1	1.967(4)	0.87	2.16
	W-O1^{iii}	2.101(4)	0.61	
	Ba2-O1^{iii}	2.649(4)	0.37	
	Ba1-O1^{ii}	2.720(4)	0.31	
O2	W-O2	1.817(5)	1.31	2.16
	Ba2-O2^{iv}	2.706(4)	0.32	
	Ba1-O2^{i}	2.759(5)	0.28	
	Ba1-O2^{iv}	2.803(4)	0.25	
O3	W-O3	1.807(4)	1.35	2.01
	Ba2-O3^{ii}	2.778(4)	0.26	
	Ba2-O3^{iii}	2.815(4)	0.24	
	Ba1-O3^{iii}	2.961(4)	0.16	
O4	W-O4	2.202(5)	0.46	0.96
	Ba2-O4	2.786(4)	0.26	
	Ba1-O4^{iv}	2.809(5)	0.24	
O5	W-O5	1.797(4)	1.38	1.92
	Ba2-O5^{ii}	2.810(4)	0.24	
	Ba1-O5^{i}	2.953(5)	0.16	
	Ba1-O5^{iii}	3.030(4)	0.14	
O6	Ba1-O6^{i}	2.625(4)	0.40	0.81
	Ba1-O6^{iii}	2.791(5)	0.26	

129

Ba2-O6^{iv}	2.976(5)	0.15

Table 3.9. Comparison of the observed infrared absorption bands for $Ba_2WO_5 \cdot H_2O$ and Li_4WO_5 (all values in cm^{-1}; standard abbreviations).

$Ba_2WO_5 \cdot H_2O$	Li_4WO_5
901 (w)	810 (m)
848 (m)	750 (s)
804 (m)	690 (s)
753 (s)	650 (s, br)
704 (s)	610 (s)

131

References

1) Byrappa, K.; Jain, A. *J. Mater. Res.* **1996**, *11*, 2869.

2) Cavalcante, L. S.; Longo, V. M.; Sczancoski, J. C.; Almeida, M. A. P.; Batista, A. A.; Varela, J. A.; Orlandi, M. O.; Longo, E.; Li, M. S. *Cryst. Eng. Comm.* **2012**, *14*, 853.

3) Dadachov, M. S.; Lambrecht, R. M. *J. Mater. Chem.* **1997**, *7*, 1867.

4) Pinlac, R. A. F.; Stern, C. L.; Poeppelmeier, K. R. *Crystals* **2011**, *1*, 3.

5) Wang, H.; Chen, H.-H.; Borrmann, H.; Zhang, Z.-J.; Zhao, J.-T. *J. Alloy. Compd.* **2012**, *545*, 135.

6) Xing, Q.; Xing, X.; Yu, R.; Du, L.; Meng, J.; Luo, J.; Wang, D.; Liu, G. *J. Cryst. Growth* **2005**, *283*, 208.

7) Arora, S. K.; Chudasama, B. *Cryst. Growth Des.* **2007**, *7*, 296.

8) Cavalli, E.; Belletti, A.; Brik, M. G. *J. Phys. Chem. Solids* **2008**, *69*, 29.

9) Cavalli, E.; Boutinaud, P.; Mahiou, R.; Bettinelli, M.; Dorenbos, P. *Inorg. Chem.* **2010**, *49*, 4916.

10) Takeda, H.; Nishida, T.; Okamura, S.; Shiosaki, T. *J. Eur. Ceram. Soc.* **2005**, *25*, 2731.

11) Thangaraju, D.; Moorthy Babu, S.; Durairajan, A.; Balaji, D.; P., S.; Y., H. *J. Cryst. Growth* **2013**, *362*, 319.

12) Bugaris, D. E.; zur Loye, H.-C. *Angew. Chem., Int. Ed.* **2012**, *51*, 3780.

13) Bugaris, D. E.; Smith, M. D.; zur Loye, H.-C. *Inorg. Chem.* **2013**, *52*, 3836.

14) Chance, W. M.; Bugaris, D. E.; Sefat, A. S.; zur Loye, H.-C. *Inorg. Chem.* **2013**, *52*, 11723.

15) Farrugia, L. J. *Acta Crystallogr. E* **2007**, *E63*, i142.

16) Swanson, H. E.; Morris, M. C.; Stinchfield, R. P.; Evans, E. H. *Natl. Bur. Stand. Monog.* **1963**, *25*, 46.

17) Radosavljevic, E. I.; Howard, J. A. K. *Acta Crystallogr. E* **2002**, *E58*, i26.

18) Blasse, G.; Van den Heuvel, G. P. M. *J. Inorg. Nucl. Chem.* **1977**, *39*, 548.

19) Obbade, S.; Dion, C.; Bekaert, E.; Yagoubi, S.; Saadi, M.; Abraham, F. *J. Solid State Chem.* **2003**, *172*, 305.

20) Kim, G. S.; Hagen, K. S.; Hill, C. L. *Inorg. Chem.* **1992**, *31*, 5316.

21) Chisholm, M. H.; Huffman, J. C.; Ratermann, A. L. *Inorg. Chem.* **1983**, *22*, 4100.

22) Kovba, L. M.; Lykova, L. N.; Balashov, V. L.; Kharlanov, A. L. *Koord. Khim.* **1985**, *11*, 1426.

23) SMART Version 5.625, SAINT + Version 6.45, and SADABS Version 2.05, Bruker Analytical X-ray Systems Inc., Madison, Wisconsin, USA 2001.

24) SHELXTL Version 6.14, Bruker Analytical X-ray Systems, Inc. Madison, Wisconsin, USA 2000.

25) Brown, I. D.; Altermatt, D. *Acta Crystallogr. B* **1985**, *B41*, 244.

26) Klevtsova, R. F.; Borisov, S. V. *Kristallografiya* **1969**, *14*, 904.

27) Grey, I. E.; Madsen, I. C.; Mills, S. J.; Hatert, F.; Peterson, V. K.; Bastow, T. J. *Am. Mineral.* **2010**, *95*, 639.

28) Jiang, H.-L.; Ma, E.; Mao, J.-G. *Inorg. Chem.* **2007**, *46*, 7012.

29) Kroger, F. A. *Some Aspects of the Luminescence of Solids*, Elsevier, Amsterdam, 1948.

Chapter 4: Crystal Growth, Structures, Photoluminescence, and Magnetism of the Sodium Rare Earth Oxyhydroxides, $Na_5RE_4(SiO_4)_4OH$ (RE = Pr-Tm, Y) and $Na_2RESiO_4(OH)$ (RE = Yb, Sc)

INTRODUCTION

Rare earth silicates represent a very large group of compounds that have been intensively studied since the late 1950s, when pure rare earth oxides became widely available. The intense luminescent properties of many rare earth ions, especially when present in silicates, as well as their low temperature magnetic properties, have made them a popular synthetic target for solid state lighting applications. In fact, the majority of these compounds were investigated primarily for their photoluminescence properties, although a number of researchers have more recently investigated the ionic conductivity of some rare earth silicates and hydroxosilicates with the goal of expanding the number of ionically conducting solids for applications in fuel cells and battery materials. In addition, they have been studied for their refractory nature and low thermal conductivity. Considering their potential for use in solid state lighting and as solid electrolytes, the rare earth silicates represent an exciting family of materials for continued exploration and materials discovery.

The rare-earth elements are known to exhibit a wide range of coordination environments due to the extensive range of their ionic radii, which when combined with the silicate tetrahedral structural building block, SiO_4, can create a very large number of possible structural motifs based on polyhedral condensation. Thus, it is not surprising that a diverse structural chemistry has been found for these compounds.[1] Investigations of rare-earth structures allow for the systematic study of the effect of ionic radius on structure and, therefore, structure-property relationships can be established.[2] For a number of reported rare-earth silicates, the compositions synthesized include the almost complete series of lanthanides with their smooth change of ionic radii across the series. In

136

many of these examples, the upper and lower size limits appear to be imposed by the radius/coordination limitations of the rare-earth elements rather than by the tetrahedral SiO_4 unit.

A large number of ternary rare earth silicates are known and have been extensively characterized. They tend to fall into one of eight distinct structure types documented by Fleet et al.[3] These compositions were commonly prepared by melt or traditional solid state techniques.[4-7] An equally impressive number of quaternary rare-earth silicates have been reported, including a large number of alkali metal containing structures, such as $NaRESiO_4$, $Na_3RESi_2O_7$,[4-7] $K_3RESi_2O_7$ (RE=Gd-Lu, Sc)[8,9], $K_3HoSi_3O_9$,[10] $K_3NdSi_6O_{15}$,[11] and $Na_5RESi_4O_{12}$ (RE = Sm-Lu).[12] Hydroxo- and hydrated compositions are equally abundant because of their structural relationship to minerals such as hydroxyapatite, toernebohmite, pellyite, and sazhinite. Interestingly, two stoichiometries holding no relation to known naturally occurring compounds are $Na_5RE_4(SiO_4)_4OH$ and $Na_2RESiO_4(OH)$, the title compounds of this paper.

The compounds investigated in this chapter were prepared from hydroxide hydroflux reactions. Previous work has shown hydrofluxes to be suitable for the growth of transition metal oxides and oxyhoydroxides. The extension of hydroflux reactions to the rare earth elements presents exciting possibilities for synthesis and investigation of optical and magnetic properties. The crystal growth, structures, luminescent properties, and magnetic properties of the title compounds are reported herein.

EXPERIMENTAL METHODS

Reagents. The following reagents were used as received: KOH (Fisher Scientific, ACS grade pellets), NaOH (Fisher Scientific, ACS grade pellets), $Pr(NO_3)_3 \cdot 5H_2O$

137

(Acros, 99.9%), Nd_2O_3 (Alfa Aesar, 99.9%), Sm_2O_3 (Alfa Aesar, 99.9%), Eu_2O_3 (Alfa Aesar, 99.9%), Gd_2O_3 (Alfa Aesar, 99.9%), Tb_4O_7 (Alfa Aesar, 99.9%), Dy_2O_3 (Alfa Aesar, 99.9%), $H_{O2}O_3$ (Alfa Aesar, 99.9%), Er_2O_3 (Alfa Aesar, 99.9%), Tm_2O_3 (Alfa Aesar, 99.9%), Yb_2O_3 (Alfa Aesar, 99.9%), Sc_2O_3 (Alfa Aesar, 99.9%), Y_2O_3 (Alfa Aesar, 99.9%), $Na_2SiO_3\cdot9H_2O$ (EM, 99+%) and WO_3 (Alfa Aesar, 99.9%).

Crystal Growth. All products were synthesized in 23 mL PTFE-lined stainless steel autoclaves heated in programmable ovens.

$Na_5RE_4(SiO_4)_4OH$
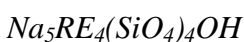
RE = **Pr, Ho**, **Er, Dy, Tm, Y**

0.5 mmols of *RE*$_2O_3$ (*RE* = Nd, Ho, Er, Dy, Tm, Y), or $Pr(NO_3)_3\cdot5H_2O$ was added to a NaOH/KOH hydroflux (0.1 mols NaOH/0.1 mols KOH, 0.33 mols H_2O) with an excess of $Na_2SiO_3\cdot9H_2O$ to push the product toward quantitative yield with respect to *RE*$_2O_3$. Reactions were heated at a rate of 5 ºC per minute to 230 ºC and held for 3 days with subsequent slow cooling at a rate of 0.2 ºC per minute to 80 ºC.

RE = **Eu, Gd, Sm**

0.5 mmols of *RE*$_2O_3$ was added to a NaOH hydroflux (0.25 mols NaOH/0.4 mols H_2O) with an excess of $Na_2SiO_3\cdot9H_2O$ to push the product toward quantitative yield with respect to *RE*$_2O_3$. Reactions were heated at a rate of 5 ºC per minute to 230 ºC and held for 2 days before cooling at a rate of 0.2 ºC per minute.

RE = **Tb**

0.5 mmols of Tb_4O_7 was added to a NaOH/KOH hydroflux (0.15 mols NaOH/0.15 mols KOH, 0.4 mols H_2O) with an excess of $Na_2SiO_3\cdot9H_2O$ to push the product toward quantitative yield with respect to Tb_4O_7. Reactions were heated at a rate of 5 ºC per

138

minute to 230 ºC and held for 4 days before cooling at a rate of 0.1 ºC per minute to 190 ºC before quenching to room temperature.

Na$_2$RESiO$_4$(OH)

RE = Yb, Sc

1 mmol of Yb$_2$O$_3$ or 0.5 mmols Sc$_2$O$_3$ was added to a NaOH hydroflux (0.25 mols NaOH/0.4 mols H$_2$O) with an excess of Na$_2$SiO$_3$•9H$_2$O to push the product toward quantitative yield with respect to *RE*$_2$O$_3$. Reactions were heated at a rate of 5 ºC per minute to 230 ºC and held for 2 days before cooling at a rate of 0.1 ºC per minute. For Na$_2$ScSiO$_4$(OH), the reaction was allowed to slow cool to 80 ºC. For Na$_2$YbSiO$_4$(OH), samples were quenched at various temperatures. Multiply twinned crystals of Na$_2$YbSiO$_4$(OH) were found in all reactions carried out this way with the sample being pure by PXRD analysis when quenched between 230 and 200 ºC. Samples allowed to cool slowly below 200 ºC had impurities of YbO(OH). WO$_3$ was found to be a good mineralizer to promote crystal growth and decrease twinning and intergrowth of crystals.

Magnetic Measurements. The DC magnetic susceptibilities were measured as a function of temperature using a Quantum Design MPMS SQUID VSM. Ground, polycrystalline samples were measured in gelatin capsules. For a typical temperature sweep experiment, the sample was first cooled to 5 K under zero-field cooled (zfc) conditions and data were collected upon warming to 300 K in an applied field of 1000 Oe. Then the sample was field cooled (fc) to 5 K from room temperature in 1000 Oe while data were collected. Values of magnetization measured were corrected by a factor of 10%, based on field calibrations obtained from a Ni standard. All magnetic data presented in this chapter are preliminary.

Luminescence. A Perkin Elmer LS 55 Fluorescence Spectrometer was used to measure emission and excitation spectra of members of the titles compounds that exhibited visible luminescence under short-wave UV excitation. The excitation wavelengths studied for $Na_5Tb_4(SiO_4)_4OH$, $Na_5Gd_4(SiO_4)_4OH$, and $Na_5Eu_4(SiO_4)_4OH$, were 237 nm, 263 nm, and 250 nm, respectively. The maximum emission wavelengths observed were 542 nm, 613 nm, and 760 nm, respectively. All measurements were conducted at room temperature.

Structure Determination. X-ray intensity data were collected at for all samples at 296(2) K using a Bruker SMART APEX diffractometer (Mo Kα radiation, λ= 0.71073 Å).[13] The raw area detector data frames were reduced and corrected for absorption effects using the SAINT+ and SADABS programs.[13] The initial structural model was obtained by direct methods using SHELXS.[14] Subsequent difference Fourier calculations and full-matrix least-squares refinement against F^2 were performed with SHELXL-2013/4[2] using the ShelXle interface.[15]

Compounds in the series $Na_5RE_4(SiO_4)_4OH$ crystallize in the tetragonal system. The pattern of systematic absences in the intensity data indicated only body-centering lattice symmetry, leaving the space groups $I4$, $I\text{-}4$ and $I4/m$. The non-centrosymmetric group $I\text{-}4$ (No. 82) was established as correct by structure solution. This space group choice was checked with the ADDSYM program in PLATON, which found no missed symmetry.[16] The asymmetric unit consists of four metal atom positions (one rare earth, one silicon and two sodium atoms) and five oxygen atom positions. All atoms occupy positions of general crystallographic symmetry (Wyckoff position 8g) except atoms Na(2) and O(5). Na(2) is located at position 4f, on a two-fold axis of rotation. O(5) is

140

located at position 2*c* with -4 site symmetry. Sodium atom Na(2), located on a two-fold axis, is 0.4 Å from the nearby fourfold inversion axis at 0,½,¾, and is disordered over two sites by the -4 axis. The maximum chemical site occupancy of Na(2) is therefore 0.5. All atoms were refined with anisotropic displacement parameters. Trial refinements of the site occupancy factors of the rare earth site and Na1 showed no significant deviations from full occupancy. The compound is assumed to be a hydroxide to preserve crystal electroneutrality. A reliable position for the hydroxy proton could not be located by difference synthesis and was not calculated. It is likely disordered about oxygen atom O(5). Refinement of the Na(2) site occupation factor resulted in small decrease from full occupancy (0.5), to 0.45(1), but with no change in the R1/wR2 values. No significant decrease in the site occupation factor for the associated hydroxide oxygen O(5) was observed. For this reason the Na(2) site was kept at full occupancy to maintain change balance.

$Na_2YbSiO_4(OH)$ and $Na_2ScSiO_4(OH)$ crystallize in the polar space group *Pca*2$_1$ (No. 29) as determined by the pattern of systematic absences in the intensity data and by structure solution. The final structural models were checked for missed symmetry elements using the ADDSYM program in PLATON,[16] which found none. All atoms were refined with anisotropic displacement parameters. The two unique hydrogen (hydroxyl) atoms necessary for crystal electroneutrality again could not be reliably located or refined, but are presumably bonded to the two unique non-silicate oxygen atoms O9 and O10. For $Na_2YbSiO_4(OH)$, A soft restraint (SHELX ISOR instruction) was applied to the displacement parameters of one oxygen atom (O3) to prevent an oblate ellipsoid shape. The reason for this is not clear, but may be due to minor positional disorder of the silicate

141

group {Si1/O1-O4} around the Si1-O4 bond, as the displacement ellipsoids for O1 and O2 are also slightly oblate. The absolute structure (Flack) parameters near convergence refined to 0.49(10) and 0.41(2) for $Na_2YbSiO_4(OH)$ and $Na_2ScSiO_4(OH)$, respectively, indicating the data crystals were two-component inversion twins. An inversion twin law was included in the final refinement cycles.

Relevant crystallographic information from the single-crystal structure refinements is compiled in Tables 4.1 and 4.2 with atomic positions for the title compounds given in Tables 4.3-4.14.

RESULTS AND DISCUSSION

Synthesis. The conditions necessary to synthesize pure samples of these oxyhydroxides varied significantly with respect to the constituent rare earth. Most of the $Na_5RE_4(SiO_4)_4OH$ series was able to be synthesized as a pure sample with a fairly simple reaction profile. For $Na_5Tb_4(SiO_4)_4OH$, however, it was necessary to increase the dwell time significantly. This is most likely due to the use of Tb_4O_7 as a terbium source. For RE = Eu, Gd, Sm, it was necessary to react with a sodium hydroflux to prevent formation of $Gd(OH)_3$ as a secondary phase. The Pr analogue was synthesized with the same reaction profile as the later rare earths, unlike Eu, Gd, and Sm. This may be due to the use of the soluble nitrate salt as a precursor. For $Na_2YbSiO_4(OH)$, a pure product was only able to be synthesized when quenched between 230–200 ºC. If allowed to cool slowly, $Na_2YbSiO_4(OH)$ dissolves completely and $YbO(OH)$ is formed instead. Crystals $Na_2YbSiO_4(OH)$ formed as clustered twins unless WO_3 was used as a mineralizer. $Na_5Yb_4(SiO_4)_4OH$ appears to form only under specific conditions as a minor polycrystalline product and always in conjunction with $Na_2YbSiO_4(OH)$ and its structure

142

has not been refined for this investigation. A lutetium analogue was not synthesized during these experiments. Highly twinned crystals of $Lu(OH)_3$ were the only product observed under reaction conditions analogous to those detailed in this report.

Structures. The $Na_5RE_4(SiO_4)_4OH$ structure has been described previously.[17,18] Isolated SiO_4 tetrahedra edge and corner share oxygens with nearly square antiprismatic REO_8 polyhedra (Figure 4.1). At the center of four face-shared REO_8 polyhedra arranged in a square is a disordered hydroxyl group. These face-shared shared polyhedra are corner-shared to eight other such units in the ab plane and separated from each other in the c axis by SiO_4 tetrahedra. This creates chains of O(2) atoms and disordered Na(2) down the c axis (Figure 4.2). Na(1) atoms are coordinated to seven oxygens in a distorted pentagonal bypyramidal environment. These polyhedra share edges to four other NaO_7 polyhedra in what can be described as a tetrahedral ladder down the c axis.

The $Na_2RESiO_4(OH)$ structure, to the best of our knowledge, crystallizes in a new structure type. Although there are related stoichiometries previously published, they do not adopt the same crystal structure. Examples of compounds related by stoichiometry, but exhibiting different structure types include $Na_2ScGeO_4(OH)$,[19] $Li_2LuSiO_4(OH)$,[20] and $Na_2LaSiO_4(OH)$.[21] This crystal structure can be described as being comprised of chains of REO_6 octahedra separated by isolated SiO_4 tetrahedra with sodium atoms filling the interstices (Figure 4.3). Each REO_6 octahedron is distorted, with $RE1$ being displaced toward O2 and O4 and $RE2$ being displaced toward O5 and O8 from the center of the idealized octahedron. Each REO_6 octahedron corner shares with two other octahedra through O9 and O10 to form the chains that propagate down the b axis (Figure 4.4)

143

Results from these experiments suggest a cutoff for each structure based on the ionic radii and, therefore, the preference for the coordination environments of each structure (8-coordinate polyhedra for the $Na_5RE_4(SiO_4)_4OH$ structure and 6 coordinate for the $Na_2RESiO_4(OH)$ structure). For comparison, the two stoichiometries can be conceptualized as members of a series of composition $(NaRESiO_4) \bullet xNaOH$ with $x = 0.25$ and 1, respectively. Although it cannot be explicitly determined from this investigation that these radius cutoffs are absolute for the structures, the formation or lack thereof for the rare earth analogues of each structure suggest that rare earth elements smaller than ytterbium cannot form the $Na_5RE_4(SiO_4)_4OH$ structure and instead adopt the $Na_2RESiO_4(OH)$. Ytterbium appears to be able to take on both structures under specific conditions. Cerium and lanthanum appear to be too large to form the $Na_5RE_4(SiO_4)_4OH$ structure, as experiments with those elements only yielded hexagonal crystals of $La_{9.33}(SiO_4)_6O_2$.[22] Rare earths that favor a six-coordinate environment under the experimental conditions studied incorporate a larger fraction of NaOH and crystallize in the $Na_2RESiO_4(OH)$ structure while rare earths that can take on an eight-coordinate environment incorporate less NaOH and adopt the $Na_5RE_4(SiO_4)_4OH$ structure. (Figure 4.5)

The vastly different crystal structures observed for the two synthesized crystal structure types suggests that there is a small range of existence for the $Na_2RESiO_4(OH)$ structure type. It is unclear at this point why this cut off is observed. In previous studies, our group has observed similar radius-dependent structural relations in the $LiLnO_2$ series, with Nd and Sm exhibiting preference for 7-coordinate environments and Eu, Gd, and Dy taking on 6-coordinate environment.[23] This suggests that it may be possible to form other

144

analogues of this structure type, though it may be necessary to pursue a different synthetic technique to achieve this.

Magnetism. The temperature dependence of the magnetic susceptibilities (χ) were measured under zfc and fc conditions. Preliminary magnetic data are presented as χ_m vs. T and $1/\chi_m$ vs. T plots (Figures 4.6-4.16). The effective moment per RE^{3+} was calculated by the formula $\mu_{eff} = (7.977\chi_m T)^{1/2}$ using the molar susceptibility at 300 K. The observed moments for the $Na_5RE_4(SiO_4)_4OH$ series compare well to the expected values and are presented in Table 4.15. The data show slightly high values for most of the compositions. The source of the high values of effective moment are unclear at this moment. Possible explanations include instrumental error, error in measured masses, and RE^{3+}-rich impurities (e.g. $RE(OH)_3$, RE_2O_3, etc.) undetected by powder diffraction, which has an approximate detection limit of 5%. No long-range magnetic ordering was observed for any of the samples.

The Eu analogue exhibits Van Vleck paramagnetism, also known as temperature independent paramagnetism (TIP), below ~100 K. (Figure 4.16) Below ~45 K, there is a positive deviation from the expected behavior. Previous studies have attributed similar increases in the low temperature susceptibility in Eu^{3+} compounds to small amounts of Eu^{2+}, which has strong Curie-like behavior at low temperatures.[24] This assignment cannot be ruled out without further investigations of the valence state of Eu, although crystallographic data indicated no significant deviation from the assigned occupancies for any atomic positions. The crystals are colorless, giving no indication of mixed-valence. Further investigations into the valence of the Eu ions are needed to clarify this nuance in the data.

145

Luminescence. The terbium, europium, and gadolinium analogues of the Na$_5$*RE*$_4$(SiO$_4$)$_4$OH structure luminesce in the visible region under UV excitation. The terbium and europium analogues both show sharp emission lines intrinsic to their respective element and emit bright green and red light, respectively, under UV excitation (Figure 4.17 and 4.18). The gadolinium analogue, however, exhibits less intense luminescence, with a weak, broad peak centered at 760 nm and a shoulder extending into the ultraviolet region (Figure 4.19). The color and relative intensity of the luminescence of each compound can be seen in Figure 4.20. A previous report of the analogous fluoride of the gadolinium composition states that undoped Na$_5$Gd$_4$(SiO$_4$)$_4$F exhibited no intrinsic luminescent properties.[25] It is not uncommon for oxyfluorides to display significant deviations from the luminescence properties of the corresponding oxides and it appears that may be the case with these hydroxides, as well. A previous report indicates that Na$_5$Gd$_4$(SiO$_4$)$_4$OH exhibits second harmonic generation (SHG).[26] Future studies could include the investigation of these compounds for their SHG properties.

CONCLUSION

A number of oxyhydroxides have been grown from a low temperature hydroflux method. The two distinctly different structure types appear to be directly related to the ionic radius and preferred coordination environment of the rare earth. Larger rare earths (Pr-Tm, Y) adopt the Na$_5$*RE*$_4$(SiO$_4$)$_4$OH structure with space group *I*-4. Smaller rare earths (Yb & Sc) adopt a new structure type with composition Na$_2$*RE*SiO$_4$(OH) which crystallizes in the polar space group *Pca*2$_1$. Na$_5$Eu$_4$(SiO$_4$)$_4$OH , Na$_5$Gd$_4$(SiO$_4$)$_4$OH , and Na$_5$Tb$_4$(SiO$_4$)$_4$OH are luminescent and their properties have been investigated. Future studies could probe the capability of these compounds for SHG There is no indication of

long range magnetic ordering for any of the compounds presented in this chapter from our preliminary investigation. Low temperature paramagnetism exhibited by $Na_5Eu_4(SiO_4)_4OH$ suggests there may be Eu^{2+} present in the crystals. More studies will be necessary to confirm the origin of this.
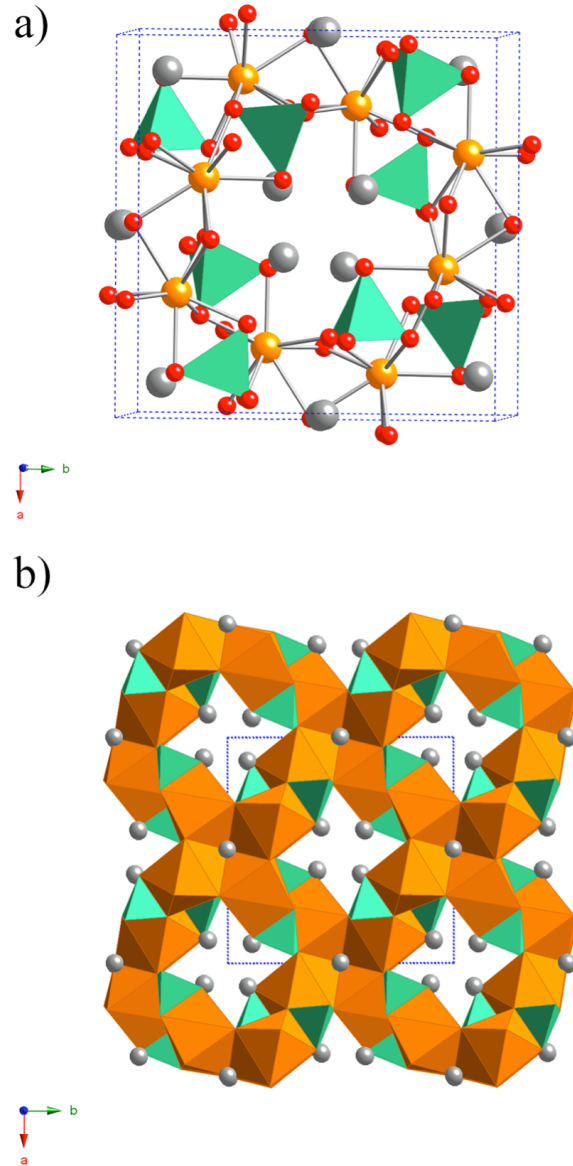
Figure 4.1. a) Polyhedral representation of the unit cell of $Na_5Tb_4(SiO_4)_4OH$, with terbium atoms shown in orange, silicon tetrahedra in turquoise, sodium atoms in grey, and oxygen atoms shown in red. b) Extended polyhedral representation displaying the interconnectivity of the rare earth and silicon environments with terbium polyhedra shown in orange, silicon tetrahedra in turquoise, sodium atoms in grey, and oxygen atoms omitted for clarity.

148
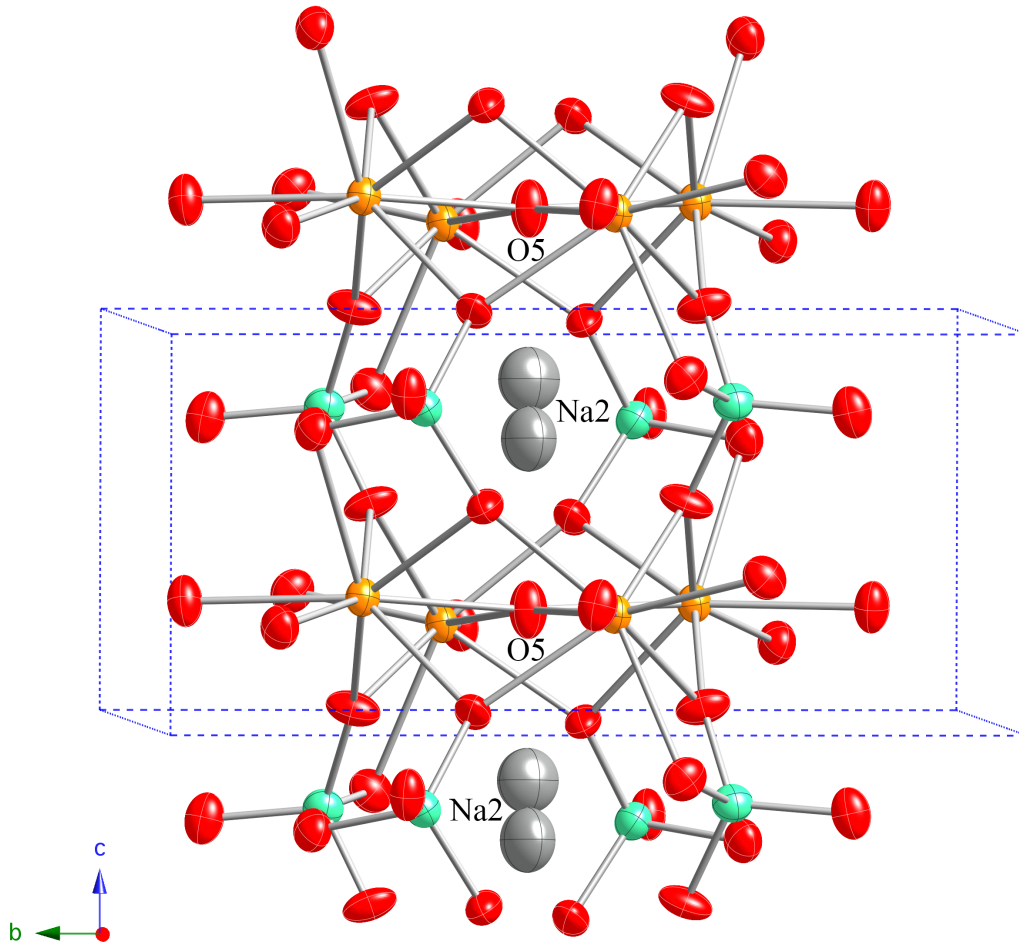
Figure 4.2. Surrounding environment of the disordered Na2 atoms and O5, the presumed hydroxyl oxygen, in $Na_5Tb_4(SiO_4)_4OH$ with terbium atoms shown in orange, silicon atoms in turquoise, and oxygen atoms shown in red. Thermal ellipsoids are drawn to 90% probability.

149
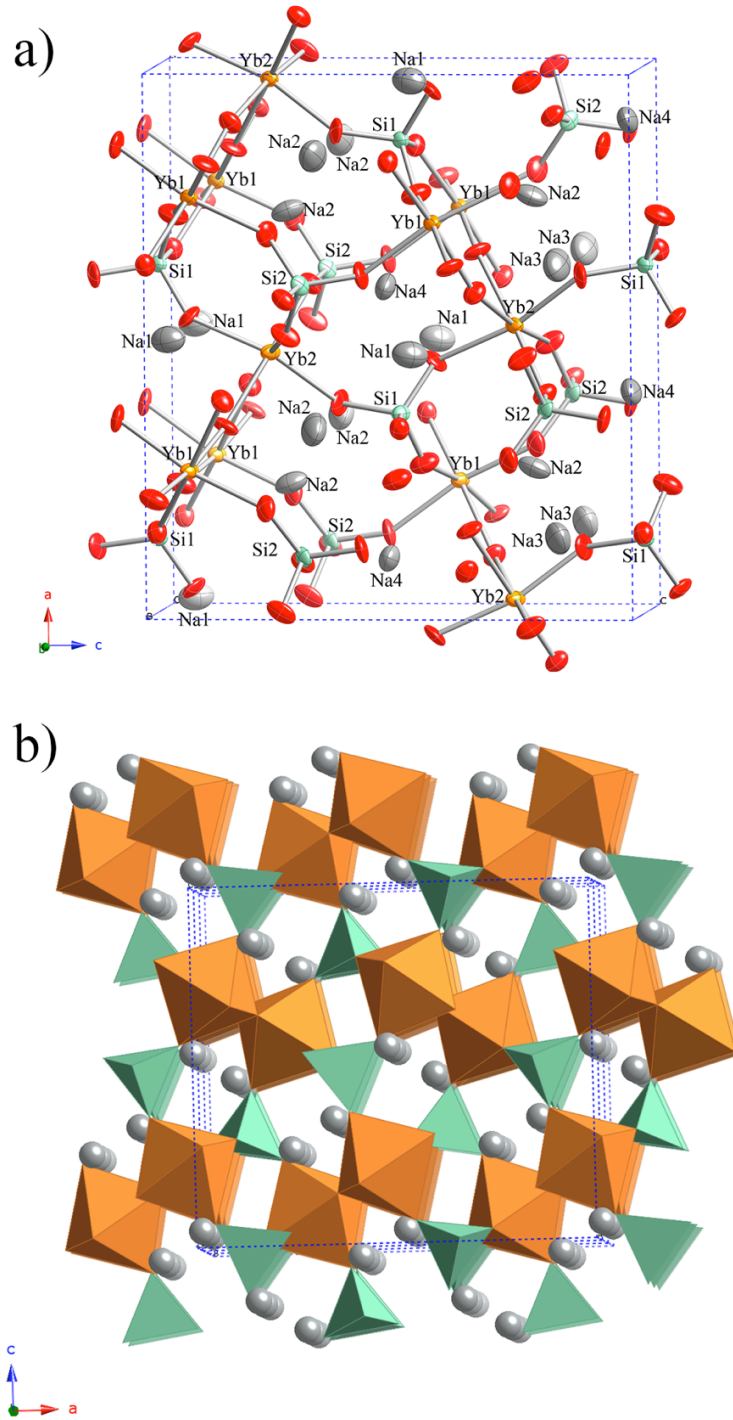
Figure 4.3. a) Unit cell of $Na_2YbSiO_4(OH)$ with thermal ellipsoids drawn at 95% probability and metal atoms labeled. B) Polyhedral view of the unit cell of $Na_2YbSiO_4(OH)$ with YbO_6 polyhedra drawn in orange, SiO_4 tetrahedra shown in turquoise, and Na atoms shown in grey. Oxygen atoms are omitted for clarity.
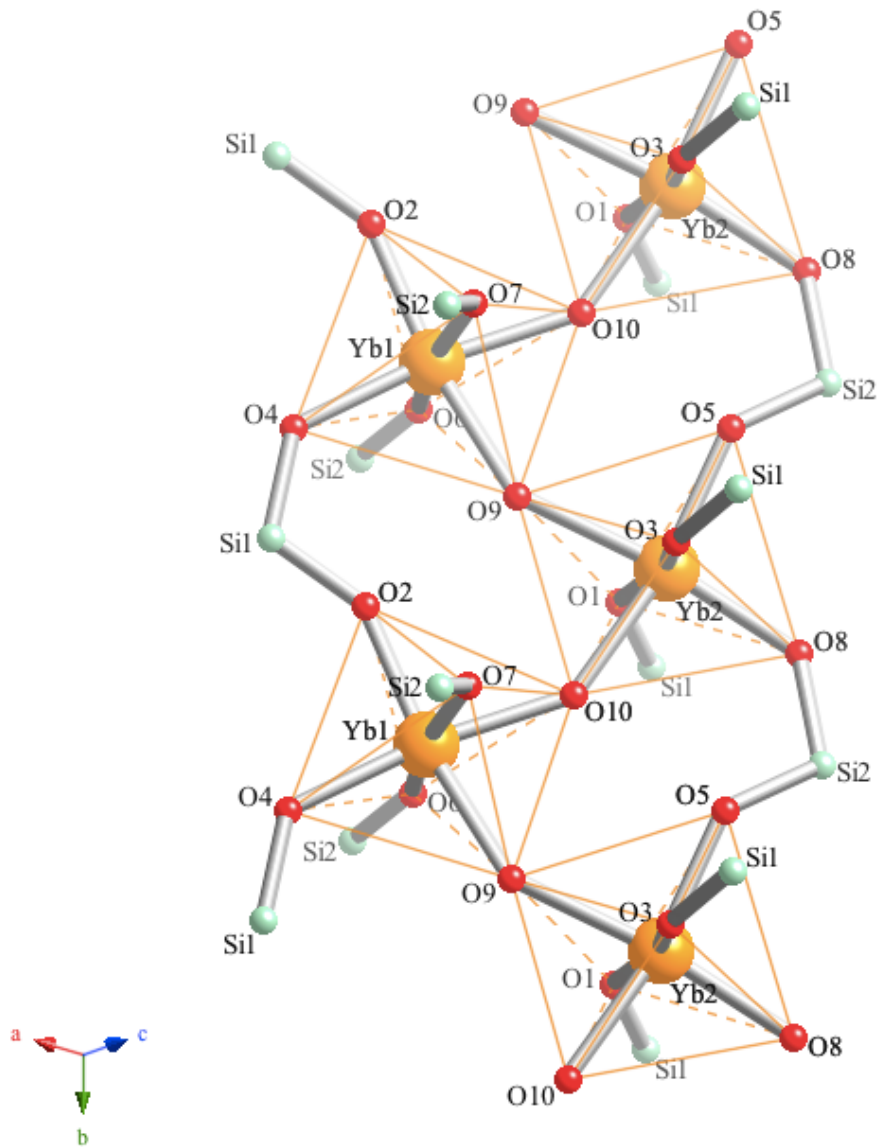
Figure 4.4. Interconnectivities between YbO$_6$ polyhedra within a chain and to the surrounding silicon atoms.
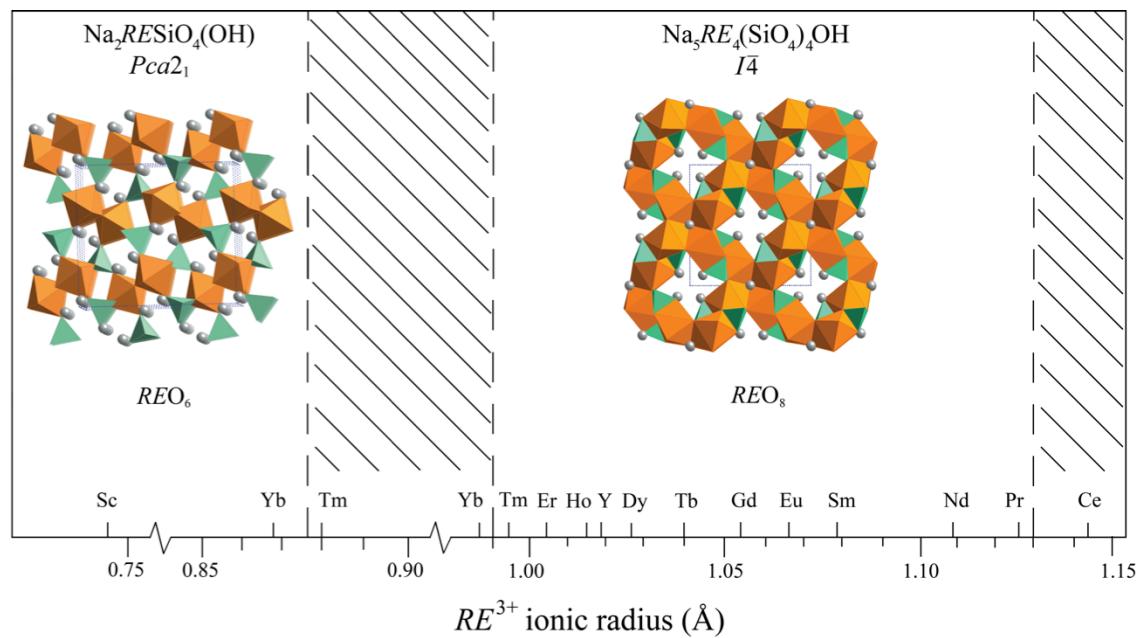
Figure 4.5. Graphic relating the observed phases to rare earth ionic radii and coordination environments. Shaded regions indicate regions where no analogue could be crystallized.
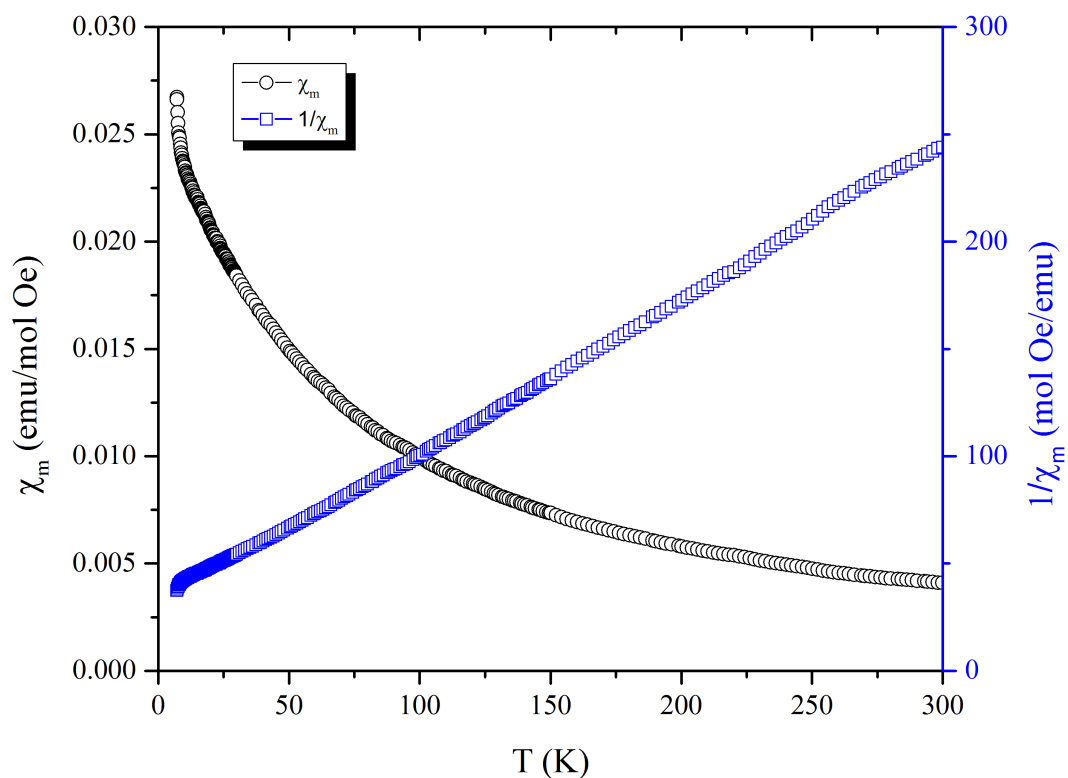
Figure 4.6. Temperature dependence of the molar magnetic susceptibility, χ_m, and inverse molar magnetic susceptibility, $1/\chi_m$ for for $Na_5Pr_4(SiO_4)_4OH$.

153
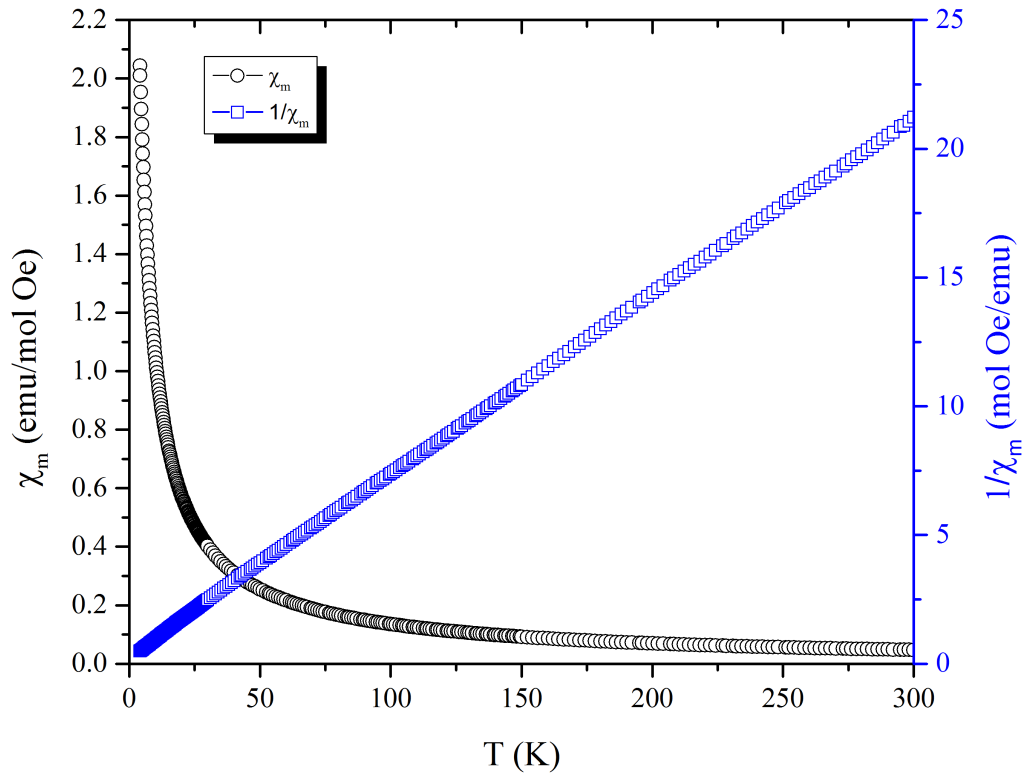
Figure 4.7. Temperature dependence of the molar magnetic susceptibility, χ_m, and inverse molar magnetic susceptibility, $1/\chi_m$ for $Na_5Nd_4(SiO_4)_4OH$.
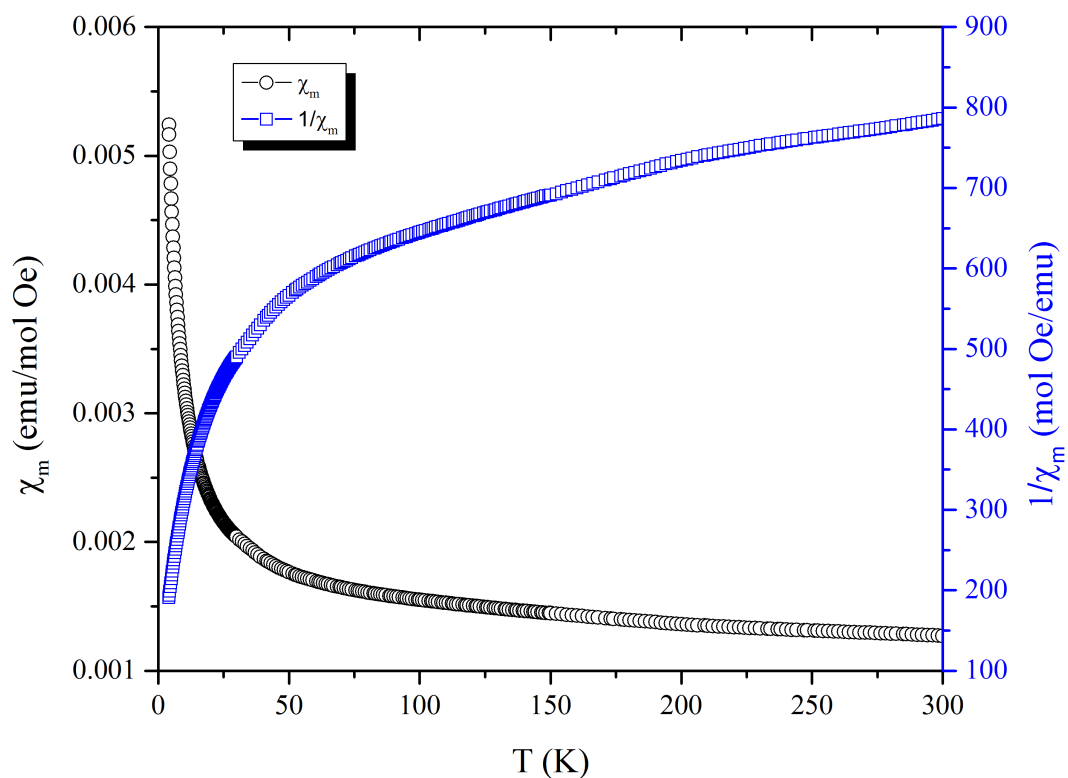
Figure 4.8. Temperature dependence of the molar magnetic susceptibility, χ_m, and inverse molar magnetic susceptibility, $1/\chi_m$ for $Na_5Sm_4(SiO_4)_4OH$.

155
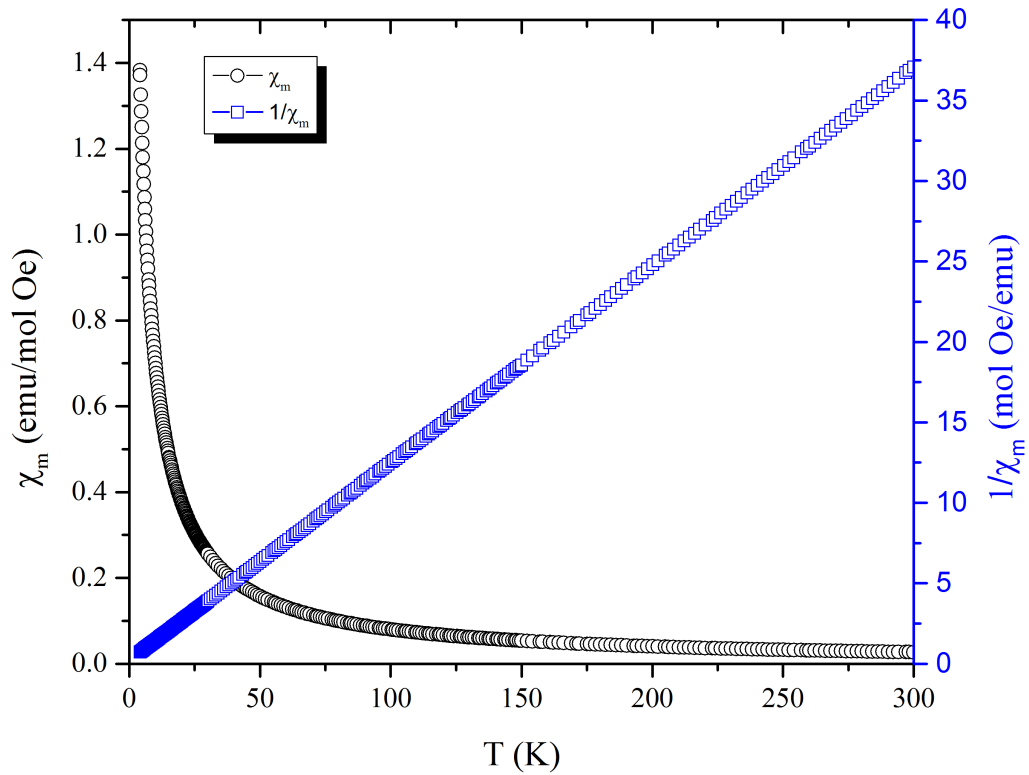
Figure 4.9. Temperature dependence of the molar magnetic susceptibility, χ_m, and inverse molar magnetic susceptibility, $1/\chi_m$ for $Na_5Gd_4(SiO_4)_4OH$.
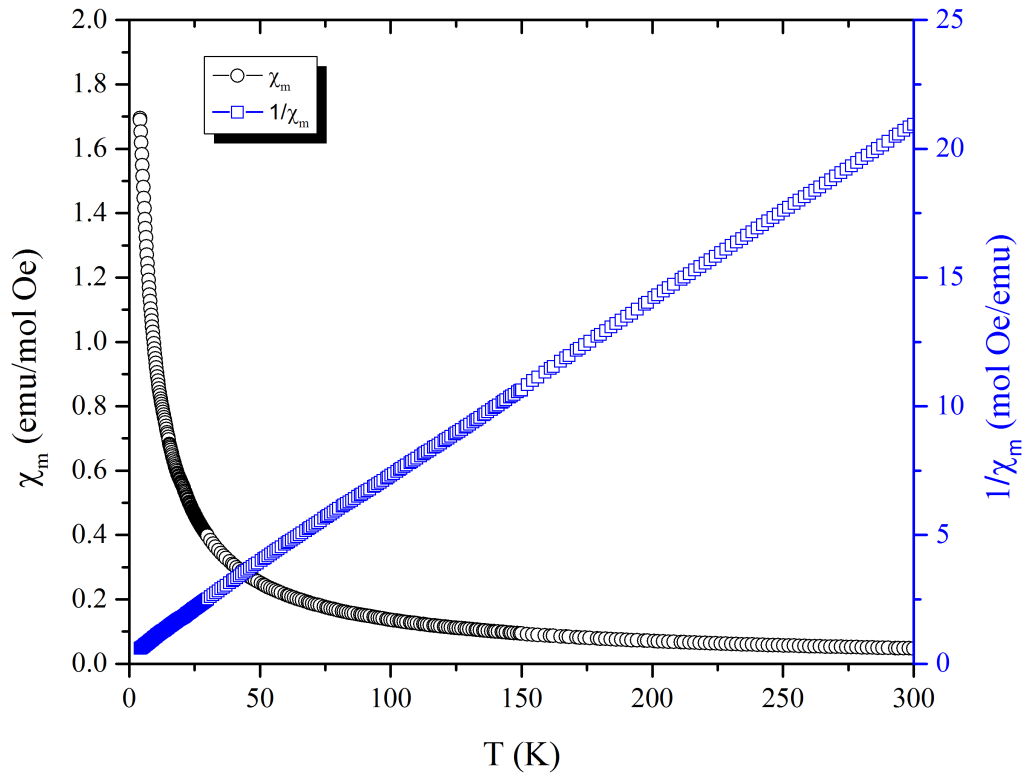
Figure 4.10. Temperature dependence of the molar magnetic susceptibility, χ_m, and inverse molar magnetic susceptibility, $1/\chi_m$ for $Na_5Tb_4(SiO_4)_4OH$.

157
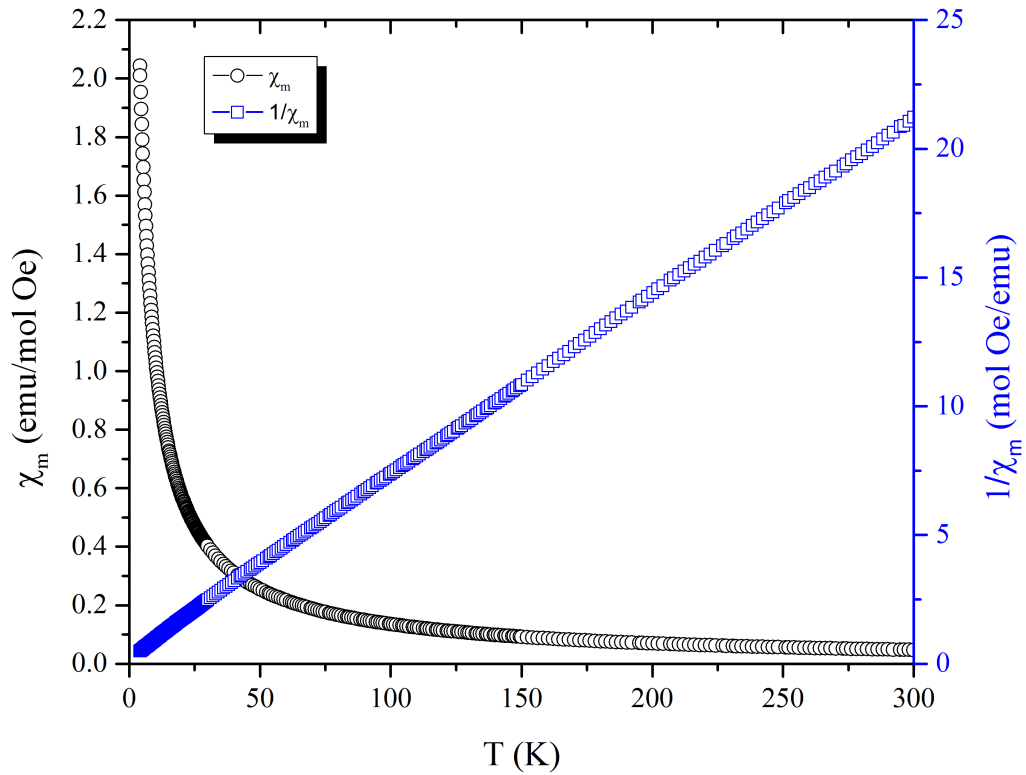
Figure 4.11. Temperature dependence of the molar magnetic susceptibility, χ_m, and inverse molar magnetic susceptibility, $1/\chi_m$ for $Na_5Dy_4(SiO_4)_4OH$.
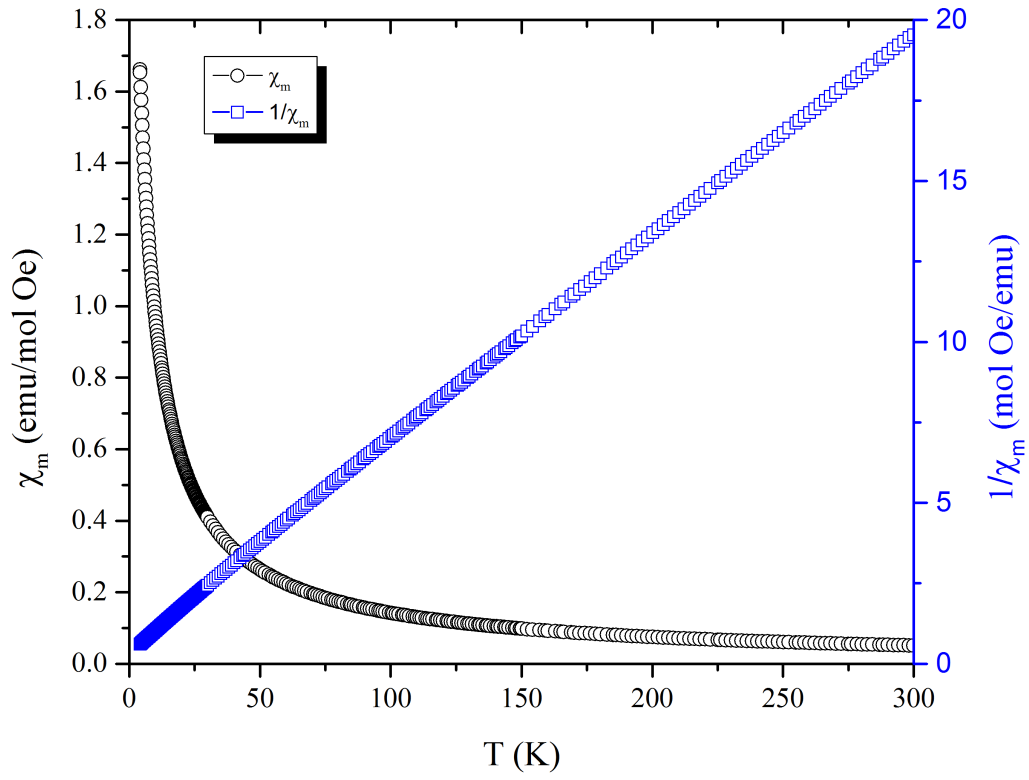
Figure 4.12. Temperature dependence of the molar magnetic susceptibility, χ_m, and inverse molar magnetic susceptibility, $1/\chi_m$ for $Na_5Ho_4(SiO_4)_4OH$.

159
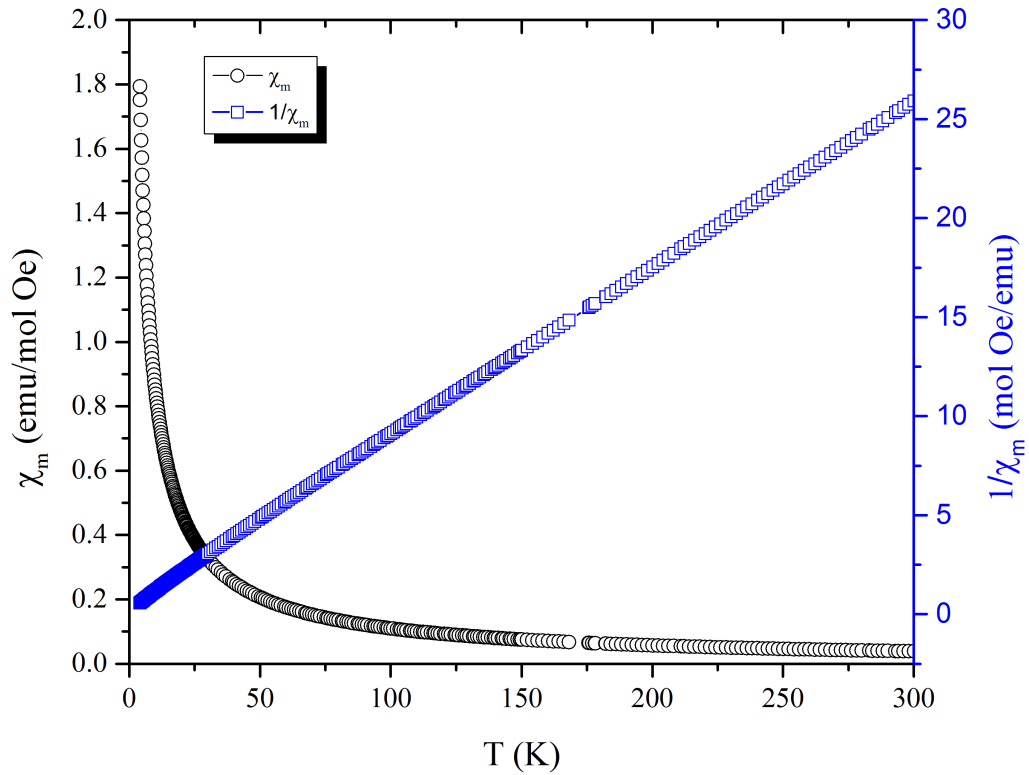
Figure 4.13. Temperature dependence of the molar magnetic susceptibility, χ_m, and inverse molar magnetic susceptibility, $1/\chi_m$ for $Na_5Er_4(SiO_4)_4OH$.
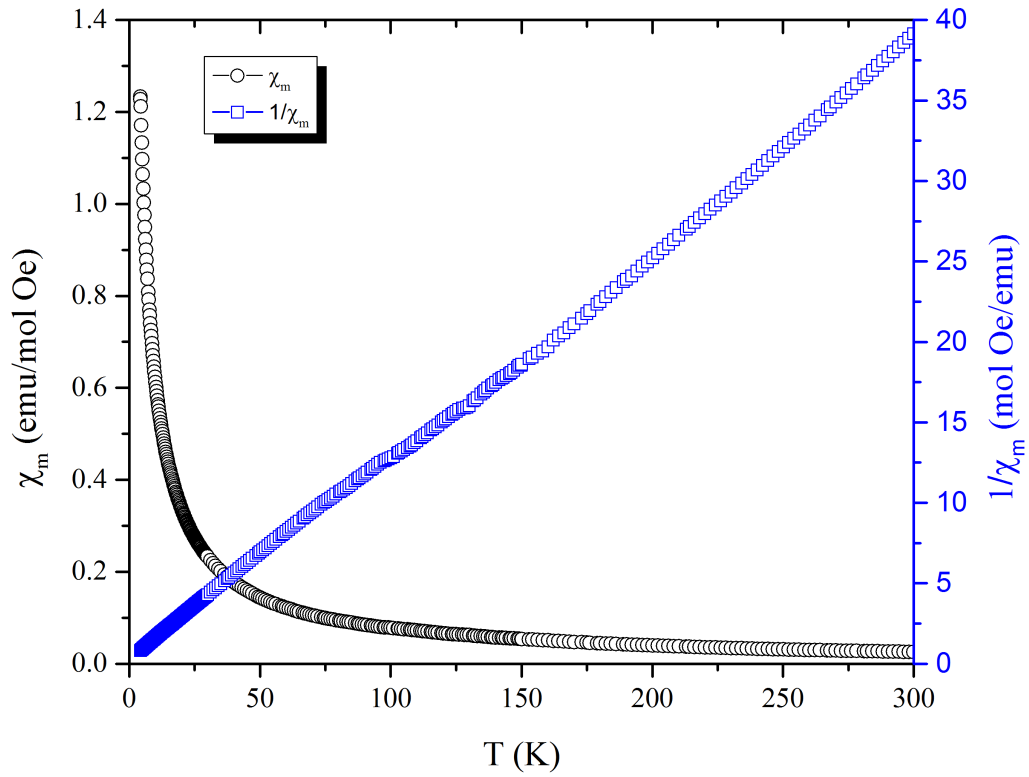
Figure 4.14. Temperature dependence of the molar magnetic susceptibility, χ_m, and inverse molar magnetic susceptibility, $1/\chi_m$ for $Na_5Tm_4(SiO_4)_4OH$.

161
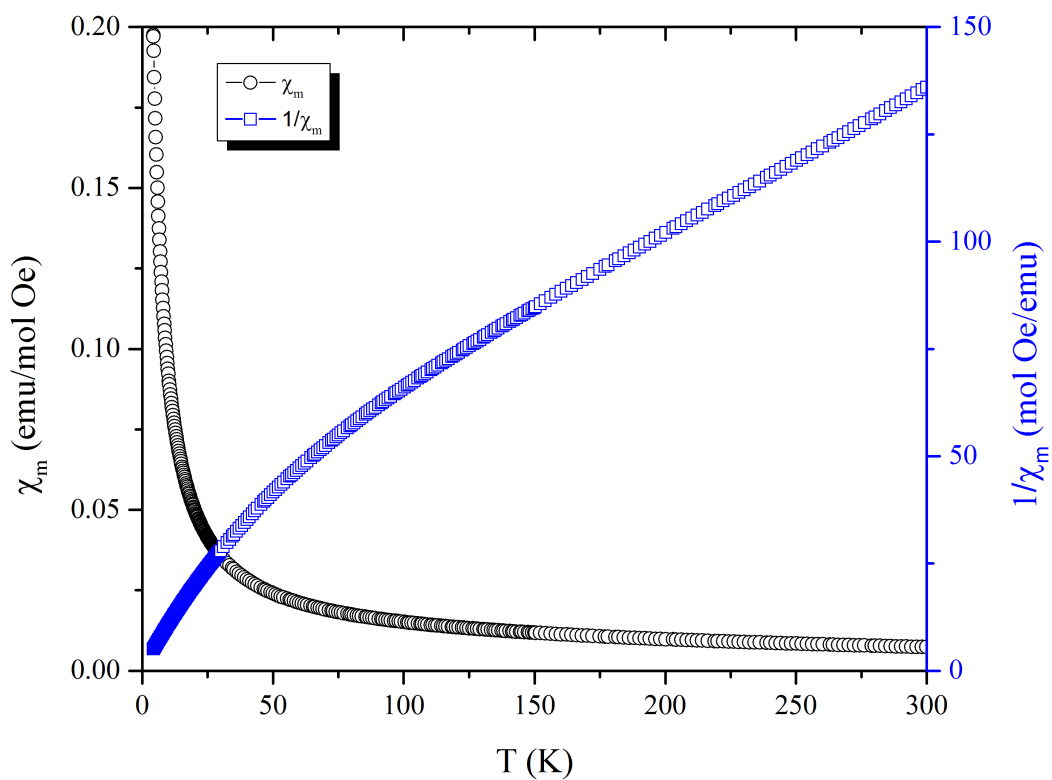
Figure 4.15. Temperature dependence of the molar magnetic susceptibility, χ_m, and inverse molar magnetic susceptibility, $1/\chi_m$ for $Na_2YbSiO_4(OH)$.

162
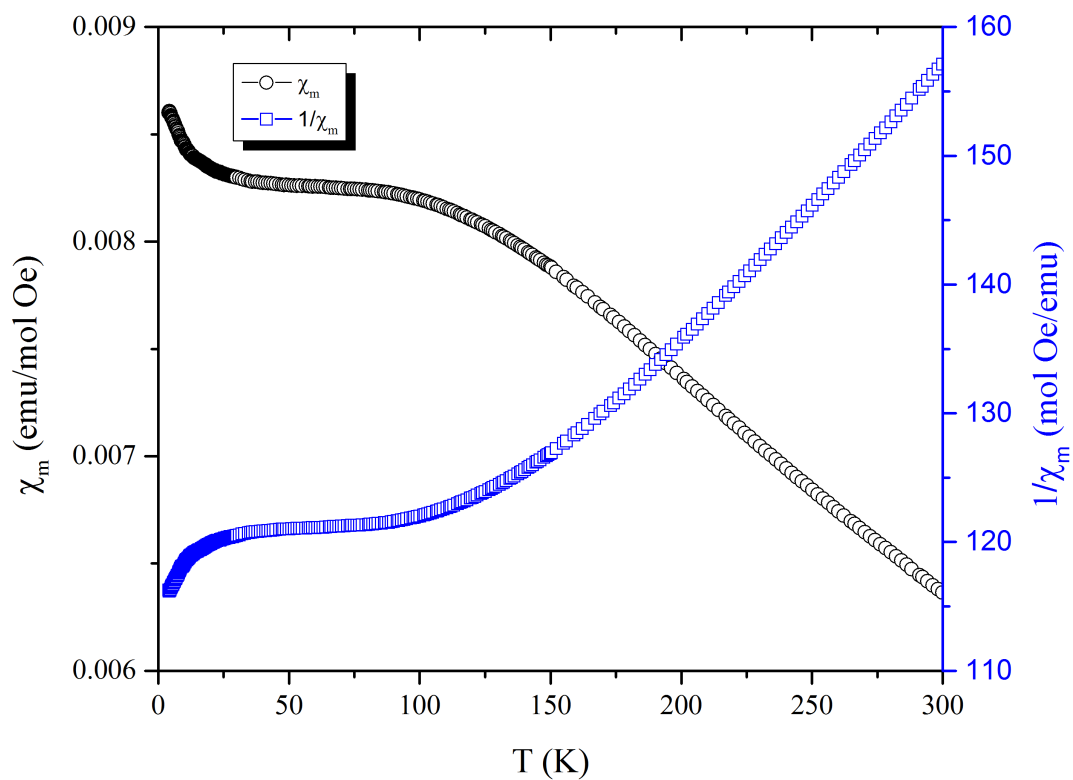
Figure 4.16. Magnetic susceptibility plot for $Na_5Eu_4(SiO_4)_4OH$ displaying Van Vleck paramagnetism with low temperature deviation.
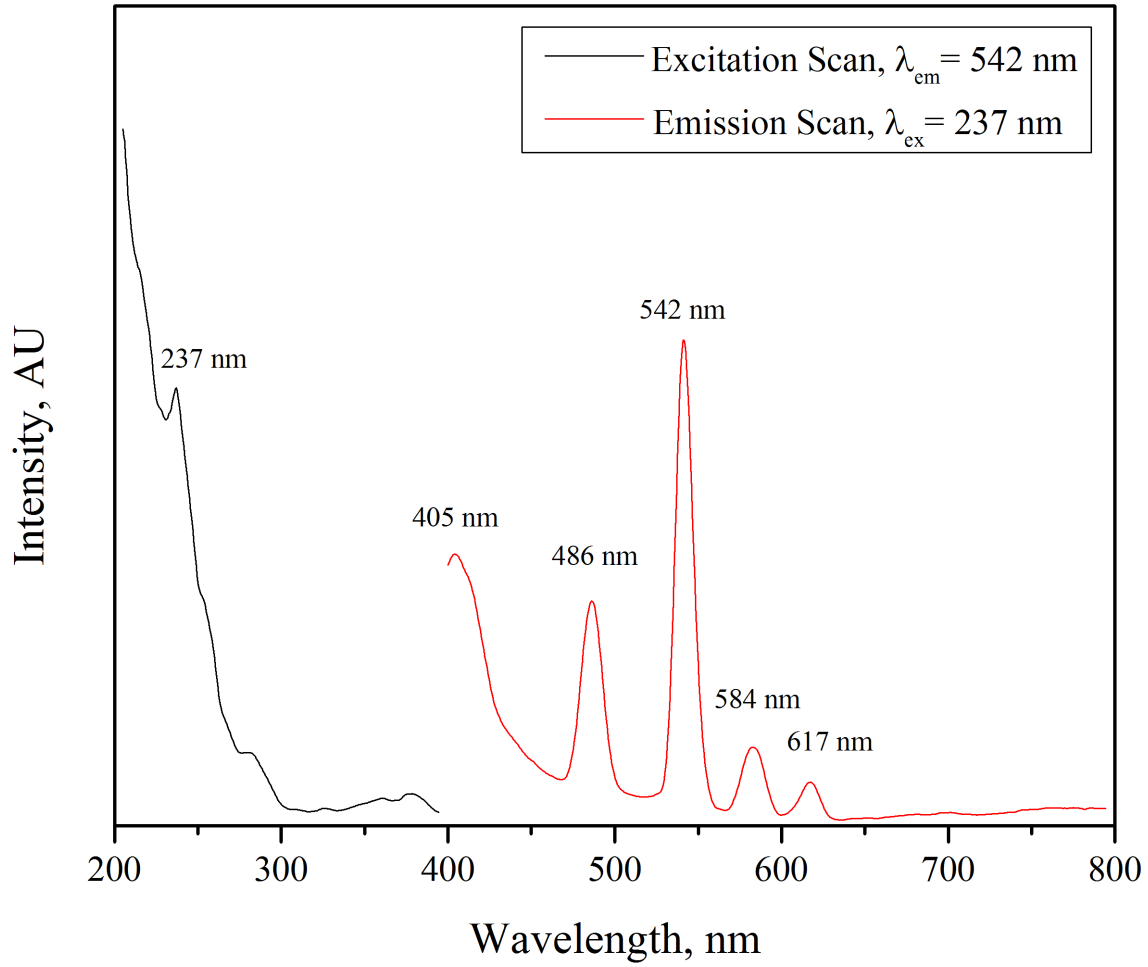
Figure 4.17. Room temperature luminescence spectra of $Na_5Tb_4(SiO_4)_4OH$.
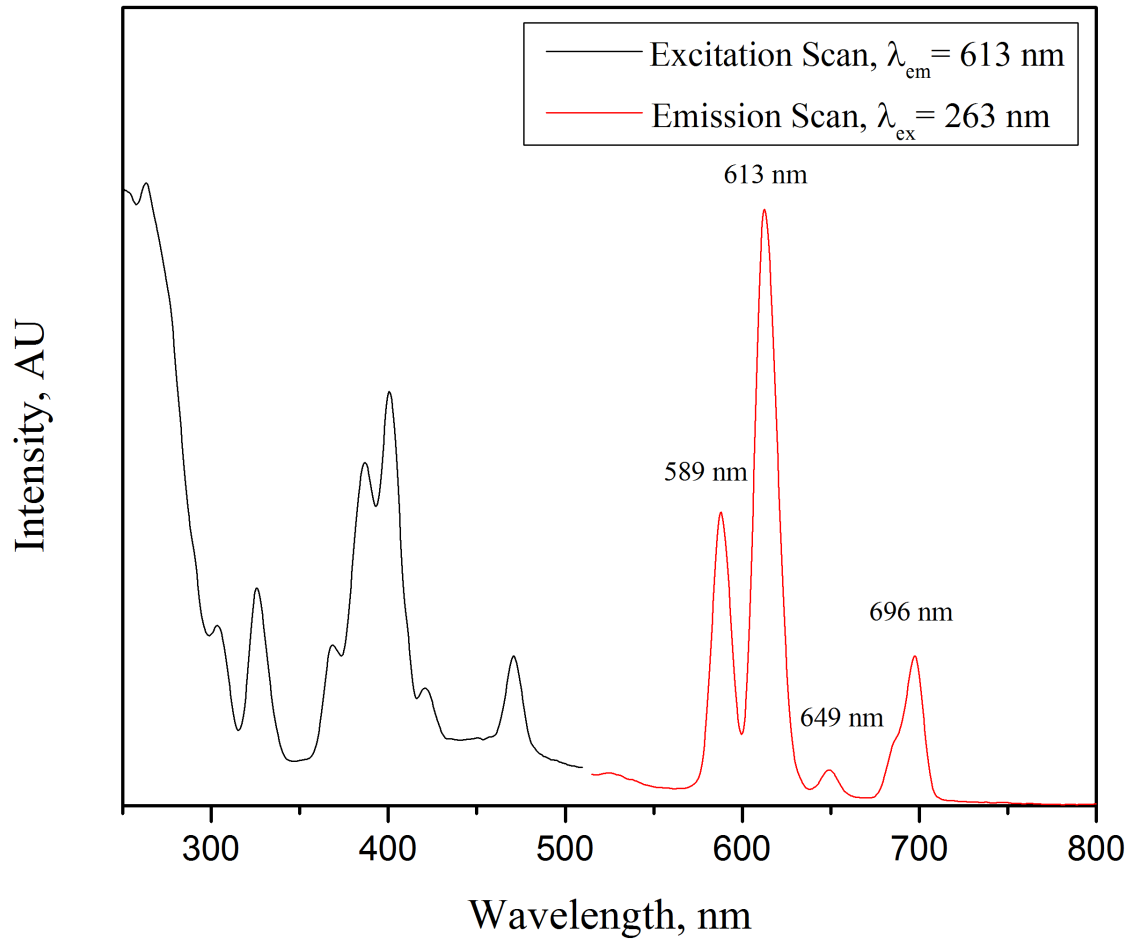
Figure 4.18. Room temperature luminescence spectra of $Na_5Eu_4(SiO_4)_4OH$.
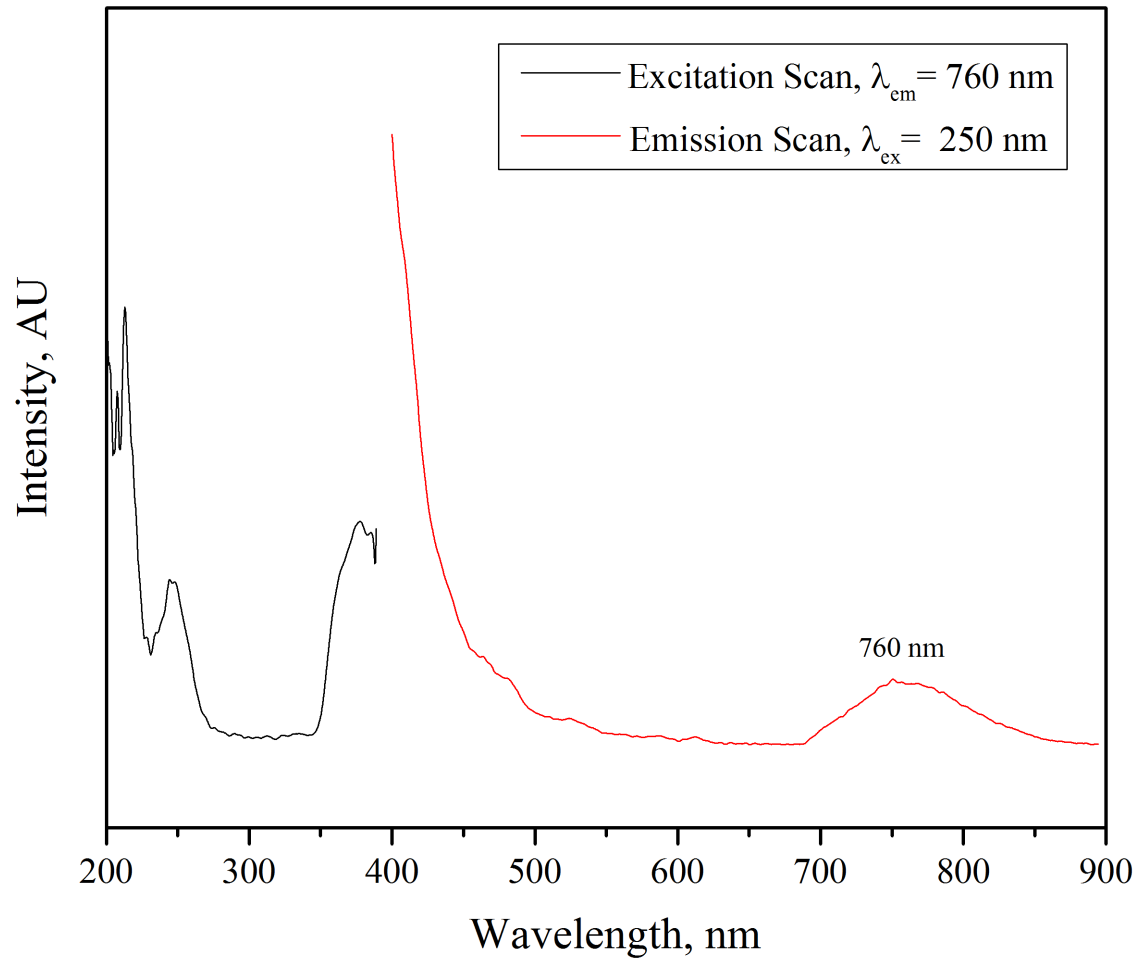
Figure 4.19. Room temperature luminescence spectra of $Na_5Gd_4(SiO_4)_4OH$.
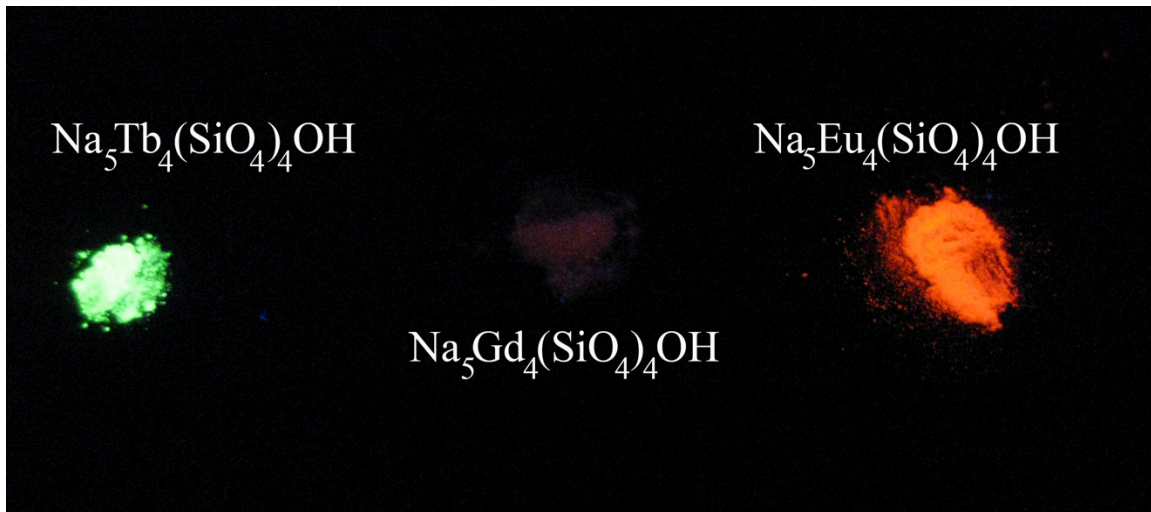
Figure 4.20. Side-by-side comparison of the room temperature luminescence of Na$_5$Tb$_4$(SiO$_4$)$_4$OH, Na$_5$Gd$_4$(SiO$_4$)$_4$OH, and Na$_5$Eu$_4$(SiO$_4$)$_4$OH.

Table 4.1. Crystallographic Data for $Na_5RE_4(SiO_4)_4OH$ (RE = Pr, Nd, Sm, Eu)[a]

Compound	$Na_5Pr_4(SiO_4)_4OH$	$Na_5Nd_4(SiO_4)_4OH$	$Na_5Sm_4(SiO_4)_4OH$	$Na_5Eu_4(SiO_4)_4OH$
formula weight (g/mol)	1063.96	1077.28	1101.72	1108.16
color and habit	light green, cube	light blue, cube	colorless, fragment	colorless, square plate
a (Å)	12.0588(3)	11.9726(3)	11.8467(14)	11.7872(2)
c (Å)	5.4668(2)	5.4824(2)	5.4846(13)	5.4813(2)
V (Å^3)	794.95(5)	785.86(5)	769.7(3)	761.56(4)
ρ_c (g cm^{-3})	4.445	4.553	4.753	4.833
μ (mm^{-1})	12.573	13.532	15.583	16.801
$F(000)$	968	976	992	1000
crystal size (μm^3)	80 x 80 x 60	60 x 60 x 50	50 x 40 x 40	70 x 60 x 40
θ_{max} (°)	36.276	36.293	36.255	36.322
index ranges	-20<=h<=18, -17<=k<=19, -9<=l<=8	-19<=h<=19, -19<=k<=17, -8<=l<=9	-19<=h<=19, -17<=k<=19, -9<=l<=8	-19<=h<=18, -19<=k<=18, -8<=l<=9

reflections collected	9092	12490	8856	11811
independent reflections	1852	1888	1811	1849
goodness-of-fit on F^2	1.039	1.086	1.042	1.059
R indices (all data)	R1 = 0.0328 wR2 = 0.0679	R1 = 0.0200 wR2 = 0.0454	R1 = 0.0372 wR2 = 0.0602	R1 = 0.0245, wR2 = 0.0488
largest peak and diffraction hole (e$^-$ Å^{-3})	1.987/-1.217	2.250/-0.790	1.641/-1.247	1.556/-0.914

[a] For all structures, T = 296(2) K, λ = 0.71073 Å, the space group is I-4, and Z = 2.

Table 4.1. continued Crystallographic Data for $Na_5RE_4(SiO_4)_4OH$ (RE = Tb, Dy, Ho)[a]

Compound	$Na_5Tb_4(SiO_4)_4OH$	$Na_5Dy_4(SiO_4)_4OH$	$Na_5Ho_4(SiO_4)_4OH$
formula weight (g/mol)	1136.00	1150.32	1160.04
color and habit	colorless, square block	light yellow, fragment	light pink, square plate
a (Å)	11.6845(7)	11.6435(3)	11.6002(3)
c (Å)	5.4574(6)	5.4322(3)	5.4231(3)
V (Å^3)	745.09(12)	736.45(5)	729.76(5)
ρ_c (g cm^{-3})	5.064	5.187	5.279
μ (mm^{-1})	19.319	20.632	22.027
$F(000)$	1016	1024	1032
crystal size (μm^3)	60 x 60 x 40	18 x 12 x 6	12 x 10 x 4
θ_{max} (°)	38.573	36.29	36.38
index ranges	-20<=h<=20, -20<=k<=20, -9<=l<=8	-16<=h<=19, -17<=k<=18, -8<=l<=9	-17<=h<=17, -17<=k<=19, -9<=l<=8

reflections collected	10635	8918	11389
independent reflections	2112	1693	1734
goodness-of-fit on F^2	1.031	1.091	1.104
R indices (all data)	R1 = 0.0334, wR2 = 0.0551	R1 = 0.0278, wR2 = 0.0589	R1 = 0.0254, wR2 = 0.0597
largest peak and diffraction hole (e^- $Å^{-3}$)	1.827/-1.337	2.239/-1.428	2.348/-1.398

[a] For all structures, T = 296(2) K, λ = 0.71073 Å, the space group is I-4, and Z = 2.

Table 4.1. continued Crystallographic Data for $Na_5RE_4(SiO_4)_4OH$ (RE = Er, Tm, Y)[a]

Compound	$Na_5Er_4(SiO_4)_4OH$	$Na_5Tm_4(SiO_4)_4OH$	$Na_5Y_4(SiO_4)_4OH$
formula weight (g/mol)	1169.36	1175.03	855.96
color and habit	pink, square plate	colorless, square plate	colorless, square plate
a (Å)	11.5731(3)	11.5275(4)	11.6025(4)
c (Å)	5.4107(2)	5.3951(4)	5.4264(5)
V (Å^3)	724.69(5)	716.92(7)	730.49(8)
ρ_c (g cm^{-3})	5.359	5.443	3.891
μ (mm^{-1})	23.506	25.100	16.310
$F(000)$	1040	1046	808
crystal size (μm^3)	60 x 50 x 50	40 x 40 x 20	50 x 40 x 20
θ_{max} (°)	36.281	36.344	32.812
index ranges	-19<=h<=19, -19<=k<=17, -8<=l<=8	-19<=h<=19, -18<=k<=17, -8<=l<=8	-17<=h<=17, -17<=k<=17, -8<=l<=8

reflections collected	10726	10447	8398
independent reflections	1652	1735	1365
goodness-of-fit on F^2	1.066	1.062	1.024
R indices (all data)	R1 = 0.0292, wR2 = 0.0660	R1 = 0.0320, wR2 = 0.0603	R1 = 0.0598, wR2 = 0.1049
largest peak and diffraction hole (e$^-$ Å^{-3})	2.811/-2.088	2.124/-1.248	1.106/-1.178

[a] For all structures, T = 296(2) K, λ = 0.71073 Å, the space group is I-4, and Z = 2.

Table 4.2. Crystallographic Data for $Na_2YbSiO_4(OH)$ and $Na_2ScSiO_4(OH)$

compound	$Na_2YbSiO_4(OH$	$Na_2ScSiO_4(OH$
formula weight (g/mol)	328.12	200.04
color and habit	colorless, needle	colorless, octahedron
a (Å)	13.9074(5)	13.6153(7)
b (Å)	5.5366(2)	5.4215(3)
c (Å)	12.4876(5)	12.1083(7)
V (Å^3)	961.54(6)	893.78(9)
ρ_c (g cm^{-3})	4.533	2.973
μ (mm^{-1})	19.806	2.027
$F(000)$	1176	784
crystal size (μm^3)	80 x 30 x 20	60 x 60 x 40
θ_{max} (°)	32.644	32.594
index ranges	-20<=h<=21, -8<=k<=8, -18<=l<=18	-20<=h<=20, -8<=k<=7, -18<=l<=18
reflections collected	27619	26026
independent reflections	3503	3246
goodness-of-fit on F^2	1.048	1.081
R indices (all data)	R1 = 0.0307, wR2 = 0.0527	R1 = 0.0626, wR2 = 0.1107
largest peak and diffraction hole (e$^-$ Å^{-3})	1.280/-1.114	0.969/-0.533

[a] For all structures, T = 296(2) K, λ = 0.71073 Å, the space group is $Pca2_1$, and Z = 8.

174

Table 4.3. Atomic coordinates (x 10^4) and equivalent isotropic displacement parameters ($\mathring{A}^2$x 10^3) for $Na_5Pr_4(SiO_4)_4OH$. U(eq) is defined as one third of the trace of the orthogonalized U_{ij} tensor.

	x	y	z	U(eq)
Pr(1)	1181(1)	1854(1)	4918(1)	14(1)
Si(1)	2482(1)	1003(1)	32(5)	12(1)
Na(1)	1054(2)	4110(2)	20(9)	24(1)
Na(2A)	0	0	1010(30)	24(2)
Na(2B)	0	0	0	24(2)
O(1)	0	0	5000	29(2)
O(2)	2055(7)	390(6)	2491(12)	23(1)
O(3)	1068(3)	6173(3)	44(15)	22(1)
O(4)	2008(4)	2276(3)	213(16)	21(1)
O(5)	3008(8)	4568(6)	2605(12)	24(1)

175

Table 4.4. Atomic coordinates (x 10^4) and equivalent isotropic displacement parameters (Å^2x 10^3) for $Na_5Nd_4(SiO_4)_4OH$. U(eq) is defined as one third of the trace of the orthogonalized U_{ij} tensor.

	x	y	z	U(eq)
Nd(1)	1177(1)	1851(1)	4828(1)	10(1)
Si(1)	2476(1)	1008(1)	76(2)	10(1)
Na(1)	1053(2)	4108(2)	63(5)	22(1)
Na(2)	0	0	714(14)	37(2)
O(1)	0	0	5000	23(2)
O(2)	2087(3)	359(3)	2520(6)	18(1)
O(3)	1066(2)	6165(2)	125(7)	17(1)
O(4)	2013(3)	2288(2)	441(6)	14(1)
O(5)	3063(3)	4536(3)	2653(6)	18(1)

176

Table 4.5. Atomic coordinates (x 10^4) and equivalent isotropic displacement parameters (Å^2x 10^3) for $Na_5Sm_4(SiO_4)_4OH$. U(eq) is defined as one third of the trace of the orthogonalized U_{ij} tensor.

	x	y	z	U(eq)
Sm(1)	1172(1)	1847(1)	4790(1)	9(1)
Si(1)	2474(2)	1017(2)	100(4)	10(1)
Na(1)	1048(3)	4105(2)	85(8)	22(1)
Na(2)	0	0	726(18)	30(2)
O(1)	0	0	5000	15(2)
O(2)	2087(6)	345(5)	2545(10)	16(1)
O(3)	1076(4)	6151(4)	149(11)	15(1)
O(4)	2016(4)	2318(4)	549(10)	13(1)
O(5)	3092(6)	4518(5)	2674(10)	15(1)

Table 4.6. Atomic coordinates (x 10^4) and equivalent isotropic displacement parameters ($\mathring{A}^2$x 10^3) for $Na_5Eu_4(SiO_4)_4OH$. U(eq) is defined as one third of the trace of the orthogonalized U_{ij} tensor.

	x	y	z	U(eq)
Eu(1)	1173(1)	1846(1)	4779(1)	10(1)
Si(1)	2470(1)	1019(1)	108(3)	11(1)
Na(1)	1048(2)	4109(2)	79(6)	21(1)
Na(2)	0	0	729(15)	27(2)
O(1)	0	0	5000	16(2)
O(2)	2075(4)	337(3)	2547(8)	16(1)
O(3)	1070(3)	6142(3)	144(8)	16(1)
O(4)	2019(3)	2328(3)	581(8)	14(1)
O(5)	3109(4)	4515(3)	2674(7)	15(1)

Table 4.7. Atomic coordinates (x 10^4) and equivalent isotropic displacement parameters (Å^2x 10^3) for $Na_5Tb_4(SiO_4)_4OH$. U(eq) is defined as one third of the trace of the orthogonalized U_{ij} tensor.

	x	y	z	U(eq)
Tb(1)	1166(1)	1839(1)	4768(1)	9(1)
Si(1)	2474(1)	1025(1)	114(4)	11(1)
Na(1)	1044(2)	4106(2)	84(7)	21(1)
Na(2)	0	0	741(17)	27(2)
O(1)	0	0	5000	15(2)
O(2)	2070(4)	336(4)	2558(9)	14(1)
O(3)	1083(3)	6136(3)	141(10)	13(1)
O(4)	2025(4)	2345(3)	631(9)	13(1)
O(5)	3117(4)	4512(4)	2669(8)	13(1)

179

Table 4.8. Atomic coordinates (x 10^4) and equivalent isotropic displacement parameters (Å^2x 10^3) for $Na_5Dy_4(SiO_4)_4OH$. U(eq) is defined as one third of the trace of the orthogonalized U_{ij} tensor.

	x	y	z	U(eq)
Dy(1)	1171(1)	1842(1)	4766(1)	10(1)
Si(1)	2463(1)	1025(1)	108(3)	12(1)
Na(1)	1044(2)	4106(2)	62(5)	20(1)
Na(2)	0	0	623(17)	34(2)
O(1)	0	0	5000	22(2)
O(2)	2054(4)	333(3)	2562(7)	15(1)
O(3)	1084(3)	6135(3)	120(8)	15(1)
O(4)	2018(3)	2351(3)	631(7)	14(1)
O(5)	3118(4)	4515(3)	2645(7)	14(1)

Table 4.9. Atomic coordinates (x 10^4) and equivalent isotropic displacement parameters (Å^2x 10^3) for $Na_5Ho_4(SiO_4)_4OH$. U(eq) is defined as one third of the trace of the orthogonalized U_{ij} tensor.

	x	y	z	U(eq)
Ho(1)	1172(1)	1840(1)	4758(1)	11(1)
Si(1)	2460(1)	1026(1)	111(3)	14(1)
Na(1)	1047(2)	4107(2)	53(6)	22(1)
Na(2)	0	0	619(19)	38(3)
O(1)	0	0	5000	25(2)
O(2)	2047(4)	322(3)	2568(8)	17(1)
O(3)	1089(3)	6130(3)	130(8)	17(1)
O(4)	2015(3)	2357(3)	649(8)	16(1)
O(5)	3121(4)	4513(3)	2639(7)	16(1)

181

Table 4.10. Atomic coordinates (x 10^4) and equivalent isotropic displacement parameters (Å^2x 10^3) for $Na_5Er_4(SiO_4)_4OH$. U(eq) is defined as one third of the trace of the orthogonalized U_{ij} tensor.

	x	y	z	U(eq)
Er(1)	1179(1)	1844(1)	4756(1)	11(1)
Si(1)	2457(2)	1024(2)	111(6)	17(1)
Na(1)	1043(3)	4110(3)	44(9)	22(1)
Na(2)	0	0	550(30)	33(3)
O(1)	0	0	5000	31(4)
O(2)	2026(6)	319(5)	2571(13)	17(1)
O(3)	1086(5)	6124(5)	97(13)	16(1)
O(4)	2006(5)	2374(5)	649(13)	16(1)
O(5)	3128(6)	4518(5)	2608(12)	15(1)

182

Table 4.11. Atomic coordinates (x 10^4) and equivalent isotropic displacement parameters ($\mathring{A}^2$x 10^3) for $Na_5Tm_4(SiO_4)_4OH$. U(eq) is defined as one third of the trace of the orthogonalized U_{ij} tensor.

	x	y	z	U(eq)
Tm(1)	1165(1)	1837(1)	4765(1)	11(1)
Si(1)	2458(2)	1030(2)	115(5)	12(1)
Na(1)	1052(3)	4104(3)	60(8)	20(1)
Na(2)	0	0	600(20)	31(4)
O(1)	0	0	5000	26(3)
O(2)	2044(6)	328(5)	2586(12)	15(1)
O(3)	1091(4)	6131(4)	116(13)	15(1)
O(4)	2019(5)	2362(4)	662(12)	12(1)
O(5)	3131(6)	4512(5)	2633(11)	14(1)

183

Table 4.12. Atomic coordinates (x 10^4) and equivalent isotropic displacement parameters (Å^2x 10^3) for $Na_5Tm_4(SiO_4)_4OH$. U(eq) is defined as one third of the trace of the orthogonalized U_{ij} tensor.

	x	y	z	U(eq)
Y(1)	1172(1)	1842(1)	4761(2)	11(1)
Si(1)	2458(2)	1024(2)	109(6)	15(1)
Na(1)	1044(3)	4111(3)	51(10)	22(1)
Na(2)	0	0	620(20)	34(5)
O(1)	0	0	5000	26(3)
O(2)	2039(7)	321(6)	2589(13)	17(2)
O(3)	1088(5)	6128(5)	118(15)	16(1)
O(4)	2017(5)	2365(5)	651(13)	15(1)
O(5)	3117(7)	4515(6)	2644(12)	14(1)

184

Table 4.13. Atomic coordinates (x 10^4) and equivalent isotropic displacement parameters (Å^2x 10^3) for $NaYbSiO_4(OH)$. U(eq) is defined as one third of the trace of the orthogonalized U_{ij} tensor.

	x	y	z	U(eq)
Yb(1)	2730(1)	219(1)	921(1)	9(1)
Yb(2)	4757(1)	5206(1)	2321(1)	9(1)
Si(1)	1360(3)	5330(6)	0(4)	9(1)
Si(2)	6137(3)	330(6)	3224(4)	9(1)
Na(1)	127(6)	297(9)	478(11)	25(2)
Na(2)	2358(5)	4775(8)	2705(11)	20(2)
Na(3)	3494(6)	194(9)	3486(8)	28(2)
Na(4)	969(5)	4695(10)	4705(7)	23(2)
O(1)	416(6)	4490(13)	672(7)	15(2)
O(2)	2310(5)	3870(12)	396(6)	18(1)
O(3)	1182(8)	4691(14)	-1292(11)	16(2)
O(4)	1547(5)	8247(11)	133(6)	11(1)
O(5)	5174(4)	-1165(11)	2840(6)	14(1)
O(6)	6306(8)	-211(12)	4450(12)	16(2)
O(7)	7052(5)	-568(13)	2506(7)	14(1)
O(8)	5959(4)	3233(11)	3048(6)	12(1)
O(9)	3447(4)	6818(11)	1475(6)	14(1)
O(10)	4058(4)	1794(11)	1700(6)	12(1)

185

Table 4.14. Atomic coordinates (x 10^4) and equivalent isotropic displacement parameters ($Å^2$x 10^3) for NaScSiO$_4$(OH). U(eq) is defined as one third of the trace of the orthogonalized U$_{ij}$ tensor.

	x	y	z	U(eq)
Sc(1)	2777(2)	217(2)	913(2)	8(1)
Sc(2)	4711(2)	5202(2)	2317(2)	9(1)
Si(1)	1399(2)	5324(4)	39(3)	8(1)
Si(2)	6115(2)	331(4)	3201(3)	10(1)
Na(1)	169(4)	310(7)	591(6)	22(1)
Na(2)	2305(4)	4773(6)	2614(6)	22(1)
Na(3)	3438(5)	162(7)	3501(5)	29(1)
Na(4)	944(4)	4633(7)	4692(4)	21(1)
O(1)	435(5)	4619(10)	762(8)	14(1)
O(2)	2343(3)	3745(9)	452(6)	16(1)
O(3)	1208(6)	4800(10)	-1272(9)	14(2)
O(4)	1645(3)	8292(8)	189(6)	13(1)
O(5)	5154(3)	-1282(8)	2807(6)	16(1)
O(6)	6318(7)	-168(9)	4488(10)	15(2)
O(7)	7051(6)	-427(11)	2460(8)	17(1)
O(8)	5858(3)	3277(9)	3033(6)	14(1)
O(9)	3503(3)	6975(8)	1475(6)	14(1)
O(10)	4014(3)	1960(8)	1731(5)	13(1)

Table 4.15. Experimental magnetic moments (μ_{eff}) compared to typically observed values (μ_{obs}). Units are in Bohr magnetons (μ_B)

	μ_{obs}	μ_{eff}
$Na_5Pr_4(SiO_4)_4OH$	3.4-3.6	3.10
$Na_5Nd_4(SiO_4)_4OH$	3.4-3.5	3.50
$Na_5Sm_4(SiO_4)_4OH$	1.6	1.72
$Na_5Eu_4(SiO_4)_4OH$	3.5	3.86
$Na_5Gd_4(SiO_4)_4OH$	7.8-7.9	7.94
$Na_5Tb_4(SiO_4)_4OH$	9.7-9.8	10.68
$Na_5Dy_4(SiO_4)_4OH$	10.2-10.6	10.50
$Na_5Ho_4(SiO_4)_4OH$	10.3-10.5	10.95
$Na_5Er_4(SiO_4)_4OH$	9.4-9.5	9.51
$Na_5Tm_4(SiO_4)_4OH$	7.5	7.73
$Na_2Yb_4(SiO_4)_4OH$	4.5	4.15

References

1. J. Felsche, in: J.D. Dunitz (Ed.), Structure and Bonding, Vol. 13, Springer, Berlin, 1973, pp. 99–197.

2. Sato, M.; Kono, Y.; Ueda, H.; Uematsu, K.; Toda, K. *Solid State Ionics* **1996**, *83*, 249.

3. Fleet, M. E.; Liu, X. *J. Solid State Chem.* **2001**, *161*, 166.

4. Chicagov, A. V.; Litvin, B. N.; Belov, N. V. *Kristallografiya* **1969**, *14*, 119.

5. Maksimov, B. A.; Litvin, B. N.; Ilyukhin, V. V.; Belov, N. V. *Kristallografiya* **1969**, *14*, 498.

6. Sebais, M.; Pobedimskaya, E. A.; Dimitrova, O. V. *Kristallografiya* **1985**, *30*, 802.

7. Tamazyan, R. A.; Malinovskii, Y. A.; Sirota, M. I.; Simonov, V. I. *Kristallografiya* **1988**, *33*, 1128.

8. Vidican, I.; Smith, M. D.; Zur Loye, H.-C. *J. Solid State Chem.* **2003**, *170*, 203.

9. Napper, J. D.; Layland, R. C.; Smith, M. D.; Zur Loye, H.-C. *J. Chem. Crystallogr.* **2004**, *34*, 347.

10. Ponomarev, V. I.; Filipenko, O. S.; Atoymyan, L. O. *Kristallografiya* **1988**, *33*, 98.

11. Haile, S. M.; Wuensch, B. J. *Acta Crystallogr. B* **2000**, *56*, 349.

12. Atovmyan, L. O.; Filipenko, O. S.; Ponomarev, V. I.; Leonova, L. S.; Ukshe, E. A. *Solid State* i*onics* **1984**, *14*, 137.

13. SMART Version 5.631, SAINT+ Version 6.45 and SADABS Version 2.10, Bruker Analytical X-ray Systems, Inc., Madison, Wisconsin, USA, 2003

14. Sheldrick, G. M. *Acta Crystallogr. A* **2008**, *64*, 112.

188

15. Hübschle, C. B., Sheldrick, G. M., Bittrich, B. *J. Appl. Cryst.* **2011**, *44*, 1281.

16. (a) LePage, Y. *J. Appl. Crystallogr.* **1987**, *20*, 264-269. (b) Spek, A. L. *J. Appl. Crystallogr.* **1988**, *21*, 578-579. (c) Spek, A. L. *Acta Crystallogr., A* **1990**, *46*, C34. (d) PLATON, A Multipurpose Crystallographic Tool, Utrecht University, Utrecht, The Netherlands, Spek, A. L. **1998**.

17. Fallon, G. D.; Gatehouse, B. M. *Acta Crystallogr. B* **1982**, *38*, 919.

18. Malinovskii, Y. A. *Soviet Physics Doklady* **1984**, *29*, 3.

19. T. A. Zhadanova, L. N. Demianets, A. A. Voronkov, Y. A. Piatenko, *Dokl. Akad. Nauk SSSR* **1975***, 224*, 1069-1072.

20. Filipenko, O. S.;,Dimitrova O. V.; Atomyan, O. L.; Leonova, L. S. *Krystallografiya* **1989**, *34*, 1009.

21. Chirag, M. I.; Mamedov, H. S. *Uchenye Zapiski Azerbaidzhanskogo Gosudarstvennogo Universiteta* **1974**, *4*, 3.

22. Okudera, H.; Masubuchi, Y.; Kikkawa, S.; Yoshiasa, A. *Solid State Ionics* **2005**, *175*, 1473.

23. Cantwell, J. R.; Roof, I. P.; Smith, M. D.; zur Loye, H.-C. *Solid State Sciences* **2011**, *13*, 1006.

24. Takikawa, Y.; Ebisu, S.; Nagata, S. *J. Phys. Chem. Solids* **2010**, *71*, 1592.

25. Kiliaan, H. S.; Van Herwijnen, F. P.; Blasse, G. *Mater. Chem. Phys.* **1987**, *18*, 351.

26. Avetisyan, E. I.; Chicagov, A. V.; Belov, N. V. *Sov. Phys. Crystallogr.* **1971**, *15*, 926.

Chapter 5: Synthesis, Crystal Structure, and Preliminary Magnetic Studies of

the First Iron Zeolites: $A_{\sim 1.5}Ba_8Fe_{12}O_{28} \cdot XH_2O$; ($A$ = Na, Na/K, K, Cs)

.

INTRODUCTION

Materials discovery through crystal growth continues to be the best way to explore phase space in the quest for new or improved physical properties.[1] Soft chemical methods allow for the investigation of regions of phase-space inaccessible via traditional synthetic routes. In developing the hydroflux crystal growth technique,[2,3] we have made a new pathway potentially leading to unique and interesting compositions. Through investigations of the barium-iron phase diagram in a hydroxide hydroflux, we have discovered what appears to be the first compound with iron tetrahedrally coordinated in three dimensions in a framework analogous to a zeolite.

Iron (III) is known to take on a tetrahedral coordination environment with oxygen in some of its compounds, though it predominately prefers an octahedral environment. Most often, these tetrahedra are isolated. However, some compounds have shown that iron tetrahedra can be condensed into higher dimensional structures. A small number of compounds have shown iron tetrahedra corner-shared to form various-membered rings such as $AFeO_2$ (A = K, Rb and Cs),[4] $Ba_4KFe_3O_9$,[5] $Na_{14}Fe_6O_{16}$,[6] and $Ba_3Fe_2O_6$.[7] This is not unlike what is observed in silicate chemistry, despite the obvious disparity between the two elements' propensity to form condensed frameworks.

Zeolites are a vast, industrially relevant class of compounds that are traditionally comprised of an aluminosilicate framework that has open space or cavities that allow for water, ions, or gases to exchange or adsorb. The series of compounds presented in this chapter represent the first iron oxides prepared that exhibit a three dimensional framework analogous to that seen in sodalite (Figure 5.1). Given the catalytic activity of the doped aluminosilicate variant,[5] these new compounds are an exciting discovery that

191

opens the door to a broad array of future experiments. The synthesis, crystal structure, and a preliminary magnetic properties investigation are presented herein.

EXPERIMENTAL METHODS

Reagents. The following reagents were used as obtained: KOH (Fisher Scientific, ACS grade pellets), NaOH (Fisher Scientific, ACS grade pellets), CsOH•H$_2$O (Alfa Aesar, 99.9%), Ba(OH)$_2$•8H$_2$O (Alfa Aesar, 99+%), and Fe(NO$_3$)$_3$•9H$_2$O (Alfa Aesar, 98%+).

Crystal Growth. All products were synthesized in 23 mL PTFE-lined stainless steel autoclaves. 4 mmols of Fe(NO$_3$)$_3$•9H$_2$O and 6 mmols of Ba(OH)$_2$•8H$_2$O were reacted in the corresponding reactive alkali hydroxide hydroflux (Na hydroflux = 0.2 mol NaOH/0.35 mol H$_2$O; Na/K hydroflux = 0.1 mol KOH/0.1 mol NaOH/0.35 mol H$_2$O; K hydroflux = 0.2 mol KOH/0.35 mol H$_2$O; Cs hydroflux = 0.1 mol CsOH/0.25 mol H$_2$O). The vessels were heated in a programmable oven from room temperature to 180 ℃ at 5 ℃/min, then to 230 ℃ at 0.3 ℃/min, held for 1 day, then slow cooled at a rate of 0.3 ℃ per minute to 80 ℃. The products were sonicated in methanol for at least three days and then isolated by filtration.

Magnetic Measurements. The DC magnetic susceptibilities were measured as a function of temperature using a Quantum Design MPMS SQUID VSM. Ground, polycrystalline samples were measured in gelatin capsules. The diamagnetic background of the sample holder was not subtracted due to its very small contribution to the measured moment. For a typical temperature sweep experiment, the sample was first cooled to 4 K under zero-field cooled (zfc) conditions and data were collected upon warming to 300 K in an applied field of 1000 Oe. Then the sample was field cooled (fc) to 4 K from room

192

temperature in 1000 Oe while data were collected. Field sweeps were performed from 0-7 T, then to -7 T, and back to 0 T.

Structure Determination. X-ray intensity data were collected at for all samples at 296(2) K using a Bruker SMART APEX diffractometer (Mo Kα radiation, $\lambda = 0.71073$ Å).[6] The raw area detector data frames were reduced and corrected for absorption effects using the SAINT+ and SADABS programs.[6] The initial structural model was obtained by direct methods using SHELXS.[7] Subsequent difference Fourier calculations and full-matrix least-squares refinement against F^2 were performed with SHELXL-2013/4[7] using the ShelXle interface.[8] In this chapter, only the structure of the Na/K mixed analogue is reported. All other analogues are isostructural, with variations in the lattice parameter. Structural refinements are not complete yet and neutron diffraction data will be used in conjunction with synchrotron X-ray data in future studies to determine the atomic and magnetic structure of this series at a number of temperatures. Structure refinement information for $Na_{\sim 1.5}Ba_8Fe_{12}O_{28} \cdot XH_2O$ is listed in Tables 5.1 and 5.2.

RESULTS AND DISCUSSION

Synthesis. Crystals were readily produced of the title compounds under the conditions reported. Similar product purity and crystal size was obtained for reactions performed on smaller scales, but not larger ones. An excess of $Ba(OH)_2 \cdot 8H_2O$ was found to promote nearly quantitative yield with respect to $Fe(NO_3)_3 \cdot 9H_2O$. Using less barium precursor lead to poor yield and formation of an unidentified iron containing byproduct. Fe_2O_3 was tested as a precursor, but was found to be inferior to the nitrate. This is most likely related to a mismatch between reaction kinetics and dissolution rate of the Fe_2O_3 in the hydroflux.

193

Structure. All compounds adopt a cubic variation of the sodalite structure (Figure 5.1) and take on block-like crystal morphologies with truncated corners (Figure 5.2). The crystal structure is best described as a 3d framework of corner shared iron tetrahedra with barium and alkali metals lying at the centers of cavities created by this framework. Each iron tetrahedra is connected to four other tetrahedra through corner-shared oxygen bonds. (Figure 5.3) Two of these tetrahedra link in a coplanar arrangement, while two others link in a perpendicular fashion. This leads to the formation of sodalite cages with no twist between tetrahedra. (Figure 5.4) One cage occupies each unit cell and can be described as four-member rings of corner-shared tetrahedra at the faces of the unit cell that are linked to each other, leading to six-member rings of iron tetrahedra down the body diagonals of the unit cell. (Figure 5.5) The barium atoms sit at the middle of these six member rings and are displaced toward the center of the cage, leading to a cubic arrangement of barium atoms. The alkali metal atoms are arranged in a bcc fashion in the unit cell, with one site at the corners of the unit cell and one in the center of the cavity.

Magnetism. The temperature dependence of the magnetic susceptibilities (χ) were measured of the under zfc and fc conditions. Temperature dependence of the inverse susceptibility data were fit to the Curie-Weiss law where $\chi = C/(T-\theta)$; C is the Curie constant, θ is the paramagnetic Weiss temperature. Both the Na and Na/K analogue exhibit strong deviations from Curie-Weiss behavior.

The χ_m vs T and $1/\chi_m$ vs. T plots are shown in Figures 5.6-5.9. The observed divergence in the zfc and fcc data at low temperatures suggests the possibility of a canted antiferromagnetic ground state with spin frustration. Approximate Neel temperatures for the examined phases at 1000 Oe are 63 K and 23 K for the Na and Na/K analogues,

194

respectively. The inverse susceptibility plot is nonlinear over the entire temperature range measured and cannot be readily fit to the Curie law. Furthermore, the χT vs T plot shows a complex change in the moment as a function of the temperature. (Figures 5.10 and 5.11) In samples with complex behavior, a plot of μ_{eff} vs. T can be useful in determining the effective moment per magnetic ion, where $\mu_{eff} = (7.977\chi_m T)^{1/2}$. The effective moments observed at 300 K are 5.57 μ_B and 3.18 μ_B for the Na and Na/K analogue, respectively. This is lower than the expected spin-only value of 5.92 μ_B (for g = 2) for a tetrahedral high-spin Fe^{3+} ion. This behavior indicates the presence of antiferromagnetic interactions between Fe^{3+} ions. Previous investigations have shown that the measured effective magnetic moment is much smaller than the theoretical magnetic moment in a number of related iron and cobalt oxides such as, for example, $BaKFeO_3$[9], $Ba_3Fe_2O_6$[10], and $Ba_4KFe_3O_9$[11] as well as cobalt(IV) compounds Cs_2CoO_3, Rb_2CoO_3 , and K_2CoO_3.[12] In some of these cases, it was suggested that the large discrepancy between the observed and theoretical magnetic moments is due to long-range antiferromagnetic ordering with Neel temperatures above the range of the magnetic measurement.[9,10] It is possible that this scenario applies to this zeolitic structure because of the close proximity and arrangement of magnetic centers. For $Na_{1.5}Ba_8Fe_{12}O_{28} \cdot 8H_2O$, a field sweep was collected at 4K. These data are presented in Figure 5.12. The compound exhibits soft magnetic behavior at 4 K with a low coercive field (<1000 Oe).

CONCLUSION

An exciting new class of compounds have been synthesized that represent the first examples of a zeolitic iron framework structure. Preliminary magnetic studies indicate complex magnetic behavior over a broad range of temperatures. Future studies will

195

include more detailed magnetic measurements at a broader range of temperatures, neutron diffractions studies, and could potentially include catalytic studies.
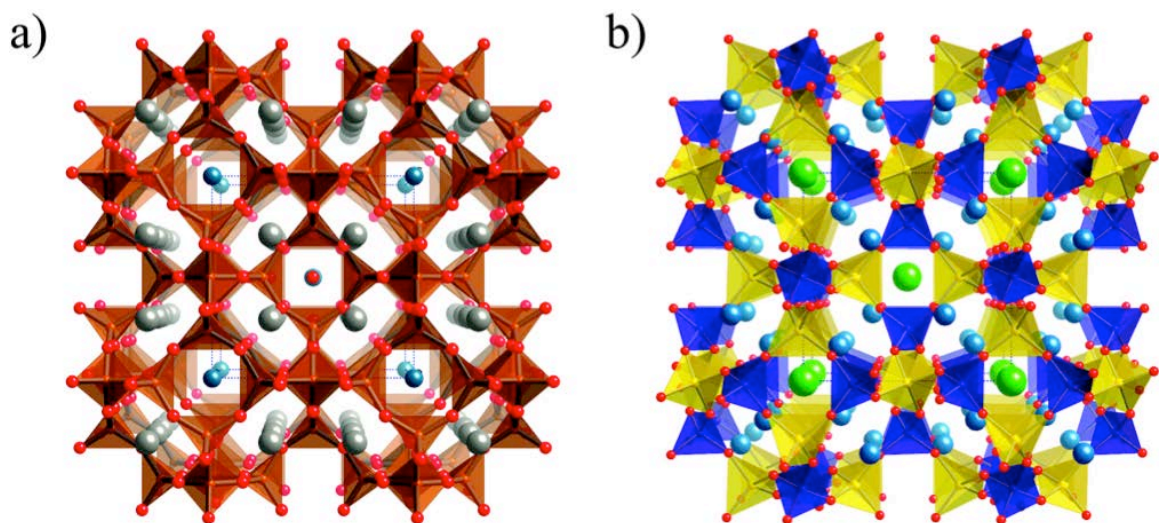
Figures 5.1. a) Crystal structure of $A_{\sim1.5}Ba_8Fe_{12}O_{28} \cdot XH_2O$ (A = Na, Na/K, K, Cs) with the A atoms shown in blue, Ba atoms shown in grey, O atoms in red, and Fe atoms and their coordination environment shown in orange. b) Analogous model of the sodalite structure with Na atoms in light blue, Cl atoms in green, O atoms in red, and Al and Si environments in yellow and dark blue, respectively.
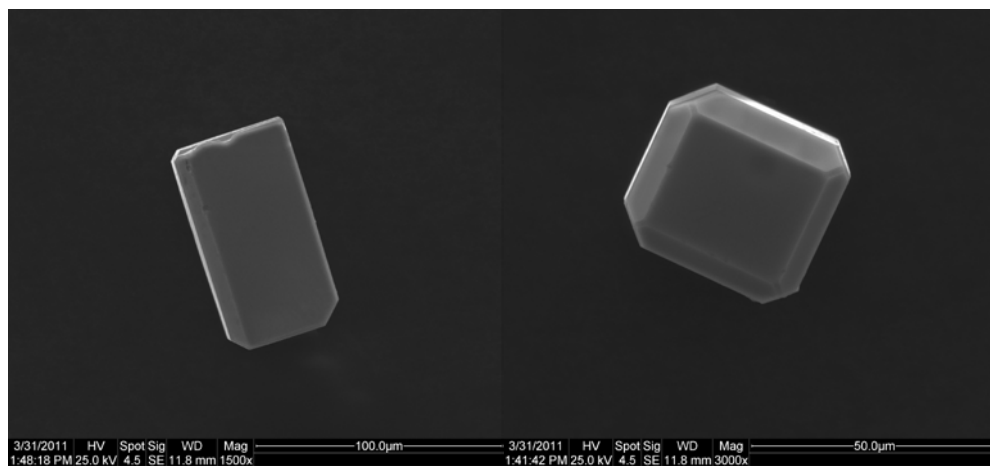
Figure 5.2. Scanning electron micrograph images of crystals of $(Na/K)_{\sim1.5}Ba_8Fe_{12}O_{28} \cdot XH_2O$.

197
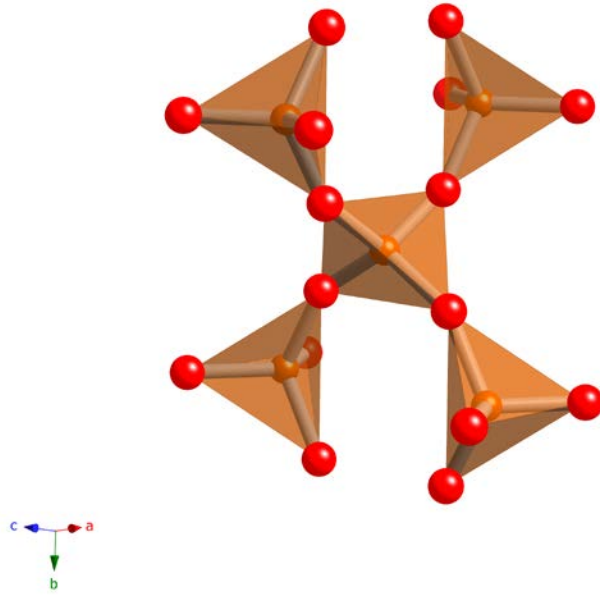
Figure 5.3. Connectivity between one FeO$_4$ tetrahedron and four surrounding units.
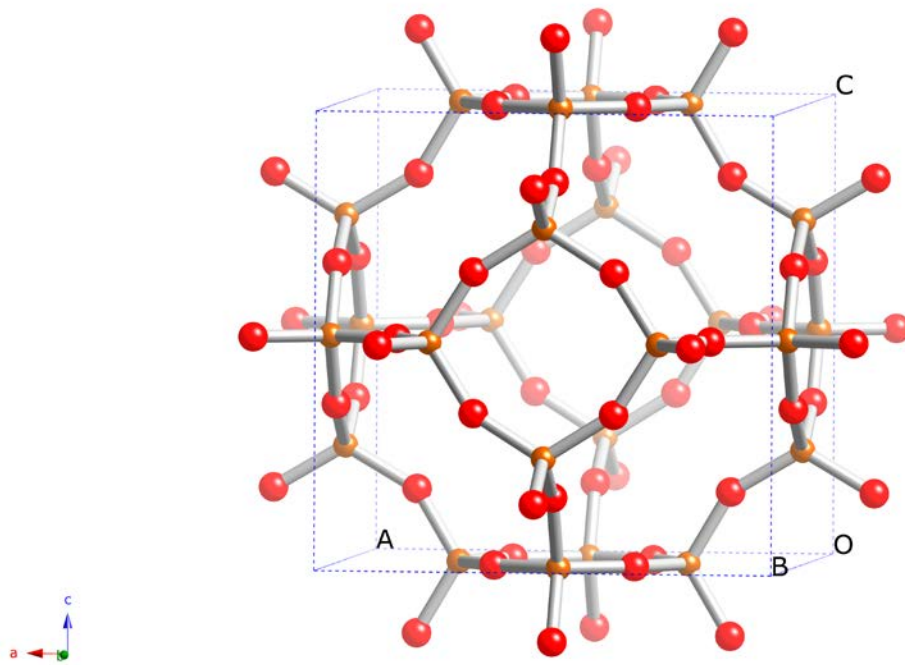
Figure 5.4. Sodalite cage exhibited by the series $A_{\sim1.5}Ba_8Fe_{12}O_{28} \cdot XH_2O$.

198
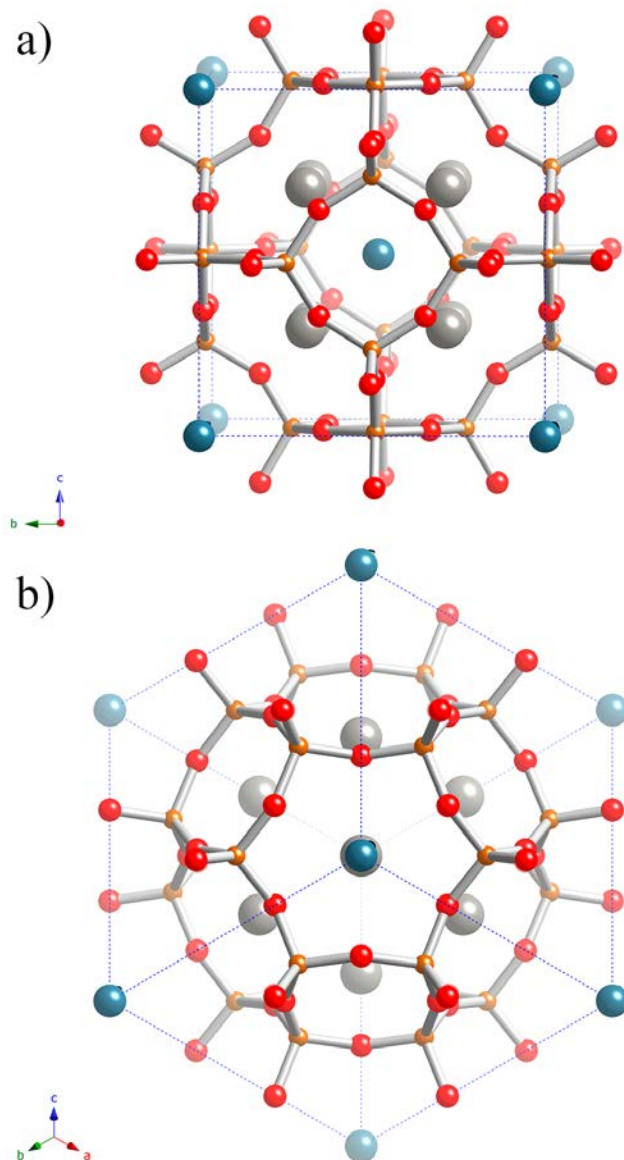
Figure 5.5. Unit cell of $(Na/K)\sim_{1.5}Ba_8Fe_{12}O_{28} \cdot XH_2O$ down the a) *a* axis and b) [111] lattice vector.
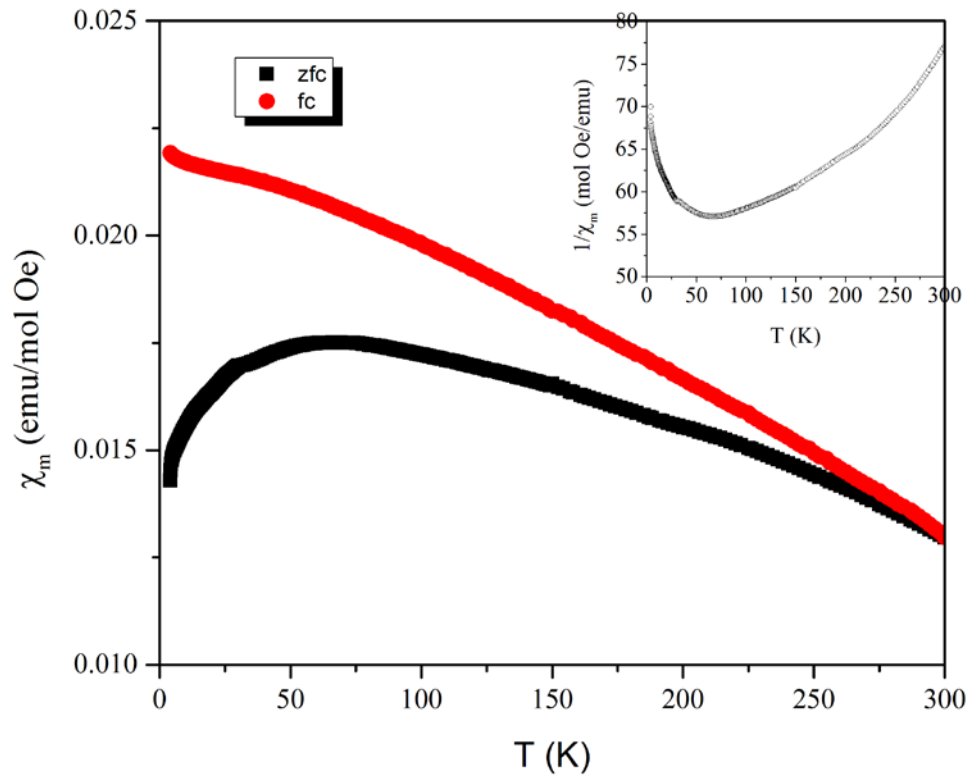
Figure 5.6. Temperature dependence of the molar magnetic susceptibility, χ_m, of Na$_{\sim1.5}$Ba$_8$Fe$_{12}$O$_{28}$•XH$_2$O measured under zfc and fc conditions. Inset is an inverse magnetic susceptibility, $1/\chi_m$, plot of the zfc data.

200
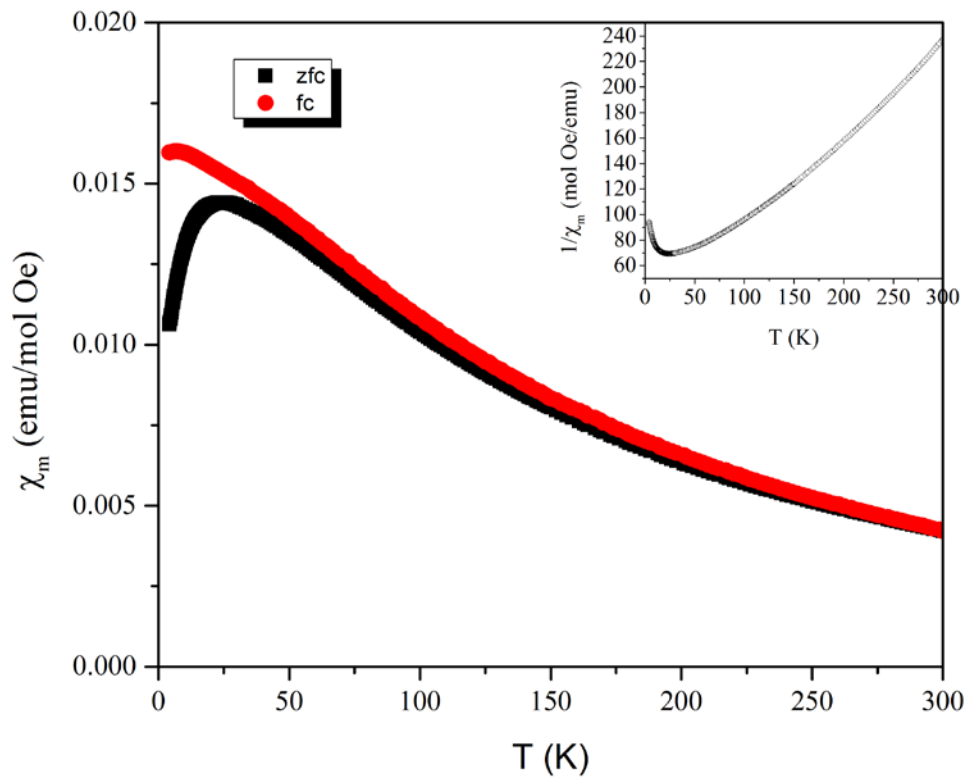
Figure 5.7. Temperature dependence of the molar magnetic susceptibility, χ_m, of $(Na/K)_{\sim 1.5}Ba_8Fe_{12}O_{28} \bullet XH_2O$ measured under zfc and fc conditions. Inset is an inverse magnetic susceptibility, $1/\chi_m$, plot of the zfc data.

201
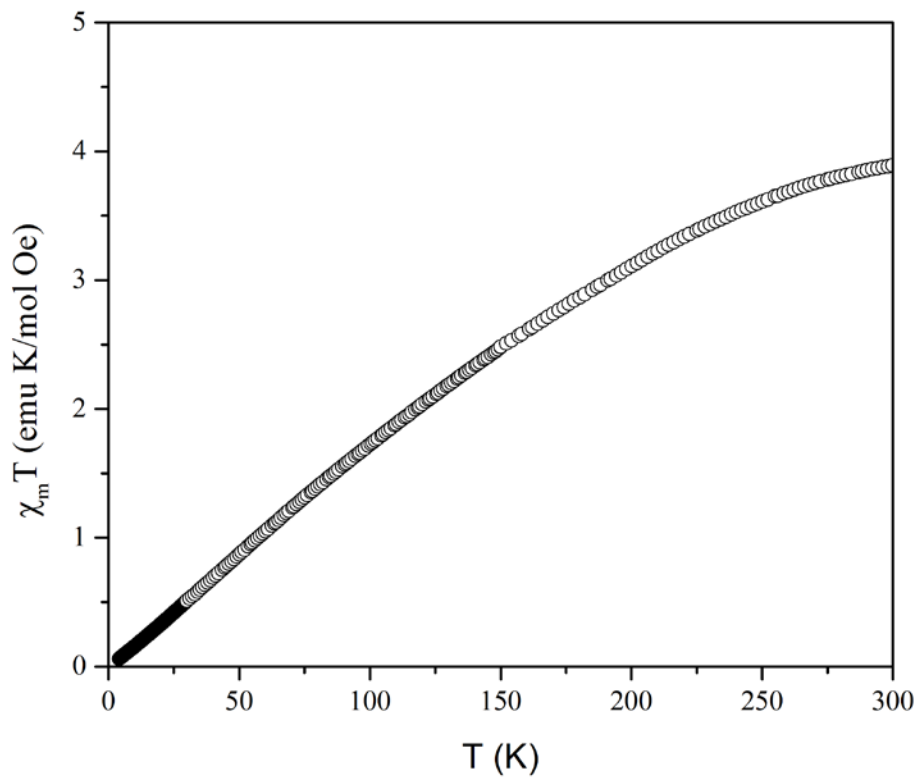
Figure 5.8. $\chi_m T$ plot for of $Na_{\sim 1.5}Ba_8Fe_{12}O_{28} \cdot XH_2O$ (zfc conditions, 1000 Oe applied field)
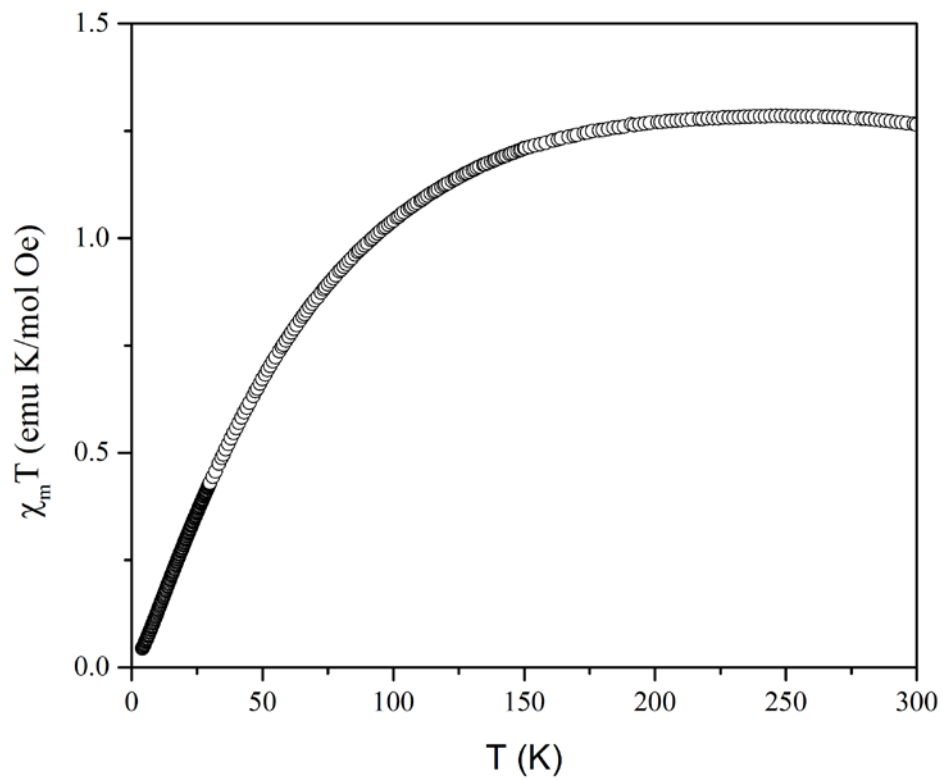
Figure 5.9. $\chi_m T$ plot for of $(Na/K)_{\sim 1.5}Ba_8Fe_{12}O_{28} \cdot XH_2O$ (zfc conditions, 1000 Oe applied field)

203
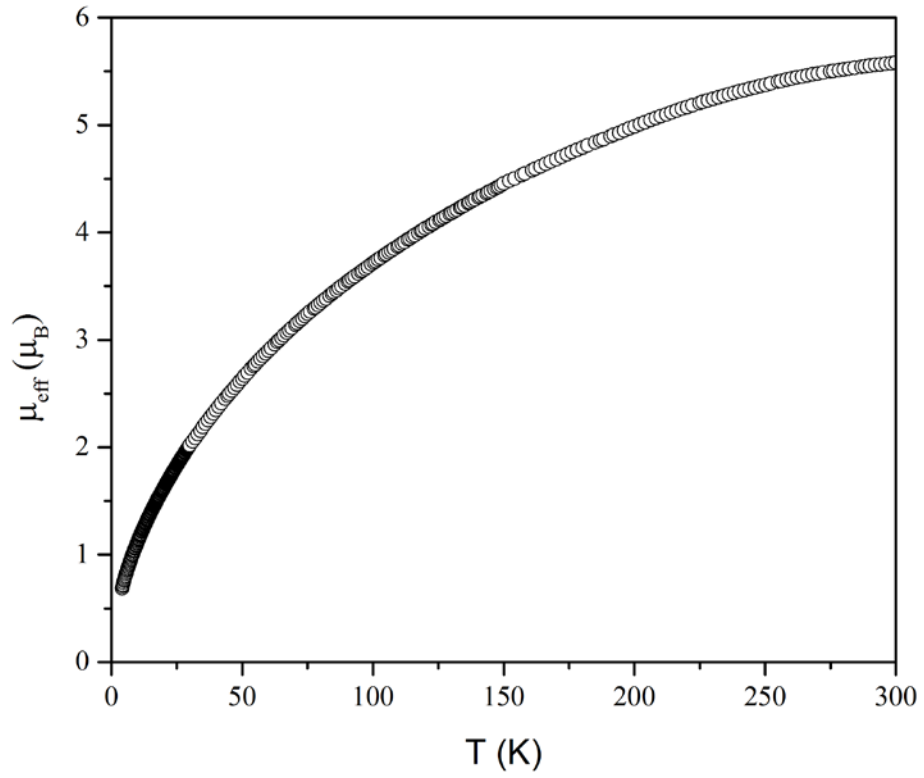
Figure 5.10. μ_{eff} plot for $Na_{\sim 1.5}Ba_8Fe_{12}O_{28} \cdot XH_2O$ (zfc conditions, 1000 Oe applied field)

204
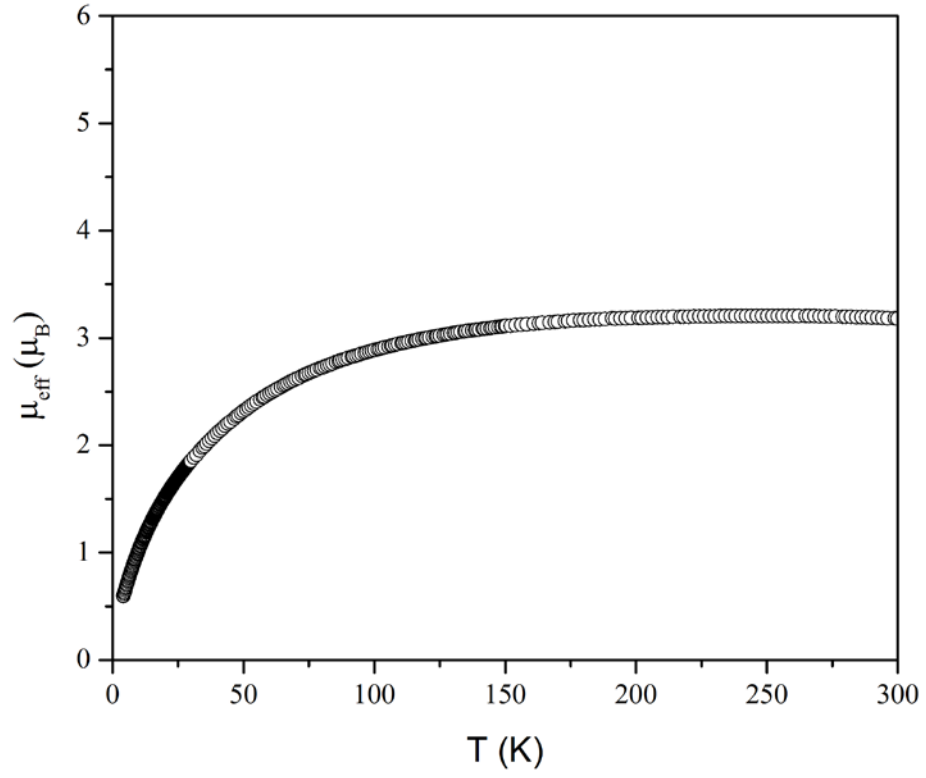
Figure 5.11. μ_{eff} plot for $(Na/K)_{\sim 1.5}Ba_8Fe_{12}O_{28} \bullet XH_2O$ (zfc conditions, 1000 Oe applied field)
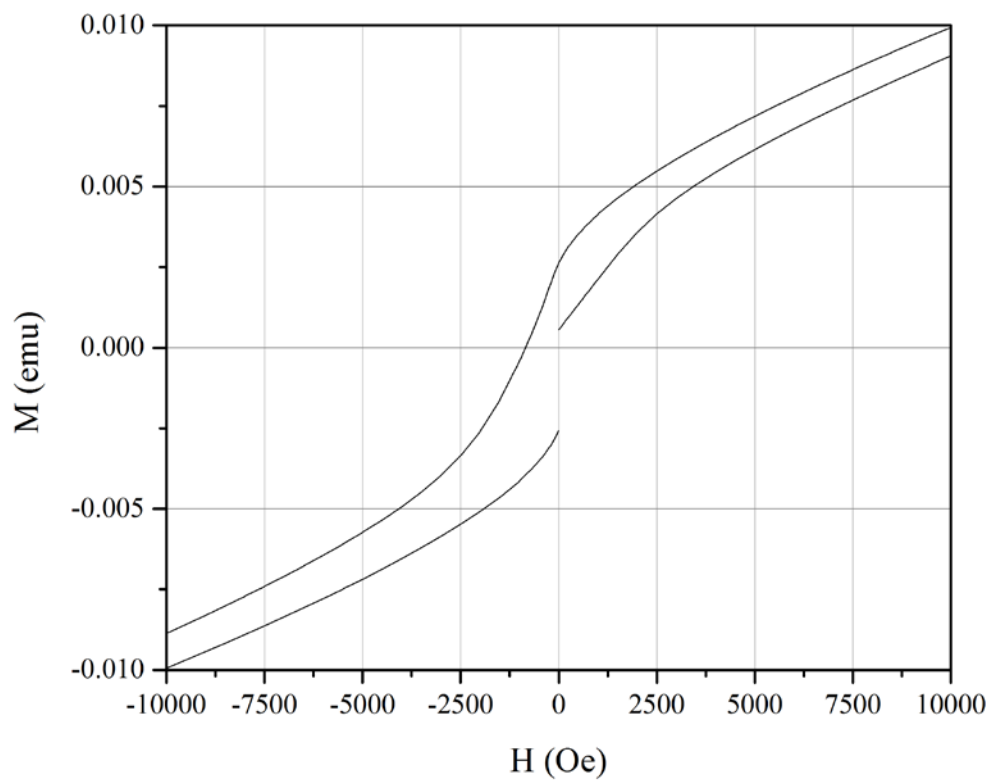
Figure 5.12. Magnetization curves (M vs. H) for Na$_{\sim1.5}$Ba$_8$Fe$_{12}$O$_{28}$•XH$_2$O at 4 K.

Table 5.1. Crystallographic Data for $(Na/K)\sim_{1.5}Ba_8Fe_{12}O_{28} \cdot XH_2O$

formula weight (g/mol)	2263.168
color and habit	amber, block
Temperature (K)	300(2)
Crystal system	cubic
Space group	*Pm-3m*
a (Å)	10.0389(17)
V (Å^3)	1011.7(5)
Z	8
ρ_c (g cm^{-3})	3.799
μ (mm^{-1})	11.365
$F(000)$	1040
crystal size (μm^3)	80 x 20 x 20
θ_{max} (°)	36.32
index ranges	-11<=h<=15, -12<=k<=15, -11<=l<=16
reflections collected	8171
independent reflections	552
goodness-of-fit on F^2	0.788
R indices (all data)	R1 = 0.0311, wR2 = 0.0962
largest peak and diffraction hole (e$^-$ Å^{-3})	0.973/-1.577

207

Table 5.2. Atomic coordinates and equivalent isotropic displacement parameters (Å^2) for. $(NaK)_{\sim 1.5}Ba_8Fe_{12}O_{28} \bullet X H_2O$ U_{eq} is defined as one third of the trace of the orthogonalized U_{ij} tensor.

	Occ	x	y	z	U_{eq}
Ba1	1	0.20348(2)	0.20348(2)	0.20348(2)	0.01155(15)
Fe1	1	0.5	0.24972(7)	0.0	0.00754(17)
Na1	0.97467	0.0	0.0	0.0	0.014(3)
K1	0.02518	0.0	0.0	0.0	0.014(3)
O1	1	0.3406(3)	0.3406(3)	0.0	0.0167(7)
O2	0.30329	0.5	0.1769(14)	0.1769(14)	0.023(6)
O2'	0.78686	0.5	0.1453(11)	0.1453(11)	0.041(4)
O3	1	0.0		0.2313(6)	0.0158(10)
O4	1	0.3682(12)	0.3682(12)	0.3682(12)	0.223(16)
O5	0.78686	0.5	0.5	0.2226(15)	0.040(4)
O6	0.99985	0.5	0.5	0.5	0.040(5)

References

1) Bugaris, D.E.; zur Loye, H-C. *Angew*. *Chem., Int. Ed.* **2012**, *51* (16)*,* 3780-3811.

2) Chance, W.M.; Bugaris, D.E.; Sefat, A.S.; zur Loye, H-C. *Inorg. Chem.* **2013**, *52* (20), 11723–11733.

3) Chance, W.M; Smith, M.D.; zur Loye, H-C. *J. Chem. Crystallogr.* **2013**, doi:10.1007/s10870-013-0477-z

4) Ali, N.Z.; Nuss, J.; Sheptyakov, D.; Jansen, M. *J. Solid State Chem.* **2010**, *183* (3), 752-759.

5) Betteridge, S.; Catlow, C. R.; Gay, D.; Grimes, R.; Hargreaves, J.; Hutchings, G.; Joyner, R.; Pankhurst, Q.; Taylor, S. *Top Catal* **1994**, *1*, 103.

6) SMART Version 5.631, SAINT+ Version 6.45 and SADABS Version 2.10, Bruker Analytical X-ray Systems, Inc., Madison, Wisconsin, USA, 2003

7) SHELXTL Version 6.14, Bruker analytical X-ray Systems, Inc., Madison, WI, 2000

8) Hübschle, C. B.; Sheldrick, G. M.; Dittrich, B. *J. Appl. Crystallogr.* **2011**, *44*, 1281.

9) Delattre, J. L.; Stacy, A. M. *J. Solid State Chem.* **2003**, *172*, 261.

10) Delattre, J.L. *"Chapter 2. Synthesis and Characterization of Barium Iron Oxides"* Ph.D. Dissertation, University of California-Berkeley, Berkeley, CA, 2002.

11) Zhao, Q.; Nellutla, S.; Son, W.J.; Vaughn S.A.; Ye, L.; Smith, M.D.; Caignaert, V.; Lufaso, M.; Pekarek, T.M.; Smirnov, A.I.; Whangbo, M.H.; zur Loye, H-C. *Inorg. Chem.* **2011**, *50*, 10310-10318.

12) Jansen, M.; Hoppe, R. *Z. Anorg. Allg. Chem*. **1974**, *408*, 75.

Chapter 6: Crystal Growth of New Arsenates and Manganates via Hydroxide

Hydrofluxes

Chapter 6.1: Crystal Growth and Optical Properties of the Hydroxyapatites:

$Sr_5(MnO_4)_3(OH)$, $Ba_5(MnO_4)_3(OH)$, and $Ba_5(AsO_4)_3(OH)$
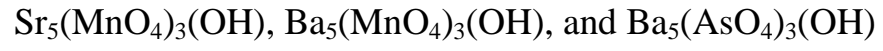
INTRODUCTION

Apatites are a large class of compounds structurally related (or analogous, but some symmetry differences) to the eponymous mineral, $Ca_5(PO_4)_3(OH,F,Cl)_2$, and can be written in the more general form $(A1)_2(A2)_3(MO_n)_3X$. The structure, usually exhibiting hexagonal ($P6_3/m$) symmetry or sometimes lower symmetry, can accommodate a wide array of substitutions at the cationic and anionic sites. [1, 2] The crystallographically distinct $A1$ and $A2$ sites can be occupied either fully or partially by a number of ions such as Ca^{2+}, Sr^{2+}, Ba^{2+}, Pb^{2+}, Na^+, and RE^{3+} in naturally occurring minerals and Cd^{2+}, Mn^{2+}, Mg^{2+}, Ni^{2+}, Sn^{2+}, Hg^{2+}, and K^+ in synthetic samples. The identity of MO_n can vary considerably as well with PO_4^{3-}, AsO_4^{3-}, VO_4^{3-}, CO_3^{2-}, SiO_4^{4-}, SO_4^{2-}, SO_3^{2-}, AsO_3^{3-} occurring naturally and CrO_4^{2-}, BO_4^{5-}, SeO_4^{2-}, GeO_4^{4-}, and MnO_4^{3-} produced in synthetic compounds. The identity of X can be OH^-, F^-, and Cl^- in nature with Br^-, I^-, and O^{2-} known as substituents in synthetic analogues with vacancies also being a common feature in this site. Due to their biological relevance, microporous nature, and their ability to host a number of important ions, apatites have found use in a number of applications such as fertilizers, waste sequestration media, [3, 4] oxide ion conductors [5 6 7 8], fluorescent phosphors [9 10], laser host materials [11 12], and catalysis [13]

Pentavalent manganese is uncommon due to its instability and tendency to disproportionate. The first reported Mn^{5+} compound was prepared by Lux in strong alkali solutions. [14] Extended structures containing MnO_4^{3-} are few and have traditionally been prepared by the solid state method under O_2 flow near 1000 ℃[15, 16] Some research has focused on the brilliant colors exhibited by Mn^{5+} compounds for use in pigments[17-20], while other work has seen investigations of Mn^{5+} for use in laser materials [21, 22] of Mn^{5+}

212

is strong due to its large absorption cross section.[16, 19] and varies from blue to green with increasing Mn^{5+} content.[15, 23] More recent studies of the magnetic properties of $Ba_3Mn_2O_8$ have brought renewed interest in the magnetic properties of solids with Mn^{5+}.[24-27]

Although Mn^{5+} is a common dopant in the apatite structure, only two crystal structures are reported with Mn^{5+} fully occupying the *B* site. $Ba_5(MnO_4)_3Cl$ and $Ba_5(MnO_4)_3F$ were prepared by solids state routes with only structural and optical characterizations performed.[15, 16] $Ba_5(MnO_4)_3(OH)_x$ was reported by Klemm via a solid state route in moist air with the magnetic moment given as evidence of Mn^{5+}.[28] Given that a range of structurally analogous pentavalent apatites exist and that the physical properties of the manganese analogues are not well studied, it makes sense to explore the crystal growth of new manganese apatites and characterize them.

Hydroflux synthesis offers a reaction media that bridges the gap between wet hydroxide fluxes and hydroxide composite hydrothermal reactions and allows for exploratory crystal growth. Previously, we have demonstrated its utility for the crystal growth of both hydroxides and oxides. [29-31] Prior work in our group with hydroxide fluxes resulted in the crystal growth of new vanadium apatites. [32] In this chapter, we describe the synthesis, crystal structure, and optical properties of $Sr_5(MnO_4)_3(OH)$, $Ba_5(MnO_4)_3(OH)$, and $Ba_5(AsO_4)_3(OH)$.

EXPERIMENTAL METHODS

Reagents. The following reagents were used as obtained: KOH (Fisher Scientific, ACS grade pellets), NaOH (Fisher Scientific, ACS grade pellets), $Sr(OH)_2 \cdot 8H_2O$ (Alfa , Aesar, 99%), $Ba(OH)_2 \cdot 8H_2O$ (Alfa Aesar, 99+%), As_2O_3 (Alfa Aesar, 99.9%),.and $KMnO_4$ (Fisher Scientific, ACS grade).

Crystal Growth. All products were synthesized in 23 mL PTFE-lined stainless steel autoclaves. 2 mmols of $Sr(OH)_2 \cdot 8H_2O$ or $Ba(OH)_2 \cdot 8H_2O$ and 1 mmol of $KMnO_4$ or As_2O_3 were added to a hydroflux made from 12 g of KOH and 6 g of water. The reaction mixtures were heated to 230 ºC at 5ºC per minute and held for 12 hours before being cooled at a rate of 0.3 ºC per minute to 80 C.

Infrared Spectroscopy. IR spectra were recorded with a Perkin Elmer Spectrum 100 FT-IR spectrometer. All samples were ground to a powder using an agate mortar and pestle and twenty scans ranging from 4500 cm^{-1} to 650 cm^{-1} were averaged.

Diffuse Relectance. A Perkin-Elmer Lambda 35 UV-visible spectrophotometer was used to collect diffuse-reflectance data in the range of 200-800 nm at room temperature. PTFE was used as a white standard. Raw data were converted from reflection to absorbance by the Kubelka-Munk function.

Structure Determination. X-ray intensity data from a single crystals of $Sr_5(MnO_4)_3OH$, $Ba_5(MnO_4)_3OH$, and $Ba_5(AsO_4)_3OH$ were collected at 296(2) K using a Bruker SMART APEX diffractometer (Mo Kα radiation, λ = 0.71073 Å). The raw area detector data frames were reduced and corrected for absorption effects with the SAINT+ and SADABS programs.[33] Final unit cell parameters were determined by least-squares refinement. Difference Fourier calculations and full-matrix least-squares refinement against F^2 of the structural model were performed with SHELXL-2013/4[34] using the ShelXle interface.[35]

The compounds adopt the apatite structure type, with the hexagonal space group $P6_3/m$. The asymmetric unit consists of two unique alkaline-earth atoms, one manganese or arsenic atom and four unique oxygen atoms. Sr(1) or Ba(1) is located on a three-fold

214

axis (Wyckoff symbol 4*f*, site symmetry 3..). Atoms Sr(2) or Ba(2), Mn(1) or As(1), O(1) and O(2) are located on mirror planes (site 6*h*, site symmetry *m*..). Oxygen O(3) is located on a general position (site 12*i*), and oxygen O(4) is located on site 4*e* with 3.. site symmetry. O(4) is disordered over two positions about the -6 symmetry element at (0,0,¼) and was refined with half-occupancy. All atoms were refined with anisotropic displacement parameters. Refinement of the site occupation factors for the metal atoms showed no significant decrease from full occupancy for all structures. The hydroxyl hydrogen atom presumably bonded to the disordered atom O(4) could not be reliably located and was not calculated. Final atomic coordinates were standardized with Structure Tidy. [36-38] Relevant crystallographic parameters are given in Tables 6.1-6.5.

RESULTS AND DISCUSSION

Synthesis. Single crystals of $Sr_5(MnO_4)_3(OH)$, $Ba_5(MnO_4)_3(OH)$, and $Ba_5(AsO_4)_3(OH)$ were grown from a hydroflux using the experimental conditions described previously. For $Ba_5(MnO_4)_3(OH)$, the formation of $BaCO_3$ could not be prevented with the experimental conditions used. As with $Ba_5(MnO_4)_3(OH)$, the synthetic conditions for $Ba_5(AsO_4)_3(OH)$ also produced a $BaCO_3$ byproduct. For $Sr_5(MnO_4)_3(OH)$, formation of s amall mass percentage of $SrMnO_{3-x}$ was not able to be prevented . All measurements were performed on samples purified by mechanical separation. Experiments testing the effect of changes to the heating profile showed no significant effect on the products formed. For both barium analogues, crystals were able to grown approximately 1 mm in length with the addition of H_3BO_3 as a mineralizer.

A large number of hydroylapatites have been previously prepared, most often by hydrothermal methods. The manganese analogues have been previously prepared as fine

215

powders via KOH flux in the case of $Sr_5(MnO_4)_3(OH)$ and precipitation from an ethanol solution in the case of $Ba_5(MnO_4)_3(OH)$. No previous reports of $Ba_5(AsO_4)_3(OH)$ exist, although the chlorapatite analogue is known from powder refinements, as is the analogous strontium hydroxyapatite. [39, 40]

Structures. The apatite structure is well known and there are multiple ways to describe it. [41-43] The structure can be thought of as consisting of AO_6 metaprisms that corner-share oxygens with MO_4 tetrahedra. (Figure 6.1) These metaprisms and tetrahedra form hexagonal rings that are interconnected, running down the c axis, creating channels in the structure. A second, crystallographically distinct A cation occupies sites in these channels and is coordinated to seven oxygens and the hydroxyl oxygen. Down the centers of the hexagonal channels are the hydroxyl groups. (Figure 6.2) The hydroxyl group is disordered over two positions inside the channels. (Figure 6.3)

One parameter to used compare apatite structures is the metaprism twist angle. [44-46] The apatite structure is very flexible and has no strict geometric constraint in its framework. This is in contrast to other, easily compared structure types such as the perovskite structure, which has a tolerance factor based on geometric packing considerations owing to the corner-shared octahedral framework. The metaprism twist angle is the angle at which the AO_6 metaprisms must contort to fit the cations and anions in the channel. The metaprism twist angles observed for the synthesized hydroxyapatites are presented in Table 6.6. The value for $Ba_5(MnO_4)_3(OH)$, 22.5 º, compares well to that of $Ba_5(MnO_4)_3Cl$, 22.3 º.

Infrared Spectroscopy. A plot of the transmittance is shown in Figure 6.4 in the range of the expected asymmetric stretch frequencies for the B-O bonds in a tetrahedral

www.manaraa.com

environment. For $Sr_5(MnO_4)_3(OH)$, two weak shoulders are observed at 803 cm^{-1} and 841 cm^{-1}. Similarly for $Ba_5(MnO_4)_3(OH)$, weak bands are observed at 790 cm^{-1} and 782 cm^{-1}, while a broader, stronger band is observed at 728 cm^{-1}. There are two bands expected in the region below 800 cm^{-1}, corresponding to $\nu_3(F_3)$ stretches. [47, 48] For $Ba_5(AsO_4)_3(OH)$, similar weak bands are observed at 758 cm^{-1} and 743 cm^{-1} along with two distinct bands at 690 cm^{-1} and 671 cm^{-1}. These small separations suggest there may be interionic coupling causing splitting of the bands. [49] If that is the case, then the data can be interpreted as two sets of split bands with the stronger of the two appearing as one broad band in the manganese analogues.

UV-Vis Spectroscopy. The diffuse reflectance spectra of $Ba_5(MnO_4)_3(OH)$ and $Sr_5(MnO_4)_3(OH)$ are plotted in Figure 6.5. There is an absorption peak in each spectrum at ~500 nm and another at ~588 nm. A number of articles have already discussed the energy states for Mn^{5+} in a tetrahedral field. According to prior assignments, the two peaks observed correspond to two electron jumps into the $^3T_1$ and $^3T_2$ energy substates. [15, 50] There are slight deviations in the energy of the observed transitions from idealized values and from each other. This is due to differences in bond energies between analogues and deviations in the coordination environment from an idealized tetrahedron. An unexpected sharp decline in the absorbance is observed at ~340 nm for both samples. This artifact can be attributed to the switching of sources from tungsten to deuterium within the instrument.

Bond Valence Analysis. The bond valence analysis results listed in Table 6.7 were obtained using parameters by Brown. [51] There is no bond valence parameter listed for Mn^{5+}, however, the parameter for Mn^{6+} is 1.79 and was used as an approximate value.

217

The calculated valence sums are in good agreement with the expected values, even for Mn^{5+}, suggesting no mixed valence for the manganese ions.

CONCLUSION

For the first time, $Sr_5(MnO_4)_3(OH)$, $Ba_5(MnO_4)_3(OH)$, and $Ba_5(AsO_4)_3(OH)$ have been grown as single crystals and their crystal structure and optical properties have been investigated. The manganese hydroxyapatites are an intense green color owing to the optical transitions from Mn^{5+}. Mn^{5+} is rare in extended solids and the crystal growth of Mn^{5+} compounds via a low temperature hydroflux warrants further investigation. Future work could include investigations of the magnetic properties of $Sr_5(MnO_4)_3(OH)$ and $Ba_5(MnO_4)_3(OH)$.
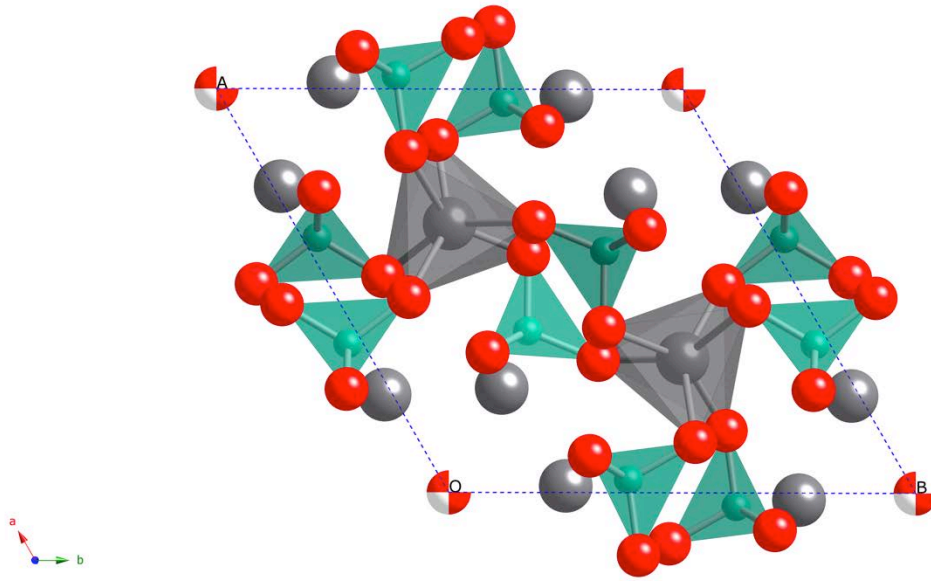
Figure 6.1. Unit cell of $Ba_5(MnO_4)_3(OH)$, with oxygen atoms in red, MnO_4 tetrahedra in turquoise, metaprisms corresponding to the Ba1 site in grey, Ba2 atoms shown as grey spheres, and hydroxyl oxygens shown as split-tone spheres.

219
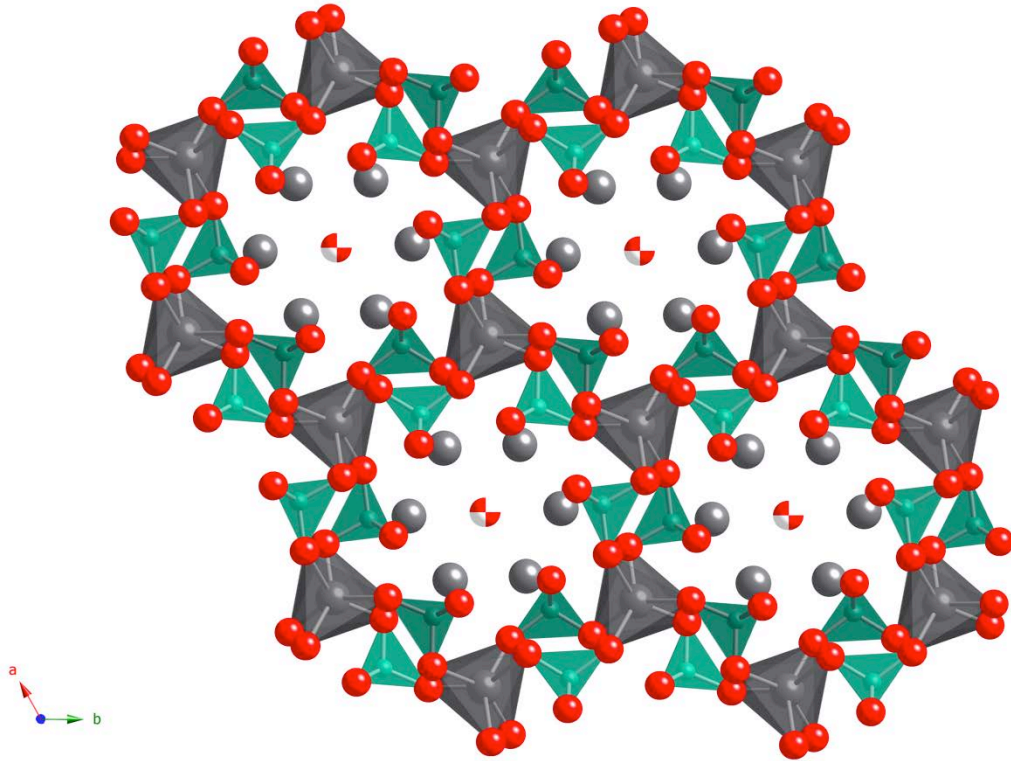
Figure 6.2. Extended polyhedral view of the crystal structure of $Ba_5(MnO_4)_3(OH)$, with oxygen atoms in red, MnO_4 tetrahedra in turquoise, metaprisms corresponding to the Ba1 site in grey, Ba2 atoms shown as grey spheres, and hydroxyl oxygens shown as split-tone spheres.
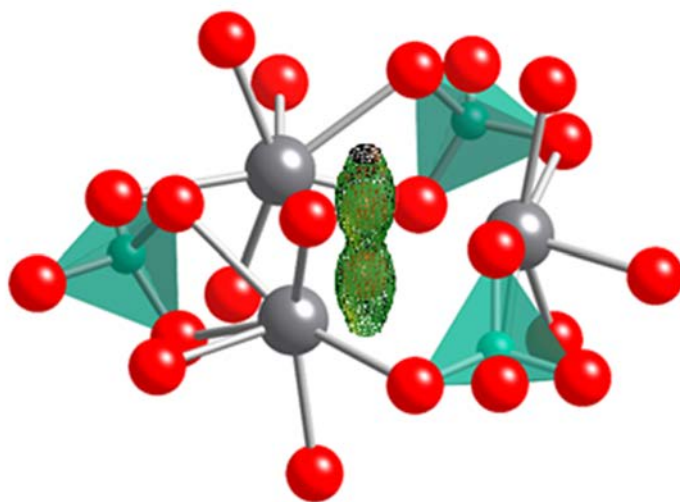
Figure 6.3. Difference electron density contour plot around the O4 position (the hydroxyl oxygen) in $Ba_5(MnO_4)_3(OH)$, showing the twofold disorderd split position. Ba2 is shown as grey spheres, MnO_4 tetrahedra are shown in turquoise and oxygen atoms are shown in red. The calculated peak magnitude is $8.04\ e^-/\text{Å}^3$.
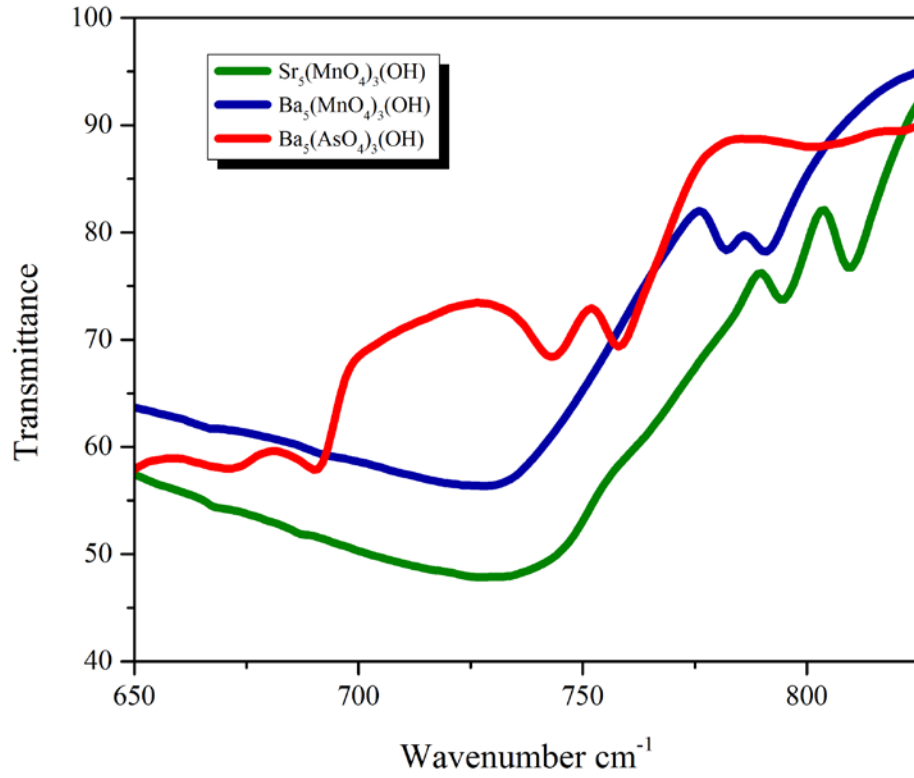
Figure 6.4. Infrared spectra of the hydroxyapatites in the range of 650-850 cm^{-1}.
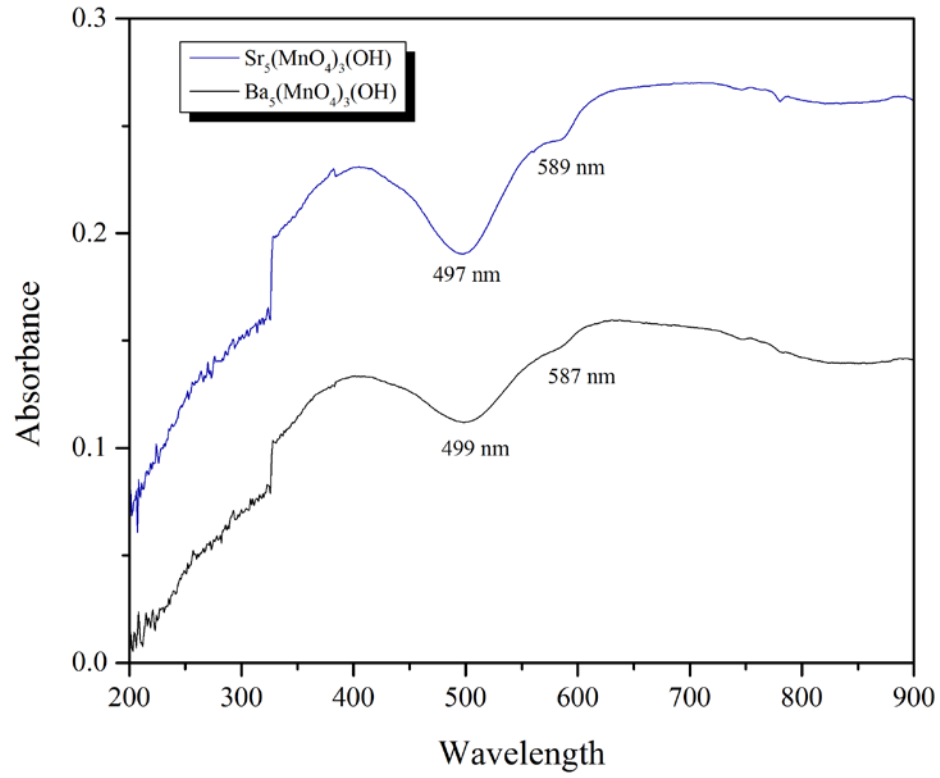
Figure 6.5. Diffuse reflectance spectra of .$Ba_5(MnO_4)_3(OH)$ and $Sr_5(MnO_4)_3(OH)$.

Table 6.1. Crystallographic Data for $A_5(MO_4)_3OH$[a]

Compound	$Sr_5(MnO_4)_3OH$	$Ba_5(MnO_4)_3OH$	$Ba_5(AsO_4)_3OH$
formula weight (g/mol)	811.93	1060.53	1120.47
color and habit	blue-green, needle	dark green, hexagonal needle	colorless, hexagonal rod
a (Å)	9.9543(12)	10.3761(2)	10.4585(2)
c (Å)	7.4270(18)	7.8582(2)	7.8391(3)
V (Å^3)	637.3(2)	732.69(3)	742.57.(4)
ρ_c (g cm^{-3})	4.231	4.807	5.011
μ (mm^{-1})	23.687	15.759	19.751
$F(000)$	740	920	968
crystal size (μm^3)	80 x 20 x 20	200 x 60 x 50	120 x 100 x 60
θ_{max} (°)	30.490	35.039	37.832
index ranges	-14<=h<=14, -14<=k<=14,	-16<=h<=16, -16<=k<=16,	-18<=h<=16, -15<=k<=18,

	-10<=l<=10	-11<=l<=12	-13<=l<=13
reflections collected	10480	18624	23400
independent reflections	701	1147	1412
goodness-of-fit on F^2	1.084	1.204	1.228
R indices (all data)	R1 = 0.0295, wR2 = 0.0502	R1 = 0.0259, wR2 = 0.0530	R1 = 0.0261, wR2 = 0.0579
largest peak and diffraction hole (e$^-$ Å^{-3})	0.793/-0.623	1.071/-1.128	2.220/-1.435

[a] For all structures, $T = 296(2)$ K, $\lambda = 0.71073$ Å, the space group is $P6_3/m$, and $Z = 2$.

Table 6.2. Atomic coordinates (x 10^4) and equivalent isotropic displacement parameters ($Å^2$x 10^3) for $Sr_5(MnO_4)_3OH$. U(eq) is defined as one third of the trace of the orthogonalized U_{ij} tensor.

	Occ	x	y	z	U(eq)
Sr(1)		3333	6667	19(1)	8(1)
Sr(2)		2557(1)	121(1)	2500	6(1)
Mn(1)		3668(1)	3973(1)	2500	6(1)
O(1)		1276(4)	5331(4)	2500	10(1)
O(2)		4822(4)	3166(4)	2500	10(1)
O(3)		2488(3)	3430(3)	691(3)	15(1)
O(4)	0.5	0	0	1931(10)	12(2)

Table 6.3. Atomic coordinates (x 10^4) and equivalent isotropic displacement parameters ($Å^2$x 10^3) for $Ba_5(MnO_4)_3OH$. U(eq) is defined as one third of the trace of the orthogonalized U_{ij} tensor.

	Occ	x	y	z	U(eq)
Ba(1)		3333	6667	16(1)	15(1)
Ba(2)		2591(1)	2420(1)	2500	16(1)
Mn(1)		328(1)	4009(1)	2500	11(1)
O(1)		4840(4)	1549(3)	2500	20(1)
O(2)		1260(4)	5904(3)	2500	20(1)
O(3)		917(3)	3475(3)	772(3)	24(1)
O(4)	0.5	0	0	1726(16)	39(3)

226

Table 6.4. Atomic coordinates (x 10^4) and equivalent isotropic displacement parameters ($Å^2$x 10^3) for $Ba_5(AsO_4)_3OH$. U(eq) is defined as one third of the trace of the orthogonalized U_{ij} tensor.

	Occ	x	y	z	U(eq)
Ba(1)		3333	6667	-11(1)	14(1)
Ba(2)		2588(1)	2419(1)	2500	14(1)
As(1)		330(1)	4015(1)	2500	11(1)
O(1)		4842(4)	1518(3)	2500	20(1)
O(2)		1235(4)	5880(4)	2500	21(1)
O(3)		877(3)	3468(3)	760(3)	25(1)
O(4)	0.5	0	0	1784(15)	30(2)

Table 6.5. Selected interatomic distances (Å) and angles (°) $A_5(MO_4)_3OH$

	$Sr_5(MnO_4)_3OH$	$Ba_5(MnO_4)_3OH$	$Ba_5(AsO_4)_3OH$
M(1)-O(3) x2	1.685(2)	1.693(2)	1.686(2)
M(1)-O(2)	1.700(3)	1.702(3)	1.689(3)
M(1)-O(1)	1.701(3)	1.702(3)	1.691(3)
O(3)-M(1)-O(3)#6	105.71(17)	106.72(16)	107.96(18)
O(3)-M(1)-O(2)	112.05(10)	106.75(11)	107.60(12)
O(3)-M(1)-O(1)	106.43(11)	112.23(11)	111.36(11)
O(2)-M(1)-O(1)	113.63(16)	111.77(16)	110.79(17)

227

Table 6.6. Metaprism twist angles, φ, (°) observed in $Sr_5(MnO_4)_3OH$, $Ba_5(MnO_4)_3OH$, and $Ba_5(AsO_4)_3OH$.

	$Sr_5(MnO_4)_3OH$	$Ba_5(MnO_4)_3OH$	$Ba_5(AsO_4)_3OH$
φ	24.8	22.5	22.1

Table 6.7. Calculated bond valence sums for $Sr_5(MnO_4)_3OH$, $Ba_5(MnO_4)_3OH$, and $Ba_5(AsO_4)_3OH$.

	A1	*A2*	*M*
$Sr_5(MnO_4)_3OH$	2.09	2.39	5.20
$Ba_5(MnO_4)_3OH$	2.24	2.38	5.20
$Ba_5(AsO_4)_3OH$	2.10	2.29	4.95

228

References

1. Pan, Y.; Fleet, M. E. *Rev. Mineral Geochem.* **2002**, *48*, 13.

2. Wu, P.; Zeng, Y. Z.; Wang, C. M. *Biomaterials* **2003**, *25*, 1123.

3. Roy, R. *Radioactive waste disposal.* Pergamon Press, New York 1982.

4. Lutze, W,; Ewing, R.C. *Radioactive waste forms for the future.* North-Holland, Amsterdam 1988.

5. Sansom, J. E. H.; Slater, P. R. *Solid State Ionics* **2004**, *167*, 23.

6. Kahlenberg, V.; Krüger, H. *Solid State Sci.* **2004**, *6*, 553.

7. Panteix, P. J.; Julien, I.; Bernache-Assollant, D.; Abélard, P. *Mater. Chem. Phys.* **2006**, *95*, 313.

8. Abram, E. J.; Kirk, C. A.; Sinclair, D. C.; West, A. R. *Solid State Ionics* **2005**, *176*, 1941.

9. Dobrowolski, R.; Mierzwa, J. *Mater. Chem. Phys.* **1993**, *34*, 270.

10. Budin, J. P.; Michel, J. C.; Auzel, F. *J. Appl. Phys.* **1979**, *50*, 441.

11. Laghzizil, A.; Barboux, P.; Bouhaouss, A. *Solid State Ionics* **2000**, *128*, 177.

12. Wright, A. O.; Seltzer, M. D.; Gruber, J. B.; Chai, B. H. T. *J. Appl. Phys.* **1995**, *78*, 2456.

13. Zahouily, M.; Abrouki, Y.; Bahlaouan, B.; Rayadh, A.; Sebti, S. *Catalysis Com.* **2003**, *4*, 521.

14. Lux, H. *Z. Naturforsch. Zeitschrift fuer Naturforschung* **1946**, *1*, 281.

15. Dardenne, K.; Vivien, D.; Huguenin, D. *J. Solid State Chem.* **1999**, *146*, 464.

16. Grisafe, D. A.; Hummel, F. A. *J. Solid State Chem.* **1970**, *2*, 160.

229

17. Reinen, D.; Rauw, W.; Kesper, U.; Atanasov, M.; Gudel, H. U.; Hazenkamp, M.; Oetliker, U. *J. Alloys Compd.* **1997**, *246*, 193.

18. Atanasov, M.; Adamsky, H.; Reinen, D. *Chem. Phys.* **1996**, *202*, 155.

19. Lachwa, H.; Reinen, D. *Inorg. Chem.* **1989**, *28*, 1044.

20. Reinen, D.; Lachwa, H.; Allmann, R. *Z. Anorg. Allg. Chemie.* **1986**, *542*, 71.

21. Merkle, L. D.; Guyot, Y.; Chai, B. H. T. *J. Appl. Phys.* **1995**, *577*, 474.

22. Merkle, L. D.; Pinto, A.; Verdun, H. R.; McIntosh, B. *Appl. Phys. Lett.* **1992**, *61*, 2386.

23. Jiang, P.; Li, J.; Ozarowski, A.; Sleight, A. W.; Subramanian, M. A. *Inorg Chem* **2013**, *52*, 1349.

24. Stone, M.; Lumsden, M.; Qiu, Y.; Samulon, E.; Batista, C.; Fisher, I. *Phys. Rev. B* **2008**, *77*,

25. Tsujii, H.; Andraka, B.; Uchida, M.; Tanaka, H.; Takano, Y. *Phys. Rev. B* **2005**, *72*,

26. Uchida, M.; Tanaka, H.; Bartashevich, M. I.; Goto, T. *J. Phys. Soc. Jap.* **2001**, *70*, 1790.

27. Uchida, M.; Tanaka, H.; Mitamura, H.; Ishikawa, F.; Goto, T. *Phys. Rev. B* **2002**, *66*, 054429.

28. Klemm, W.; Krause, J.; Wahl, K.; Huss, E.; Hoppe, R.; Weise, E.; Brandt, W. *Forschungsber. Wirtsch.-u. Verkehrsministeriums Nordrhein-Westfalen* **1955**, *N60*, 38.

29. Bugaris, D. E.; Smith, M. D.; zur Loye, H.-C. *Inorg. Chem.* **2013**, *52*, 3836.

30. Chance, W. M.; Bugaris, D. E.; Sefat, A. S.; zur Loye, H.-C. *Inorg. Chem.* **2013**, *52*, 11723.

230

31. Chance, W. M.; zur Loye, H.-C. *Solid State Sciences* **2014**, *28*, 90.

32. Mugavero, S. J.; Bharathy, M.; McAlum, J.; zur Loye, H.-C. *Solid State Sciences* **2008**, *10*, 370.

33. SMART Version 5.631, SAINT+ Version 6.45 and SADABS Version 2.10, Bruker Analytical X-ray Systems, Inc., Madison, Wisconsin, USA, 2003

34. Sheldrick, G. M. *Acta Crystallogr. A* **2008**, *64*, 112.

35. Hübschle, C. B.; Sheldrick, G. M.; Dittrich, B. *J. Appl. Crystallogr.* **2011**, *44*, 1281.

36. Parthé, E.; Gelato, L. M. *Acta Crystallogr. A.* **1984**, *40*, 169.

37. Gelato, L. M.; Parthé, E. *J. Appl. Crystallogr.* **1987**, *20*, 139.

38. Hu, S.-Z.; Parthe, E. *Chinese J. Struct. Chem. 23*, 1150.

39. Bell, A. M.; Henderson, C. M.; Wendlandt, R. F.; Harrison, W. J. *Acta Crystallogr. E* **2008**, *64*, i63.

40. Weil, M.; Đorđević, T.; Lengauer, C. L.; Kolitsch, U. *Solid State Sciences* **2009**, *11*, 2111.

41. Elliott, J. C. *Clinic Orthopaedics Related Res.* **1973**, *93*, 313.

42. O'Keeffe, M.; Hyde, B. G. *Struct. Bonding* **1985**, *61*, 79.

43. Beevers, C. A.; McIntyre, D. B. *Mineral Mag.* **1946**, *27*, 254.

44. Dong, Z.-L.; White, T. J. *Acta. Crystallogr. B* **2004**, *60*, 138.

45. Mercier, P. H. J.; Le Page, Y.; Whitfield, P. S.; Mitchell, L. D.; Davidson, I. J.; White, T. J. *Acta. Crystallogr. B* **2005**, *61*, 635.

46. White, T. J.; Dong, Z.-L. *Acta. Crystallogr. B* **2003**, *59*, 1.

47. Baran, E. J.; Aymonio, P. J. *Spectrochimica Acta.* **1963**, *24A*, 291.

48. Jellinck, F. J. *Inorg. Nucl. Chem.* **1960**, *13*, 329.

49. Steger, E.; Schmidt, W. *Ber. Busenges. Phys. Chem.* **1964**, *68*, 102.

50. Johnson, P. D.; Prener, J. S.; Kingsley, J. D. *Science* **1963**, *141*, 1179.

51. Brown, I. D. *The Chemical Bond in Inorganic Chemistry: The Bond Valence Model;* Oxford University Press: 2006.

Chapter 6.2: Crystal Growth, Structure, and Physical Properties of

KBaMnO$_4$

INTRODUCTION

Pentavalent manganese is rare in extended structures. Mn^{5+} in an oxide was first prepared by Lux from strong alkali solutions.[1] Most Mn^{5+} compounds previously synthesized were prepared by the solid state method under O_2 flow near 1000 °C[2, 34]. More recent investigations have prepared manganates via low temperature routes such as hydrothermal synthesis or flux growth. Much of the literature has focused on the intense colors exhibited by Mn^{5+} compounds [4-8], while other investigations have focused on the near infrared emission of manganates and their potential use in laser materials.[9, 10]. More recent studies of the magnetic properties of $Ba_3Mn_2O_8$ have brought renewed interest in the magnetic properties of solids with Mn^{5+}.[11-14]

Hydroflux synthesis offers a reaction media that bridges the gap between wet hydroxide fluxes and hydroxide composite hydrothermal reactions and allows for exploratory crystal growth. Previously, we have demonstrated its utility for the crystal growth of both hydroxides and oxides. [15-17] In the previous subchapter, the utility of hydroflux reactions for the synthesis of Mn^{5+} compounds was demonstrated and is further investigated herein. The synthesis of a new oxometallate, $KBaMnO_4$, is reported along with its crystal structure, optical, and magnetic properties.

EXPERIMENTAL METHODS

Reagents. The following reagents were used as obtained: KOH (Fisher Scientific, ACS grade pellets), NaOH (Fisher Scientific, ACS grade pellets), $Ba(OH)_2 \cdot 8H_2O$ (Alfa Aesar, 99+%), and $KMnO_4$ (Fisher Scientific, ACS Grade).

Crystal Growth. Crystal growth was carried out in a custom fabricated, virgin PTFE vessel with~23 mL total volume. No secondary containment was necessary for

237

pressure. 1.5 mmols of $Ba(OH)_2 \cdot 8H_2O$ and 1 mmol of $KMnO_4$ were added to a hydroflux made from 12 g of KOH and 4 g of water. The reaction mixtures were heated to 230 ºC at 5ºC per minute and held for 12 hours before being cooled at a rate of 0.3 ºC per minute to 80 C.

Magnetic Measurements. The DC magnetic susceptibility of $KBaMnO_4$ was measured as a function of temperature using a Quantum Design MPMS SQUID VSM. For a typical temperature sweep experiment, the sample was first cooled to 5 K under zero-field cooled (zfc) conditions and data were collected upon warming to 300 K in an applied field of 1000 Oe. Then the sample was field cooled (fc) to 5 K from room temperature in 1000 Oe while data were collected. Values of magnetization measured were corrected by a factor of 10%, based on field calibrations obtained from a Ni standard. All magnetic data presented in this chapter are preliminary.

Structure Determination. X-ray intensity data from a single crystal of $KBaMnO_4$ were collected at 296(2) K using a Bruker SMART APEX diffractometer (Mo Kα radiation, λ = 0.71073 Å).[18] The raw area detector data frames were reduced with SAINT+.[18] Data were corrected for absorption effects using the multi-scan technique implemented in SADABS.[18] The reported unit cell parameters were determined by least-squares refinement of large sets of strong reflections taken from each data set. Full-matrix least-squares refinement against F^2 of the structural models and difference Fourier calculations were performed with SHELXTL.[19] Detailed crystallographic data and selected interatomic distances for $KBaMnO_4$ are reported in Tables 6.8, 6.9, and 6.10.

RESULTS AND DISCUSSION

Synthesis. Phase pure samples of $KBaMnO_4$ crystals were obtained from the

hydroflux synthesis with a yield of 72% (Figure 6.6 and 6.7) from the experimental conditions described previously. Initially, crystals were grown from an open atmosphere reaction in a PTFE cup on a hot plate with the same hydroflux composition. Crystal quality was greatly increased by switching to sealed vessels and slow cooling in an oven. The solid hydroflux was still green after the reaction, indicating the incomplete reaction of the MnO_4^{3-}. Crystals were isolated by sonication in methanol. Small amounts of $BaCO_3$ were also formed and removed with a sieve.

Structure. The β-K_2SO_4 structure type (A_2MO_4), including structural variants, is often observed for oxometallates and simple salts such as Tl_2SO_4, Ba_2TiO_4, Ba_2CoO_4, Ba_2CrO_4, K_2CrO_4 and Tl_2CrO_4. More complex compositions, namely those containing two cations ($AA'MO_4$) (A = Na, K; A' = Sr, Ba) are found among the phosphates and vanadates, such as $KBaPO_4$, $KBaVO_4$, and some structurally related phases are found among the aluminates and gallates, including $BaLaAlO_4$ and $BaLaGaO_4$.

$KBaMnO_4$ crystallizes in the orthorhombic space group *Pnma*. The structure, shown in Figure 6.8, consists of isolated MnO_4^{3-} tetrahedra with the charge balance maintained by K^+ and Ba^{2+} cations. Each MnO_4 tetrahedron is surrounded by six K^+ and five Ba^{2+} cations, and shares its corner/edge with KO_{10} polyhedra and corner/edge/face with BaO_9 polyhedra, respectively. The KO_{10} polyhedra are connected to each other via face-sharing along the *b*-axis and corner/edge-sharing in the *ac*-plane. One interesting structural feature is the presence of hexagonal channels, created by the arrangement of the KO_{10} polyhedra, along the *a*-axis, which contain Ba^{2+} cations. (Figure 6.9) The BaO_9 polyhedra share their face, corner, and edge along the *a*-, *b*-, and *c*-axes, respectively, forming a 3D structure. The Mn-O bond distances in the MnO_4 tetrahedra range from

239

1.680(5) Å to 1.692(4) Å, which correspond well with previously reported Mn^{5+}-O bond lengths. Both K^+ and Ba^{2+} cations are observed in irregular polyhedra with distances to oxygen atoms of 2.774(5) – 3.205(4) and 2.688(4) – 3.133(2) for KO_{10} and BaO_9 polyhedra, respectively.

Bond Valence Analysis. Bond valence sum calculations[20] resulted in values of 2.20 and 0.87 for barium, and potassium, respectively. These values are in good agreement with the expected values for Ba^{2+} and K^+. There is no bond valence parameter listed for Mn^{5+}, however, the parameter for Mn^{6+} is 1.79 and was used as an approximate value. Using this value, the bond valence sum for manganese is calculated as 5.20.

Diffuse Reflectance. The diffuse reflectance spectra of $KBaMnO_4$ is plotted in Figure 6.10. There is an absorption peak in the spectrum at ~500 nm and another at ~582 nm. A number of articles have already discussed the energy states for Mn^{5+} in a tetrahedral field. According to prior assignments, the two peaks observed correspond to two electron transitions into the $^3T_1$ and $^3T_2$ energy substates. [2, 21] The slight deviation from previous reports can be ascribed to differences in bond energies and coordination environment compared to an idealized tetrahedron. An unexpected sharp decline in the absorbance is observed at ~340 nm for both samples. This artifact can be attributed to the switching of sources from tungsten to deuterium within the instrument.

Magnetism. The temperature dependence of the magnetic susceptibility (χ) for $KBaMnO_4$ was measured under zfc and fc conditions. Temperature dependence of the inverse susceptibility data were fit to the Curie-Weiss law where $\chi = C/(T-\theta)$; C is the Curie constant, and θ is the paramagnetic Weiss temperature. Paramagnetic behavior was observed down to ~5 K. $KBaMnO_4$ exhibits a moment of 2.80 μ_B, in good agreement

240

with that expected for Mn^{5+} (μ_{eff} = 2.83 μ_B, S = 1). (Figure 6.11) Below 7 K, a negative deviation from Curie-Weiss behavior was observed. The shortest intramanganese distance is 4.97 Å. No impurity was observed in the powder diffraction pattern, leaving the source of the deviation from idealized behavior unknown. One possible explanation is the existence of a nonmagnetic ground state, while another would be a small impurity of an antiferromagnetic material with a Neel temperature ~7 K. Further studies would need to be conducted to elucidate the cause of this behavior.

CONCLUSION

$KBaMnO_4$ has been grown for the first time using a low temperature hydroflux. The compound takes on the β-K_2SO_4 structure type. The crystals are a deep green color and optical properties have been investigated. The magnetic properties have been preliminarily investigated, suggesting no long range ordering and simple paramagnetic behavior down to ~7 K. Below that, a negative deviation from Curie-Weiss behavior is observed. Further investigation is needed to determine whether or not this feature is intrinsic to the structure.
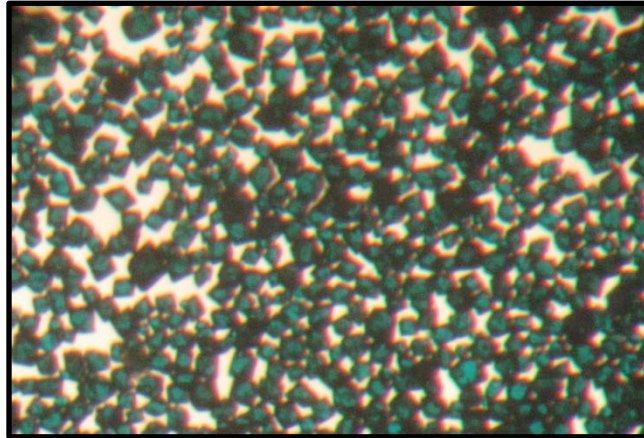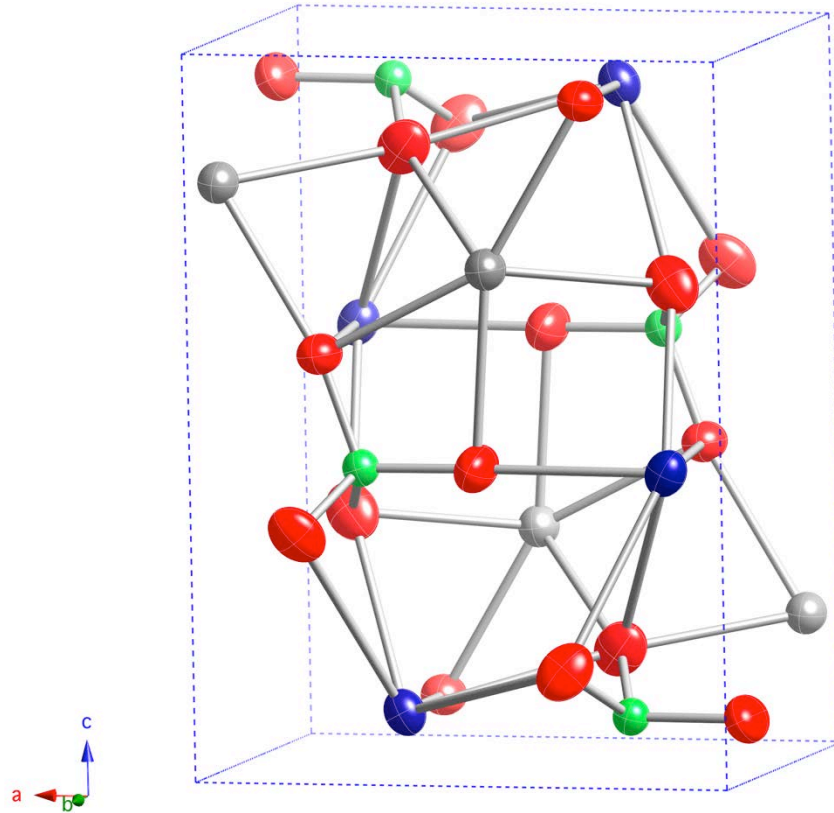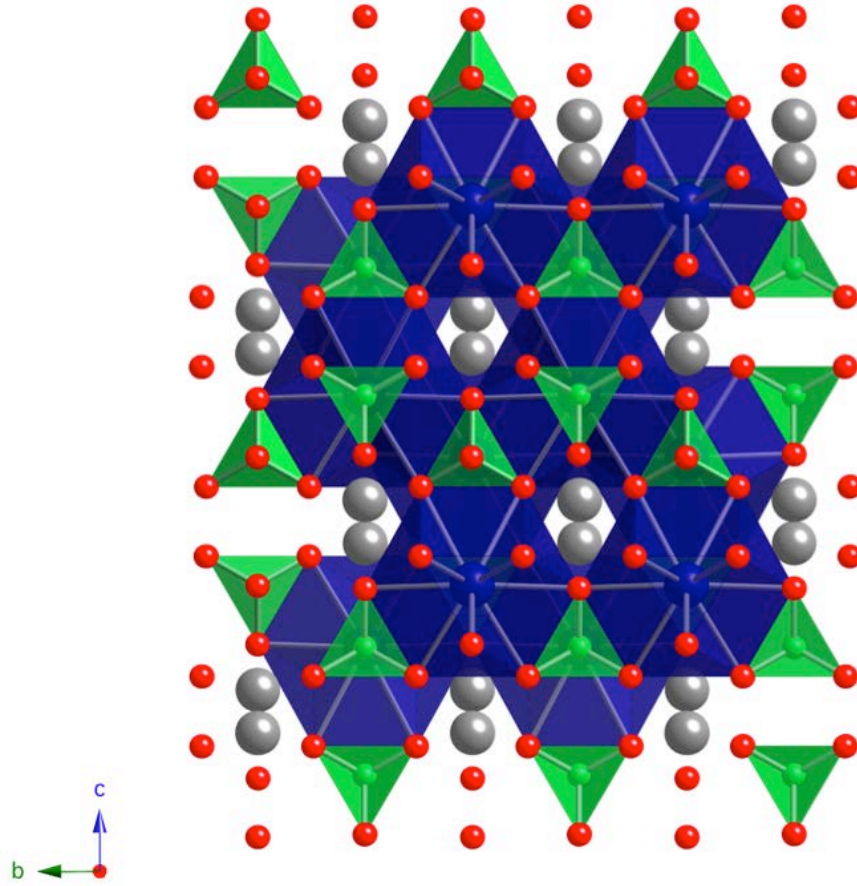
Figure 6.6. Optical image of a set of KBaMnO$_4$ crystals.
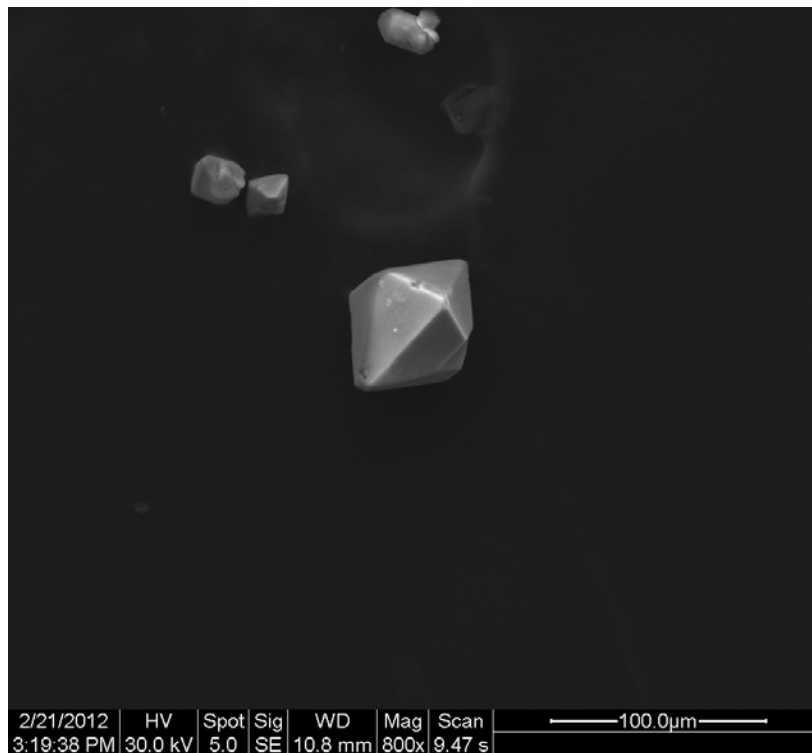
Figure 6.7. Scanning electron micrograph image of a KBaMnO$_4$ crystal.

242

Figure 6.8. Unit cell of KBaMnO₄, with oxygen atoms in red, manganese in green, barium atoms in grey, and potassium atoms in blue. All atoms are drawn as thermal ellipsoids at 90% probability.

Figure 6.9. Extended view of the crystal structure of KBaMnO$_4$, with oxygen atoms in red, MnO$_4$ tetrahedra in green, barium atoms in grey, and potassium coordination polyhedra shown down the *a* axis.

244
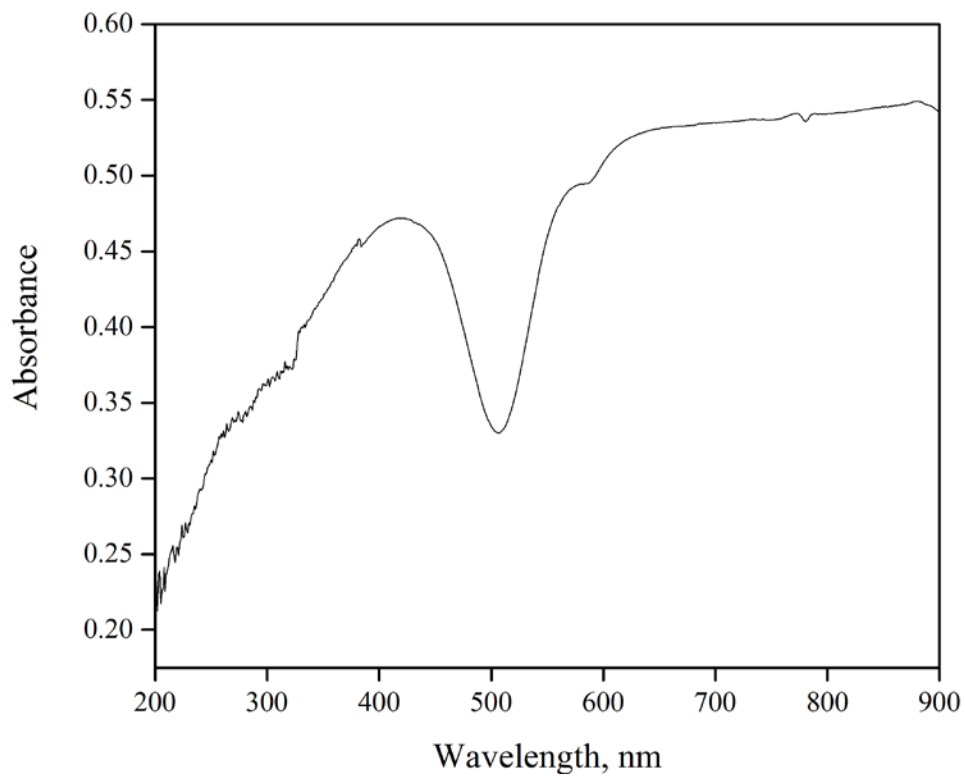
Figure   6.10.   Diffuse   reflectance   spectra   of   KBaMnO₄.
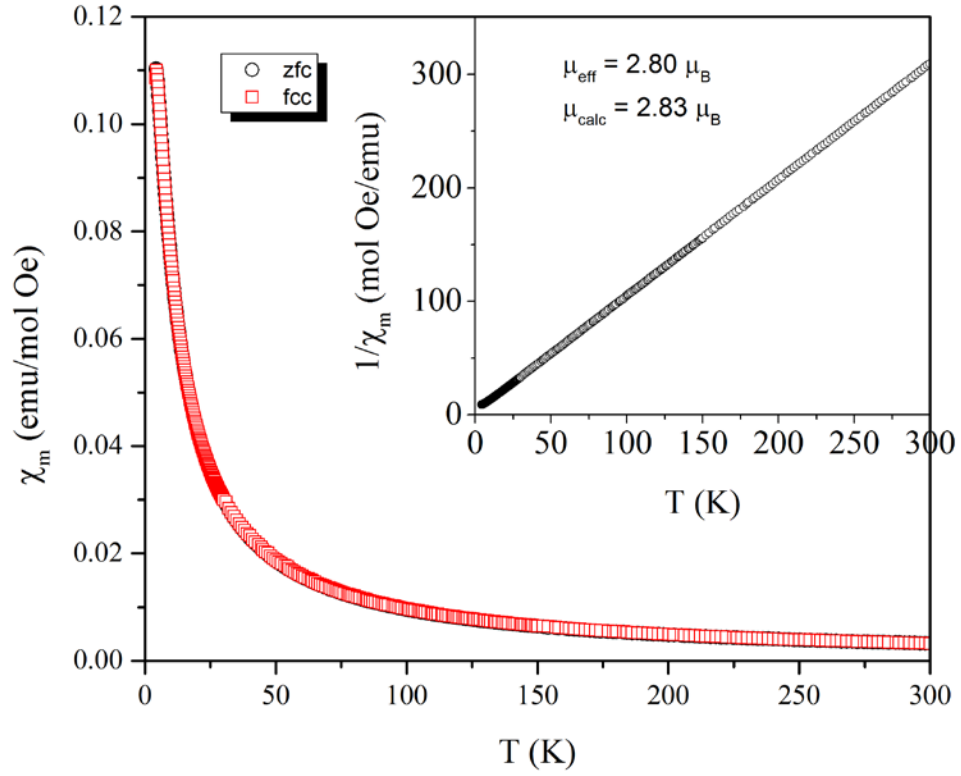
Figure 6.11. Temperature dependence of the molar magnetic susceptibility, χ_m, and inverse molar magnetic susceptibility, $1/\chi_m$, for KBaMnO$_4$ inset in the figure.

Figure 6.12. Low temperature region of the molar magnetic susceptibility, χ_m, and inverse molar magnetic susceptibility, $1/\chi_m$, for KBaMnO$_4$ inset in the figure.

Table 6.8. Crystallographic Data for $KBaMnO_4$[a]

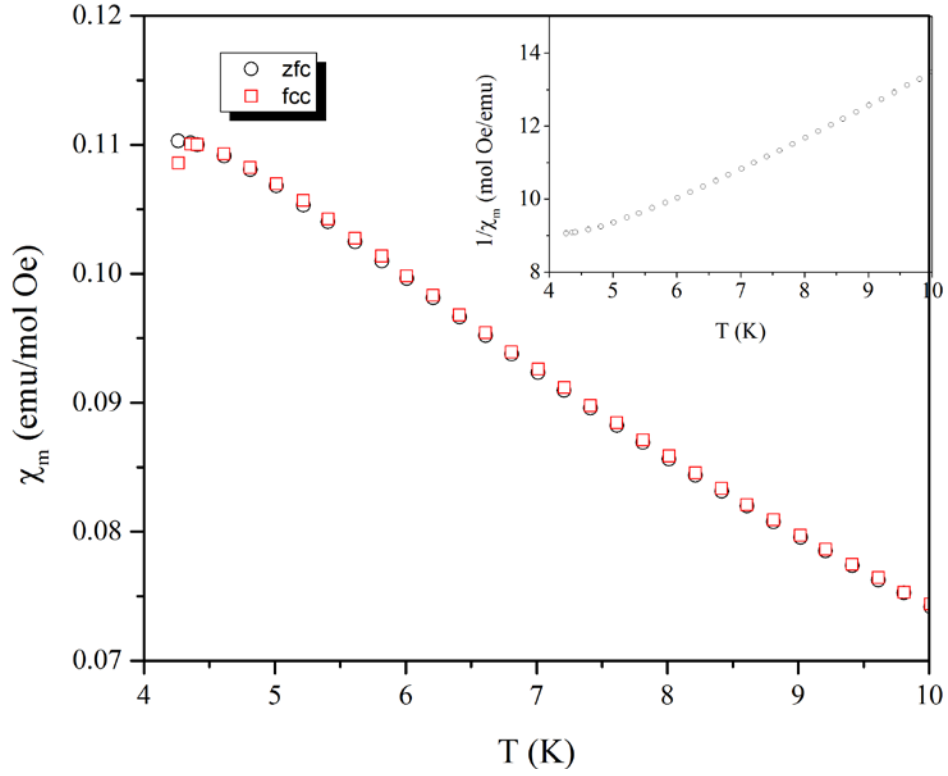| Compound	$KBaMnO_4$
formula weight (g/mol)	315.36
crystal system	Orthorhombic
space group	$P n m a$
color and habit	blue-green, polyhedral
a (Å)	7.7795(4)
b ((Å)	5.8263(3)
c (Å)	10.3104(13)
V (Å^3)	466.18(11)
Z	4
ρ_c (g cm^{-3})	4.436
μ (mm^{-1})	11.884
$F(000)$	528
crystal size (μm^3)	150 x 80 x 30
θ_{max} (°)	28.2594
index ranges	-10<=h<=10, -7<=k<=7, -13<=l<=13
reflections collected	5970
independent reflections	632
goodness-of-fit on F^2	1.172
R indices (all data)	R1 = 0.0258, wR2 = 0.0693
largest peak and diffraction hole (e$^-$ Å^{-3})	0.750/-1.413

[a] $T = 296(2)$ K, $\lambda = 0.71073$ Å

248

Table 6.9. Atomic coordinates and equivalent isotropic displacement parameters (Å^2) for KBaMnO$_4$. U_{eq} is defined as one third of the trace of the orthogonalized U_{ij} tensor.

	x	y	z	U_{eq}
Ba(1)	0.5093(1)	0.25	0.3070(1)	0.015(1)
K(1)	0.8416(2)	0.25	0.5833(2)	0.015(1)
Mn(1)	0.2677(1)	0.25	0.5819(1)	0.011(1)
O(1)	0.1941(7)	0.25	0.4265(5)	0.017(1)
O(2)	0.1973(5)	0.0105(6)	0.6582(4)	0.022(1)
O(3)	0.4851(6)	0.25	0.5809(6)	0.023(1)

Table 6.10. Selected interatomic distances (Å) and angles (°) KBaMnO$_4$

Mn(1)-O(3)	1.680(5)
Mn(1)-O(2)	1.680(3)
Mn(1)-O(2)	1.680(3)
Mn(1)-O(1)	1.692(4)
O(3)-Mn(1)-O(2)	109.04(17)
O(2)- Mn(1)-O(2)	111.1(3)
O(3)- Mn(1)-O(1)	109.3(3)
O(2)- Mn(1)-O(1)	109.14(16)

References

1. Lux, H. *Z. Naturforsch. Zeitschrift fuer Naturforschung* **1946**, *1*, 281.

2. Dardenne, K.; Vivien, D.; Huguenin, D. *J. Solid State Chem.* **1999**, *146*, 464.

3. Grisafe, D. A.; Hummel, F. A. *J. Solid State Chem.* **1970**, *2*, 160.

4. Jiang, P.; Li, J.; Ozarowski, A.; Sleight, A. W.; Subramanian, M. A. *Inorg Chem* **2013**, *52*, 1349.

5. Reinen, D.; Rauw, W.; Kesper, U.; Atanasov, M.; Gudel, H. U.; Hazenkamp, M.; Oetliker, U. *J. Alloys Compd.* **1997**, *246*, 193.

6. Atanasov, M.; Adamsky, H.; Reinen, D. *Chem. Phys.* **1996**, *202*, 155.

7. Lachwa, H.; Reinen, D. *Inorg Chem.* **1989**, *28*, 1044.

8. Reinen, D.; Lachwa, H.; Allmann, R. *Z. Anorg. Allg. Chemie* **1986**, *542*, 71.

9. Merkle, L. D.; Guyot, Y.; Chai, B. H. T. *J. Appl. Phys.* **1995**, *577*, 474.

10. Merkle, L. D.; Pinto, A.; Verdun, H. R.; McIntosh, B. *Appl. Phys. Lett.* **1992**, *61*, 2386.

11. Stone, M.; Lumsden, M.; Qiu, Y.; Samulon, E.; Batista, C.; Fisher, I. *Phys. Rev. B* **2008**, *77*,

12. Tsujii, H.; Andraka, B.; Uchida, M.; Tanaka, H.; Takano, Y. *Phys. Rev. B* **2005**, *72*,

13. Uchida, M.; Tanaka, H.; Bartashevich, M. I.; Goto, T. *J. Phys. Soc. Jap.* **2001**, *70*, 1790.

14. Uchida, M.; Tanaka, H.; Mitamura, H.; Ishikawa, F.; Goto, T. *Phys. Rev. B* **2002**, *66*, 054429.

15. Bugaris, D. E.; Smith, M. D.; zur Loye, H.-C. *Inorg. Chem.* **2013**, *52*, 3836.

251

16. Chance, W. M.; Bugaris, D. E.; Sefat, A. S.; zur Loye, H.-C. *Inorg. Chem.* **2013**, *52*, 11723.

17. Chance, W. M.; zur Loye, H.-C. *Solid State Sciences* **2014**, *28*, 90.

18. SMART Version 5.631, SAINT+ Version 6.45 and SADABS Version 2.10, Bruker Analytical X-ray Systems, Inc., Madison, Wisconsin, USA, 2003

19. SHELXTL Version 6.14, Bruker analytical X-ray Systems, Inc., Madison, WI, 2000

20. Brown, I. D. *The Chemical Bond in Inorganic Chemistry: The Bond Valence Model;* Oxford University Press: 2006.

21. Johnson, P. D.; Prener, J. S.; Kingsley, J. D. *Science* **1963**, *141*, 1179.